Faculty of Science

Institute of Earth and Environmental Science

Geohazards Research Group

OBJECT-BASED IMAGE ANALYSIS FOR DETECTING LANDFORMS DIAGNOSTIC OF NATURAL HAZARDS

Dissertation

For the Degree of Doctor of Natural Sciences (Dr. rer. nat.)

In the Scientific Discipline of Geohazards

University of Potsdam

Submitted by

Karolina KORZENIOWSKA

Potsdam, Germany

April 2017

Published online at the
Institutional Repository of the University of Potsdam:
URN urn:nbn:de:kobv:517-opus4-402240
http://nbn-resolving.de/urn:nbn:de:kobv:517-opus4-402240

Contents

Declaration of Authorship

I, Karolina Korzeniowska, declare that this thesis entitled, “Object-based image analysis for detecting landforms diagnostic of natural hazards” and the work presented within it are my own. I confirm that:

- This work was conducted wholly while in candidature for a research degree at Potsdam University.
- Where any part of this thesis has previously been submitted for a degree or any other qualification at this University or any other institution, this has been clearly stated.
- Where I have consulted the published work of others, this is always clearly attributed.
- Where I have quoted from the work of others, the source is always provided. With the exception of such quotations, this thesis is entirely my own work.
- I have acknowledged all main sources of help.
- Where the thesis is based on work conducted by myself jointly with others, I have made clear exactly what was done by others and what I have contributed myself.

Signed: _____

Date: _____

Acknowledgments

I would like to thank Dr. Roland Stengele and BSF Swissphoto GmbH, who provided me with an opportunity to perform my PhD research under the ALErT project. I would like to express my appreciation to my supervisor Prof. Dr. Oliver Korup for teaching me precision in performing scientific work, and for the hard questions, which incentivised me to widen my research from various perspectives. My sincere thanks also go to Dr. Yves Bühler and WSL-Institute for Snow and Avalanche Research SLF for their cooperation, and sharing data and knowledge concerning snow avalanches. I would like to express my sincere gratitude to Prof. Dr. Norbert Pfeifer and GEO, TU Wien for tutoring and sharing knowledge concerning remote sensing in the time before I started my PhD study. Finally, yet importantly, I thank all co-authors of my articles for their insightful comments and suggestions that helped to improve the quality of my work.

This research was funded by the European Union under the Marie Curie Initial Training Network ALErT, project-number: FP7-PEOPLE-2013-ITN-607996.

The LiDAR data used in the study were provided by the U.S. Geological Survey through the Open Topography Facility, with support from the National Science Foundation under NSF Award Numbers 0930731 and 0930643, available from http://opentopo.sdsc.edu/, and the Alaska Division of Geological & Geophysical Surveys online map “Elevation Datasets in Alaska”, available from http://maps.dggs.alaska.gov/elevationdata/. The LANDSAT images were provided by the U.S. Geological Survey, available from http://espa.cr.usgs.gov/. The SRTM DEM version 4 data were provided by the CGIAR-CSI, available from http://srtm.csi.cgiar.org/. The ADS40 airborne images and historical snow avalanche data for Switzerland were provided by the WSL-Institute for Snow and Avalanche Research SLF, Davos.

Abstract

Natural and potentially hazardous events occur on the Earth's surface every day. The most destructive of these processes must be monitored, because they may cause loss of lives, infrastructure, and natural resources, or have a negative effect on the environment. A variety of remote sensing technologies allow the recoding of data to detect these processes in the first place, partly based on the diagnostic landforms that they form. To perform this effectively, automatic methods are desirable.

Universal detection of natural hazards is challenging due to their differences in spatial impacts, timing and longevity of consequences, and the spatial resolution of remote-sensing data. Previous studies have reported that topographic metrics such as roughness, which can be captured from digital elevation data, can reveal landforms diagnostic of natural hazards, such as gullies, dunes, lava fields, landslides and snow avalanches, as these landforms tend to be more heterogeneous than the surrounding landscape. A single roughness metric is often limited in such detections; however, a more complex approach that exploits the spatial relation and the location of objects, such as object-based image analysis (OBIA), is desirable.

In this thesis, I propose a topographic roughness measure derived from an airborne laser scanning (ALS) digital terrain model (DTM) and discuss its performance in detecting landforms principally diagnostic of natural hazards. I further develop OBIA-based algorithms for the detection of snow avalanches using near-infrared (NIR) aerial images, and the size (changes) of mountain lakes using LANDSAT satellite images. I quantitatively test and document how the level of difficulty in detecting these very challenging landforms depends on the input data resolution, the derivatives that could be evaluated from images and DTMs, the size, shape and complexity of landforms, and the capabilities of obtaining the information in the data. I demonstrate that surface roughness is a promising metric for detecting different landforms in diverse environments, and that OBIA assists significantly in detecting parts of lakes and snow avalanches that may not be correctly assigned by applying only the thresholding of spectral properties of data and their derivatives.

The curvature-based surface roughness parameter allows the detection of gullies, dunes, lava fields and landslides with a user's accuracy of 0.63, 0.21, 0.53, and 0.45, respectively. The OBIA algorithms for detecting lakes and snow avalanches obtained user's accuracy of 0.98, and 0.78, respectively. Most of the analysed landforms constituted only a small part of the entire dataset, and therefore the user's accuracy is the most appropriate performance measure that should be given in a such classification, because it tells how many automatically-extracted pixels in fact

represent the object that one wants to classify, and its calculation does not take the second (background) class into account. One advantage of the proposed roughness parameter is that it allows the extraction of the heterogeneity of the surface without the need for data detrending. The OBIA approach is novel in that it allows the classification of lakes regardless of the physical state of their water, and also allows the separation of frozen lakes from glaciers that have very similar water indices used in purely optical remote sensing applications. The algorithm proposed for snow avalanches allows the detection of release zones, tracks, and deposition zones by verifying the snow heterogeneity based on a roughness metric evaluated from a water index, and by analysing the local relation of segments with their neighbouring objects. This algorithm contains few steps, which allows for the simultaneous classification of avalanches that occur on diverse mountain slopes and differ in size and shape.

This thesis contributes to natural hazard research as it provides automatic solutions to tracking six different landforms that are diagnostic of natural hazards over large regions. This is a step toward delineating areas susceptible to the processes producing these landforms and the improvement of hazard maps.

Zusammenfassung

Naturgefahren und potenziell gefährliche Ereignisse der Erdoberfläche treten jeden Tag auf. Prozesse mit Zerstörungswirkungen sollten identifiziert werden, weil sie Gefahren für besiedelte Gebiete sowie menschliches Leben haben können. Naturgefahren haben erhebliche Einflüsse auf die Umwelt. Eine Vielzahl von Fernerkundungstechnologien, die heutzutage verfügbar sind, erlauben die Aufnahme und Speicherung von Datensätzen, die bei der Erkennung solcher Naturgefahren helfen können. Eine wichtige Grundlage dafür stellt die diagnostische Landform dar, welche die Naturgefahr ausbildet. Für eine effiziente Analyse sind automatische Methoden wünschenswert.

Die Verwendung einer universellen Methode zur Erkennung von Naturgefahren ist deshalb eine Herausforderung, weil die räumlichen Ausdehnungen unterschiedlich sind. So können diese unterschiedlichen Alters sein und verschiedene räumliche Auflösungen in Fernerkundungsdaten besitzen. Dies beeinflusst den Detailierungsgrad bei der Abbildung der Erdoberfläche. Frühere Studien zeigen, dass Ableitungen wie beispielweise die Rauheit, die von Fernerkundungsdaten erfasst werden kann, es erlauben, Naturgefahrenphänomene wie z. B. Erosionsrinnen, Dünen, Lavafelder, Erdrutsche und Schneelawinen zu erkennen, weil sie heterogener sind als umgebende Objekte. Dennoch ist es nicht zulässig, allein mittels der eigenständigen Rauheit eine Unterscheidung zwischen den erfassten Landschaftsformen vorzunehmen. Hier ist ein komplexer Ansatz wie die Objektbasierte Bildanalyse (OBIA) wünschenswert, weil ein solcher sowohl die räumliche Relation als auch die Lage von Objekten verwendet.

In dieser Dissertation schlage ich einen Oberflächenrauhigkeitsindex, abgeleitet aus einem durch Airborne Laserscanning (ALS) erfassten digitalen Geländemodells (DTM), vor und diskutiere die Faktoren, die die Darstellung von Naturgefahrenphänomenen mittels dieser Variable beeinflussen. Ich präsentiere auch OBIA-basierte, automatische Algorithmen für die Erkennung von Schneelawinen welche aus Nah-Infrarot (NIR) Luftbildern ausgewertet wurden sowie den Verlauf einer Seegrenze, die auf LANDSAT Satellitenbildern abgebildet wird. Ich zeige weiterhin, dass der Schwierigkeitsgrad für die Erfassung der analysierten Phänomene variabel und abhängig von den Dateneigenschaften, der Komplexität der getrackten Phänomene sowie von den qualitativen Ausprägungen des Informationsgehaltes ist. Ferner werde ich zeigen, dass die vorgeschlagene Oberflächenrauhigkeit die räumliche Ausdehnung der verschiedenen Phänomene zu bestimmen erlaubt, und dass der OBIA-Ansatz deutlich bei der Erkennung von

Objekten und derjenigen Teile hilft, die nicht korrekt nur durch Verwendung spektraler Eigenschaften von Daten und deren Derivaten zugewiesen werden konnten.

Der krümmungsbasierte Oberflächenrauhigkeitindex ermöglicht die Erkennung von Erosionsrinnen, Dünen, Lavafeldern, und Erdrutschen mit einer Benutzergenauigkeit von: 0.63, 0.21, 0.53 und 0.45. Vergleichend dazu erzielen die vorgestellten OBIA-Algorithmen für die Erfassung von Seen und Schneelawinen eine Benutzergenauigkeit von 0.98 und 0.78. Die in dieser Arbeit analysierten Landformen stellen einen Ausschnitt aus dem Gesamtspektrum vorkommender Strukturen dar. Die Benutzergenauigkeit stellt dabei den am besten geeigneten Leistungsindex dar, auf dem basierend eine Klassifikation durchgeführt werden kann. Die Benutzergenauigkeit gibt an, wie viele der automatisch extrahierten Pixel das zu klassifizierende Objekt tatsächlich repräsentieren. Eine Betrachtung einer zweiten (Hintergrund-) Klasse muss durch diesen Ansatz nicht erfolgen. Ein Vorteil des vorgeschlagenen Oberflächenrauhigkeitindex ist, dass er die Extraktion der Heterogenität der Oberfläche ohne die Notwendigkeit eines Daten-detrendings ermöglicht. Der OBIA-Ansatz für die Erfassung von Seegrenzen erlaubt es einerseits, Seen ungeachtet der physikalischen Zustände des Wassers zu klassifizieren und anderseits gefrorene Seen von den Gletschern zu unterschieden, welche ähnliche Eigenschaften beim Wasserindex aufweisen. Der für Schneelawinen vorgeschlagene Algorithmus wiederum ermöglicht insgesamt die Erfassung von Anbruchgebieten, Sturzbahnen und Ablagerungszonen durch Verifikation der Schneeheterogenität sowie die lokalen Beziehungen zu benachbarten Objekten. Dieser Algorithmus enthält einige Schritte, die es erlauben, gleichzeitig Lawinen zu klassifizieren, die in verschiedenen Berghängen auftreten und unterschiedliche Größen und Formen haben.

Diese Dissertation trägt zur Naturgefahrenforschung bei, da sie automatische Lösungen für das Monitoring von sechs verschiedenen Landformen bietet, die typisch für Naturgefahren sind. Es wird somit dazu beigetragen, Gebiete abgrenzbar zu machen, welche für das Auftreten von Gefahrenphänomenen besonders anfällig sind. Zudem können damit auch Verbesserungen bei der Erstellung von Gefahrenkarten erreicht werden.

Abbreviations

ALS	Airborne Laser Scanning
a.s.l.	above sea level
AUC	Area Under the Curve
$AWEI_{nsh}$	Automated Water Extraction Index for non-shadows
$AWEI_{sh}$	Automated Water Extraction Index for shadows
DEM	Digital Elevation Model
DSM	Digital Surface Model
DTM	Digital Terrain Model
FN	false negatives
FP	false positives
GEOBIA	Geographical Object-Based Image Analysis
GLCM	grey-level co-occurrence matrix
GWEM	LANDSAT GeoCover™ mosaics
LiDAR	Light Detection and Ranging
MAD	Directional Image Texture Analysis Operator
MNDWI	Modified Normalised Difference Water Index
MODIS	Moderate Resolution Imaging Spectroradiometer
μ	(gr. Mu) Roughness Index
NDAI	Normalised Difference Angle Index
NDVI	Normalised Difference Vegetation Index
NDWI	Normalised Difference Water Index
NIR	near-infrared
OBIA	Object-Based Image Analysis

$\mathbf{p_e}$	hypothetical probability of chance agreement
$\mathbf{p_o}$	relative observed agreement among rates
ρ	(gr. Rho) image band
RAMMS	Rapid Mass Movement Simulation
RMS	root-mean-square
ROC	Receiver Operating Characteristic
$\mathbf{SD_{NDWI}}$	Standard Deviation of Normalised Difference Water Index
SR	at-sensor spectral radiance
SRTM	Shuttle Radar Topography Mission
SWIR	short-wave infrared
TanDEM-X	TerraSAR-X-Add-on for Digital Elevation Measurements
TN	true negatives
TOA	top-of-atmosphere
TP	true positives
UAV	Unmanned Aerial Vehicles
WI	Water Index

List of Figures

List of Tables

Chapter 1

Introduction

1.1. Motivation

Natural hazards are processes on the Earth that have a possible negative impact on people and the environment (Gill and Malamud, 2017). Most of the landforms formed by these processes can be detected, monitored and systematically analysed from remote sensing data. For larger regions and increasing amounts of sensors and data, however, automatic methods are becoming increasingly essential for allowing fast, objective and standardised processing. Satellite and aerial photos, together with elevation data, are the basis for a variety of derivatives that use the spectral properties of pixels and the topography that gives rise to natural hazards. Apart from traditional pixel-based approaches, object-based image analysis (OBIA) classification has emerged as a machine-learning method that groups pixels together with their spatial arrangement. This is an advantage in classifying natural hazard landforms on the Earth's surface, because every object has its general spatial context (Blaschke, 2010). In this thesis, I selected different types of landforms diagnostic to natural hazards with different sizes and patterns to test how OBIA performs on such a variety of objects. My work will address five specific research questions regarding tested several derivatives that can be evaluated from remote sensing data and their use in an OBIA method for detecting different types of natural hazards. Fast and effective tracking of these phenomena is necessary to quantify the frequency and the size of events, to improve warning systems, and to estimate how hazards change with time (Liu and Hodgson, 2016).

1.2. Landforms diagnostic of natural hazards

From a variety of natural hazards occurring across the world, I selected six different types of diagnostic landforms: gullies, dunes, lava fields, and landslides located in the eastern part of the United States, North America; lakes spread throughout the Tibetan Plateau, Asia; and snow avalanches triggered in the Swiss Alps, Europe (Fig. 1.1). All of these landforms attest to past or potential impacts on human activity and safety. For example, gullies are landforms that result from soil erosion and degradation, and are often tied to agricultural use (Poesen, 2011). Dunes may also arise in this context, but more generally result from Aeolian erosion and deposition. Active dunes may destroy forests by backfilling trees, or may block roads and or other

communication tracks (Lam et al., 2011). Lava fields occur as a consequence of the outflow of lava from a crater (Deardorff and Cashman, 2012); this process is often very rapid and may be dangerous to human lives. Landslides arise from unstable hill slopes and may occur rapidly, via sudden movement of soil, debris, or rocks down a slope, or very slowly, by constant movement of hill slope-forming materials (Pike, 1988). Lakes may also be considered natural hazards, especially when changing in size (Song et al., 2014a). A decrease in lake size reduces water

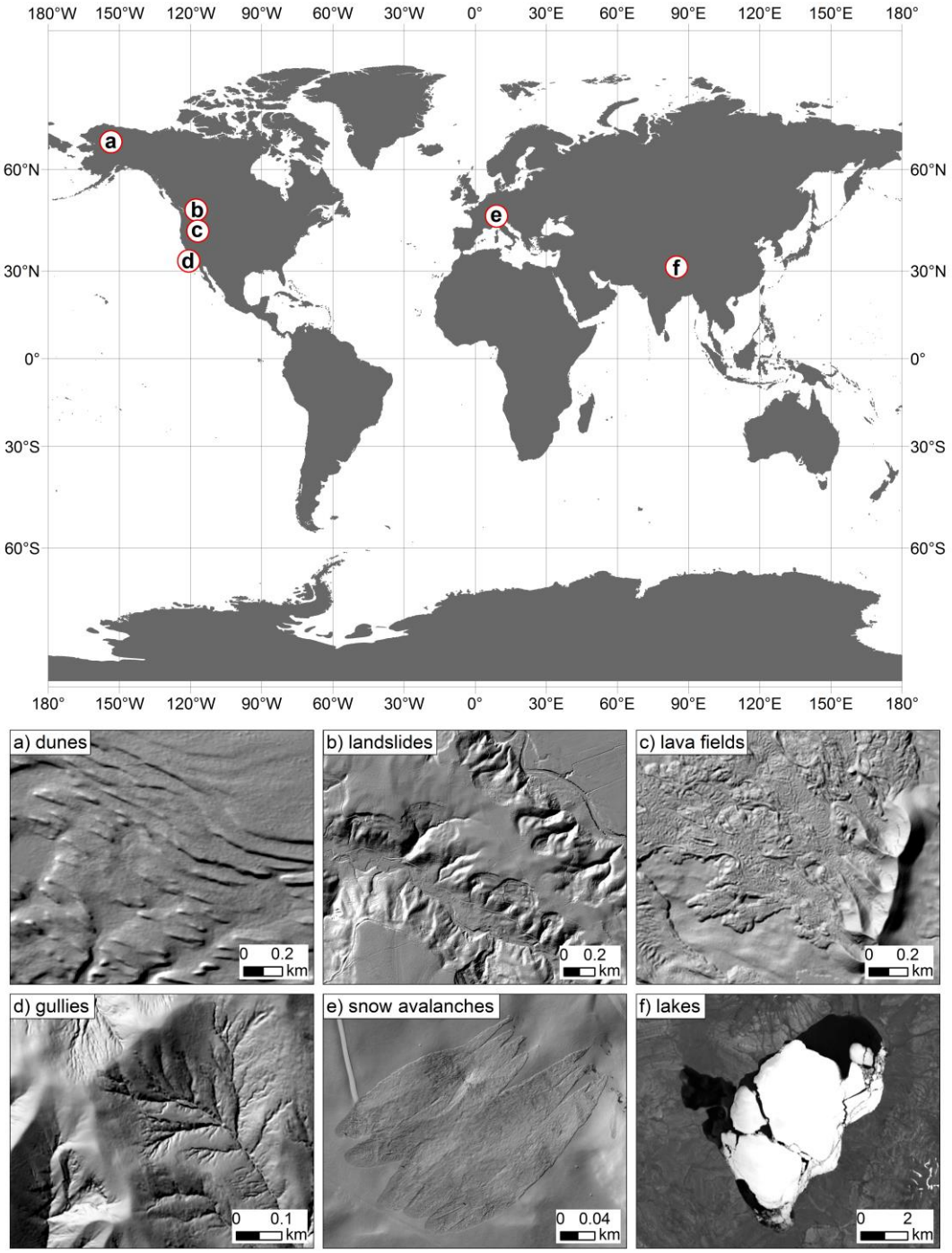

Figure 1.1 | Selected natural-hazard phenomena and their geographical location: a) dunes in Alaska, USA; b) landslides in Oregon, USA; c) lava fields at Collier Cone, Oregon, USA; d) gullies on Santa Cruz Island, California, USA; e) snow avalanches in the Swiss Alps, Switzerland; and f) lakes on the Tibetan Plateau, China.

availability and compromises freshwater resources, whereas an increase in lake size may flood areas intended for land use. Changes in lake size may also be indicators of climate changes, because the supply of water from a glacier may suggest that the average temperature in the region has risen. Snow avalanches cause many deadly accidents in the winter season in mountainous areas (Techel et al., 2016) and their rapid occurrence makes it difficult to have sufficient warning. Hence, analysing the weather and snow conditions, combined with the mapping of past events, may improve the safety of people by generating more accurate and detailed snow avalanche hazard maps.

1.3. Remote sensing data and their application for natural hazards

Remote sensing technologies provide us with optical, thermal, hyperspectral, radar, and 3D information about the Earth, which can be used to recognise a variety of landforms and to track their spatio-temporal changes (Singh, 1989; Melesse et al., 2007; Arp et al., 2012). To collect these data, we can use passive remote sensing, where the sensor detects electromagnetic waves reflected from the Earth's surface, or active remote sensing, where the object reflects an electromagnetic wave signal from the instrument (Fig. 1.2). An advantage of active over passive methods is that they are capable of being used anytime, even during the night when there is no daylight to illuminate the Earth's surface. Another factor influencing the resolution and the accuracy of the data collected is the satellite, aircraft, or terrestrial platform from which data is acquired, and the altitude at which the platform is located.

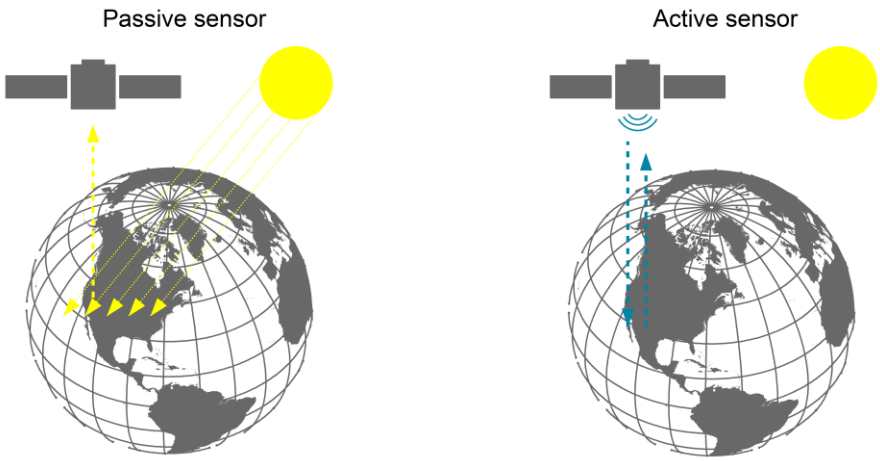

Figure 1.2 | Differences in data acquisition when using passive and active sensors. Passive sensors detect the sun's energy reflected from the Earth's surface, whereas active sensors send a signal and measure the information that is reflected by the object.

Optical remote sensing data have applications in classifying many kinds of objects on the Earth's surface (Cheng and Han, 2016), and most studies have focused on land cover classification (Chen et al., 2007; Friedl et al., 2010; Schneider, 2012) and tracking changes in land cover (Byrne et al., 1980; Collins and Woodcock, 1996; Lunetta et al., 2006). Nevertheless, some attempts to use remote sensing data in detecting processes and landforms diagnostic to natural hazards exist. For

example, LANDSAT and MODIS satellite images were used to identify environmental hazards, such as the extent of glaciers in Svalbard (Pope and Rees, 2014), the beginning of forest fire season in Canada (Sekhon et al., 2010), and mapping tidal flats over a large area in China (Murray et al., 2012). In contrast, elevation data from the released Shuttle Radar Topography Mission (SRTM) were used to identify different types of topography nearly worldwide (Drăguţ and Eisank, 2012). Higher resolution light detection and ranging (LiDAR) data found an application in mapping terrain landforms such as drumlins (Eisank et al., 2014), including those diagnostic of natural hazards such as landslides (Booth et al., 2009; Van Den Eeckhaut et al., 2012; Chen et al., 2014) and gullies (Perroy et al., 2010; Baruch and Filin, 2011; Höfle et al., 2013). In addition, remote sensing data have been used for other hazardous processes, such as detecting changes in Himalayan glaciers (Chand and Sharma, 2015), flood modelling in the United Kingdom (Mason et al., 2016), and the measurement of global volcanic degassing (Carn et al., 2016).

In this thesis, I used both passive and active data, with different resolutions and acquired from diverse aircraft, to automatically identify and map gullies, dunes, lava fields, landslides, lakes, and snow avalanches. The active airborne laser scanning (ALS) LiDAR data allow for representation of the Earth's surface in a three-dimensional point cloud, and their spatial resolution allows one to obtain higher level of details than that with SRTM data, what makes them sufficient to evaluate the local heterogeneity of selected natural-hazard landforms. The passive LANSDAT images that I used have a 30 × 30 m resolution and provide information on visible, near-infrared (NIR), and short-infrared (SWIR) light spectra, providing an opportunity to find the best band ratio separating lakes from other land cover classes. In addition, NIR aerial images with 0.25 m resolution obtained with sufficient coverage allow the generation of 3D information from image stereomatching. Using spectral information of images and elevation data in combination is an advantage when mapping snow avalanches and assigning their release and runout zones.

1.4. Object-based image analysis and its application for natural hazards

With the increase in the amount of available remote sensing data, automatic approaches for their classification are required to keep up. Numerous algorithms have been developed in this regard, and most operate on a pixel-by-pixel basis. In contrast, OBIA, or geographical object-based image analysis (GEOBIA), is a method which may be applied to extract different types of objects on the Earth's surface, and a viable alternative to the pixel-based approach (Blaschke, 2010; Blaschke et al., 2014). Furthermore, OBIA includes two main steps – image segmentation and object classification (Cheng and Han, 2016). The segmentation step allows information to be gathered the statistics of every segment, such as the minimum, the maximum, the mean, the median, and the standard deviation (Blaschke, 2010). This offers a greater diversity from which

to select the most suitable variable to reduce random, unstructured noise (salt-and-pepper noise) in the classification, which usually occurs when operating on pixels only. In addition, OBIA allows verification of the shape, texture, and spatial relation between neighbouring segments by analysing their topology, distances, and spatial relation (Blaschke et al., 2014). This enables the analysis of the local neighbourhood of segments that represent the objects of interest, but do not fulfil the assumptions to be assigned to this class due to their spectral properties (Price, 1994).

In the segmentation step of OBIA, pixels are partitioned into larger, more compact pieces called 'segments' or 'objects' (Cheng and Han, 2016). Segmentation can to be conducted by many different algorithms (Dey et al., 2010). In eCognition version 9.1, which I used in this thesis, to perform the segmentation and OBIA workflow, several methods are available: chessboard segmentation, quadtree-based segmentation, contrast split segmentation, multiresolution segmentation, special difference segmentation, multi-threshold segmentation, contrast filter segmentation and watershed segmentation (Trimble, 2015). Among these methods, I will focus here only on the first four, as these allow for the first stage of segmentation. The chessboard segmentation (Fig. 1.3.a) splits an image into square segments with a specified object size; by selecting the object size equal to unity, each individual pixel is maintained as a separate segment. The quadtree-based segmentation (Fig. 1.3.b) splits an image by subdividing the image each time into four smaller squares successively; this process ends when the homogeneity inside the square does not exceed the specified maximal colour difference, which is set as a threshold. The contrast split segmentation (Fig. 1.3.c) initially uses chessboard segmentation to tile an image into smaller pieces, and then divides the image into bright and dark objects by maximising the contrast of pixels with respect to a user-defined threshold. Finally, the multiresolution segmentation (Fig. 1.3.d) uses the average heterogeneity of image objects to compute homogeneous segments; the parameters that control the segmentation process here are scale, shape, and compactness. The choice of a segmentation method is essential, because the selected algorithm and its parameters control the subsequent workflow in the classification. For example, chessboard segmentation with an object size equal to unity (one pixel = one segment) should be chosen when one desires to operate on pixels and additionally apply assumptions regarding the neighbouring pixels and their special location. Using this approach with larger objects, such as those in Figure 1.3.a, would be pointless, however, because it would no longer reflect the real boundaries of objects on an image. Here, quadtree-based segmentation may offer a solution; however, for many areas it produces oversegmentation, meaning the generation of many small segments that are disproportionate in size with respect to objects in the image. With split segmentation, it is possible to delineate more realistic boundaries of objects, but their correctness depends on the selected tile size for chessboard segmentation and on the objects occurring in every tile. The algorithm that allows for a more realistic representation of objects' boundaries is the multiresolution

segmentation (Baatz and Schäpe, 2000), because it does not use a square area as the basis to split an image into segments.

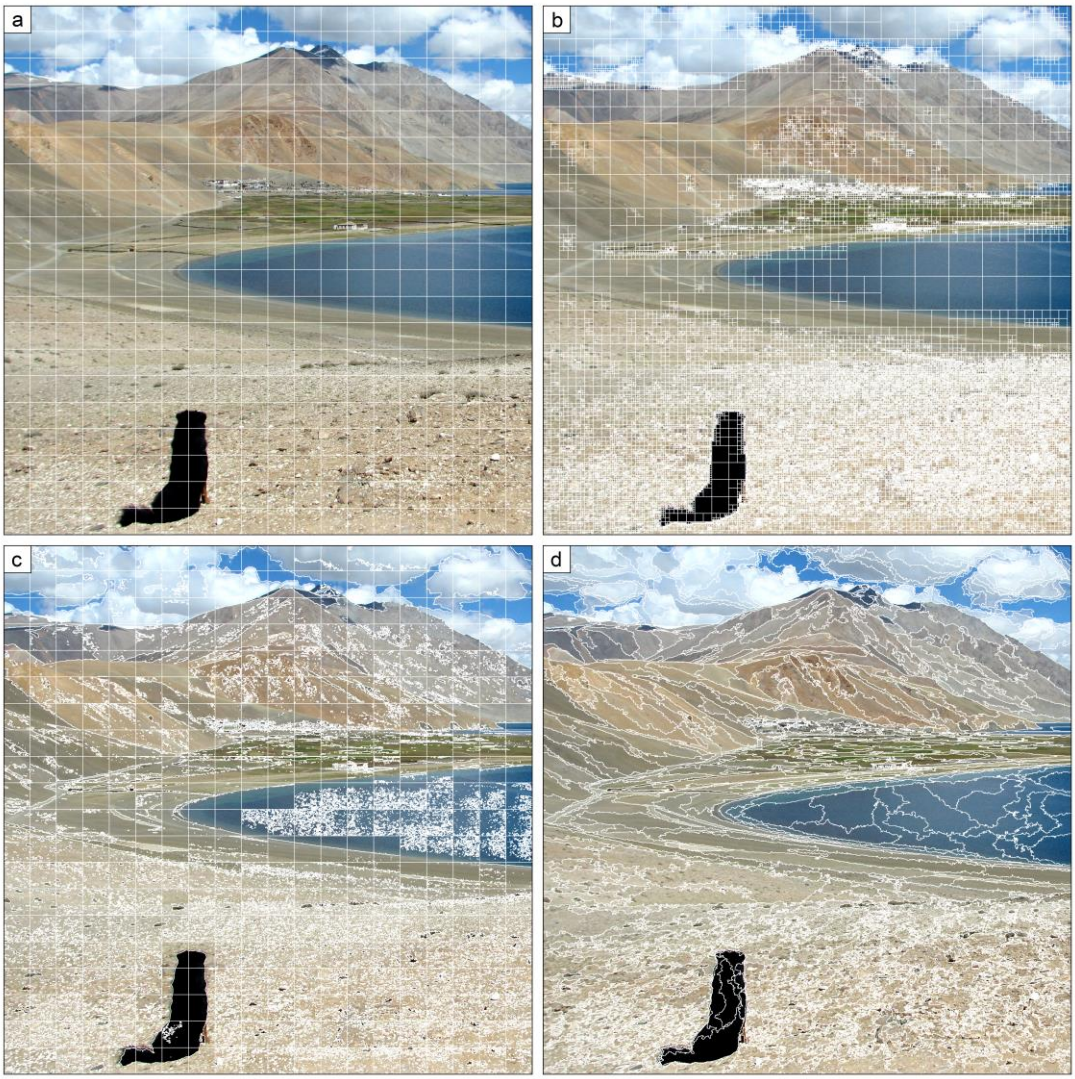

Figure 1.3 | Selected segmentation methods available in eCognition Developer 9.1 software: a) chessboard segmentation; b) quadtree-based segmentation; c) contrast split segmentation; and d) multiresolution segmentation. Photo credits: © Henry Munack.

After performing segmentation, the objects are classified; here several different steps in OBIA are available, allowing the segments to be assigned to relevant classes. The first group of features is related to the objects, where the attributes that may be used are the mean, the mode, the standard deviation, the quantile and the skewness of every segment, as well as the segment's value with respect to the neighbouring segments. This especially helps to reduce the salt-and-pepper noise of classification that usually takes place in the pixel-based approach. Another attribute that may be useful is the geometry of the segment, its shape, the area and the relation of these properties with respect to other segments. These properties can be used in classifying landforms that have defined shape or those that occur only under specific topographic conditions, such as a specific

slope of the terrain. Another important attribute is the texture of the object in the image. Texture attributes, such as homogeneity, contrast, dissimilarity and entropy can distinguish objects with differing textures. The second group of features is related to the classification. Here, it is possible to verify the classification of each segment with respect to its neighbour by analysing the number of neighbours or the relative border to the segments assigned into a specific class. Despite the large amount of available options in OBIA, not all the features mentioned above are required to classify a specific phenomenon. Only those that are significant in solving a specific problem should be used. For example, measuring a segments' shape may help to distinguish linear rivers from more circular lakes. In contrast, checking the classification of neighbouring segments may help to classify a segment that represents the same object as its neighbours, but is out of the thresholding range due to its spectral values.

The OBIA approach has been successfully used in delineating and classifying objects diagnostic of natural hazards, such as landslides (Lu et al., 2011; Martha et al., 2012; Van Den Eeckhaut et al., 2012; Hölbling et al., 2015), gullies (d'Oleire-Oltmanns et al., 2014; Shruthi et al., 2015), and glaciers (Aubrey et al., 2015). Most of these studies analysed the spectral properties of images to classify these objects. Additionally, OBIA has found an application in damage analysis and risk management. Myint et al. (2008) used it to identify tornado damaged areas in Oklahoma, USA, and Van der Sande et al. (2003) used it to assist in flood risk and damage assessment in the Netherlands. Other studies have reported the use of OBIA in detecting building damages caused by the Izmit, Turkey earthquake in 1999 (Turker and Sumer, 2008) and tracking snow avalanche-deposition zones in Switzerland (Bühler et al., 2009) and Norway (Lato et al., 2012). In addition, OBIA has been successfully applied in classifying glaciovolcanic landforms in Iceland (Pedersen, 2016), delineating freshly-erupted deposits around active volcanoes in Indonesia (Thouret et al., 2015), and tracking ice cliffs and ponds in the Himalayas (Kraaijenbrink et al., 2016).

1.5. Morphometric variables for landform detection

From digital topographic data, it is possible to extract several derivatives that often provide additional and physically meaningful insights. From a digital elevation model (DEM), for example, we are able to evaluate a slope map with information about the steepness of the terrain, or an aspect map of the direction of the slope (Grohmann, 2015). The relevance of these parameters is that they control the flux of water and sediment downhill, while also controlling slope stability. I used these two derivatives in my algorithms to detect lakes (Section 3), and snow avalanches (Section 4), to distinguish lakes from glaciers, and to verify the occurrence of avalanches with respect to the direction of the maximum slope. Furthermore, we are able to estimate the curvature of the terrain, which shows whether the surface is curved convex-upward

or concave-upward to a specified pixel (Zevenbergen and Thorne, 1987). This provides information concerning the diversity of the terrain, and can be used to estimate terrain surface roughness – a significant variable when dealing with landforms diagnostic of natural hazards. For example, gullies, dunes, lava fields and landslides are characterised by higher roughness than their surrounding areas. In Section 2, I explore and introduce a curvature-based terrain surface roughness index (μ) as a source in detecting the abovementioned landforms from ALS LiDAR data (Fig. 1.4.a).

An important index that can be evaluated from the images, and which I used for detecting lakes and snow avalanches, is the water index (Fig. 1.4.b). This is the ratio between two spectral bands, which allows the separation of water/snow from other land cover. I used two previously published algorithms: the normalised difference water index (NDWI; McFeeters, 1996) to classify snow

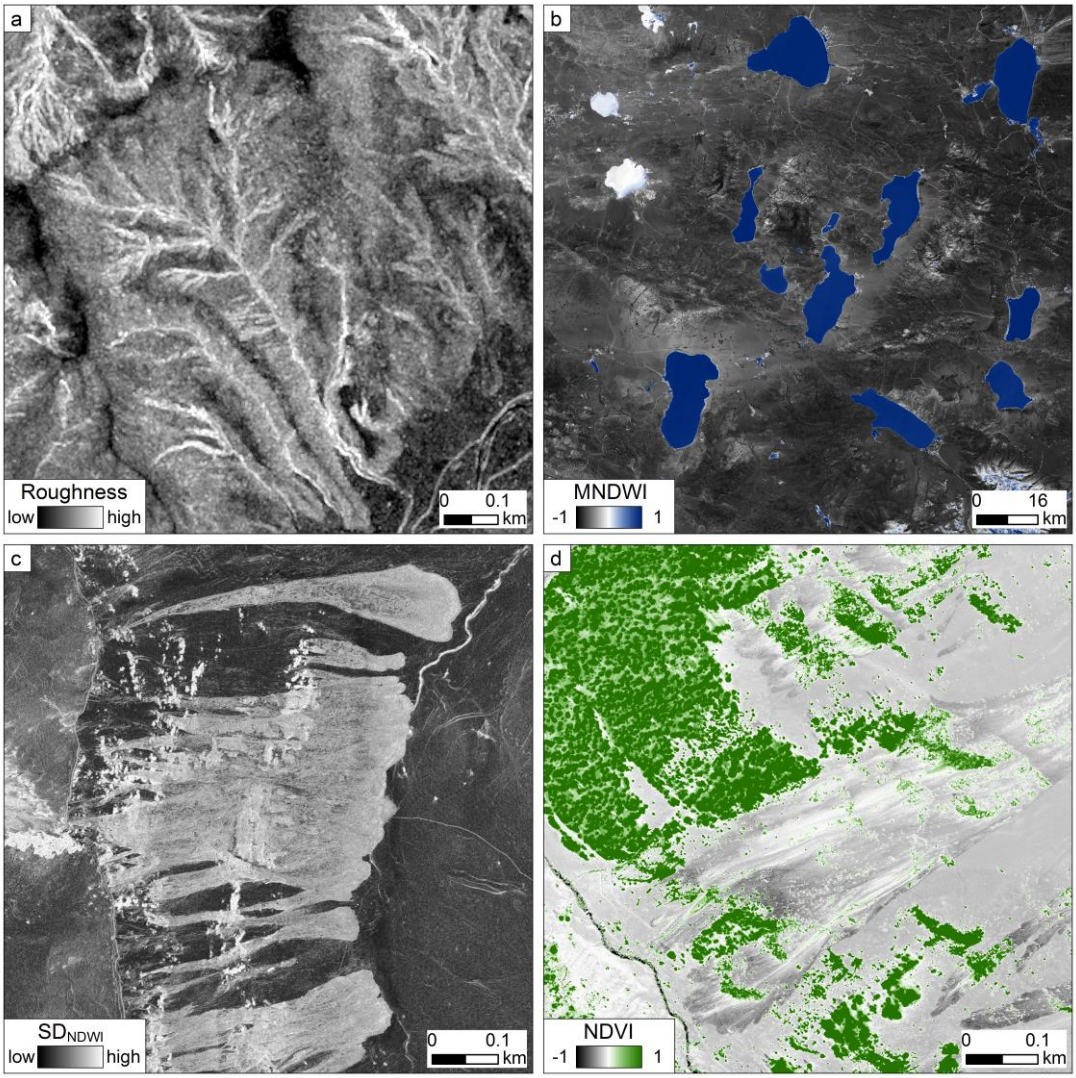

Figure 1.4 | Derivatives evaluated from remote sensing data that were used in this study: a) curvature-based terrain surface roughness (μ) representing gullies; b) modified normalised difference water index (MNDWI) for lakes on the Tibetan Plateau; c) standard deviation of normalised difference water index (SD_{NDWI}) showing snow avalanches; and d) normalised difference vegetation index (NDVI) for snow avalanches.

and the modified normalised difference water index (MNDWI; Xu, 2006) to classify lakes with different states of ice cover on the Tibetan Plateau. Previous studies have reported that the MNDWI has the most stable threshold for separating water on LANDSAT images (Ji et al., 2009); however, it requires a short-infrared band (ρ_{SWIR}), so its application for NIR aerial images is not possible. In such cases, the NDWI can instead be applied, which requires only the green band (ρ_{Green}) and NIR band (ρ_{NIR}).

The water index may additionally be used to calculate the heterogeneity of water classes on the optical image by analysing the texture of the pixels. Here, I suggest a heterogeneity measure, which is computed from the optical NIR aerial data as the standard deviation of the water index SD_{NDWI}, to separate smooth and rough snow representing snow cover and snow avalanches, respectively (Fig. 1.4.c). I assumed that the higher heterogeneity between neighbouring pixels in relation to the water index gives information about the diversity of the snow, allowing the detection of areas where avalanches occur.

A supplementary band ratio derivative that may be useful in detecting snow avalanches is the normalised difference vegetation index (NDVI; Townshend and Justice, 1986), which was developed to automatically map the state of vegetation (Fig. 1.4.d). I tested the application of this index in Section 4 for distinguishing vegetation from other objects that are similarly dark when analysing image brightness, but do not represent any kind of vegetation. I verified whether this index helps in delineating areas where an avalanche can be blocked by dense vegetation, and in tracking parts of avalanches where the process revealed the vegetation occurring under the snow cover.

1.6. Research questions

In this thesis, I focused on the automatic detection of landforms diagnostic of natural hazards from remote sensing data with an OBIA approach. Many challenges are linked with this topic in reference to data properties, such as spatial resolution, pixel values, and brightness; data derivatives, such as slope, curvature, roughness, and water and vegetation indices; and the used methodology of segmentation and classification. Here, I address several research questions that should be answered when performing and adapting the developed algorithms for areas and data other than those used in this work. The first research question refers to the surface roughness metric, which I introduce in Section 2 of this thesis to detect landforms such as gullies, dunes, lava fields and landslides, which are diagnostic of natural hazards. The question relates to the advantages of my method and the parameters that control the evaluated roughness:

RQ1. *Does curvature-derived surface roughness appropriately extract the properties of landforms diagnostic of natural hazards? How do the kernel and*

pixel sizes set for evaluated roughness affect the accuracy in detecting the analysed landforms diagnostic of natural hazards?

The second question discusses the use of spectral properties of images compared to derivatives that can be computed from image bands, such as the water index. This question refers mostly to Section 3, which focuses on classifying lakes with different states of water based on the water index compared to the visual information of such lakes:

RQ2. *What are the advantages and disadvantages of detecting landforms diagnostic of natural hazards from remote sensing data with their derived indices vs. visual information?*

The spectral information and image derivatives can be used together for segmentation, which is the first step in the OBIA approach. The third research question of this thesis elaborates upon the significance of the chosen segmentation method and the influence of parameters that can be set in segmentation to control their size and shape, for further object classification:

RQ3. *Are the segmentation method and its parameters the most significant when using OBIA? How the selected segmentation method controls the subsequent stages of classification?*

After performing segmentation in OBIA, the objects are classified based on data properties (spectral information, derivatives), and available algorithms for segment size, shape, and spatial context should be chosen according to the classified objects. Here, I address two research questions that are related to detecting lakes with different states of water from LANDSAT images (RQ4), and snow avalanches from NIR aerial images (RQ5). The ice cover on lakes is an important issue, because it usually causes misclassification of parts of a lake when using the spectral properties of the images. In such cases, a water index is advantageous in reducing this misclassification because water, irrespective of whether or not it is frozen, has positive values on the water index. A water index may confuse water with glaciers; however, so for the area of the Tibetan Plateau, which I used as my research area in Section 3, it assigned many glaciers as lakes. A spatial context, which can be used in OBIA, may therefore be an asset for distinguishing frozen lakes from glaciers, which I addressed RQ4:

RQ4. *What are the advantages and disadvantages of OBIA in detecting lakes prone to seasonal ice cover in an area with glaciers?*

For detecting snow avalanches, in Section 4 I investigated several NIR aerial image derivatives to separate snow avalanches from other objects. I applied brightness and NDVI to find vegetation, NDWI to classify snow, and SD_{NDWI} to assign rough snow. In this respect, I address the research

question concerning the importance of these variables in detecting avalanches using an OBIA approach:

RQ5. *Which variables are the most useful in detecting snow avalanches from NIR images with OBIA?*

The visual illustration of these five research questions in Figure 1.5 shows the connections and mutual dependencies among them. These questions are partly answered in Sections 2, 3, and 4, and broadly discussed and summarised in Section 5.

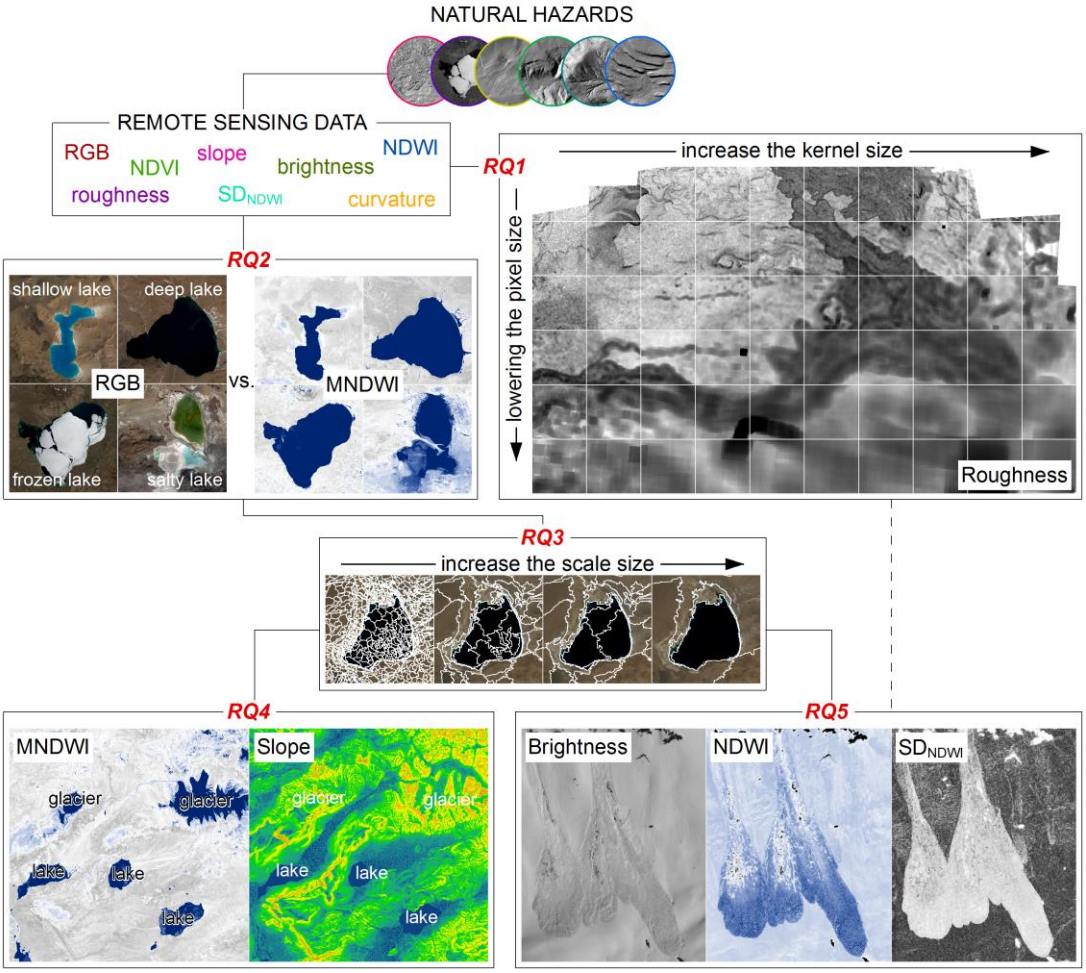

Figure 1.5 | Graphical abstract of research questions (RQ1 – 5). The abbreviations on the figure are modified normalised difference water index (MNDWI), normalised difference water index (NDWI), and standard deviation of normalised difference water index (SD_{NDWI}).

1.7. Author contributions and structure of the thesis

For this thesis, I performed all data analysis. Overall, I designed the research, processed the remote sensing data, developed the algorithms, performed the analysis, drew the conclusions, and wrote the manuscript text. Several co-authors contributed by commenting and discussing the applied methods and the results. The studies presented in Chapters 2–4 have been submitted as

manuscripts to three international peer-reviewed journals. Furthermore, Prof. Dr. Oliver Korup advised the research and contributed to writing the articles.

Chapter 2 investigates the applicability of terrain surface roughness for detecting natural hazard-related landforms, such as gullies, dunes, lava fields and landslides. In this chapter, I propose a new curvature-based surface roughness algorithm and discuss the parameters used in the algorithm and their influence on the computed roughness.

Chapter 3 proposes an OBIA approach for delineating mountain lake boundaries, which are prone to seasonal ice cover, from LANDSAT images. I demonstrate the insensitivity of the algorithm to seasonal lake ice cover and discuss further applications, including transferring the algorithm to other areas with different environmental conditions.

Chapter 4 introduces a new OBIA algorithm for detecting snow avalanches at the catchment scale, using high-resolution NIR aerial images. In this chapter, I propose a new methodology using image derivative maps, and discuss the resulting pattern of automatically-detected snow avalanches. I propose a simple automatic approach for the classification of avalanche parts, such as release zones, tracks, and runout zones.

Chapter 5 synthesises and summarises the key findings of Chapters 2–4, revisits the research questions, and outlines the prospects for future research concerning the application of remote sensing data and OBIA in detecting natural hazards.

Chapter 2

Gullies, dunes, lava fields, & landslides

Submitted to *Geomorphology* as: Korzeniowska, K., Pfeifer, N., Landtwing, S., Korup, O. Mapping gullies, dunes, lava fields, and landslides via surface roughness.

Abstract

Gully erosion is a widespread and significant process involved in soil and land degradation. Mapping gullies helps to quantify past, and anticipate future, soil losses. Digital terrain models offer promising data for automatically detecting and mapping gullies, although methods vary widely measures of local terrain roughness are the most varied and debated among these methods. Rarely do studies test the performance of roughness metrics for mapping gullies, limiting their applicability to small training areas. To this end, we systematically explored how local terrain roughness derived from high-resolution Light Detection And Ranging (LiDAR) data can aid in the unsupervised detection of gullies. We also tested expanding this method for other landforms diagnostic of similarly abrupt land-surface changes, including lava fields, dunes, and landslides, as well as investigating the influence of different roughness thresholds, resolutions of kernels, and input data, and comparing our method with previously published roughness algorithms. Our results show that total curvature is a suitable metric for recognising gullies and lava fields from LiDAR data, with comparable success to that of more sophisticated roughness metrics. Dunes or landslides remain difficult to distinguish from the surrounding landscape, partly because they are not easily defined in terms of their topographic signature.

2.1. Introduction

Gullying is a natural consequence of overland flow, which erodes soils or unconsolidated cohesive materials; additionally, several land-use practices may enhance this erosion. Gullies are distinguished from other landforms because of their high levels of local roughness (Ionita et al., 2015), and are diagnostic of degrading land (Poesen et al., 2003; Valentin et al., 2005; Shruthi et al., 2015) and altered runoff conditions (Avni, 2005; Vanmaercke et al., 2016). In a systematic review, Poesen et al. (2003) reported that soil loss caused by various gullying types produced

between 10% and 94% of total water-borne sediment from individual catchments verified across the world. Factors promoting gully growth include climate, land use, soil characteristics, topography, snow melt, and seismicity (Vanmaercke et al., 2016). Understanding these factors better and monitoring their dynamics are essential for mitigating gully erosion (Conoscenti et al., 2014; Torri and Poesen, 2014).

Geomorphologists routinely use high-resolution digital terrain models (DTMs) obtained from Light Detection And Ranging (LiDAR) scans to map, either manually or automatically, gullies and other landforms. This approach has been instrumental in informing natural hazard studies, as DTMs can reveal diagnostic landforms, or 'silent witnesses', of past processes, even those hidden below dense vegetation cover (Deardorff and Cashman, 2012; Jaboyedoff et al., 2012).

In this study, we explored ways of automatically discerning gullies from LiDAR-derived DTMs using terrain roughness as a diagnostic. Terrain roughness has many synonyms, including 'microtopography' (Dunne et al., 1995), 'microrelief' (Potter et al., 1990; Helming et al., 1993), 'ruggedness' (Riley et al., 1999), and 'rugosity' (Brasington et al., 2012), hence it is likely the least standardised terrain mapping diagnostic (Shepard et al., 2001; Smith, 2014; Milenković et al., 2015). We chose to use roughness because it is a topographic attribute that expresses the heterogeneity of the terrain; however, how well surface roughness aids the automatic detection of gullies and other natural-hazard landforms remains only partly understood. We followed the footsteps of previous efforts to automatically detect specific landforms (Glenn et al., 2006; Sagy and Axen, 2007; Bishop et al., 2012), but expanded by testing how well our method, designed to detect gullies, works for other landforms, including lava fields, dunes, and landslides.

Flowing water that erodes soil creates gullies and often compromises agricultural use. Determining future trends in gully erosion processes and the potential material losses remains challenging (Poesen, 2011). Dunes instead result from wind activity and may bury farmland, destroy forests by backfilling trees, block roads, or encroach on infrastructure (Lam, Remmel, and Drezner, 2011). Lava fields record some of the flow properties of molten rock, indicating the size of past effusive eruptions (Deardorff and Cashman, 2012). Landslides result from the unstable hillslope, and involve the downward movement of soil, debris or rock (Pike, 1988). Detecting areas caused by all these different processes is important for producing susceptibility or hazard maps.

We hypothesise that all these landforms share significant roughness contrast with respect to the surrounding terrain, and that a single metric should be able to capture these. Hence our main objectives were to explore a new curvature-based roughness index, to quantify how sensitive this index is to input data resolution and kernel size, and to compare how the index performs in relation to previous roughness metrics for gullies and other landforms.

2.2. Previous work

2.2.1. Detecting gullies from high-resolution digital topography

Gullies may change rapidly over large areas, making systematic methods for detecting, mapping, and monitoring essential for estimating rates of changes and predicting environmental consequences (Perroy et al., 2010; Shruthi et al., 2011). The simplest, but most subjective, method is to map gullies manually using air photos or DTMs (e.g. Martinez-Casasnovas, 2003). Stereomatching of aerial photos allows the generation of high-resolution (down to cm-scale) DEMs for different time slices, and thus enables estimation of the area affected by gullying, including local sources and sinks, as well as changes in eroded soil volumes (Marzolff and Poesen, 2009). Unmanned aerial vehicles (UAV) are capable of producing high-resolution DTMs via stereomatching or structure-from-motion methods. For example, Peter et al. (2014) surveyed the Souss valley, Morocco, for land-use changes using such data, but resorted to manually digitising the edges of gullies instead of using automated methods, whereas Stöcker et al. (2015) generated digital topographic data from UAV images complemented by terrestrial field photos to obtain detailed 3D surfaces of gullies in steep areas (>50°). They found that this combination produced more comprehensive and spatially-accurate models of gullies. In contrast, d'Oleire-Oltmanns et al. (2014) used object-based image analysis (OBIA) of UAV-derived images, mostly edge contrasts, segments size, and roundness, to automatically delineate active gully erosion with only moderate accuracy. Previously, d'Oleire-Oltmanns et al. (2013) used Quick Bird-2 images to map gullies, and OpenStreetMap data to mask greenhouses, residential areas, and plantations identified from the normalised difference vegetation index (NDVI), as these might have been misclassified as gullies. They also used OBIA to extract gullies based on spectral and boundary segment data, again with moderate accuracy. Shruthi et al. (2011) analysed 4-m resolution IKONOS images and a 1-m DEM generated from GEOEYE-1 stereo images for detecting gullies, based on slope, specific catchment area, flow direction, NDVI, image texture, contrast, and edge metrics. They concluded that this method was transferable, with limitations set by subjectively selecting thresholds. James et al. (2007) tested the suitability of LiDAR data for mapping gullies and channel networks in forested areas in South Carolina, USA, and stated that a 4-m DTM paired with GPS-supported field checks improved their ability to map drainage elements below the forest canopy, even though these elements were missing on 1:24,000 topographic maps. Evans and Lindsay (2010) followed a similar strategy, but focused on topographic lows with high positive planar curvature, whereas Baruch and Filin (2011) argued that the many sizes and forms of gullies made detection at a fixed scale intractable, and instead used multiple scales for extracting gullies of different ages. Höfle et al. (2013) mapped gully sidewalls with terrestrial LiDAR DTMs using edge and sink filling, and achieved approximately 93% consistency with field-based reference data, finding this method successful for smooth topography with distinct

gully sidewalls. Passalacqua et al. (2010) proposed a geometric framework for extracting the channel network from LiDAR data, using a GeoNet computational tool. The algorithm defines the channels as curves of minimal effort, where the effort is evaluated based on flow accumulation and the curvature.

2.2.2. Concepts of terrain roughness

Views of terrain roughness depend largely on the scale and purpose of the study (Milenković et al., 2015). Roughness is a morphometric variable expressing the local heterogeneity of the land surface. Roughness measurements must therefore be (a) able to discriminate between surfaces of different amplitudes, frequencies, and correlations; (b) an intrinsic property of the surface, invariant with respect to rotation or translation; (c) a local, not global, measure of the surface; (d) intuitive or physically meaningful (Hoffman and Krotkov, 1990; Hani et al., 2011); and (e) simple enough to be computationally efficient (Berti et al., 2013). Most ways of computing terrain roughness from gridded data use the variability of elevation or slope in a local neighbourhood (Riley et al., 1999). One prominent representative of this method is the Terrain Ruggedness Index, which measures the square root of the average squared elevation difference between the centre pixel and its eight neighbours within a moving window or kernel (Grohmann and Riccomini, 2009). Frankel and Dolan (2007) measured the standard deviation of local slope in the cardinal directions with the aim of detecting alluvial fans in Death Valley, United States, and found that this roughness metric varied consistently with rock type. Shepard et al. (2001) proposed several algorithms based on the root-mean-square (RMS) of elevation, relief, and slope, but de-trended their data first by subtracting the DTM from a best-fit plane. Kreslavsky and Head (1999) pointed out that RMS-based metrics are sensitive to outliers, and suggested using a median slope instead. Haneberg et al. (2005) used the difference between the topography and its locally smoothed derivative within a moving square five pixels in width (Cavalli and Marchi, 2008). Similarly, Cavalli et al. (2008) recommended using this residual topography for filtering out large-scale landforms while eliminating the artefacts in steep landscapes, especially when generating hazard maps, mapping alluvial fan surfaces, and recognising riffle and steep-pool reaches in rivers. Haneberg et al. (2005) also found that terrain roughness helps to distinguish debris landslides from rock slumps, and even identifies individual lobes on debris fans.

LiDAR point clouds also contain roughness information. Glenn et al. (2006) binned point-cloud data into 5 m × 5 m grid squares, and computed surface roughness from the standard deviation of the heights of LiDAR points above a spline interpolated through local elevation minima. This method worked well for detecting patterns in landslide morphology and activity. In contrast, Pollyea and Fairley (2011) derived roughness from point clouds with orthogonal distance regression to identify fracture and rubble zones in basalt outcrops, using the standard deviation

of the point-to-plane distances. McKean and Roering (2004) explored direction cosines of normal vectors of LiDAR pixels, and evaluated the logarithm of the ratios of normalised eigenvalues S_1 and S_2 in a three-by-three cell window. This method detected abrupt topographic changes, especially fresh landslide deposits. Trevisani et al. (2012) used roughness for identifying rockfall deposits, debris-flow channels, and rocky outcrops, and suggested varying kernel size to find the most appropriate for smoothing the DTM. A standard variogram with short lags captured fine-scale roughness, whereas log-transformed roughness values helped in detecting rocky outcrops. Variograms account for anisotropic terrain data, and Trevisani and Rocca (2015) introduced a multi-scale, directional image texture analysis operator (MAD) to improve their variogram models, obtaining robust roughness estimates even from noisy data. Booth et al. (2009) chose a two-dimensional discrete Fourier and a continuous wavelet transform to characterise the topographic signatures of deep-seated landslides, although Berti at al. (2013) questioned if spectral parameters used in these methods had any intuitive meaning or counterparts in moving window-based methods. Hani et al. (2011) estimated terrain roughness using a multi-scale, wavelet lifting scheme, and found this method to be independent of rotation and translation, and overall intuitive, recommending its use for distinguishing valleys and ridges, and quantifying convex and concave regions.

Overall, however, few studies have systematically compared different roughness metrics for detecting landforms. Grohmann et al. (2011) estimated the ratio between real surface area and planform area, and evaluated the mean, strength, and dispersion of each cell of normal vectors for regularly spaced elevation values. They stressed that data resolution and kernel size was important for computing roughness statistics, and concluded that metrics such as the standard deviation of slope, standard deviation of profile curvature, and vector dispersion detected most terrain features. Berti et al. (2013) reviewed ten different surface roughness algorithms for identifying active landslides, and found only minor differences in their discriminatory and predictive capability; many simple methods performed reasonably well or even better than more complex ones. The authors argued that larger kernels only marginally improved the predictive capability, and suggested using higher resolutions and moving windows to retain local details.

2.3. Research area and data

Our review of previous work shows that gullies and several other landforms have a distinctly different roughness compared to the surrounding landscape (McKean and Roering, 2004; Haneberg et al., 2005). Our study area was a grassland on Santa Cruz Island, the largest of California's Channels Islands (Fig. 2.1). The island has been prone to land degradation due to increased animal populations in the 19th century, which have reduced the vegetation cover

(Perroy et al., 2010). Efforts to re-establish vegetation in this area have stabilised some hillslopes, but active gullies still occur (Perroy, 2009).

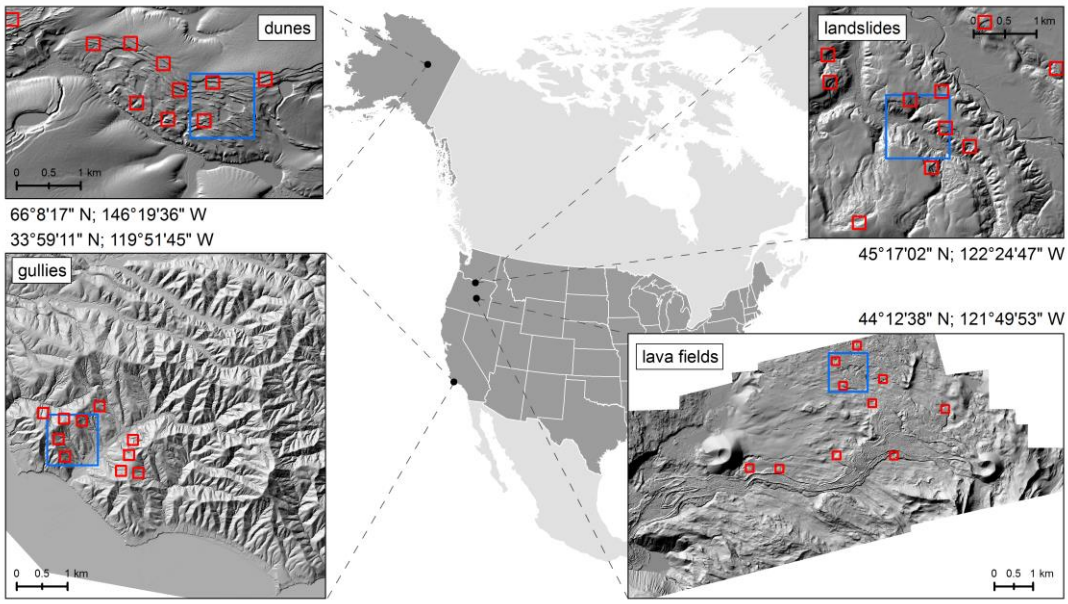

Figure 2.1 | Test sites selected for evaluating the detectability of landforms from surface roughness: dunes in Alaska; landslides in Oregon; gullies on Santa Cruz Island, California; and lava fields at Collier Cone, Oregon. The blue squares indicate 1km² training areas. The red squares indicate samples taken for Otsu thresholding. The coordinates indicate the central locations of the 1km² samples. For LiDAR parameters, see Table 2.1.

To test whether roughness-based metrics are capable of detecting not only these gullies, but also other landforms indicative of sudden disturbance such as lava fields, dunes, and landslides, we selected three other study areas in the western United States (Fig. 2.1): 1) lava fields on the north flank of North Sister stratovolcano ~45 km northwest of Bend City, Oregon (Deardorff and Cashman, 2012); 2) dunes on Yukon Flats, a vegetated permafrost area ~70 km southwest of Fort Yukon, Alaska; and 3) >150-year old landslides in a forested region between Redland, Estacada, and Beavercreek, Oregon (SLIDO, 2015). Our rationale for selecting landforms was a mixed one: On the one hand, we aimed at testing our algorithm on as diverse landforms as possible, subject to vary differing environmental conditions. On the other hand, we focused on vegetated areas, because for such areas LiDAR data offers more opportunities for detecting hidden features than optical data. On bare-ground landforms can be detected easily from satellite or aerial images, which are also more widely available and cheaper than LiDAR. Finally, wishing for maximum reproducibility and comparability, we decided to test our algorithm on LiDAR data that are freely available for download. For all of these areas, we used vegetation-corrected LiDAR data of the bare-ground surface (Korzeniowska et al., 2014), obtained from Open Topography (Open Topography, 2015), and the Alaska Division of Geological & Geophysical Surveys (ADGGS, 2015) online portals (Table 2.1). The differing objectives of the data collection campaigns resulted in point densities of 3–10 points m-2 (Table 2.1). The selected landforms varied with

respect to their shape and size, which allowed us to test the applicability of our roughness algorithm on a wider spectrum. The size of our study areas ranged from 15 to 50 km² (Table 2.1). To generate DTMs from those data, we used the classification for terrain and off-terrain points specified by Open Topography and the Alaska Division of Geological & Geophysical Surveys.

Table 2.1 | Parameters of LiDAR data used in the current study.

Test area	Date of data collection	Point density [pts m^{-2}]	Area size [km^2]
Dunes	24 Oct 2009	4	15
Landslides	15 Mar 2007 – 3 Sep 2010	10	15
Gullies	11 Mar 2010 – 8 Apr 2010	8	50
Lava fields	28 Sep 2008	3	50

We processed the raw point cloud and generated the DTMs using the LiDAR Processing Toolbox for ArcGIS 10.1 (ESRI, 2016), using the LAS dataset to Raster function with default binning interpolation, average cell assignment, and linear void fill. We saved the data as 1-m GeoTIFF rasters, owing to the low density of points in some test areas.

2.4. Methods

We have introduced a new method for calculating terrain surface roughness, which does not require data detrending, an issue that is often crucial in hilled, and mountainous areas. We used roughness for unsupervised classification of four different landform types that we compared with manually digitised reference data. We assessed the accuracy of detecting these landforms with roughness evaluated with different data resolutions and kernels using confusion matrices, receiver operating characteristic (ROC), area under the curve (AUC), and logistic regression. In addition, we proposed an approach for finding the optimal decision boundary threshold, and compared our roughness algorithm with several previously-published methods.

We first computed local total curvature, selecting the method by Zevenbergen and Thorne (1987) from several options (Evans, 1972; Shary, 1995; Schmidt et al., 2003). A positive (negative) curvature indicates that the surface is concave (convex) in the cell coordinate evaluated; a zero value indicates a planar surface (Kimerling et al., 1995). Total curvature in a 3 × 3 matrix for the central point Z5 (x = y = 0) can be approximated by fitting a surface Z to nine elevation points in a moving window three pixels wide (Fig. 2.2):

$$Z = Ax^2y^2 + Bx^2y + Cxy^2 + Dx^2 + Ey^2 + Fxy + Gx + Hy + I \qquad (1)$$

where coefficients *A*-*I* are:

$$A = [(Z_1 + Z_3 + Z_7 + Z_9) \div 4 - (Z_2 + Z_4 + Z_6 + Z_8) \div 2 + Z_5] \div L^4 \quad (2)$$

$$B = [(Z_1 + Z_3 - Z_7 - Z_9) \div 4 - (Z_2 - Z_8) \div 2] \div L^3 \quad (3)$$

$$C = [(-Z_1 + Z_3 - Z_7 + Z_9) \div 4 + (Z_4 - Z_6) \div 2] \div L^3 \quad (4)$$

$$D = [(Z_4 + Z_6) \div 2 - Z_5] \div L^2 \quad (5)$$

$$E = [(Z_2 + Z_8) \div 2 - Z_5] \div L^2 \quad (6)$$

$$F = (-Z_1 + Z_3 + Z_7 - Z_9) \div 4L^2 \quad (7)$$

$$G = (-Z_4 + Z_6) \div 2L \quad (8)$$

$$H = (Z_2 - Z_8) \div 2L \quad (9)$$

$$I = Z_5 \quad (10)$$

From the above equations, the total curvature is:

$$Curvature = -2(D + E) * 100 \quad (11)$$

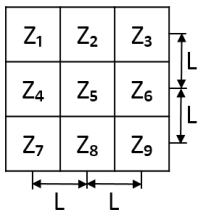

Figure 2.2 | A 3 × 3 matrix for evaluating coefficients *A* – *I* in Equations 2 – 10. Z_1-Z_9 are the elevation values of the terrain surface, Z_5 is the central point in the matrix, and *L* is the distance between matrix points in the row and column directions, and defines the raster resolution.

We estimated terrain roughness from the standard deviation of Equation (11) within a 5 × 5-pixel neighbourhood (Fig. 2.3; Berti et al., 2013) and further tested other kernel sizes (Roering et al. 2010). The distribution of surface roughness was positively skewed for each study area, with most values being near zero. We thus log-transformed the data (Trevisani et al., 2012), and defined a roughness index:

$$\mu = \log_{10} \sqrt{\frac{\sum_{i=1}^{n} (x_i - \bar{x_i})^2}{n}} \quad (12)$$

where x_i is the curvature value of the centre cell, $\bar{x_i}$ is the mean curvature in the moving window, and n = 25 (for a 5 × 5 kernel), which is the number of pixels in the local environment. We implemented this algorithm as a free toolbox for ESRI's ArcGIS 10.3 (http://itn-alert.org).

We manually digitised landform boundaries by visually interpreting shaded slope maps and high-resolution satellite imagery to create a reference data set for testing our roughness metric. Convex upward dunes had the highest contrasts, although deeply incised gullies and large lava fields were also distinct; landslides were the most difficult to map, and in places we only found remnant landslide scarps (Fig. 2.4). Following previous work (Cohen, 1960; Congalton, 1991; Stehman,

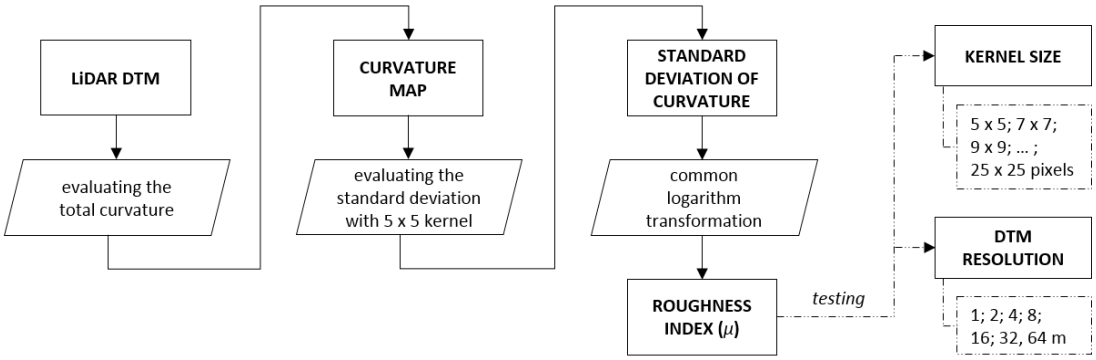

Figure 2.3 | Workflow for estimating and testing our terrain surface roughness (μ).

1997; Sithole and Vosselman, 2004), we first computed confusion matrices (Fig. 2.5) using true positives (TP), false positives (FP), false negatives (FN), and true negatives (TN). We then computed several statistical performance measures for our roughness-based method of detecting the mapped landforms in 1-km^2 sample areas (Fig. 2.1), including Type I errors (the fraction of FP over all positives), Type II errors (the fraction of FN over all negatives), total error (the fraction of misclassified pixels; Sithole and Vosselman, 2004), overall accuracy (the fraction of correct classifications), producer's accuracy (the fraction of TP over all positives), user's accuracy (the fraction of TP over TP and FN; Congalton, 1991), and Cohen's kappa (a measure of how far the classification deviates from a chance classification; Cohen, 1960).

We also computed ROC curves (Swets, 1988) that map the performance of our method with changing decision boundaries, where decision boundaries mark the predictor-based thresholds separating the data into two classes. An ROC curve shows the TP rate (TP/TP+FN) of the

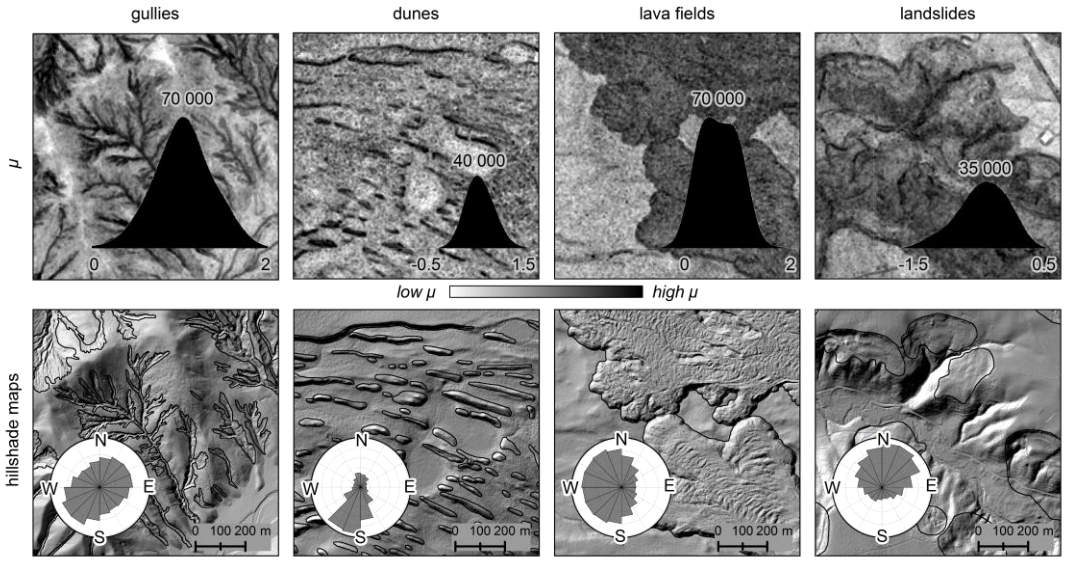

Figure 2.4 | The μ index with histograms evaluated from 2m DTM with 5 × 5 kernel size of standard deviation of total curvature, hillshade maps with digitised reference data, and rose diagrams representing aspect. The black polygons on hillshade maps are the manually mapped boundaries of the landforms, and are used as reference data.

classification as a function of the FP rate (FP/FP+TN); a classification is considered perfect when the ROC curve passes through the upper left corner of the graph. The AUC, in contrast, encapsulates the model skill; values of 0.5–0.7 indicate poor accuracy, whereas values of 0.7–0.9 indicate useful accuracies. AUC values >0.9 are considered highly accurate (Swets, 1988).

We also used the *mnrfit* function in MATLAB R2014b (Matlab, 2016) to run a logistic regression to estimate the probability of a given roughness pixel belonging to a gully or not.

		Predicted	
		YES	NO
Reference	YES	TP	FP
	NO	FN	TN

Performance statistics
Type I error = FP/TP+FP
Type II error = FN/FN+TN
Total error = FP+FN/TP+FP+FN+TN
Overall accuracy = TP+TN/TP+FP+FN+TN
Producer's accuracy = TP/TP+FP
User's accuracy = TP/TP+FN
Cohen's kappa = p_o-p_e/1-p_e

Figure 2.5 | Confusion matrix and performance statistics for reference data and predicted automatic classification, where TP is true positive, TN is true negative, FP is false positive, FN is false negative, p_o is relative observed agreement among rates, and p_e is hypothetical probability of chance agreement.

To compare the performance of our proposed roughness metric, hereafter referred to as μ, in detecting natural-hazard landforms with respect to previously published methods, we computed four additional roughness indices: planar and profile curvature, which we evaluated using the same workflow as for μ through replacing total curvature by planar and profile curvature computed with the *curvature* tool in ArcGIS 10.3 software; the standard deviation of residual topography (Haneberg et al., 2005); and the standard deviation of slope (Frankel and Dolan, 2007), where we applied 5 × 5 kernel size and used log-transformed data throughout.

2.5. Results

2.5.1. Influence of data resolution and kernel size

Visual checks of the mapped μ values confirm that most of the target landforms possessed high roughness, irrespective of their aspect (rose diagrams in Figure 2.4). We checked how different resampled DTM resolutions and kernel sizes influenced values of μ, testing pixel sizes of 1, 2, 4, 8, 16, 32, and 64 m, and resampling all μ values to the original 1-m resolution. The visual representation of surface roughness for the gully study area (Fig. 2.6) shows that larger kernels reduced the local roughness contrast of gullies and other linear landforms. Similarly, the

estimated ROC curves and Cohen's kappa values reveal that larger kernels consistently reduced the ability to detect gullies (Fig. 2.6). With increasing kernel size, the ROC moves closer to random prediction, and the Cohen's kappa decreases. Coarser DTMs emphasised the role of kernel size, so that larger kernels and coarser DTMs made gully boundaries nearly undetectable.

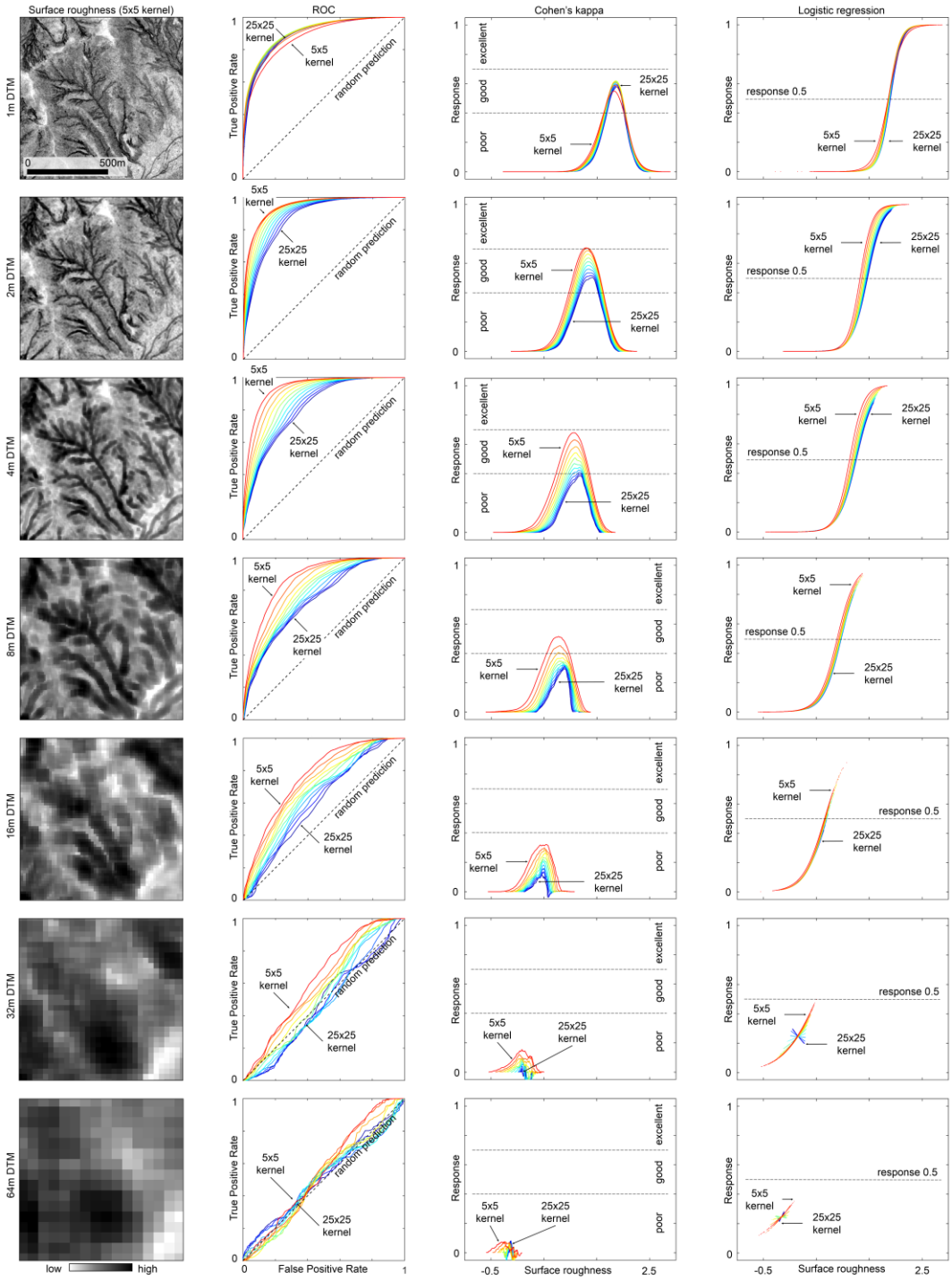

Figure 2.6 | The μ index for a 1-km² sample for the gully study area; receiver operating characteristic (ROC) curves, Cohen's kappa, and logistic regression for roughness evaluated from 1, 2, 4, 8, 16, 32, and 64 m DTM with different kernel sizes of the standard deviation of curvature: 5 × 5 pixels, 7 × 7 pixels, …, and 25 × 25 pixels. The 1-km² sample is shown as a blue square on Figure 2.1.

Predictions were marginal for DTMs with a resolution lower than 8 m, regardless of kernel size. Lowering the local contrast produced less random, unstructured noise (salt-and-pepper noise) from isolated high-roughness pixels. The logistic regression curves (Fig. 2.6) showed that the highest probabilities (~1) of classifying gullies were tied to small kernels and high DTM

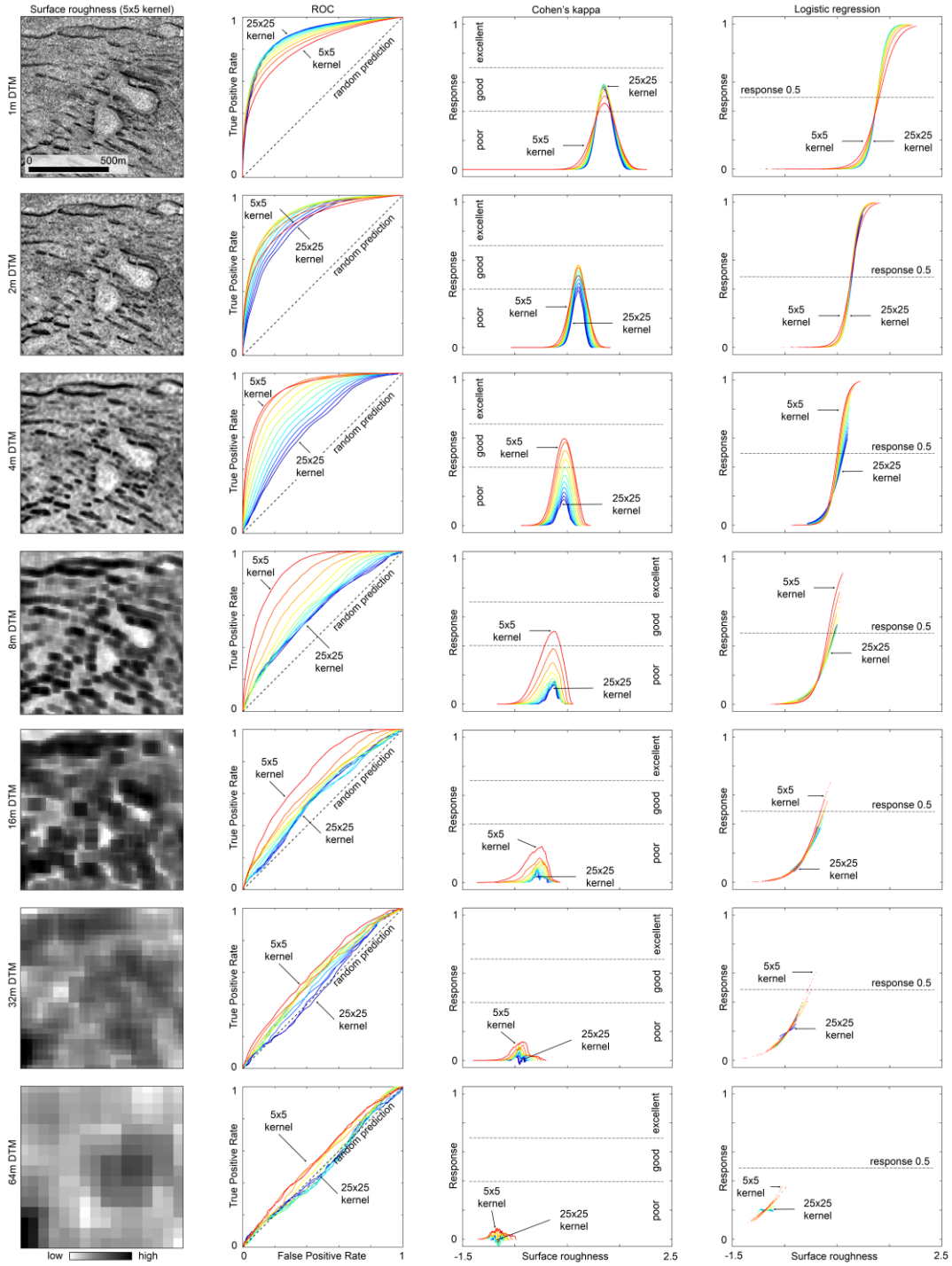

Figure 2.7 | The μ index for a 1-km² sample for the dune study area; receiver operating characteristic (ROC) curves, Cohen's kappa, and logistic regression for roughness evaluated from 1, 2, 4, 8, 16, 32, and 64 m DTM with different kernel sizes of the standard deviation of curvature: 5 × 5 pixels, 7 × 7 pixels, …, and 25 × 25 pixels. The 1-km² sample is shown as a blue square on Figure 2.1.

resolution; for 16-m and 32-m elevation data, the highest probabilities of correctly classifying gullies dropped to <0.8 and <0.5, respectively.

We obtained comparable results when detecting dunes (Fig. 2.7). The resolution of the DTM largely controlled our roughness estimates, such that coarser (lower than 4 m) DTMs allowed for

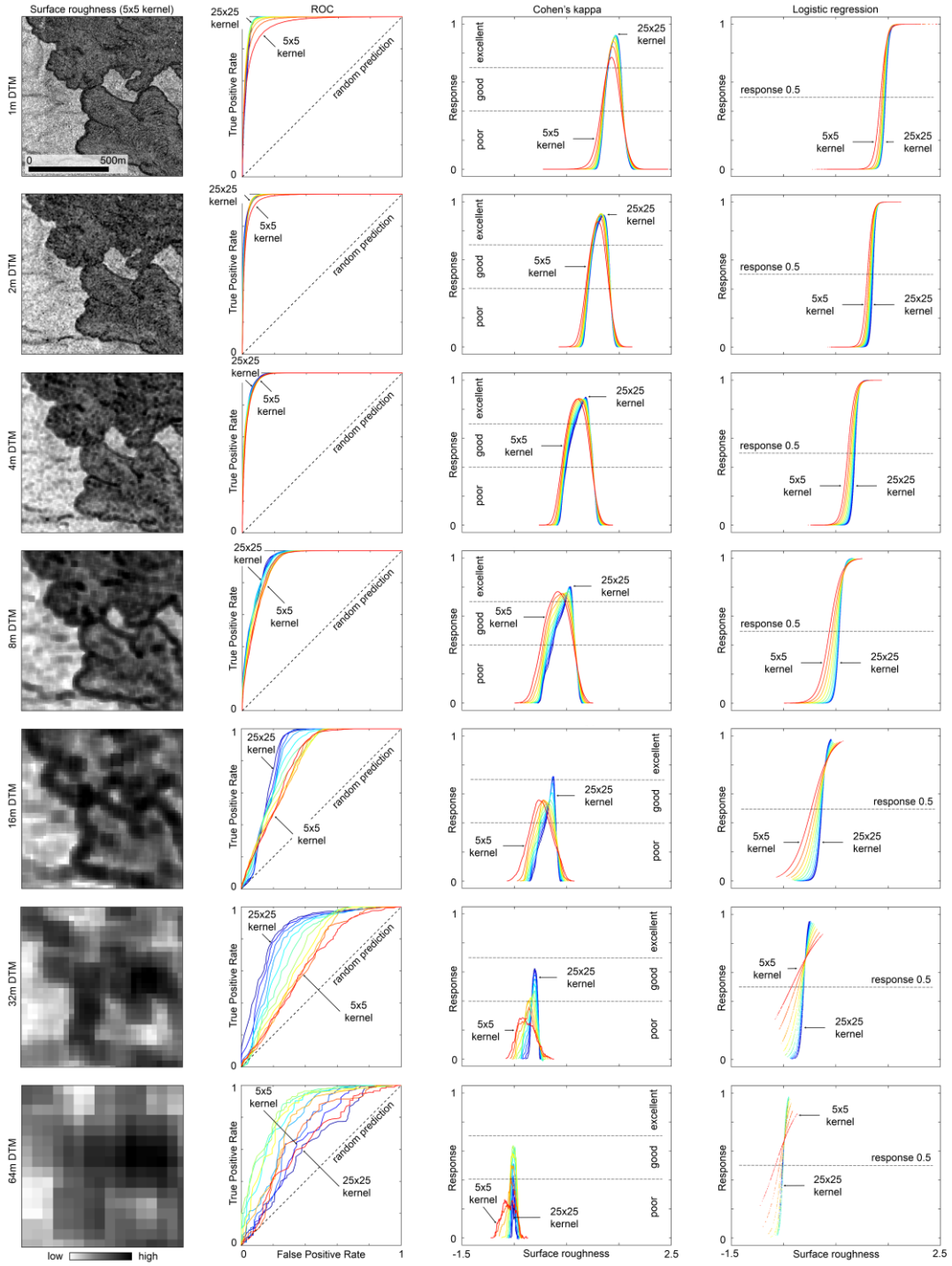

Figure 2.8 | The μ index for a 1-km² sample for the lava field study area; receiver operating characteristic (ROC) curves, Cohen's kappa, and logistic regression for roughness evaluated from 1, 2, 4, 8, 16, 32, and 64 m DTM with different kernel sizes of the standard deviation of curvature: 5 × 5 pixels, 7 × 7 pixels, …, and 25 × 25 pixels. The 1-km² sample is shown as a blue square on Figure 2.1.

the detection of fewer dunes. The logistic regression results for dunes depended more on kernel size and DTM resolution than did those for gullies. Our method worked best for detecting lava fields, judging from high values of AUC and Cohen's kappa (Fig. 2.8). The logistic regression curve was also very steep, with a narrow range of roughness values separating lava fields from

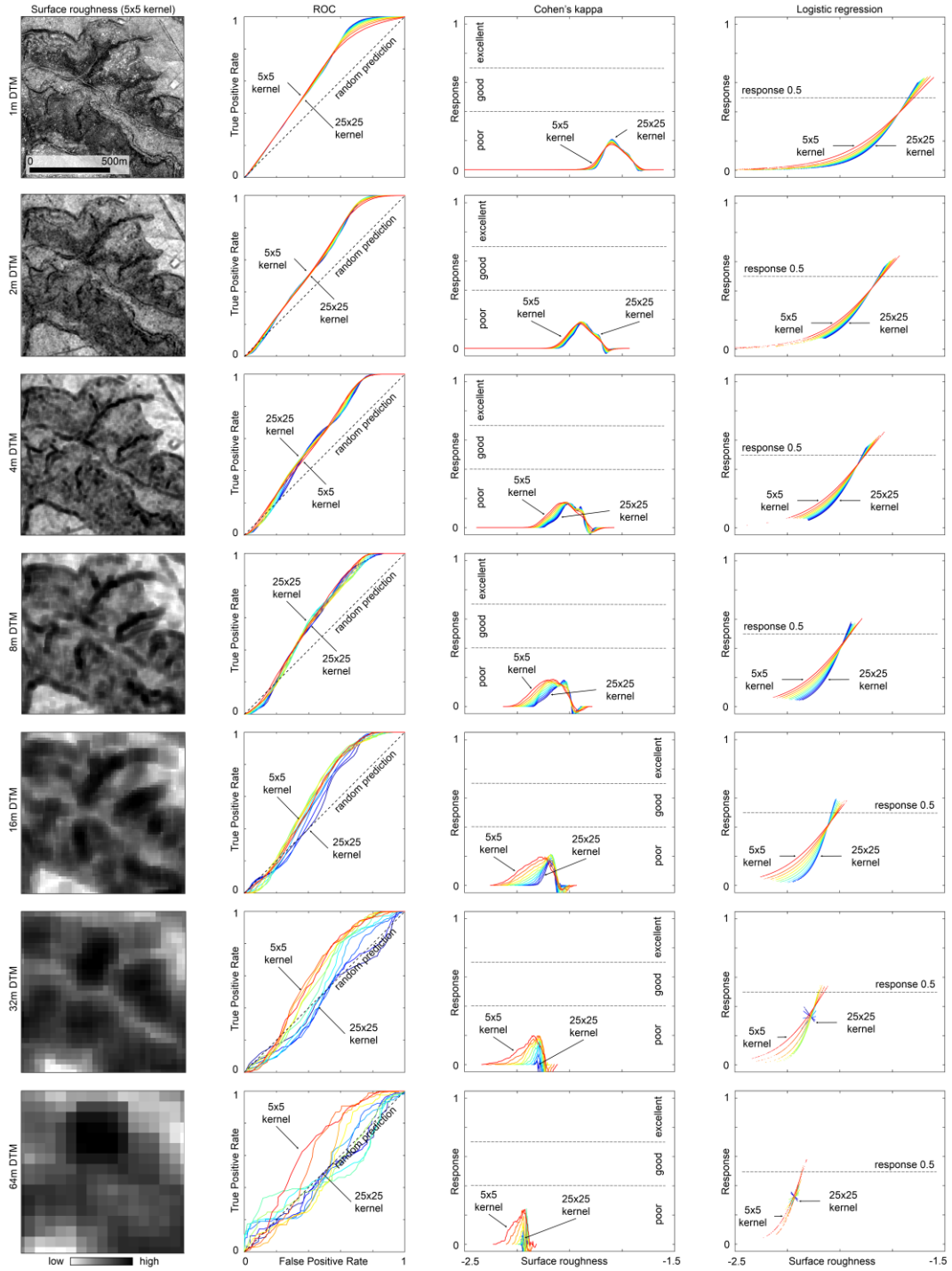

Figure 2.9 | The μ index for a 1-km² sample for the landslide study area; receiver operating characteristic (ROC) curves, Cohen's kappa, and logistic regression for roughness evaluated from 1, 2, 4, 8, 16, 32, and 64 m DTM with different kernel sizes of the standard deviation of curvature: 5 × 5 pixels, 7 × 7 pixels, …, and 25 × 25 pixels. The 1-km² sample is shown as a blue square on Figure 2.1.

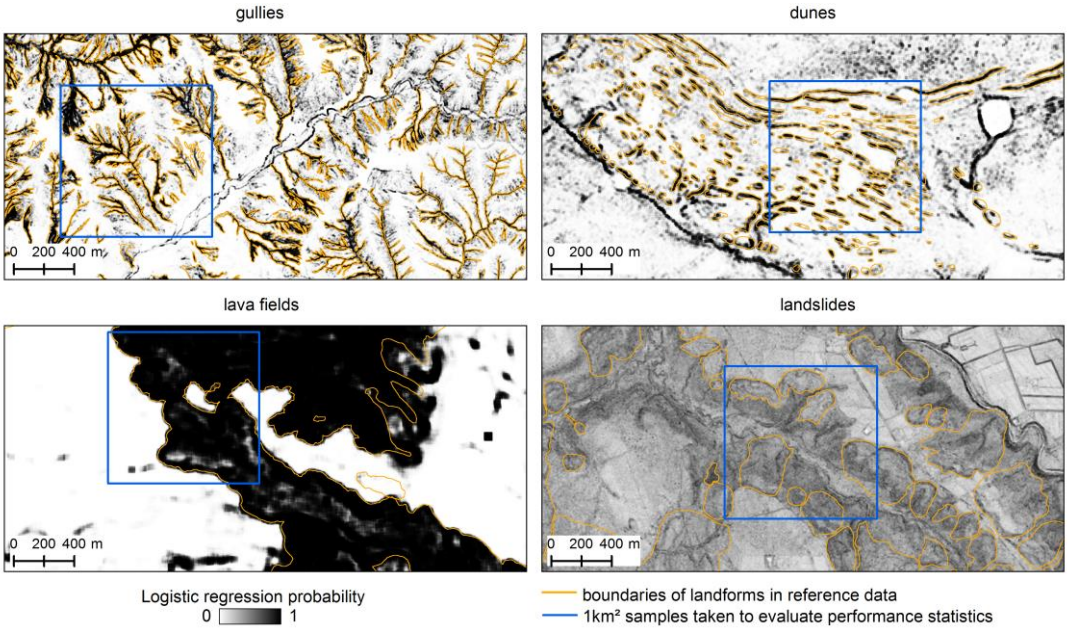

Figure 2.10 | Logistic regression probability of a pixel belonging to a specified landform type based on our μ index. The probability maps are for μ evaluated for: 2-m DTM with 5 × 5 kernel (gullies); 4-m DTM with 5 × 5 kernel (dunes); 2-m DTM resolution with 25 × 25 kernel (lava fields); and 2m DTM with 5 × 5 kernel (landslides).

Table 2.2 | Matrix for the area under the curve (AUC) probability of our calculated surface roughness for different DTM resolutions and kernel sizes.

		Resolution of DTM [m]							Resolution of DTM [m]						
		1	2	4	8	16	32	64	1	2	4	8	16	32	64
		Gullies							Dunes						
Kernel [pixels]	5×5	0.875	**0.945**	0.937	0.873	0.768	0.634	0.550	0.812	0.840	**0.906**	0.884	0.731	0.626	0.565
	7×7	0.894	0.945	0.921	0.846	0.747	0.607	0.544	0.836	0.870	0.903	0.819	0.660	0.595	0.565
	9×9	0.903	0.940	0.904	0.824	0.726	0.584	0.521	0.853	0.885	0.881	0.756	0.633	0.578	0.543
	11×11	0.907	0.932	0.888	0.806	0.705	0.584	0.504	0.865	0.890	0.852	0.707	0.620	0.581	0.536
	13×13	0.908	0.923	0.872	0.792	0.688	0.544	0.497	0.874	0.887	0.820	0.672	0.606	0.590	0.503
	15×15	0.907	0.914	0.859	0.781	0.674	0.527	0.488	0.880	0.880	0.787	0.651	0.592	0.585	0.492
	17×17	0.905	0.905	0.846	0.770	0.659	0.507	0.494	0.884	0.869	0.757	0.640	0.576	0.574	0.491
	19×19	0.902	0.896	0.835	0.760	0.644	0.491	0.504	0.887	0.855	0.729	0.633	0.568	0.558	0.487
	21×21	0.899	0.888	0.825	0.750	0.632	0.477	0.504	0.887	0.841	0.705	0.627	0.572	0.541	0.493
	23×23	0.895	0.879	0.815	0.741	0.618	0.470	0.513	0.886	0.826	0.685	0.621	0.579	0.523	0.499
	25×25	0.891	0.871	0.807	0.733	0.602	0.477	0.521	0.883	0.810	0.668	0.615	0.582	0.511	0.504
		Lava fields							Landslides						
Kernel [pixels]	5×5	0.951	0.976	0.974	0.919	0.789	0.648	0.658	0.619	**0.609**	0.612	0.624	0.612	0.608	0.655
	7×7	0.971	0.983	0.975	0.915	0.783	0.657	0.698	0.624	0.609	0.613	0.615	0.611	0.612	0.611
	9×9	0.978	0.984	0.976	0.917	0.783	0.681	0.758	0.627	0.609	0.612	0.610	0.613	0.614	0.533
	11×11	0.981	0.984	0.977	0.921	0.787	0.702	0.830	0.628	0.609	0.611	0.606	0.618	0.596	0.516
	13×13	0.981	0.985	0.977	0.926	0.797	0.729	0.867	0.630	0.609	0.609	0.605	0.621	0.582	0.511
	15×15	0.981	0.985	0.978	0.931	0.810	0.756	0.854	0.630	0.608	0.607	0.606	0.618	0.559	0.509
	17×17	0.980	0.986	0.979	0.935	0.823	0.782	0.834	0.631	0.607	0.605	0.607	0.610	0.529	0.494
	19×19	0.979	0.987	0.980	0.938	0.832	0.802	0.777	0.631	0.607	0.604	0.608	0.600	0.505	0.515
	21×21	0.978	0.987	0.980	0.939	0.837	0.823	0.719	0.632	0.606	0.602	0.608	0.589	0.484	0.512
	23×23	0.977	0.988	0.980	0.938	0.842	0.843	0.677	0.632	0.605	0.600	0.607	0.579	0.470	0.488
	25×25	0.975	**0.988**	0.980	0.937	0.846	0.864	0.635	0.632	0.604	0.599	0.607	0.571	0.472	0.478

Increasing intensity of the blue colour in the table represents the increase of the AUC value

the surrounding terrain, although the margins of the lava field were prone to offsets if larger kernels were used. Landslides were the most difficult formations to detect using our method (Fig. 2.9), largely regardless of kernel size or DTM resolution. Even logistic regression afforded little potential for distinguishing landslides from the surrounding landscape, with maximum probabilities of <0.6.

The performance metrics, performed using different combinations of resolution and kernel size, showed that DTM resolution affects landform detection more than does kernel size. Mapping the membership probabilities derived from logistic regression revealed a high visual agreement between pixels classified as gullies, and lava fields, and the manually digitised reference data (Fig. 2.10). Judging from the performance statistics (Table 2.2), we decided to work with the best parameter combinations for each land formation type: gullies (2-m DTM, 5 × 5 kernel), dunes (4-m DTM, 5 × 5 kernel), lava fields (2-m DTM, 25 × 25 kernel), and landslides (2-m DTM, 5 × 5 kernel).

2.5.2. Finding the optimal decision boundary

We tested various ways of finding an optimal decision boundary for distinguishing the landforms from the surrounding terrain. One of the simplest unsupervised means of discerning gullies (or other landforms) seeks a suitable threshold value in the distribution of μ sampled for a given area. From the many thresholding algorithms available (Saho et al., 1988; Sezgin and Sankur, 2004), we selected one of the simplest and most common non-parametric ones, by Otsu (1979). This method finds the optimal threshold by maximising the separability of the resultant classes, and minimising the weighted sum of variances within each class. Otsu's algorithm works well for bimodal data. Our μ are more unimodal in character (Fig. 2.4), so we restricted our threshold search to the bimodal range of the data, using the multithresh function in MATLAB for ten sample subsets for each landform type (Table 2.3; Fig. 2.1). We used an effectiveness metric representing the variance between classes, with higher values indicating higher separability and

Table 2.3 | Otsu thresholds and the effectiveness of thresholding.

Test area	Parameter	Whole dataset	Sample 1	Sample 2	Sample 3	Sample 4	Sample 5	Sample 6	Sample 7	Sample 8	Sample 9	Sample 10	Samples median
Gullies	Threshold[1]	1.0260	1.2971	1.2429	1.1503	1.2151	1.2309	1.1267	1.1414	1.3049	1.2254	1.2587	**1.2282**
	Effectiveness	0.6248	0.7110	0.7040	0.7326	0.6577	0.6902	0.7381	0.7455	0.7226	0.6884	0.7137	
Dunes	Threshold[2]	0.2879	0.3975	0.4149	0.4384	0.3891	0.4127	0.4010	0.4454	0.3765	0.3857	0.3950	**0.3993**
	Effectiveness	0.5819	0.6327	0.6567	0.6566	0.7019	0.6828	0.7508	0.6957	0.7595	0.7198	0.6724	
Lava fields	Threshold[3]	1.1056	1.1490	1.1199	1.1394	1.1821	1.1031	1.1380	1.2093	1.2083	1.2415	1.1348	**1.1442**
	Effectiveness	0.6731	0.8533	0.9072	0.8766	0.8803	0.8072	0.8419	0.8412	0.8224	0.8073	0.8275	
Landslides	Threshold[4]	-0.3005	-0.1076	-0.0993	-0.1943	-0.3244	-0.1620	-0.3413	-0.4145	-0.1015	-0.1940	-0.1944	**-0.1943**
	Effectiveness	0.6456	0.6206	0.6798	0.6928	0.7349	0.7265	0.7428	0.6874	0.6850	0.6434	0.7580	

[1] thresholds for μ evaluated from 2-m DTM with 5 × 5 kernel for standard deviation of the total curvature
[2] thresholds for μ evaluated from 4-m DTM with 5 × 5 kernel for standard deviation of the total curvature
[3] thresholds for μ evaluated from 2-m DTM with 25 × 25 kernel for standard deviation of the total curvature
[4] thresholds for μ evaluated from 2-m DTM with 5 × 5 kernel for standard deviation of the total curvature

higher bimodality in the histogram; effectiveness denotes the maximum thresholds in the range between zero and one. We also tested how the thresholds selected for the subsets differed from those for the full data. The effectiveness was lower when using all data than when only subsets were used (Table 2.3).

2.5.3. Qualitative and quantitative assessment of classification and the role of threshold uncertainty

We tested how varying Otsu thresholds affected the ability to correctly detect gullies and other landforms, selecting the optimal threshold where Type I and Type II errors, or producer's and user's accuracies, were equal (Strumpf and Kerle, 2011; Fig. 2.11). Other criteria, such as the lowest total error, the highest Cohen's kappa, or the overall accuracy are also possible to select the optimal threshold (Table 2.3, Fig. 2.11). Because we used a kernel size for estimating roughness, our thresholds were shifted by the kernel width. To remove this effect, we applied an

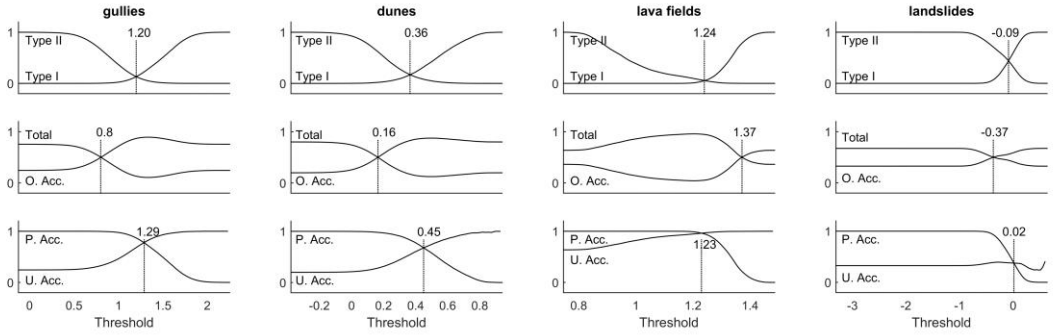

Figure 2.11 | Type I, Type II, and total errors, overall (O. Acc.), producer's (P. Acc.), and user's (U. Acc.) accuracies for thresholds used for natural hazard-related landforms classification. The figure represents the results for a 1-km² data subset.

Table 2.4 | Quantitative evaluation of the classification for thresholds evaluated by Otsu algorithm.

	Statistic measure	Type I	Type II	Total	O. Acc.	P. Acc.	U. Acc.	Kappa	Type I	Type II	Total	O. Acc.	P. Acc.	U. Acc.	Kappa
		Gullies							Dunes						
1km² sample	Otsu	0.16	0.11	0.12	0.88	0.84	0.71	0.70	0.22	0.13	0.15	0.85	0.78	0.60	0.59
	Otsu & erosion	0.32	0.04	0.11	0.89	0.68	0.84	0.69	0.34	0.07	0.12	0.88	0.66	0.70	0.60
	P&U Acc.	0.23	0.07	0.11	0.89	0.77	0.78	0.71	0.32	0.08	0.13	0.87	0.68	0.68	0.60
All dataset	Otsu	0.14	0.13	0.13	0.87	0.86	0.52	0.57	0.22	0.18	0.18	0.82	0.78	0.17	0.22
	Otsu & erosion	**0.31**	**0.06**	**0.10**	**0.90**	**0.69**	**0.63**	**0.60**	**0.33**	**0.13**	**0.14**	**0.86**	**0.67**	**0.21**	**0.27**
	P&U Acc.	0.21	0.09	0.10	0.90	0.79	0.59	0.61	0.31	0.12	0.13	0.87	0.69	0.22	0.28
		Lava fields							Landslides						
1km² sample	Otsu	0.00	0.15	0.05	0.95	1.00	0.92	0.88	0.27	0.56	0.46	0.54	0.73	0.39	0.14
	Otsu & erosion	0.01	0.03	0.02	0.98	0.99	0.98	0.96	0.40	0.47	0.44	0.56	0.60	0.39	0.12
	P&U Acc.	0.04	0.07	0.05	0.95	0.96	0.96	0.90	0.63	0.30	0.41	0.59	0.37	0.38	0.07
All dataset	Otsu	0.04	0.32	0.27	0.73	0.96	0.44	0.44	0.33	0.35	0.34	0.66	0.67	0.44	0.28
	Otsu & erosion	**0.07**	**0.22**	**0.19**	**0.81**	**0.93**	**0.53**	**0.55**	**0.48**	**0.25**	**0.32**	**0.68**	**0.52**	**0.45**	**0.25**
	P&U Acc.	0.13	0.19	0.18	0.82	0.87	0.54	0.56	0.73	0.14	0.31	0.69	0.27	0.43	0.14

Type I error (Type I); Type II error (Type II); Total error (Total); Overall accuracy (O. Acc.); producer's accuracy (P. Acc.); user's accuracy (U. Acc.); Cohen's kappa (Kappa); performance statistics evaluated for balanced producer's and user's accuracy (P&U Acc.).

erosion morphological filter (Haralick et al., 1987) and reclassified all pixels assigned to gullies along their boundaries in an n-pixel corridor, where n was determined by the kernel size. For a 5 × 5-pixel kernel, for example, n = 2. This approach yields higher overall accuracy, user's accuracy, and Cohen's kappa, as well as lower total error for all landforms (Table 2.4), while making the results for the balanced producer's and user's accuracies nearly equal.

Figure 2.12 shows the differences between the classification results for Otsu's threshold with and without morphological erosion. For example, the boundaries of lava fields were detected more accurately when applying morphological erosion (25 × 25 kernel). For other landforms, however, this treatment did not work as well, because we used a 5 × 5 kernel. For landslides, neither

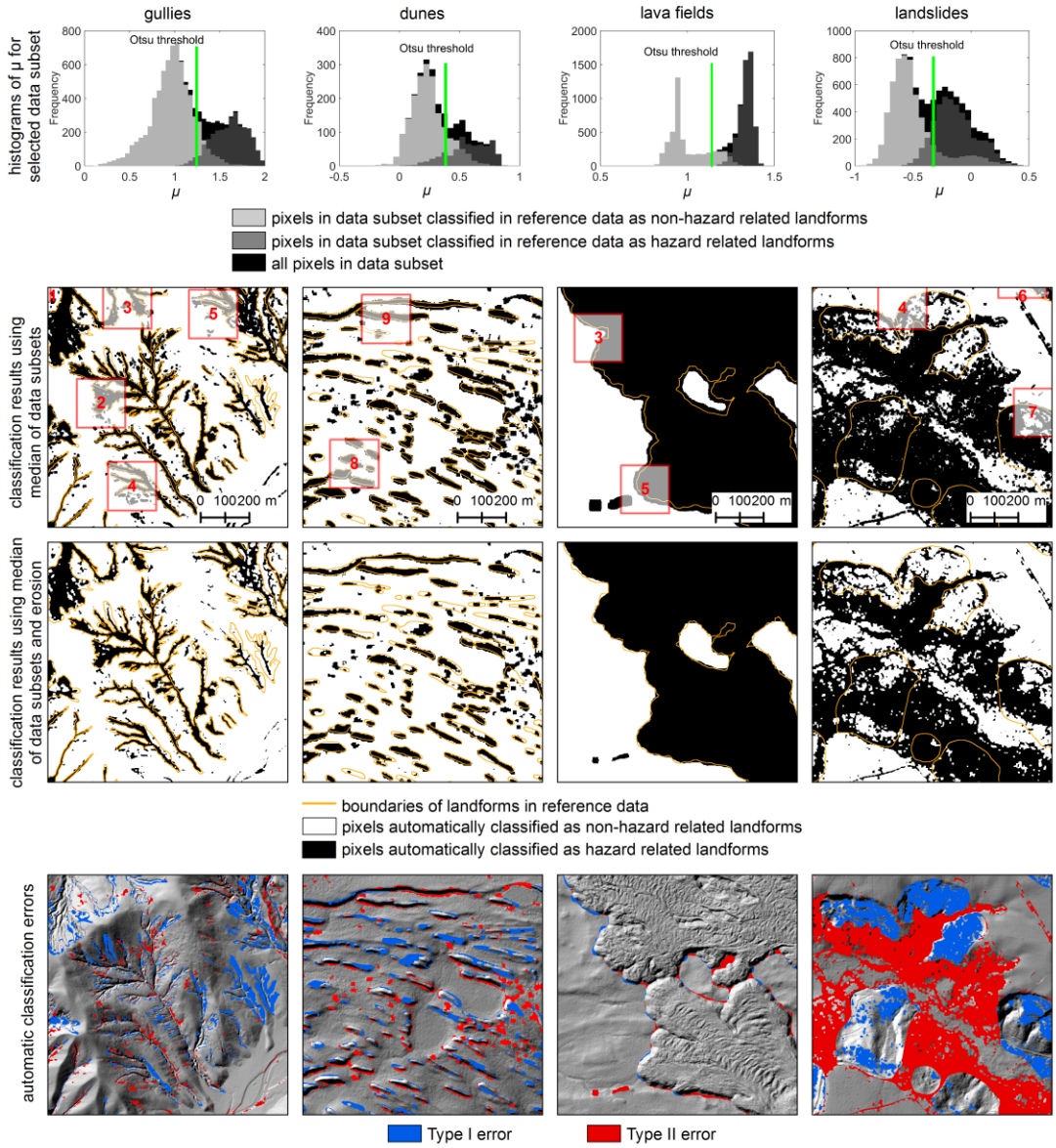

Figure 2.12 | Histograms for reference data with Otsu threshold for μ. Below are the predicted landforms based on: histogram threshold of data subsets, and histogram threshold of data subsets and erosion, as well as errors of the classification. The red numbered squares on the figures indicate the subset areas used to generate the histograms and evaluate the median of the optimal threshold.

approach worked, because they are broad and generate a less dramatic contrast in terrain orientation. Although landslide scarps were reasonably well discerned by our roughness index, it failed to capture the outline of the deposits, regardless of the choice of threshold. Our approach did, however, allow for reasonably good detection of gullies and lava fields (Fig. 2.11). In terms of performance, a morphological erosion filter increased the user's accuracy for the 1-km² sample areas (Table 2.4).

Finally, we tested our method for detecting gullies and other landforms for the larger study areas, obtaining a lower user's accuracy of 0.63 and a Cohens' kappa of 0.60 (Table 2.4). For other analysed landforms, the overall and producer's accuracies remained high, with the exception of, the user's accuracy, which decreased more than for gullies. More pixels representing the target landforms were correctly classified; however, many pixels of the surrounding terrain were still misclassified, especially for landscapes with dunes and landslides.

2.5.4. Comparison with other algorithms

We compared the performance of our method with that of others that use the standard deviation of residual topography (Haneberg et al., 2005) or the standard deviation of slope (Frankel and Dolan, 2007), using log-transformed data throughout. The methods of Haneberg et al. (2005) and Frankel and Dolan (2007) were slightly more successful in detecting dunes than was our method, but less successful for lava fields. None of the methods detected landslides sufficiently well. We also tested our approach on profile and planar curvature alone, and found that total and planar curvatures worked best (Fig. 2.13), with the exception of detecting dunes, where profile curvature gave better results.

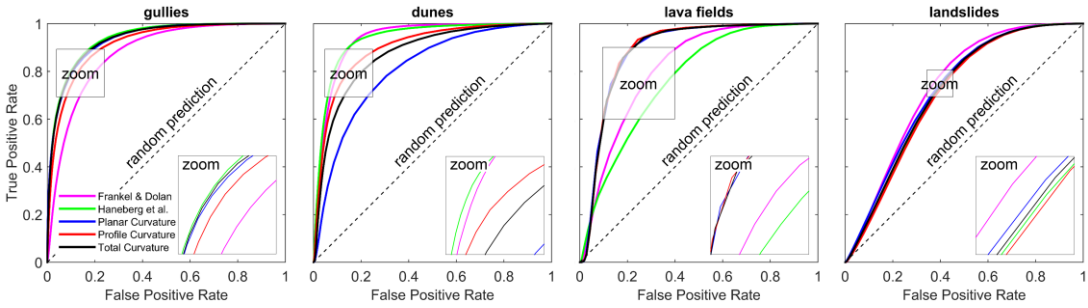

Figure 2.13 | Comparison of our μ (*Total Curvature*) with different surface roughness indexes: roughness based on profile curvature (*Profile Curvature*), roughness based on planar curvature (*Planar Curvature*), roughness based on slope (*Frankel & Dolan*), and roughness based on detrended DTM (*Haneberg et al.*). All the methods were evaluated for the same DTM resolution and using the same moving window as our total curvature-based μ, along with application of log-transformation.

2.6. Discussion

Surface roughness is a terrain metric that is widely-used in detecting terrain landforms (Riley et al., 1999; McKean and Roering, 2004; Cavalli et al., 2008; Pollyea and Fairley, 2011). Many previously-published roughness algorithms, however, await sufficient testing of their

performance outside their training areas. Our results demonstrate that this lack of testing can cause misinterpretations if applied for detecting different landforms or study areas. In our study areas, we found that our roughness method outperformed previous ones (Haneberg et al., 2005; Frankel and Dolan, 2007) when detecting gullies and lava fields. We also found that using total curvature yielded overall better results than did the profile curvature, in contrast to the findings of previous work (Grohmann et al., 2011), offering an alternative for evaluating surface roughness without needing to de-trend a DTM. Moreover, we demonstrated that increasing kernel size may improve the detectability of landforms that are commensurately larger, although at the expense of smaller landforms. Larger kernels also compromised the accuracy of landform boundaries more than it did their correct classification. Indeed, coarser DTMs limited the overall detection potential, creating more generalised and less accurate landform outlines. Comparing the results from Figures 2.6–2.9, we see that coarser resolution with grid spacing >8 m appears to be insufficient for detecting any of the landforms, as larger pixels increase the area of averaging and compromise local roughness details. For example, logistic regression showed that using a 16-m DTM came close to using a random classifier for nearly all landform types. These trends did not apply to landslides, most likely because the manual mapping of landslides was the most difficult, as the deposits were not fresh and their boundaries were partly diffuse. Some landslides were the forest, producing a coarser DTM than for unvegetated areas. This comparatively low quality of the training data may be responsible for producing less convincing ROC curves. Our μ did not detect landslides with sufficient accuracy, likely because their age and occurred exogenous processes had caused blurring of the landforms, making them difficult to distinguish from other landforms.

We recommend larger kernel sizes only for detecting the largest landforms in a study area, such as lava fields, especially for first-order reconnaissance where precise landform outlines are not important. Kernels that are too large, coupled with resolution that is too low, will compromise unsupervised landform detection. Eventually, the length scale of the landform dictates the success of detection, whereas data resolution affects our roughness index more than does kernel size, as coarser topographic data smooth out topographic details (Li et al., 2011; Grohmann, 2015).

Automatically selected Otsu's thresholds, together with a morphological filter, yield acceptable results for nearly all landform types (Fig. 2.11, Table 2.4). The shape and aspect of landforms appeared to be largely irrelevant for unsupervised detection. For the same data resolution and kernel size, we achieved a similar user's accuracy for linear gullies <10-m in width and irregular lava fields >300-m in width. Landform size and shape do play an important role in varying data resolution and kernel size, however, which in turn depend on the study objective. The performance of our method was also independent of the fraction of test area covered by the

candidate landforms: dunes covering <1% of the area were detected with higher accuracy than were landslides covering 28% of the area (Table 2.4).

Otsu's nonparametric method for selecting the best decision boundary is less time-consuming and produces more accurate and objective results than does a trial-and-error approach (d'Oleire-Oltmanns et al., 2013; Table 2.4; Fig. 2.11). Subsetting data with two different landform types produced optimal results with Otsu's algorithm, but these deteriorated for fuzzier landform outlines, such the landslides we studied (Table 2.2). Subsets of data containing landform boundaries allowed for more accurate thresholds because the separability in the histogram was better. We stress that the specific threshold values of our classification cannot be readily applied to other areas containing the same landforms.

Image segmentation into small homogenous pieces (Baatz and Schäpe, 2000; Blaschke, 2010) is commonly used in OBIA to remove salt-and-pepper noise. In addition, OBIA allows using neighbourhood relations to assign classified objects. Future work could thus merge our roughness approach with OBIA to improve classification. Segmentation may be especially helpful for spuriously-detailed DTMs where the "topographic variations are unknown or are indistinguishable from instrument error" (Smith, 2014). Such errors on DTMs can distort roughness estimates, as curvature errors strongly increase with elevation errors (Schmidt et al., 2003). Thus, we recommend that before using our method, one should verify the quality of the input DTM and remove these errors. The high sensitivity of curvature to errors and high contrasts was only slightly apparent in our study, however. Indeed, roughness metrics are designed to pick up local spikes in curvature and the more important issue is whether the DTM duly reflects real terrain roughness or contains artefacts from inadequate processing. Our method may also be useful for coarser Shuttle Radar Topography Mission data if the aim is to recognise large-scale landforms with approximately zero roughness at the regional scale, such as large lakes.

2.7. Conclusions

We systematically tested the usefulness of surface roughness—defined here as the local variability of total curvature—for detecting gullies, dunes, lava fields, and landslides from high-resolution LiDAR DTMs in an unsupervised manner. The algorithm is freely available as a toolbox for ArcGIS software and allows the evaluation of surface roughness without data detrending, because it uses the total curvature as an input source. We found that data resolution has a greater effect on the performance of detecting these landforms with surface roughness than does kernel size. We also found that this simple method aided in the automated mapping of several landform types, provided that they have sufficient roughness contrasts compared to the surrounding terrain. Our method is limited, however, in that it is neither capable of, nor designed to, recognising the type of detected landforms. Expert knowledge is still necessary to correctly

identify the detected landforms. Future research may wish to focus on combining roughness-based landform detection with characteristics of landform shape, position, and neighbourhood. With further development, our method may be suitable not only for detecting landforms, but also for tracking landform dynamics through time.

Acknowledgments

This research was funded by the European Union under the Marie Curie Initial Training Network ALErT (Creation of an interactive CAP natural-hazard database), project-number: FP7-PEOPLE-2013-ITN-607996. The LiDAR data used in the study were provided by the U.S. Geological Survey through the Open Topography Facility (http://opentopo.sdsc.edu/) with support from the National Science Foundation under NSF Award Numbers 0930731 & 0930643 and the Alaska Division of Geological & Geophysical Surveys online map "Elevation Datasets in Alaska" (http://maps.dggs.alaska.gov/elevationdata/). We thank R. Stengele, G. Mandlburger, and W. Schwanghart for discussions, and three reviewers for their comments on an earlier version of this manuscript.

Supplementary material

The code for evaluating terrain surface roughness is in the Appendix A.

Chapter 3

Lakes

Published as: Korzeniowska, K., Korup, O., 2017. Object-based detection of lakes prone to seasonal ice cover on the Tibetan Plateau, *Remote Sensing* 9(4), 339, doi:10.3390/rs9040339.

Abstract

The Tibetan Plateau, the world's largest orogenic plateau, hosts thousands of lakes that play prominent roles as water resources, environmental archives, and sources of natural hazards such as glacier lake outburst floods. Previous studies have reported that the size of lakes on the Tibetan Plateau has changed rapidly in recent years, possibly because of atmospheric warming. Tracking these changes systematically with remote sensing data is challenging given the different spectral signatures of water, the potential for confusing lakes with glaciers, and difficulties in classifying frozen or partly frozen lakes. Object-based image analysis (OBIA) offers new opportunities for automated classification in this context, and we have explored this method for mapping lakes from LANDSAT images and Shuttle Radar Topography Mission (SRTM) elevation data. We tested our algorithm for most of the Tibetan Plateau, where lakes in tectonic depressions or blocked by glaciers and sediments have different surface colours and seasonal ice cover in images obtained in 1995 and 2015. We combined a modified normalised difference water index (MNDWI) with OBIA and local topographic slope data in order to classify lakes with an area >10 km². Our method derived 323 water bodies, with a total area of 31,258 km², or 2.6% of the study area (in 2015). The same number of lakes had covered only 24,892 km² in 1995; lake area has increased by ~26% in the past two decades. The classification had estimated producer's and user's accuracies of 0.98, with a Cohen's kappa and F-score of 0.98, and may thus be a useful approximation for quantifying regional hydrological budgets. We have shown that our method is flexible and transferable to detecting lakes in diverse physical settings on several continents with similar success rates.

3.1. Introduction

The Tibetan Plateau is the world's largest orogenic plateau, with a mean elevation of more than 4000 m above sea level (a.s.l.), and is known as "the Roof of the World" or "the 3rd Pole of the Earth" (Qiu, 2008; Song et al., 2014a; Wang, 2016). The Plateau is surrounded by the Himalayas to the south, the Kunlun Shan to the north, the Pamir to the west, and the Qilian Shan to the northeast (Liu and Chen, 2000). Together with these ranges, the Tibetan Plateau serves as "the Water Tower of Asia" (Immerzeel et al., 2010; Song et al., 2013; Immerzeel et al., 2014), hosting glaciers and thousands of lakes that play prominent roles as water resources, environmental archives, and potential sources of natural hazards, such as glacier lake outburst floods (Yao et al., 2012).

The Tibetan Plateau is among the most sensitive places to atmospheric warming (Zhang et al., 2011). Temperatures on the plateau have risen by 0.3°C per decade – three times the global average (Qiu, 2008; Yao et al, 2012). Symptoms attributed to atmospheric warming on the plateau include retreating glaciers (Liu and Chen, 2000; Yang et al., 2008), degrading permafrost (Qiu, 2008; Yang et al., 2010), and rapidly changing lake areas (Yang and Lu, 2014). The glaciers in the surrounding mountain ranges are prone to changing hydrological and meteorological conditions, potentially contributing to changes in the size of the Plateau's lakes (Immerzeel et al., 2014). Many studies have tried to detect and monitor these changes (Zhang et al., 2011; Shao et al., 2007; Zhu et al., 2010; Zhang et al., 2011; Phan et al., 2012). Some researchers (Song et al., 2014a; Yang et al., 2008) have argued that the meltwater from glaciers largely drives the size distribution of these lakes. Ground surveys (Ouma and Tateishi, 2006) help to verify the changes in detail; however, such field measurements are difficult, expensive, and time consuming for large regions, especially if needed regularly. Here, satellite-based monitoring offers a solution in terms of repeated and standardised images of lakes, their surface colour, and seasonal ice cover.

Yang and Lu (2014) used LANDSAT images covering several decades to capture how the size of lakes on the Tibetan Plateau has changed. Seasonal changes in size are evident for at least 105 lakes (Song et al., 2014b), with those in the south, central, and northeastern parts of the plateau having higher water levels between March and October, but showing almost no changes between November and February. Many lakes in the north, however, have lower water levels in the warm season, mainly because of strong evaporation and low precipitation. Ma et al. (2010) reported that between 1960 and 2006, most existing lakes grew in size, while 60 new lakes >1 km² appeared on the Tibetan Plateau and surrounding areas. Fang et al. (2016) revealed different trends in how 35 lakes changed over the past 40 years. For example, Siling Co, the largest lake on the plateau, has increased by >600 km², whereas lakes in the Himalayas have shrunk; lakes in the north and northeastern Tibetan Plateau mainly grew. A local study of Nam Co reported that

this lake expanded by 51.8 km² between 1970 and 2010 (Liu et al., 2010), owing to increasing annual precipitation, air temperature, and runoff, and decreasing evaporation, similar to trends of other lakes such as Siling Co, Bam Co, Pung Co, Darab Co, and Zige Tangco (Lei et al., 2013).

Few methods of detecting lakes and their changes on the Tibetan Plateau have been developed further. Li et al. (2011) proposed an algorithm applying a normalised difference water index, topographic slope, and hillshading to discern glacial lakes from shadows on LANDSAT ETM+ images. They found that pixels classified as water were bimodally distributed, as opposed to pixels representing other land cover, and thus distinct from melting glaciers and shadows. Song et al. (2013) estimated changes in lake-water storage on the Tibetan Plateau from the early 1970s to 2011. Using LANDSAT images and ICESat altimetry data, they reported an increase in lake areas and total water storage. They noted a more positive water balance in the northern and central plateau, but a decreasing water balance in the southeastern part, mostly related to glacier melt. Comparable results (Phan et al., 2012; Wang et al., 2013) from ICESat data apply to level changes for 154 lakes on the Tibetan Plateau between 2003 and 2009.

Systematically tracking lake changes offers new challenges and opportunities for automatic classification methods, such as object-based image analysis (OBIA; Blaschke, 2010). Such automatic mapping of landforms reduces the operator bias produced by manual digitisation, and allows rapid investigation of large regions. The training of OBIA algorithms requires careful design, however, especially for areas like the Tibetan Plateau, where simple thresholding frequently confuses lakes with glaciers, ice and cloud cover, or highly reflecting sediments. We address this issue and present an OBIA approach to classifying large lakes on the Tibetan Plateau based on LANDSAT images and the Shuttle Radar Topography Mission (SRTM) digital elevation model (DEM). Our objective was to find a suitable workflow using an object-based approach for detecting large lakes based on a water index and digital topography, aiming for a metric insensitive to glaciers and ice cover, running water, or mountain shadows. We present here a method for rapidly delineating lake boundaries and for examining general trends in lakes size for a large area, such as the Tibetan Plateau. Specifically, we used a modified normalised difference water index (MNDWI; Xu, 2006) to detect water pixels, and OBIA to extract lake boundaries and distinguish them from rivers and glaciers. We then further tested whether our method is readily applicable to classifying lakes of different origins and in different environmental settings elsewhere.

3.2. Previous work

Remote sensing data are indispensable for delineating surface objects and tracking how they change (Singh, 1989; Melesse et al., 2007; Arp et al., 2012). The continuity of data collection with set parameters (Chander et al., 2009) enables consistent and accurate long-term analyses.

Satellite images have a long tradition in classifying water (Frazier and Page, 2000; McFeeters, 2013; Mueller et al., 2016), streams (Yang and Smith, 2013), changes in lake volumes (Fitzpatrick et al., 2014), and lake monitoring (Zhu et al., 2014).

3.2.1. Thresholding methods

Methods for automatically detecting water bodies from remote sensing data use various spectral properties of water (Song et al., 2014a; Nath and Deb, 2010). The most common approach uses thresholds on a single band or a ratio of bands, and is easy, quick, and quite accurate in delineating boundaries of water bodies (Song et al., 2014a; Ryu et al., 2002). Frazier and Page (2000) were among the first to use density slicing on a single band (ρ) of LANDSAT 5 TM images, determining the optimal threshold on each band (i.e., ρ_{Blue}, ρ_{Green}, ρ_{Red}, ρ_{NIR} (ρ near-infrared), ρ_{SWIR1} (ρ short-wave infrared), and ρ_{SWIR2} (ρ short-wave infrared)). They found that ρ_{SWIR1} offered the most accurately classified water areas, only marginally inferior to those obtained via a more costly maximum likelihood-based approach to slicing six bands in total. McFeeters (1996) introduced a band-ratio method for separating water from other land cover classes. His normalised difference water index (NDWI; McFeeters, 1996) makes assumptions similar to those used for computing the normalised difference vegetation index (NDVI; Townshend and Justice, 1986; Table 3.1), where vegetated surfaces have positive NDVI values, bare-ground areas have values close to zero, and water surfaces have negative values. McFeeters (1996) found that replacing ρ_{Red} with ρ_{Green} emphasised water areas more than other land-surface objects (Table 3.1), where water surfaces have positive NDWI values, and other objects have negative values. The NDWI remains widely used and has motivated the search for alternative band ratios to allow

Table 3.1 | Band ratio indices proposed in previous studies to classify vegetation and water.

Index	Equation	Author
Normalised Difference Vegetation Index	$\text{NDVI} = (\rho_{\text{NIR}} - \rho_{\text{Red}}) / (\rho_{\text{NIR}} + \rho_{\text{Red}})$	Townshend and Justice, 1986
Normalised Difference Water Index	$\text{NDWI} = (\rho_{\text{Green}} - \rho_{\text{NIR}}) / (\rho_{\text{Green}} + \rho_{\text{NIR}})$	McFeeters, 1996
Normalised Difference Water Index	$\text{NDWI} = (\rho_{\text{Red}} - \rho_{\text{SWIR1}}) / (\rho_{\text{Red}} + \rho_{\text{SWIR1}})$	Rogers and Kearny, 2004
Modified Normalised Difference Water Index	$\text{MNDWI} = (\rho_{\text{Green}} - \rho_{\text{SWIR1}}) / (\rho_{\text{Green}} + \rho_{\text{SWIR1}})$	Xu, 2006
Automated Water Extraction Index (for non-shadow areas)	$\text{AWEI}_{\text{nsh}} = 4 \times (\rho_{\text{Green}} - \rho_{\text{SWIR1}}) - (0.25 \times \rho_{\text{NIR}} + 2.75 \times \rho_{\text{SWIR2}})$	Feyisa et al., 2014
Automated Water Extraction Index (for shadow areas)	$\text{AWEI}_{\text{sh}} = \rho_{\text{Blue}} + 2.5 \times \rho_{\text{Green}} - 1.5 \times (\rho_{\text{NIR}} + \rho_{\text{SWIR1}}) - 0.25 \times \rho_{\text{SWIR2}}$	Feyisa et al., 2014
Water Index	$\text{WI} = 1.7204 + 171\rho_{\text{Green}} + 3\rho_{\text{Red}} - 70\rho_{\text{NIR}} - 45\rho_{\text{SWIR1}} - 71\rho_{\text{SWIR2}}$	Fisher et al., 2016

better separation of water bodies from other land cover. For example, Rogers and Kearny (2004) suggested using the ratio of ρ_{Red} and ρ_{SWIR1} to automatically delineate water boundaries, arguing that only water is more reflective in ρ_{SWIR1} than ρ_{Red}. The NDWI often misclassifies noise in urban areas, because the reflectance pattern of built-up areas on ρ_{Green} and ρ_{NIR} mimics that of water (Xu, 2006). Built-up areas also reflect much stronger in ρ_{SWIR1} than in ρ_{NIR}, so that Xu (2006) proposed a modified normalised difference water index (MNDWI; Table 3.1), which maintains a robust threshold (Ji et al., 2009). Nonetheless, new and more complex indices are on the rise. Feyisa et al. (2014) suggested a non-normalised automated water extraction index (AWEI) from multi-band ratios of LANDSAT 5 TM data, as an alternative for areas that are easily misclassified as water, such as dark surfaces ($AWEI_{nsh}$) and mountainous areas with deep shadows: ($AWEI_{sh}$; Table 3.1). The non-normalised water index (WI) proposed by Fisher et al. (2016) combines five LANDSAT ETM+ bands (Table 3.1), and is intended mainly for regional applications. Upon testing several band-ratio indices, Ouma and Tateishi (2006) reported that in general the NDWI overestimated water areas by including non-water pixels, whereas the MNDWI underestimated water areas by rejecting some water pixels. Amongst all these methods, simple thresholding can be very accurate only in relatively flat areas, whereas in mountainous terrain it frequently misclassifies shadows, snow, ice, and clouds with spectral properties similar to those of water. Thresholding is also unable to distinguish between rivers and lakes. Combining the water index with more advanced methods such as OBIA, segmentation, and spectral matching is preferable (Jawak et al., 2015).

3.2.2. Classification methods

Several methods have been designed for extracting lake outlines from remote sensing data. Habib et al. (2006) combined the spectral angle mapper classification method, the irregular pyramid, and the watershed-with-markers methods in order to identify lakes from SPOT images. They evaluated the angular spectral deviation between every pixel and a set of reference spectra, and assigned each pixel to the closest reference spectrum. Using graph theory and a bottom-up approach to merge neighbouring pixels into bigger segments (irregular pyramids), they also incorporated watershed segmentation. To avoid oversegmentation, they applied markers, which they used as the minima of the gradient image.

Texture analysis is an approach aiding the regional mapping of larger lakes (>200 m^2), involving thresholding and supervised classification of LANDSAT GeoCoverTM mosaics (GWEM; Verpoorter et al., 2012). The method uses a low-pass filter with 3 × 3 kernel size to remove small objects (<10 pixels). Thus, derived lake polygons are then combined with hillshade data to find shadows wrongly classified as lakes, as shadows and clouds are major sources of misclassification for this approach. Alternatives include an automated method for extracting

rivers and lakes from LANDSAT TM and ETM+ images (Jiang et al., 2014), which combines the NDWI, MNWDI, and AWEI for more reliable mapping, especially when considering neighbour effects of mixed pixels at lake shores (Jiang et al., 2014). All these methods, however, were tested in ice- and snow-free areas only.

A global mapping study addressing the problem of ice in detecting water bodies from LANDSAT images (Yamazaki et al., 2015) relied on the MNDWI, and on a SRTM DEM to exclude ice, snow, and shadows. Sheng et al. (2016) proposed a similar method at continental and global scales using LANDSAT 8 and segmenting the NDWI with an arbitrary initial threshold to detect lakes. They analysed each lake separately to determine individual thresholds, while SRTM-derived slope and hillshade data helped to remove shadows in mountainous terrain. Again, none of these approaches catered to the detection of lakes in a (partly) frozen state.

3.2.3. Classification methods and monitoring

The water indices and other more advanced classification methods find use in monitoring long-term changes of water areas. An example of small-scale change detection is a study by Gao et al. (2012), who investigated a global database of large reservoirs with 250-m resolution Moderate Resolution Imaging Spectroradiometer (MODIS) data. They analysed changes in the areas of 34 reservoirs between 1992 and 2010 by thresholding and clustering the NDVI for delineating water bodies. This approach worked well and consistently for classifying reservoirs, particularly those with small shoreline-to-area ratios. Similarly, Deus and Gloaguen (2013) used MODIS data, the MNDWI, and histogram thresholding to quantify changes in Lake Manyara in East Africa, detecting significant decreases in lake area that were strongly correlated with annual rainfall variability. Bai et al. (2011) used LANDSAT MSS, TM, and ETM+ images, as well as segmentation of the NDWI to study lake changes in arid central Asia, and found that lakes decreased in size by ~50% between 1975 and 2007, with shrinkage spreading from east to west along major precipitation gradients. Rokni et al. (2014) used LANDSAT TM, ETM+, and OLI images to automatically extract water areas and model the changes of Lake Urmia, Iran, from 2000 – 2013, and found that the NDWI was the most suitable of the various indices for mapping a shrinking lake area.

3.3. Study area and data

Our study covered nearly 1,187,000 km², the greater part of the Tibetan Plateau (Fig. 3.1), where lakes mostly formed in tectonic depressions, or behind glaciers and sediments. The lakes have different colours due to sediment concentrations, mineral content (salinity), water depths, aquatic vegetation, and seasonal ice cover (Fig. 3.2). We excluded from our analysis the southeastern Tibetan Plateau because few cloud-free LANDSAT images were available for this area. We analysed 47 LANDSAT 5 images taken in 1995 and 47 LANDSAT 8 images taken in

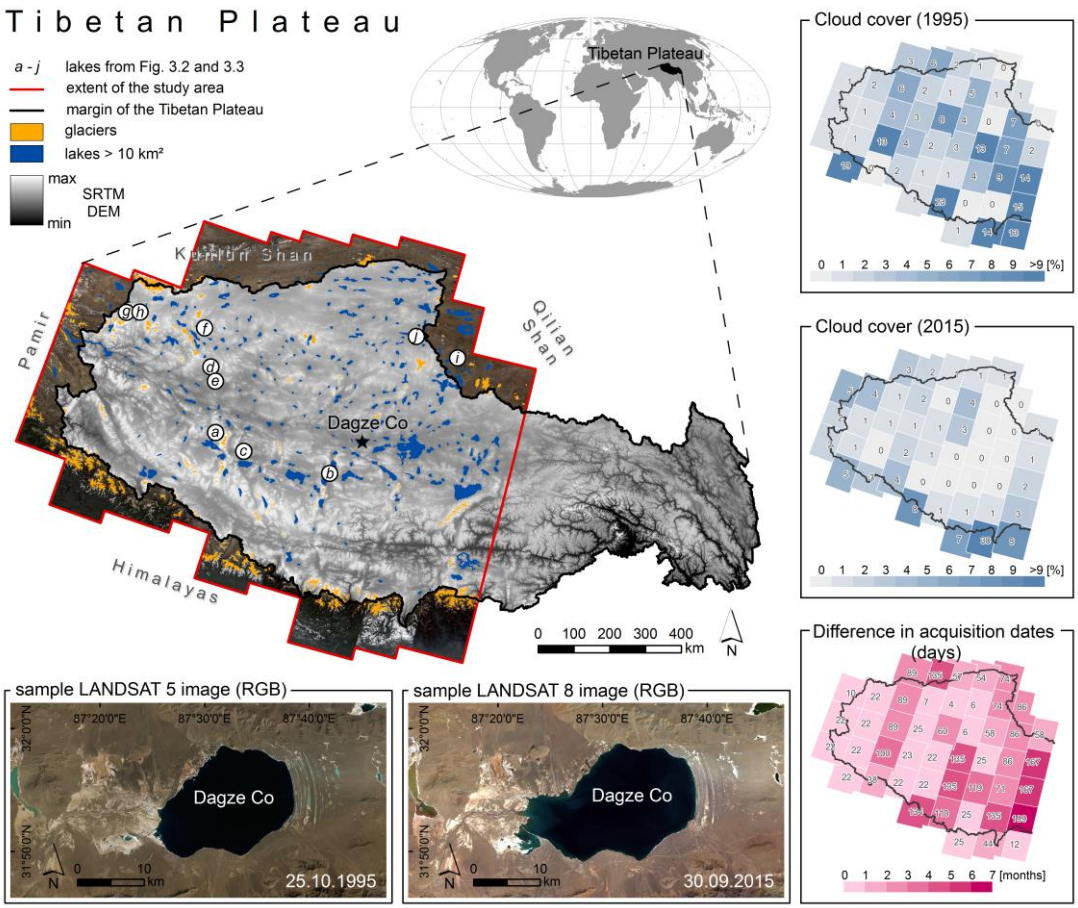

Figure 3.1 | Study area of the Tibetan Plateau, showing glaciers and lakes with an area >10 km². Cloud cover and acquisition dates differ between images for the two time slices in 1995 and 2015. LANDSAT image credits: U.S. Geological Survey (http://espa.cr.usgs.gov/); SRTM data credits: CGIAR Consortium for Spatial Information (http://srtm.csi.cgiar.org/).

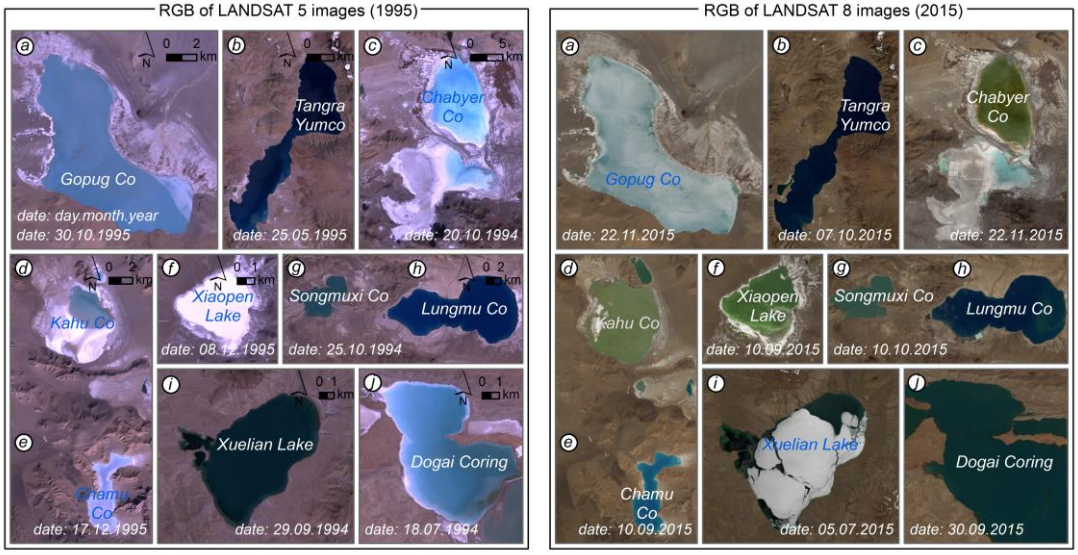

Figure 3.2 | Examples of seasonal differences in lake-ice cover and corresponding RGB values in LANDSAT 5 (1995) and LANDSAT 8 (2015) images. For lake locations on the Tibetan Plateau see corresponding labels on Figure 3.1. LANDSAT image credits: U.S. Geological Survey (http://espa.cr.usgs.gov/).

2015. The size of the study area and the different weather conditions captured on these images required that we analyse different days of the year (i.e. 25 April – 17 December 1995, and 8 June – 22 November 2015). High-quality images were few for 1995, so we included 22 images from 1994 and four images from 1996. To avoid bias due to seasonal lake-level changes we selected, whenever possible, image pairs that were less than three months apart (Fig. 3.1); for most of the study area, we obtained 36 out of 47 pairs. We selected only images with negligible cloud cover (Fig. 3.1), and atmospheric and sun angle correction provided by the U.S. Geological Survey (http://espa.cr.usgs.gov/). We used top-of-atmosphere (TOA) reflectance bands instead of at-sensor spectral radiance (SR) because the cosine effect of different solar zenith angles linked to different acquisition times was already removed (Chander et al., 2009). TOA reflectance compensates for different values of exoatmospheric solar irradiance arising from spectral band differences; TOA data also account for the varying distance between the Earth and the Sun (Chander et al., 2009). To distinguish frozen lakes from glaciers and mountain shadows, we used the SRTM DEM version 4 (Reuter et al., 2007; http://srtm.csi.cgiar.org/) as a supporting layer in the OBIA, generating a local slope map from the maximum elevation change between pixels in a 3 × 3 neighbourhood.

3.4. Methods

We developed an algorithm for mapping lakes with seasonal ice cover, combining a water index with digital elevation models using OBIA principles. Our algorithm is insensitive to the physical state of water and allows us to distinguish between frozen lakes and glaciers. We estimated the accuracy of our automatic classification for two time slice datasets for the Tibetan Plateau collected in 1995 and 2015 using a confusion matrix. Furthermore, we tested the transferability of our approach to areas with different environmental conditions. In addition, we verified changes in lake size and general trends over the last 20 years.

An OBIA approach allows the classification of objects from images, by combining spectral properties of pixels and analysing the spatial relation between them. The principle in using this approach is to classify objects that are not uniform across a large area, and to reduce randomly distributed noise that occurs when using pixel-based classification algorithms. The first step in OBIA is segmentation, where pixels are merged into bigger homogenous objects. In the next step, it is possible to build assumptions based on segments' spectral values. Here. algorithms defining their shape, geometry, spatial position, and connections to the neighbouring segments, are considered an advantage over other classifiers. In OBIA, it is also possible to combine layers of different types of data, such as satellite images and DEM, to extract objects of interest. We chose this approach because attempts to classifying water boundaries based on colour alone have had limited success. From the broad range of available normalised water indices, we selected the

MNDWI (Xu, 2006), as it produces the smallest differences between water, snow, and ice, compared to other indices. This allowed us to more easily combine the 'frozen' and 'non-frozen' parts of a single lake together, while maintaining a stable threshold (Ji et al., 2009). We also tested the applicability and the performance of our OBIA workflow for three recently proposed non-normalised water indices: the automated water extraction indices $AWEI_{nsh}$ and $AWEI_{sh}$ (Feyisa et al., 2014), and the water index WI (Fisher et al., 2016; Fig. 3.3). For each of these indices, water areas should have positive values, and all other surfaces should have negative values. Glaciers and mountain shadows also have positive values, however, making the classification of lakes in mountainous and glaciered areas like the Tibetan Plateau more difficult.

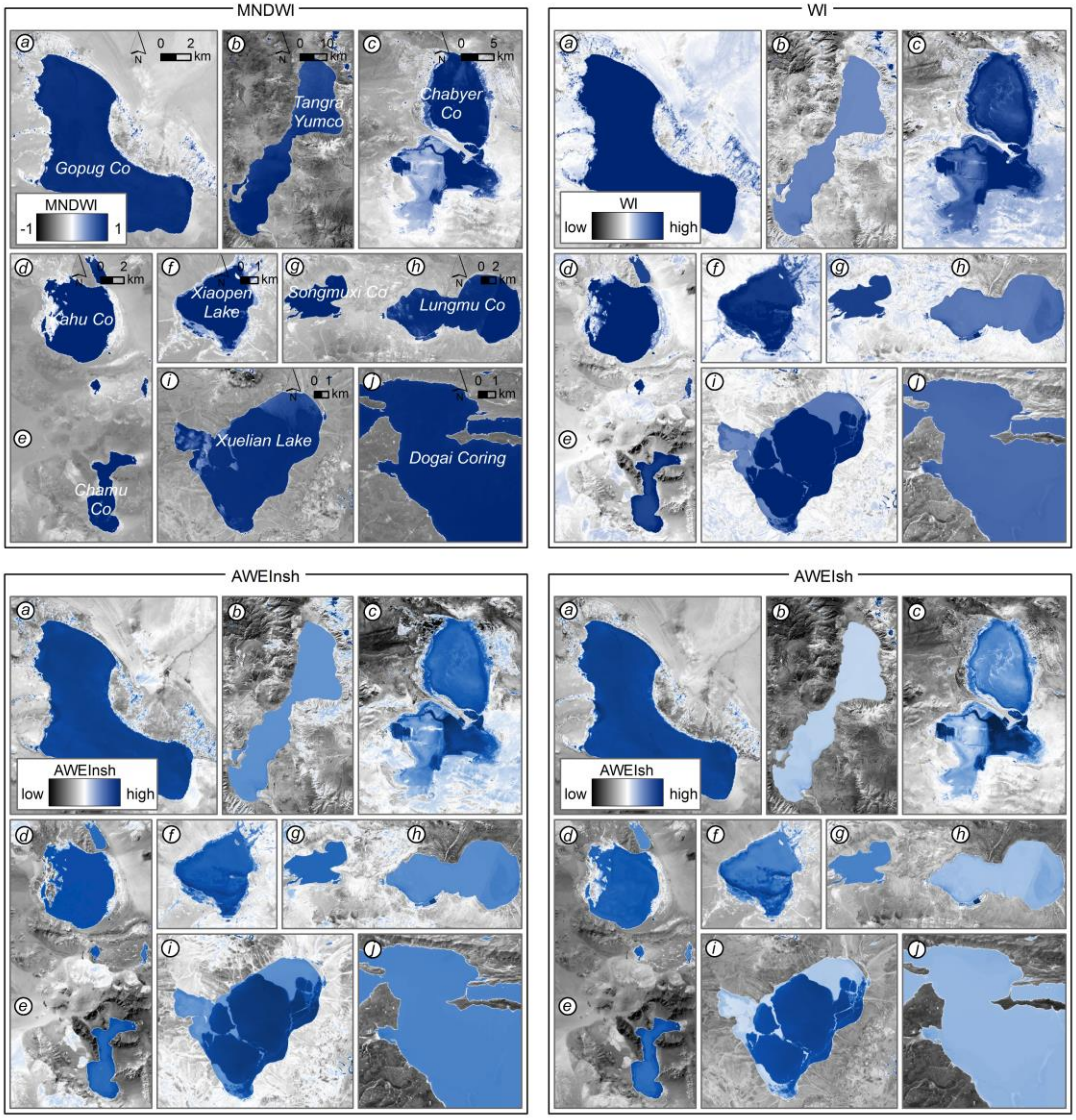

Figure 3.3 | The modified normalised difference water index (MNDWI), water index (WI), automated water extraction index for areas without shadows ($AWEI_{nsh}$), and automated water extraction index for areas with shadows ($AWEI_{sh}$) for selected lakes on the Tibetan Plateau, based on LANDSAT 5 (1995) and LANDSAT 8 (2015). For lake locations on the Plateau see Figure 3.1.

We generated mosaics from all images for 1995 and 2015 via the *Mosaic to New Raster* method available in ArcGIS 10.3 software. To speed up the OBIA process, we stretched the MNDWI, AWEI, and WI values into a 0 – 255 scale (Fig. 3.4.b), converting them to 8-bit unsigned integer rasters. We then used a multiresolution segmentation algorithm (Baatz and Schäpe, 2000; Fig. 3.4.c) on the MNDWI, AWEI, and WI values. We segmented each index separately, but omitted information on local slope, as the underlying SRTM data were obtained in February 2000, and may thus have biased the segmentation. We also avoided automatic scale selection methods, such as scale-parameter estimation (Drăguţ et al., 2010) or plateau objective functions (Martha et al., 2011), as they turned out to be mostly redundant and time consuming. For example, applying the segmentation algorithm to a single LANDSAT image without automatic scale selection using an Intel Core i7-4600U processor with 16GB RAM memory took less than five minutes, whereas using scale-parameter estimation for the same task took more than one hour, partly because some of the segmentation process produced redundant data. The distribution of index values for water

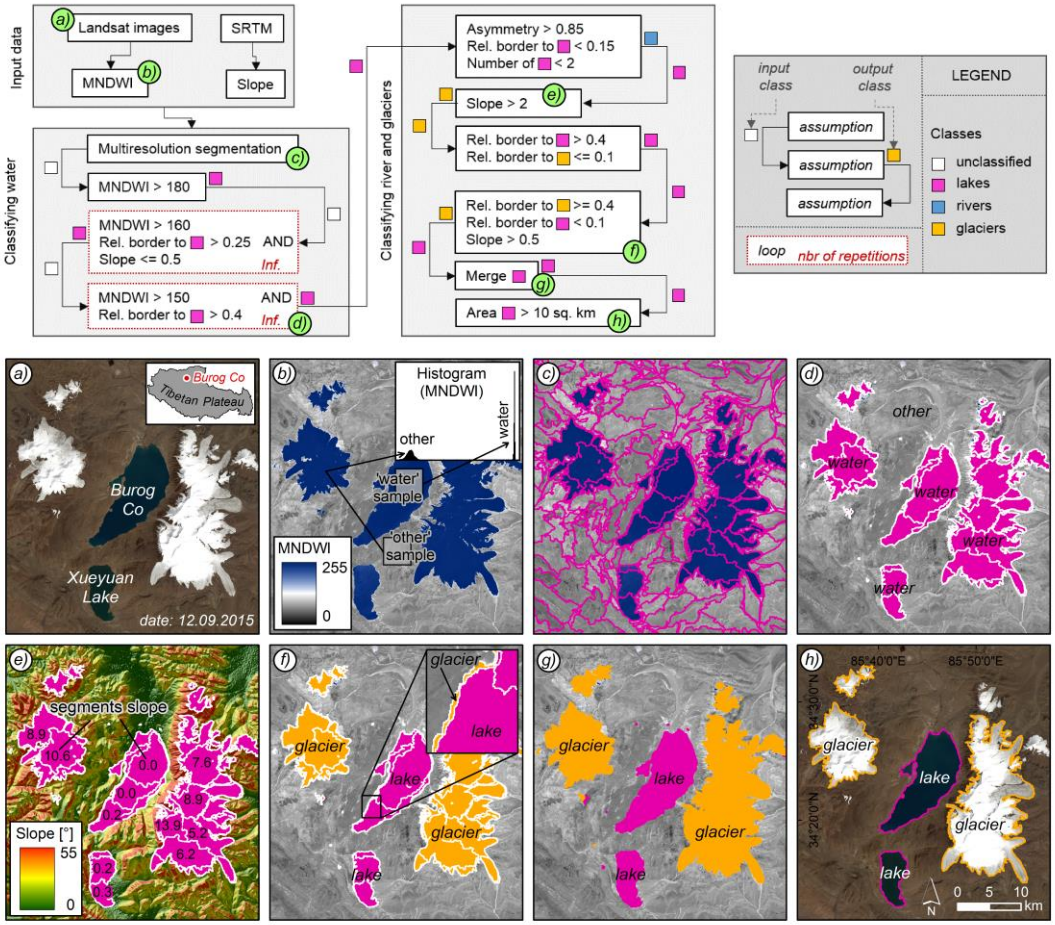

Figure 3.4 | Object-based workflow used for lake classification using eCognition software, and visual representation of individual steps in the classification; a) example of LANDSAT 8 input image; b) modified normalised difference water index (MNDWI); c) multiresolution segmentation of MNDWI; d) MNDWI thresholding; e) SRTM slope derived map; f) neighbourhood analysis of incorrectly classified segments; g) merging neighbouring segments assigned to the same class; h) final classification of lakes > 10 km².

bodies (Fig. 3.4.b) is more homogenous than those of other types of land cover (Li et al., 2011). The segments for water areas are therefore mostly larger and more compact than for the surrounding landscapes. The multiresolution segmentation algorithm uses three parameters – 'scale', 'shape', and 'compactness' – which control segment size, roundness, and the degree of homogeneity of values inside the segments, respectively. The crucial point in our OBIA approach was to select an appropriate segment size so that it remained below the smallest lake to be analysed, while remaining large enough to warrant feasible computing times. We selected a scale of 100, shape of 0.1, and a compactness of 0.7 (Fig. 3.4.c, and 3.5), after running tests with different parameter combinations, and observing that high values of 'shape' and low values of 'compactness' performed poorly in classifying water bodies.

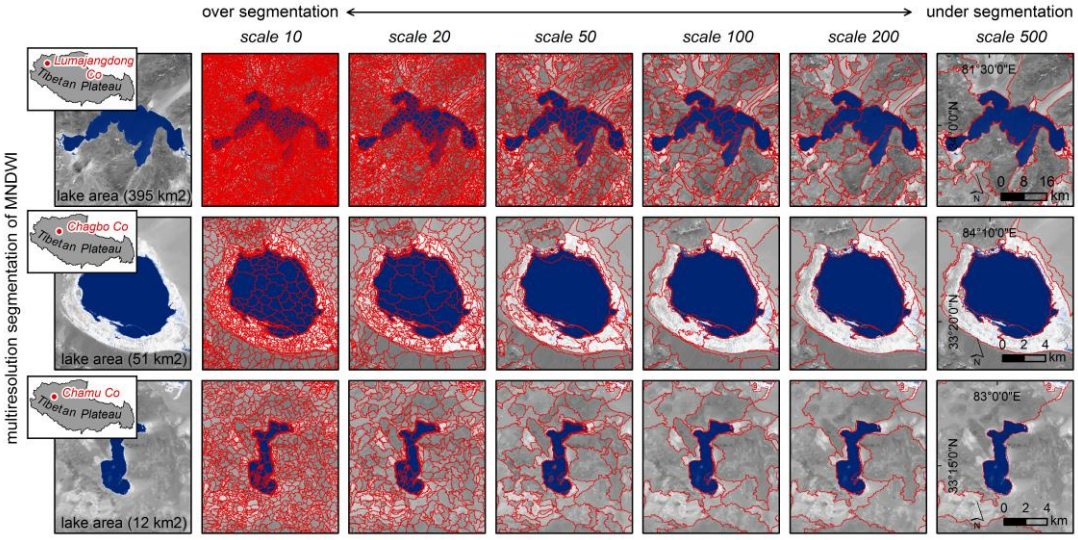

Figure 3.5 | Effects of model parameters 'scale', 'shape', and 'compactness' in the multiresolution segmentation algorithm applied to stretched (0 – 255) modified normalised difference water index (MNDWI) for 2015; all 'scales' are shown for fixed 'shape' = 0.1, and 'compactness' = 0.7.

We then used the thresholding of the water indices to classify segments as either 'water' or 'other' (Fig. 3.4.d). Due to the different histogram ranges of MNDWI, $AWEI_{nsh}$, $AWEI_{sh}$, and WI, we developed four individual workflows with different thresholds. First, we applied higher thresholds (MNDWI >180) to find areas clearly representing water, then incrementally lowered the thresholds (MNDWI >160) in an infinite loop, adding more neighbourhood assumptions regarding sharing the boundary with segments already classified as water (relative border to water >0.25) and with slopes ≤0.5°. The lowest threshold of MNDWI we applied was >150, with a stricter assumption regarding the segment borders; a threshold of >0.4 helped to assign additional water areas, especially those along lake shores or covered by cloud. To distinguish lakes from rivers, we further used the asymmetry of segments and their relation to neighbouring segments. We used the *Asymmetry* function in the eCognition 9.1 software, defined as the segment length relative to a regular polygon drawn around the segment; asymmetry can range from 0 to 1, with

higher values expressing more asymmetric segments. We found that rivers can be separated from lakes for an *Asymmetry* >0.85, a relative border to other water segments <0.15, and a boundary shared by a single water segment at the most. Many glaciers on the Tibetan Plateau have MNDWI, AWEI, and WI values similar to those of lakes, so that a pure OBIA-based classification based on a water index produced many misclassifications. We therefore used a local slope map generated from SRTM DEM as a supporting layer; as most glaciers occupy areas with slopes >2˚ (Fig. 3.4.e), we reclassified all segments accordingly. In a neighbourhood analysis, we corrected segments that were misclassified as glaciers (Fig. 3.4.f). We reclassified all segments from the glacier class with relative borders to water bodies and glaciers of >0.4 and ≤0.1, respectively, as water. Accordingly, we reclassified water class segments with relative borders to glaciers and water bodies of ≥0.4 and <0.1, respectively, and with a mean slope >0.5°, as glaciers, merging neighbouring segments assigned to the same class (Fig. 3.4.g).

To reduce errors arising from the resolution of satellite images and the DEM, we focused on lakes that were >10 km² in size in 2015 (see Section 3.5.1), and exported these as vector polygons for further quality assessment (Fig. 3.4.h). The whole procedure for automatic lake detection using an Intel Core i7-4600U processor with 16GB RAM memory took us ~15 min for each processed tile (we had 16 tiles in total), where each individual raster tile contained 12.156 columns and 10.405 rows (~113,835 km²). We used the lake polygons to generate reference data, visually checking the accuracy of each single lake boundary based on natural colour mosaics, and manually improving the automatically-extracted lakes where necessary. Manual digitising of each lake was necessary because the lakes on the Tibetan Plateau change their size seasonally and in the long term, resulting in no available accurate reference data. We applied the same digitisation scheme and rules for all manually-generated lake polygons.

We digitised the reference data by photographic interpretation of LANDSAT images in 2D in ArcMap 10.3 at scales between 1:5,000 and 1:20,000, depending on the complexity of the lake shores. We selected this scale range by taking into account the minimum mapping unit of our images, which was 30 × 30 meters. We also checked whether lakes were overlooked by the automatic classification or other objects were falsely assigned as lakes. Several lakes, had diffuse boundaries due to lake salinity, clouds, or mountain shadows, which hindered correct interpretation of images. In such cases, we used water index maps and images with higher resolution, available at ArcGIS online, as supporting layers to delineate the lake boundary. In total, we generated 323 reference lakes for each time slice. We used these reference data to estimate the accuracy of the classification (Table 3.2) in terms of type I error, type II error, total error (Sithole and Vosselman, 2004), overall accuracy, producer's accuracy, user's accuracy (Congalton, 1991), Cohen's kappa (Cohen, 1960), and F-score measures. In addition, we estimated root mean square error, mean absolute error, and mean error (bias; Table 3.2). The

most significant measure is user's accuracy, because it describes whether the automatically-extracted lakes were captured in the reference data.

Table 3.2 | Summary of performance metrics of the classification of lakes on the Tibetan Plateau.

Performance metrics		
Type I error	FP/(TP + FP)	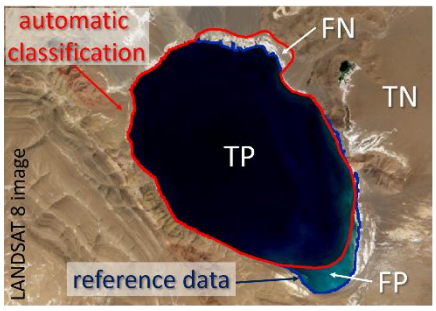
Type II error	FN/(FN + TN)	
Total error	(FP + FN)/(TP + FP + FN + TN)	
Overall accuracy	(TP + TN)/(TP + FP + FN + TN)	
Producer's accuracy	TP/(TP + FP)	
User's accuracy	TP/(TP + FN)	
Cohen's kappa	$(p_o - p_e)/(1 - p_e)$	
F-score	2TP/(2TP + FP + FN)	
Root mean square error	$\sqrt{\frac{1}{N}\sum_{i=1}^{N}(x_i - \hat{x}_i)^2}$	
Mean absolute error	$\frac{1}{N}\sum_{i=1}^{N}\lvert x_i - \hat{x}_i\rvert$	
Bias (Mean error)	$\frac{1}{N}\sum_{i=1}^{N}(x_i - \hat{x}_i)$	

TP – true positive; FP – false positive; FN – false negative; TN – true negative; p_o – relative observed agreement among rates; p_e – hypothetical probability of chance agreement; x_i – predicted value; $\hat{x}_i$ – observed value; N – number of observations.

3.5. Results

Our classification of Tibetan lakes detected 323 lakes with areas of >10 km² in the study area in 2015, with a total area of 31,258 km², or 2.6% of the study area. Twenty years earlier, the same lakes covered only 24,892 km², meaning that their total area grew by ~26% (see detailed data online at http://arcg.is/1r8Mj4a).

3.5.1. Accuracy of extracted lakes

We selected a minimum lake area of 10 km2, given the 30-m resolution of the satellite images and to minimise the influence of mixed pixels from low-resolution images. The proportion of mixed pixels to total lake pixels increases with decreasing lake area (Fig. 3.6). For lakes <10 km², this proportion is >0.2, whereas for lakes >50 km² it is <0.07. Estimating the accuracy of lakes with high percentages of mixed pixels may therefore misrepresent the accuracy of the method. We compared the classified lake boundaries with the manually-generated reference data and computed several performance metrics for the entire study area (Table 3.3).

Our OBIA method for extracting lakes >10 km² had an overall accuracy of 0.99, and the producer's and user's accuracy, Cohen's kappa, and the F-score for both time slices were >0.98

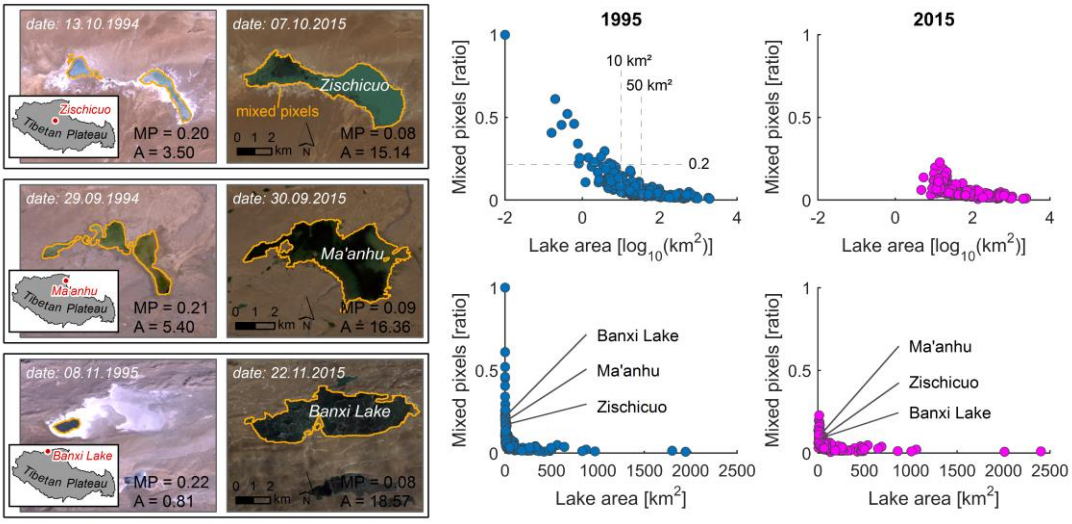

Figure 3.6 | Proportion of mixed pixels versus lake size; MP is the ratio of mixed pixels; A is the lake area in km².

Table 3.3 | Performance metrics for OBIA-based extraction of lakes on the Tibetan Plateau with MNDWI, WI, $AWEI_{nsh}$, and $AWEI_{sh}$ for 1995 and 2015.

Performance metric	1995				2015			
	MNDWI	WI	$AWEI_{nsh}$	$AWEI_{sh}$	MNDWI	WI	$AWEI_{nsh}$	$AWEI_{sh}$
Type I	0.0134	0.0089	0.0234	0.0140	0.0169	0.0081	0.0337	0.0143
Type II	0.0003	0.0016	0.0005	0.0022	0.0005	0.0018	0.0007	0.0016
Total	**0.0006**	0.0018	0.0010	0.0024	**0.0010**	0.0020	0.0016	0.0020
O. Acc.	0.9994	0.9982	0.9990	0.9976	0.9990	0.9980	0.9984	0.9980
P. Acc.	0.9866	0.9911	0.9766	0.9860	0.9831	0.9919	0.9663	0.9857
U. Acc.	**0.9850**	0.9292	0.9778	0.9073	**0.9808**	0.9376	0.9732	0.9428
Kappa	**0.9855**	0.9583	0.9767	0.9438	**0.9815**	0.9630	0.9690	0.9628
F-score	**0.9858**	0.9592	0.9772	0.9450	**0.9819**	0.9640	0.9698	0.9638
RMSE	**0.0244**	0.0420	0.0309	0.0490	**0.0309**	0.0442	0.0398	0.0442
MAE	**0.0005**	0.0018	0.0010	0.0024	**0.0010**	0.0020	0.0016	0.0020
ME	**−0.0003**	−0.0014	0.0003	−0.0018	**−0.0001**	−0.0015	0.0002	−0.0012

Type I error (Type I); Type II error (Type II); Total error (Total); Overall accuracy (O. Acc.); Producer's accuracy (P. Acc.); User's accuracy (U. Acc.); Cohen's kappa (Kappa); Root mean square error (RMSE); Mean absolute error (MAE); Mean error (ME).

when using the MNDWI (Table 3.3). The performance with $AWEI_{nsh}$, $AWEI_{sh}$ and WI was slightly lower, albeit >0.94, with the exception of the user's accuracy for WI ~0.92. The accuracy in classifying lakes with respect to their physical states of water (frozen, partly frozen, and unfrozen) was similar. All lakes, irrespective of ice cover, were detected with very high producer's accuracy (Fig. 3.7). The MNWDI achieved the highest accuracy and the lowest root mean square error, mean absolute error, and mean error; we checked the performance of standalone water indices in extracting lakes >10 km² (Fig. 3.8), and found that the area under the curve (AUC) of MNWDI exceeded those of the AWEI and WI indices.

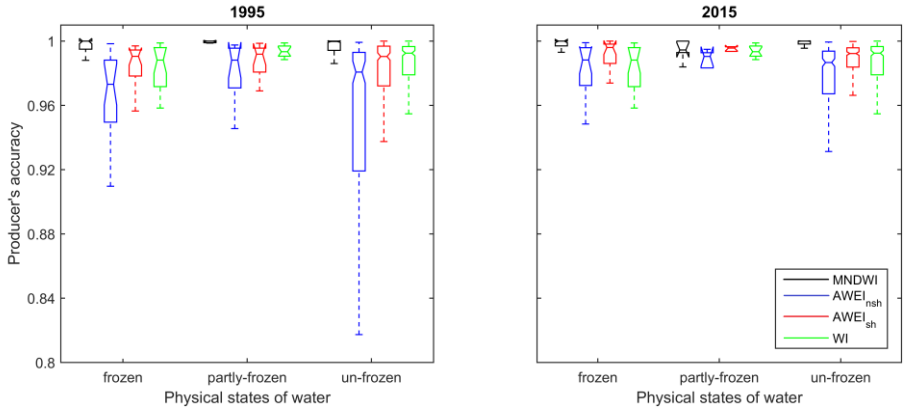

Figure 3.7 | Box-and-whisker plots of the estimated producer's accuracy in classifying lakes on the Tibetan Plateau with respect to their ice cover, using one of four different water indices.

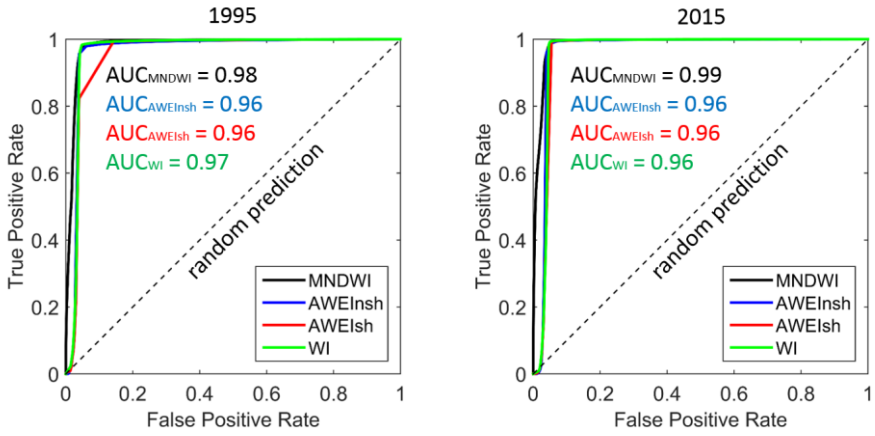

Figure 3.8 | Receiver operating characteristics (ROC) with area under the curve (AUC) for estimating the performance in classifying lakes on the Tibetan Plateau using different water indices.

Visual cross checks revealed that using the $AWEI_{sh}$ in our OBIA approach misclassified many land areas as lakes, especially by falsely assigning border segments adjacent to lakes (Fig. 3.9, Table 3.3). The $AWEI_{nsh}$ appeared to be the least useful for selecting thresholds between water and non-water pixels (Fig. 3.9). Histograms showed that the zero threshold was more reliable to use on MNDWI than any other water index. Most misclassified areas were along the border of lakes, particularly irregular shorelines; river deltas were also often represented by single segments in our method. Clouds also caused some misclassification of lakes (Fig. 3.9), whereas glaciers were a lesser problem. In some cases, small islands in the lakes were also misclassified.

We note that seasonal lake ice had little influence on our data; however, with our OBIA approach, lakes were mostly classified correctly regardless. We studied Siling Co, in detail, which is the largest lake in our study area (though not on the entire Tibetan Plateau). We selected additional images for the two time slices, covering more seasonal variations in lake ice and snow cover on shorelines. To this end, we used the OBIA classification with the MNDWI without changing any

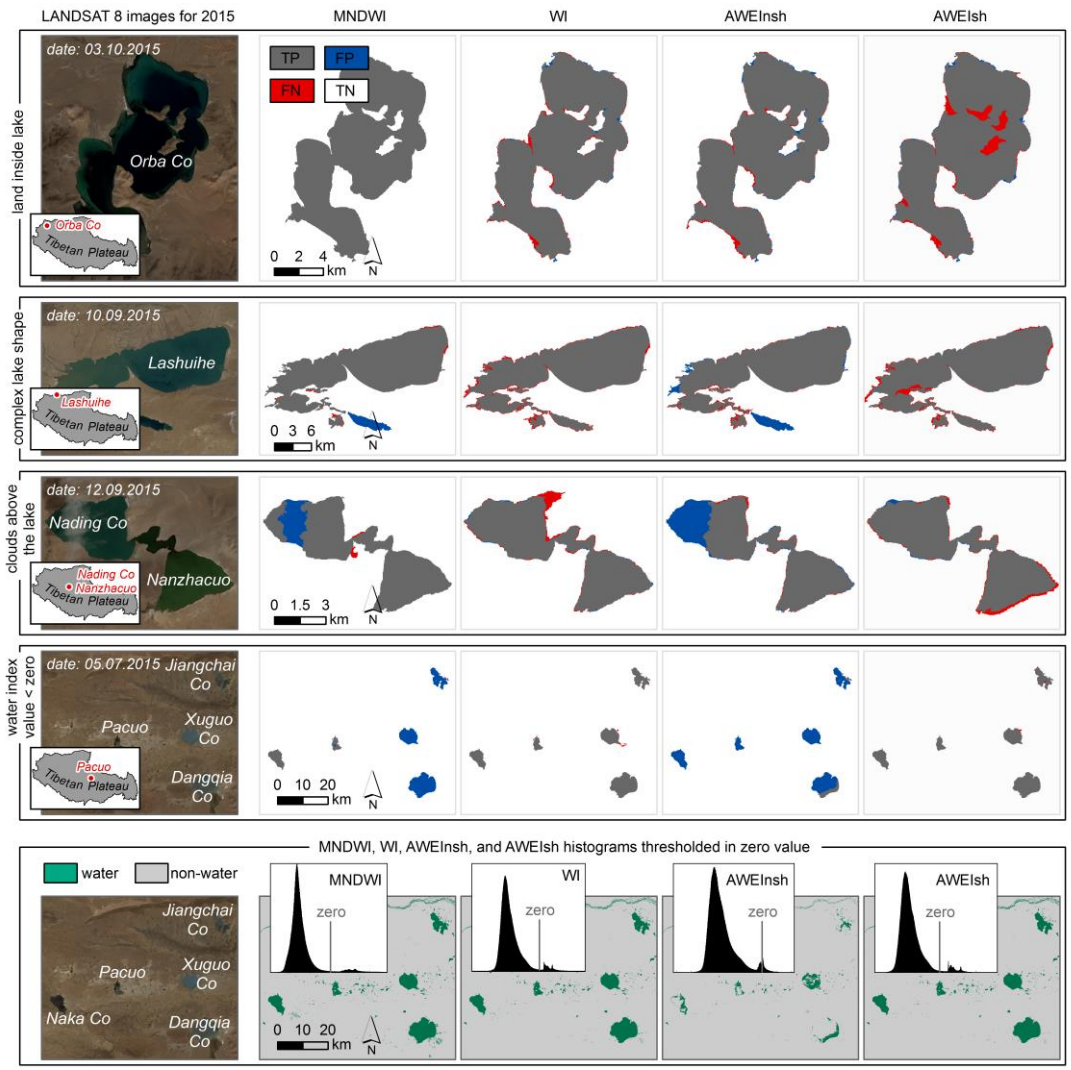

Figure 3.9 | Estimated accuracy of OBIA classification of lakes on the Tibetan Plateau using different water indices: MNDWI, WI, $AWEI_{nsh}$, and $AWEI_{sh}$; TP is the true positive rate; FP is the false positive rate; FN is the false negative rate; and TN is the true negative rate.

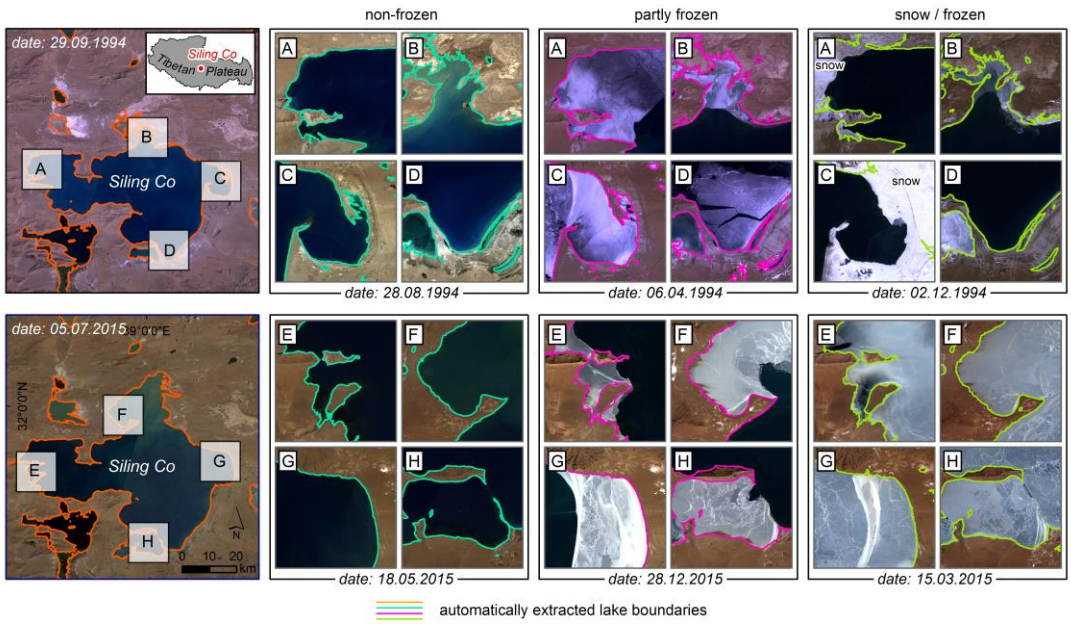

Figure 3.10 | Results from OBIA classification of Siling Co (see inset for location on the Tibetan Plateau) with different degrees of seasonal ice cover.

parameter in the workflow. We found our method to be robust throughout and capable of detecting lakes with high accuracy (Fig. 3.10). Misclassification occurred only in an image obtained on 2 December 1994, in which shores were covered by snow, violating the assumptions of our OBIA approach designed exclusively for snow-free images.

3.5.2. Sources of error in the analyses

Although our classification has very high accuracy, we have highlighted several sources of error unrelated to the algorithm, but nevertheless influencing our classification. The first source of error arose from splitting the data into smaller tiles. To make our analysis feasible, we had to separate the study area into 16 square tiles with two pixels of overlap between neighbouring tiles. This led to misclassifying small parts of lakes along the borders of the tiles.

Another source of error concerned reference data that solely relied on LANDSAT images. The 30-m resolution of images made it difficult to delineate some of the blurrier lake images. The roundness of the lakes also played a role, as rounded shapes with a lower perimeter-area ratio are easier to digitise. This ratio translated into the number of pixels along lake borders for which correct classification was difficult. Another important point is that manually-generated reference data are always prone to operator bias, as different people are likely to map the same lakes with minor differences. Such differences may produce fake changes in lake areas, and therefore we treated any lake-area changes of <1km² as potentially suspicious.

3.5.3. Lake-area changes (1995 – 2015)

Our analysis showed that the total area of lakes >10 km² on the Tibetan Plateau increased by 6,366 km². Out of 323 lakes, 25 increased their area by >50 km², eleven lakes grew by >100 km², and one lake by >500 km². These changes were not evenly spread throughout the study area. The highest relative increase occurred in the northern part of the Tibetan Plateau, where most lakes are concentrated (Fig. 3.11); these grew mostly by between 100% and 200%, and up to 50 km² in absolute area (Fig. 3.11). The highest increase in total lake area (2,404 km²) occurred in internal basin '6' on the northeastern part of the plateau, where 108 lakes were detected (Fig. 3.11). In basin '5', which has a similar number of lakes (112), the total lake area increased by 1,037 km². Most lakes that underwent moderate changes (<10 km²) are in the southwestern Tibetan Plateau, mainly along the Himalayas and adjacent mountain belts (see detailed data online at https://uni-potsdam.maps.arcgis.com/apps/webappviewer/index.html?id=3595915b0af244c89750823133a9e165). Between 1995 and 2015, eighteen new lakes >1 km² formed mostly in the northeastern part of the plateau, at elevations between 4,700 and 5,000 m a.s.l., slightly below the most dominant elevation (Fig. 3.11). This narrow elevation band also featured the greatest increase in lake size, whereas most lakes with lesser changes lie at lower elevation. We

notice a weak correlation of lake growth with incoming solar radiation, especially for basins '7' and '8' (Fig. 3.11).

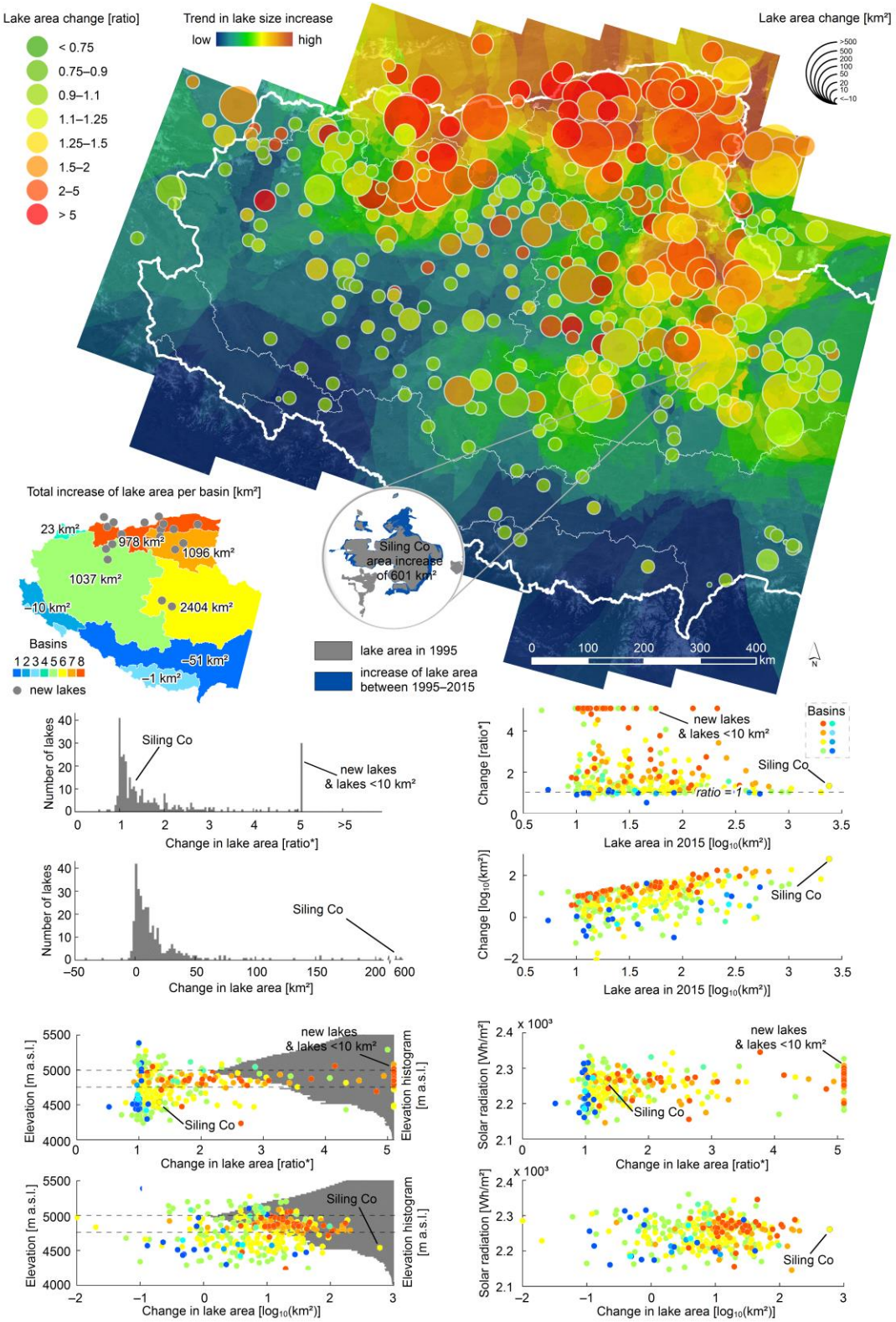

Figure 3.11 | General trends in lake-area changes and the ratio of changes between 1995 and 2015 on the Tibetan Plateau; * lakes with ratio > 5 are set to 5.1 for better legibility.

3.5.4. Transferability of OBIA approach

We tested the global transferability of our method for extracting lakes with the MNDWI, as this index achieved the highest accuracy. We selected six LANDSAT 8 images capturing areas with numerous lakes on five continents, representing environments greatly different to that of the Tibetan Plateau (Fig. 3.12, Table 3.4).

We maintained our OBIA workflow for these selected areas without changing any parameters, and found that nearly all classified test areas yielded overall, producer's, and user's accuracies of >0.95, with a Cohen's kappa and F-score of >0.96, with low root mean square errors, mean absolute errors, and mean errors (Table 3.5). For one test area, the lakes in Lago Cochrane National Reserve, Chile, the performance metrics were much lower, mainly because the

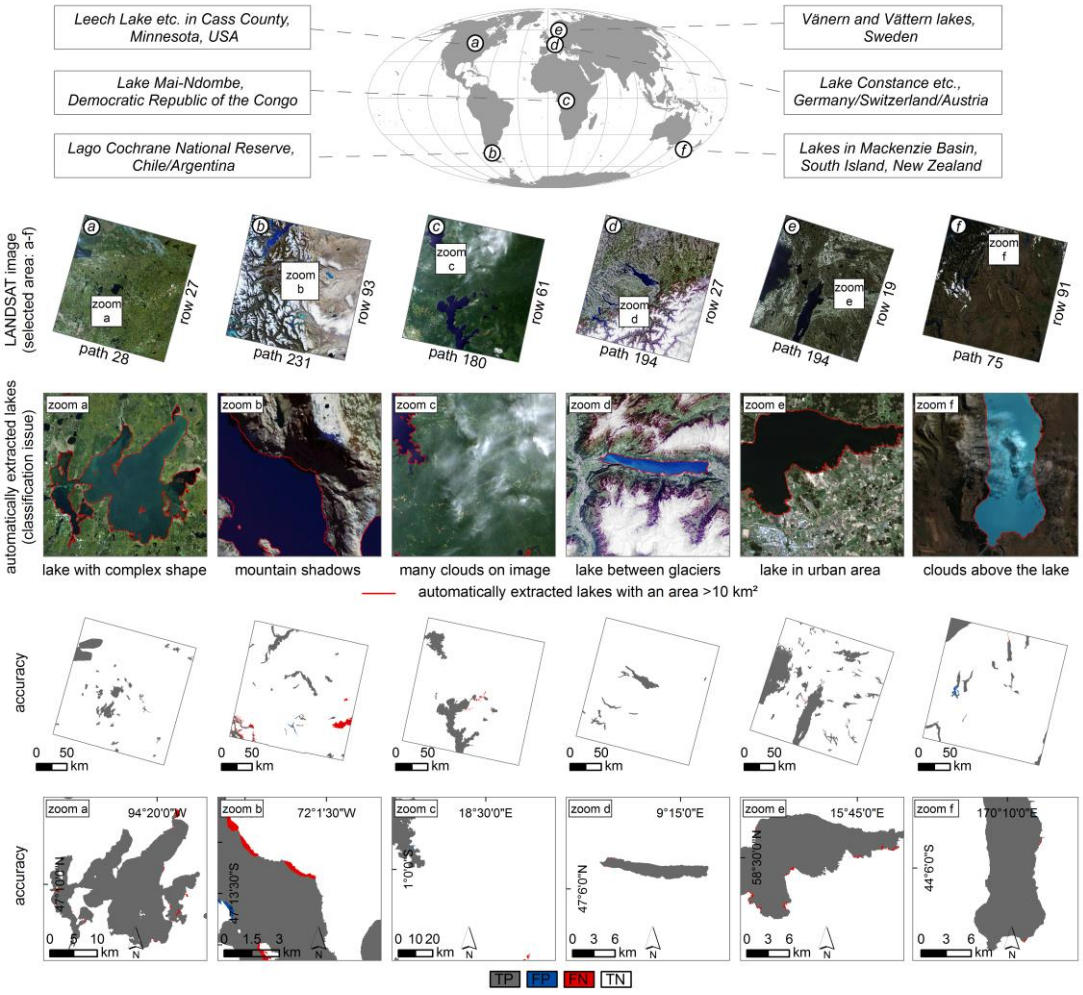

Figure 3.12 | Transferability and accuracy assessment of OBIA method for extracting lakes in areas other than the Tibetan Plateau; TP is the true positive rate; FP is the false positive rate; FN is the false negative rate; and TN is the true negative rate.

Table 3.4 | Characteristics of test sites across the world used to verify the transferability of our OBIA method for lake classification (see Figure 3.12 for locations).

TS	Continent (Country)	Landscape Type	Extracted Lakes	Date	TA
a	North America (USA)	Flat area	Leech Lake, etc. in Cass County, Minnesota	29.09.2015	2,156.28
b	South America (Chile/Argentina)	Mountains	Lakes in Lago Cochrane National Reserve	01.04.2014	1,518.87
c	Africa (Democratic Republic of the Congo)	Flat forested area	Mai-Ndombe Lake, etc.	12.01.2016	2,812.52
d	Europe (Germany/Switzerland/Austria)	Mountains with glaciers	Constance Lake, etc.	22.05.2016	802.76
e	Europe (Sweden)	Lakeland—flat postglacial area	Vänern and Vättern Lakes, etc.	09.05.2016	5,848.82
f	Australia (New Zealand)	Hilly region	Lakes in Mackenzie Basin	17.03.2016	1,696.70

TS (test site); Date (Image acquisition date [day.month.year]); TA (Total area [km²] of lakes >10 km² on image).

Table 3.5 | Performance metrics for OBIA-based lake extraction using MNDWI for lakes in different test areas across the world (see Figure 3.12 for locations).

Performance Metrics	Test Area					
	a	b	c	d	e	f
Type I error	0.0022	0.0216	0.0021	0.0050	0.0025	0.0471
Type II error	0.0004	0.0120	0.0014	0.0001	0.0012	0.0005
Total error	0.0005	0.0124	0.0014	0.0002	0.0014	0.0027
Overall accuracy	0.9995	0.9876	0.9986	0.9998	0.9986	0.9973
Producer's accuracy	0.9978	0.9784	0.9979	0.9950	0.9975	0.9529
User's accuracy	0.9940	0.7825	0.9835	0.9948	0.9939	0.9899
Cohen's kappa	0.9956	0.8631	0.9898	0.9948	0.9949	0.9697
F-score	0.9959	0.8695	0.9906	0.9949	0.9957	0.9711
Root mean square error	0.0220	0.1113	0.0381	0.0149	0.0369	0.0515
Mean absolute error	0.0005	0.0124	0.0014	0.0002	0.0014	0.0027
Mean error	−0.0002	−0.0106	−0.0011	−0.0001	−0.0006	0.0017

algorithm misclassified a single large river delta (Fig. 3.12b). Visual checks indicated that flat and hilly regions allow for better delineation of lake boundaries than high mountains. Shadows were correctly distinguished from lakes; however, where shadows overlapped with lakes, misclassifications arose. Small and thin clouds were usually correctly distinguished from lakes (Fig. 3.12f); however, thicker clouds increased misclassification (Fig. 3.9). Overall, our method performed well for nearly all landscape types, including low-gradient environments without glaciers (Fig. 3.12a) and alpine environment with glaciers (Fig. 3.12d, Table 3.5).

3.6. Discussion

In the second part of the 20th century, 82% of the Tibetan Plateau glaciers retreated; if this trend continues, two-thirds of the current Tibetan Plateau glaciers could be gone in the coming centuries (Qiu, 2008). Changes in evaporation may significantly increase this trend, supplying water to lakes and enhancing their growth. Systematically monitoring lake areas therefore supports estimates of the rates of change. Our comparative analysis confirms previous findings

that have reported that expanding lakes are not spread uniformly across the Tibetan Plateau (Song et al., 2013; Song et al., 2014b; Fang et al., 2016), but are instead focused in the northeastern part of the Plateau. Compared to the distribution of glaciers (Fig. 3.1), we found that lakes grew by the smallest amount where glaciers in the Himalayan Mountains Range are most numerous. This may be due to the temperature increase, which may promote stronger evaporation (Wang et al., 2013).

Accurate automated mapping of lake boundaries may aid regional studies of the hydrological balance of tens to thousands of lakes. Our OBIA based approach provides a tool that allows, in a short time and an easy way, to delineate the shorelines of large lakes, thus assisting the monitoring of regional changes in lake size, both seasonal and in the long term. The performance of our automatic classification tested on the Tibetan Plateau is surprisingly high. Tests of our method on lakes in other environments, without changing any parameters, were similarly successful, and most lakes were correctly detected with only minor misclassification at the boundaries of lakes, especially where shorelines were complex. This high accuracy largely draws from using a water index in an OBIA context. The water index we used, the MNDWI, is generally highly accurate; however, misclassifying glaciers, shadows, and clouds, as well as its varying threshold for separating 'water' from other land-cover types—which should be around zero value—makes it difficult to transfer the method to areas outside of the training area. We implemented water index thresholding in the OBIA using few thresholds, which more correctly detected the lakes' boundaries than did single thresholding. Applying neighbourhood assumptions for every segment allowed us to distinguish lakes from other objects falsely assigned by the water index. By using a multiresolution segmentation algorithm, we reduced unwanted salt-and-pepper noise that is a characteristic of simple water index thresholding. The OBIA rule set relied on relations between the segments and their spatial location, allowing us to more realistically separate lakes from other objects with similar water index values. The OBIA protocol found segments that were incorrectly classified by the MNDWI thresholding due to their low values caused by clouds above the lakes, MNDWI values that were too low, or shadows, and subsequently re-classified them as lakes. The topographic slope information excludes glaciers and other falsely included objects. Although our method is designed for lakes >10 km², it is capable of extracting numerous smaller lakes accurately; however, we omitted some small lakes (<1 km²) owing to the choice of 'scale' parameter. For detecting lakes <10 km² more correctly, we recommend decreasing the 'size' of segments. The smallest correctly-identified lake for the 1995 images had an area of 0.0135 km² (15 pixels). The correctness of its predicted boundaries is difficult to check, however, given the 30-m data resolution.

Mixed pixels along lake shores remain a major challenge for classification. We have shown that they can form a large proportion of the classified lake area, especially for small lakes and low-

resolution images, thus increasing the cost of classifying them compared to large lakes. We suggest that this proportion should not exceed 10% of the area of the smallest object of interest. This is why we focused only on lakes >10 km², as for most of these lakes the mixed pixels ratio was <10% (Fig. 3.6).

We found that MNDWI accurately indicated of water areas, detecting nearly all lakes in our study area. Compared to several other water indices, the MNDWI ROC curve indicated the best performance in detecting lakes >10 km²; additionally its derivation is physically more intuitive than those for the WI and AWEI. In computing the MNDWI, one may neglect erroneous pixels in the input bands, because for such errors the absolute value of MNDWI will be >1, thus enabling fast and easy quality checks. For computing the AWEI and WI, this issue remained pending; therefore, one must check all input bands carefully and exclude erroneous values from the bands separately. The MNWDI is a normalised metric, and therefore it is easier to manipulate, contrast, and stretch the data as desired, while the range of values remains the same with respect to SR or TOA data, making it possible to use the same threshold independently of the input data.

Combining optical images with elevation models enabled us to build more sophisticated assumptions in OBIA and separate lakes from glaciers, which have similar spectral properties on LANDSAT images. A slope map derived from DEM gives adequate information on the differences between these two landforms. Lakes have a slope of approximately zero, whereas the slope for glaciers is mostly larger. Although the slope of some lake shores may be similar to that of glaciers, the use of common boundaries with other flatter lake segments promotes a correct assignment to the lake class. In very steep terrain, lake-shore pixels can have spuriously high slopes as an artefact of including nearby hillslopes. Using a more accurate DEM may allow us to achieve better results, especially if the DEM data were gathered shortly before or after the time slice of interest. We used a DEM from 2000 to analyse lakes in 1995 and 2015, so that five and 15 years of geomorphic change could have affected our elevation data. LANDSAT images are available for the entire globe; however, SRTM data are only available between 56° S and 60° N. The lack of more digital topographic data for areas with higher altitude therefore curtails our method, particularly in Arctic regions featuring thousands of glacial and periglacial lakes. In such cases, however, a new global 0.4 arc second (~12m) DEM gathered by the TerraSAR-X-Add-on for Digital Elevation Measurements (TanDEM-X) mission (https://tandemx-science.dlr.de/) may open new doors.

We also recall that, in snow-covered areas, the multiresolution segmentation algorithm is unable to properly delineate lake boundaries using a water index, so we recommend using our method only for images without snow cover. Using a metric of the spread of water-index values, such as their standard deviation, may help to distinguish water from snow. Similarly, clouds remain an

issue in detecting lake boundaries. The fraction of cloud cover provided with LANDSAT images may be insufficient because even an image with low cloud cover may introduce classification errors, where clouds obscuring parts of lakes can be crucial. Visual checks of images remain indispensable. We recommend tools such as the LAND Viewer (http://lv.eosda.com), which enables verification of the RGB and different band compositions of LANDSAT-8 and SENTINEL-2 images in relation to date, percentage of cloud, and sun angle in detail before downloading.

Our method fills in a gap in classifying lakes prone to seasonal ice cover, as such lakes are notoriously difficult to detect automatically. Our automatic and fast classification allows the mapping of water bodies, irrespective of landscape type, with an accuracy similar to those of previous approaches (Verpoorter et al., 2012; Jiang et al., 2014; Jawak and Luis, 2014). The added value of our algorithm is that it detects lakes regardless of whether they are partly or completely frozen. We therefore believe that our OBIA algorithm has great potential for tracking in detail not only long-term changes, but also seasonal variations in lake areas, especially given the increasing access to free high-resolution satellite images, such as those from the SENTINEL sensor, which revisits a given area every five days.

3.7. Conclusions

We have proposed an approach for automatically detecting large lakes prone to seasonal ice cover. We developed our method for the Tibetan Plateau, where such ice cover and surrounding glaciers make the use of various remote-sensing-based water indices problematic. Our method is insensitive in this regard and distinguishes with high estimated accuracy between lakes, glaciers, and shadows, giving the opportunity to track annual and seasonal changes of mountain lakes, especially those surrounded by many glaciers. Our approach combines a satellite-image-derived water index, OBIA, and a DEM-derived slope map to automatically extract lakes. The method can be applied in areas where acquiring images in ice-free seasons is difficult. Testing of our method on LANDSAT images for two time slices (1995 and 2015) showed that lakes on the Tibetan Plateau grew ~26% in total, and that the changes were not evenly spread through the whole tested area. The largest increase occurred in the northeast, whereas the southwestern Tibetan Plateau saw the largest decrease. Further tests of our method in areas abundant in lakes throughout the world showed that our approach may be general and flexible enough for regional, if not global, monitoring of lake changes.

Acknowledgments

This research was funded by the European Union under the Marie Curie Initial Training Network ALErT (Creation of an interactive CAP natural-hazard database), project number FP7-PEOPLE-2013-ITN-607996. The LANDSAT images used in the study were provided by the U.S. Geological Survey, available from http://espa.cr.usgs.gov/. The SRTM DEM version 4 data were provided by the CGIAR-CSI, available from http://srtm.csi.cgiar.org/. We thank the four reviewers for their comments, which helped to improve the manuscript.

Supplementary material

The code for delineating lake boundaries is in the Appendix B.

Chapter 4

Snow avalanches

Submitted to *Natural Hazards and Earth System Sciences* as: Korzeniowska, K., Bühler, Y., Marty, M., Korup, O. Regional snow-avalanche detection using object-based image analysis of near-infrared aerial imagery.

Abstract

Snow avalanches are destructive natural hazards in mountain regions that continue to claim lives, and cause infrastructural damage and traffic detours. Given that avalanches often occur in remote and poorly-accessible steep terrain, their detection and mapping is extensive and time consuming. Nonetheless, systematic avalanche detection over large areas could help to generate more complete and up-to-date inventories (cadastres) necessary for validating avalanche forecasting and hazard mapping. In this study, we have focused on automatically detecting avalanches and classifying them into release zones, tracks, and runout zones based on 0.25-m near-infrared (NIR) ADS80-SH92 aerial imagery using an object-based image analysis (OBIA) approach. Our algorithm takes into account the brightness, the normalised difference vegetation index (NDVI), and the normalised difference water index (NDWI) and its standard deviation (SD_{NDWI}) in order to distinguish avalanches from other land-surface elements. Using normalised parameters allows readily applying this method across large areas. We trained the method by analysing the properties of snow avalanches at three 4-km² areas near Davos, Switzerland. We compared the results with manually-mapped avalanche polygons, and obtained a user's accuracy of >0.9 and a Cohen's kappa of 0.79 – 0.85. Testing the method for a larger area of 226.3 km², we estimated producer's and user's accuracies of 0.61 and 0.78, respectively, with a Cohen's kappa of 0.67. Detected avalanches that overlapped with reference data by >80% occurred randomly throughout the testing area, showing that our method avoids overfitting. Our method shows potential in large-scale avalanche mapping, although further investigations into other regions are desirable to verify the stability of our selected thresholds and the transferability of the method.

4.1. Introduction

Snow avalanches are frequent and destructive mountain hazards, particularly during the winter and spring months. They are fast mass movements controlled by weather conditions, snowpack, and the topography of the terrain (Schweizer et al., 2003; Castebrunet et al., 2012). Avalanches can cause loss of lives, disrupt infrastructure, and affect buildings (Bründl et al., 2004; McClung and Schaerer, 2006; Eckerstorfer and Malnes, 2015).

Despite numerous efforts aimed at reducing the risk posed by avalanches, most fatalities in Europe occur during sporting activities, caused by avalanches triggered by the victims themselves (Techel et al., 2015). Past research indicates that poor decision-making and forecasting are the main causes of deadly avalanche accidents (Techel et al., 2015; McClung, 2016). Techel et al. (2015) stated that most destructive events occur on days when the snow avalanche risk is very critical and the snowpack layer is weak. In total, 4,750 people lost their lives in the European Alps between 1970 and 2015 (Techel et al., 2016); in the past two decades, avalanches in the Swiss Alps alone have killed 461 people (Fig. 4.1). Most fatal accidents have occurred in the cantons of Valais and Grison, which are the two largest in Switzerland and contain some of the highest areas in the Swiss Alps. Since 1946, avalanches in Switzerland have had the highest share of victims (37%) in comparison to other natural hazards, including lightning (16%), floods (12%), windstorms (10%), rockfalls (8%), and landslides (7%; Badoux et al., 2016).

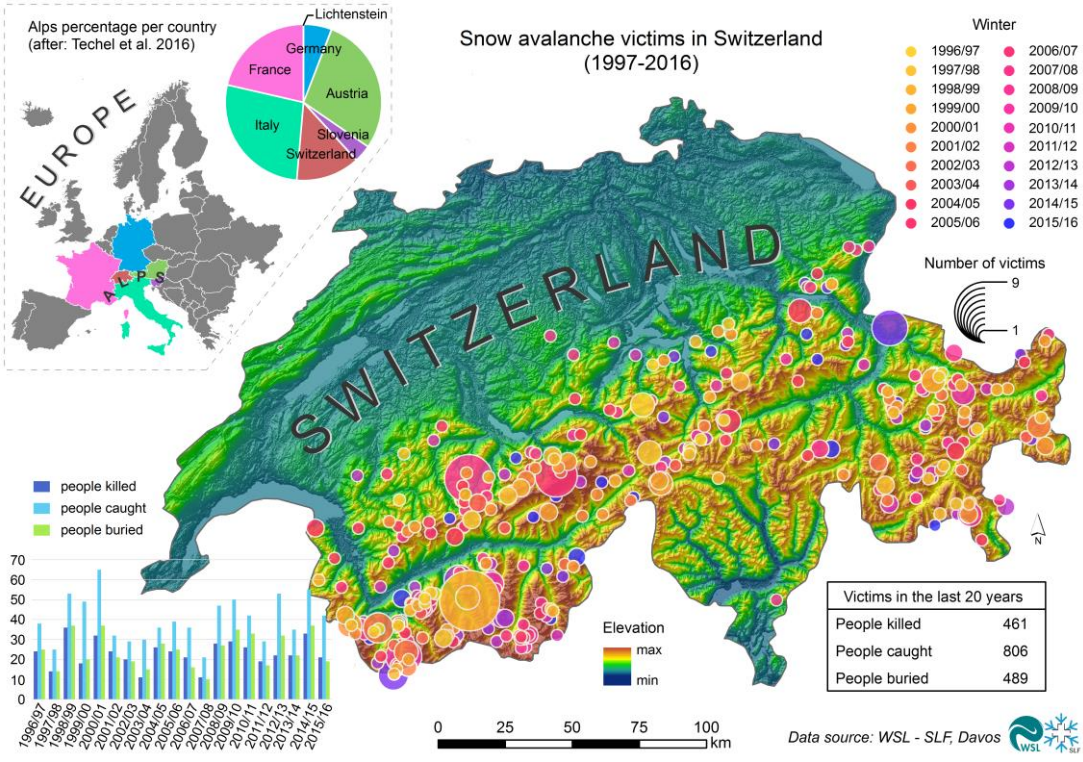

Figure 4.1 | Snow avalanche accidents with victims in Switzerland in the winters of 1996/97 to 2015/16, and the Alps percentage per country. Data from: Swiss Federal Institute for Snow and Avalanche Research (WSL-SLF), Davos, Switzerland.

Avalanches killed a total of 36 people in Switzerland in the fatal winter of 1998/99 (Fig. 4.1). Between 27 January and 25 February, 17 people died in villages and on roads, and material losses surpassed 600 million Swiss Francs. This catastrophic winter spurred an initiative aimed at improving avalanche safety and reducing concomitant losses (Wilhelm et al., 1999; Bründl et al., 2004). This initiative included establishing an information system for exchanging data between the WSL Institute for Snow and Avalanche Research SLF and local authorities; the development of hazard maps showing zones with high avalanche susceptibility (Bründl et al., 2004); and an increase in the artificial release of avalanches to decrease hazard levels. In this context, the need for documenting avalanches also increased, to allow for learning from past accidents.

This initiative showed clearly that regional-scale mapping of avalanches and identifying potential release zones is not only desirable, but also essential for producing avalanche cadastre maps to be used for quality-checking hazard mapping and forecasting (Bühler et al., 2015). To date, experts (Bühler et al., 2009) map most avalanches manually, focussing mainly on geographic coordinates, but rarely on any detailed information about their extent or area. Moreover, avalanche inventories are biased toward damaging events or those reported from accessible terrain. Hence, avalanches remain notoriously underreported over larger regions. To more broadly collect information concerning avalanches, non-expert observers in Switzerland are now able to report sightings via an app (http://www.slf.ch/lawinenbulletin/rueckmeldung/index_EN), where they can enter the location and date of their observation. Optical remote sensing data, both airborne and satellite, offer coverage that is more systematic, and are therefore increasingly used to track avalanches. Satellite images allow the collection of a picture for the same area with a time interval equal to one satellite orbit around the Earth. Airborne images can be acquired even more often, although in the winter season it is not preferable to continue the campaign due to financial aspects, because such images, which represent mostly only snow, are not convenient for any purposes other than the assessment of the risk of snow avalanches.

Automatic methods for detecting snow avalanches are still in the developing stage (Eckerstorfer et al., 2016), and different kinds of data, such as optical and radar images, and classification approaches are used to verify their suitability to track avalanche events. This motivated us to verify the usability of near infrared (NIR) aerial images and their calculated derivatives, in mapping avalanches over a large area in Switzerland, as well as verifying the topographic conditions of their occurrence. We have proposed an automatic OBIA-based method for detecting avalanche runout zones, as well as their tracks and release areas. We tested whether normalised indices of water and vegetation derived from aerial ADS80-SH92 images are suitable in this regard, and introduced a simple method for roughly distinguishing these zones, because knowledge concerning potential release zones critically aids in hazard assessments and runout models. Our motivation was to develop an algorithm widely applicable to mountain regions, as

relying on image spectral properties alone (Lato et al., 2012) may limit such portability, because objects may have a similar brightness to that of snow.

Most avalanches start on slopes with a median inclination of 39° (Schweizer and Jamieson, 2001), hence on slopes most difficult for skiing. We distinguish two types of avalanche: loose avalanches start from a point and gradually increase in size as they move downslope, whereas slab avalanches involve the detachment of large planar packs of snow (Fig. 4.2; Schweizer et al., 2003; Bagli and Schweizer, 2009). Path length defines whether an avalanche is small (10 – 100

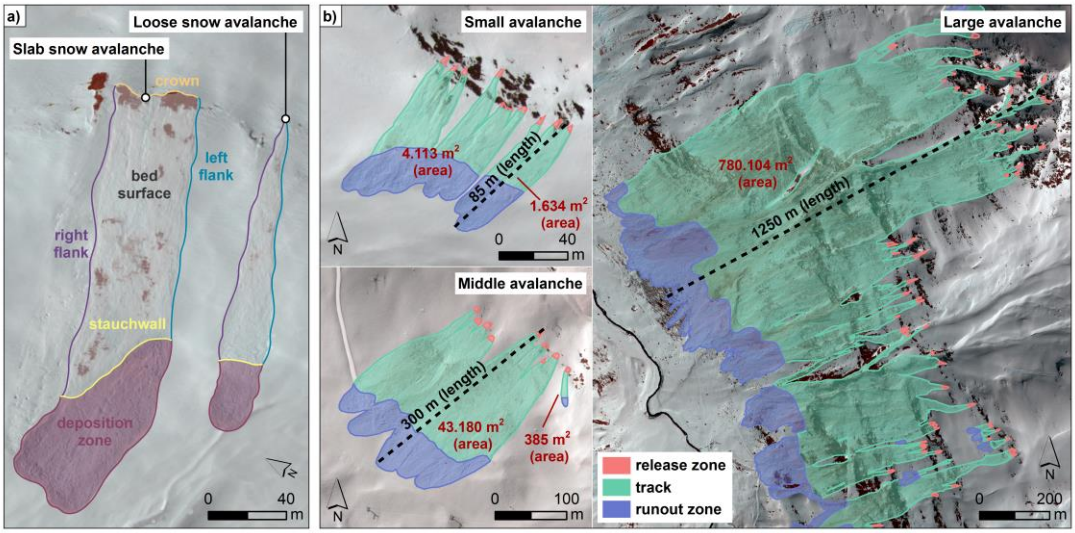

Figure 4.2 | a) Types of avalanche release: slab avalanches and loose avalanches, with marked avalanche body parts (crown, bed surface, stauchwall, deposition zone, and right and left flanks; Schweizer et al., 2003); b) Avalanche classification with respect to length: small, middle, and large [m], with the avalanche area [m²] and marked parts of avalanches: release zone, track, and runout zone. Data from: WSL Institute for Snow and Avalanche Research (SLF), Davos, Switzerland.

m), medium (100 – 1,000 m), or large (>1,000 m; Eckerstorfer et al., 2016). Most large avalanches, such as that shown in Figure 4.2, are slab avalanches because to bring down a large amount of snow, planar snow detachment is necessary; however, new smaller loose snow avalanches may occur and overlap with the previous one, thus complicating their detection in the field. In terms of avalanche deposit area, we distinguish between large deposits (>2,000 m²), small deposits (100 – 2,000 m²), and very small deposits (<100 m²; Bühler et al., 2009). Every avalanche has a release zone – a part where the avalanche is triggered, a track, a part where the snow is transported down the slope – and a runout, or deposition, zone (Fig. 4.2).

4.2. Previous work

Most previous work devoted to mapping avalanches from optical remote sensing data has focused on delineating runout zones. The idea of using object-based image analysis (OBIA) for detecting avalanches has been used in conjunction with brightness information from aerial images and local slope data taken from digital elevation models (DEM), and with numerical modelling (Bühler et

al., 2009), whereas others have used only the spectral information of aerial and satellite images to detect snow avalanches (Lato et al., 2012). Bühler et al. (2009) proposed an approach for mapping snow-avalanche deposits from ADS40 20-cm aerial images, which they resampled to 1 m and then combined with 25-m elevation data. They used the numerical simulation tool RAMMS (Rapid Mass Movement Simulation; Christen et al., 2010) to exclude slopes >35° from the runout calculation, as they assumed these slopes could not accumulate snow-avalanche debris. They also used spectral thresholds to exclude snow-free areas. To separate rough avalanche debris from surrounding smooth and undisturbed snow, they used the normalised difference angle index (NDAI), evaluated from nadir and backwards NIR bands. They computed the NDAI difference between neighbouring pixels with a grey-level co-occurrence matrix (GLCM), which represents the distribution of pixel values at a given offset, and found that the thresholding of an entropy measure evaluated via the GLCM achieved the best separability of rough and smooth snow. Ski lifts and other objects characterised by a similar entropy were removed using OBIA. The estimated accuracy of this method in terms of the fraction of correctly-detected avalanche deposits was 94%, and the producer's accuracy was 87%. Lato et al. (2012) applied OBIA for detecting avalanche deposits from panchromatic images only. They tested their algorithm with Quick Bird images in Norway, and aerial ADS40 images in Switzerland, relying on six variables (i.e. GLCM entropy, GLCM dissimilarity, brightness, contrast, similarity, and neighbour distance) in their procedure, in which segments failing to meet the OBIA assumptions were sequentially discarded. They started by eliminating dark regions from brightness data before detecting rough snow with edge contrast. The similarity filter and density helped to remove isolated pixels and small objects, respectively. Finally, the neighbour distance helped to fill gaps inside the extracted snow-avalanche deposits. The user's and producer's accuracies of this classification were both >90%. Both these studies (Bühler et al., 2009; Lato et al., 2012) regarded OBIA as suitable for detecting snow-avalanche deposits, because it considers the spatial relation of the analysed segments in addition to their spectral properties.

Larsen et al. (2013) suggested an approach for optical Quick Bird imagery using directional filters evaluated based on image texture classification (Varma and Zisserman, 2004) to distinguish avalanches from another objects. They assumed that avalanches have a texture pattern with a linear structure on the snow that coincides with the local hillslope aspect. Similar to other strategies, their classification took into account neighbouring pixels, while parameters such as area, area perimeter ratio, aspect direction difference, co-occurrence mean, correlation, and entropy were used to assist in excluding misclassified instances. Based on a visual comparison, the authors concluded that their classification was acceptable, allowing the detection of many fresh avalanches with a low number of false alarms (Larsen et al., 2013). They pointed out,

however, that some of the detected avalanches were split into parts; they therefore recommended additional processing to re-connect those fragments.

Eckerstorfer and Malnes (2015) manually detected avalanche debris based on its higher backscatter contrast, compared to the surrounding undisturbed snow cover, in Radarsat-2 Ultrafine SAR imagery. They assumed that avalanches are tongue-shaped features with high surface roughness and higher snow density than surrounding terrain. Surface roughness and snow density were determined from backscatter, which increased in cases of higher surface roughness, and absorption, which increased for denser snow, respectively. They found that release zones and tracks were mostly difficult to detect. In a similar context, the automatic method of Vickers et al. (2016) evaluates backscatter in 50 × 50 pixel regions of Sentinel-1A images, subsequently masking out areas with a predicted probability of snow-avalanche occurrence of zero; pixels with a DEM-derived local slope of >35° were removed from the occurrence of avalanches. From the test pixels, they selected those with a backscatter difference above a specified threshold. Randomly-selected pairs of pixels gave a total dissimilarity of pixels and class representatives for a K-mean clustering with two classes, 'avalanche' or 'not avalanche'. The detection rate (producer's accuracy) of this algorithm was 60%, and the authors highlighted its potential for avalanche monitoring despite masking out large amounts of data. Finally, Bühler et al. (2016) tested an unmanned aerial vehicle (UAV) that allows for fast, repeatable, flexible, and cost-efficient measurements of snow depths in alpine terrain, possibly generating digital surface models of homogenous snow surfaces (Bühler et al., 2017). Legal regulations in Switzerland and elsewhere currently limit broad coverage of UAV imagery, however.

4.3. Study area and data

Our study area is centred around Davos, in the Swiss canton of Grisons; the area has alpine relief, with the highest local peak at Schwarzhorn (3,146 m a.s.l.; Fig. 4.3). Many slopes in this area exceed 28° and have dominant northeastern and southwestern aspects (Fig. 4.3). We used 0.25-m resolution NIR aerial images in conjunction with abundant avalanche information acquired via a ADS80-SH92 large-format Digital Pushbroom Sensor (Leica Geosystems AG, Heerbrugg, Switzerland; Bühler et al., 2009) at the end of the 2012/13 winter season. The sensor recorded information with five spectral bands: panchromatic, blue, green, red, and NIR (Bühler et al., 2009). We have data for the area for more than five time slices starting from the winter of 2007/08 and continuing from 2011/12 to 2015/16. The images we used were taken at the end of the winter of 2012/13, where the highest expected snow depths were between 2,000 and 3,000 m a.s.l., and covered ~226 km².

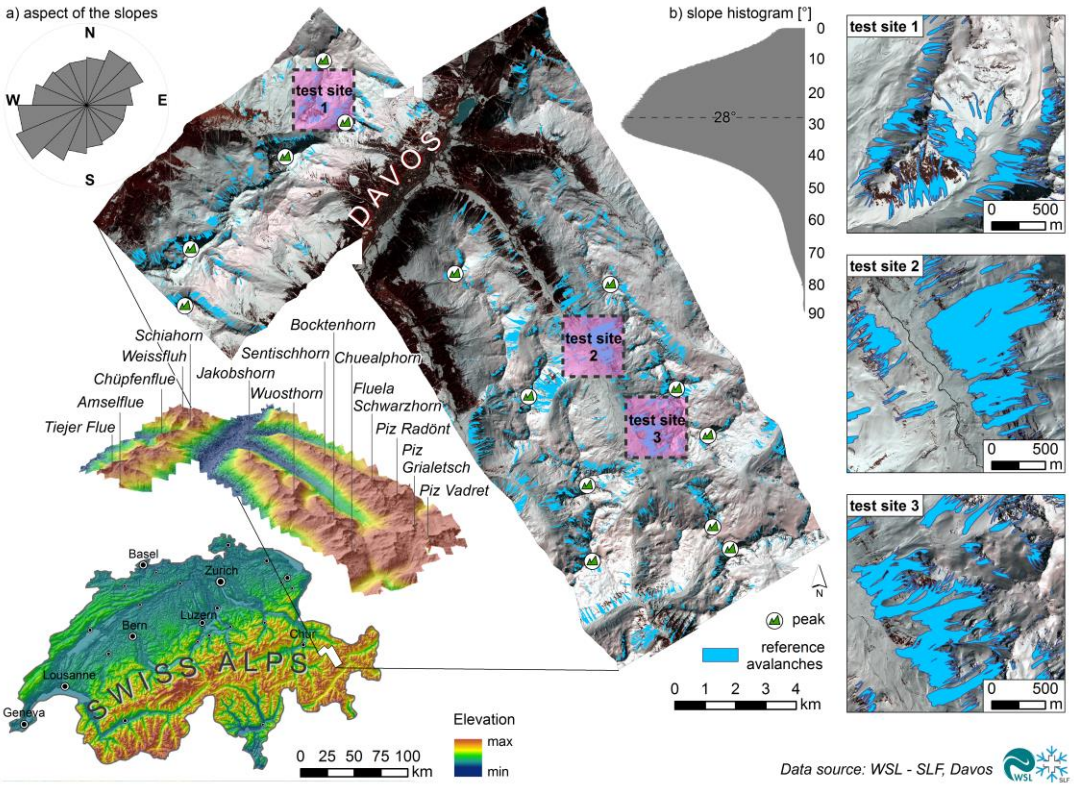

Figure 4.3 | Topographic setting of research area and ADS 80 NIR aerial images with test sites (1 – 3) and digitally mapped snow avalanches. Inset histograms show a) the main slope aspect and b) distribution of local slope.

4.4. Methods

We have introduced an automatic method for mapping release zones, tracks, and runout zones of avalanches using NIR 0.25-m aerial images. We compared the automatic classification with manually-digitised reference data and assessed the accuracy of detecting snow avalanches using confusion matrices. Furthermore, we verified the topographical conditions on which most mapped avalanches occurred and verified two approaches for visualising the avalanche density. In addition, we proposed a probability approach to representing release and runout zones of avalanches and the automatic classification of snow avalanche parts.

4.4.1. Automatic OBIA snow avalanche classification

We implemented a multi-step OBIA approach for detecting avalanches in eCognition Developer 9.1.1 software (Fig. 4.4). As input for the classification, we used the green, red, and NIR bands, and computed from these the normalised difference vegetation index (NDVI = $\rho_{NIR} - \rho_{Red} / \rho_{NIR} + \rho_{Red}$; Townshend and Justice, 1986), and the normalised difference water index (NDWI = $\rho_{Green} - \rho_{NIR} / \rho_{Green} + \rho_{NIR}$; McFeeters, 1996) and its standard deviation in a 5 × 5 kernel (SD_{NDWI}). We derived brightness as the mean of the green, red, and NIR bands to classify 'dark objects', such as rivers, rocks, and buildings. The NDVI helped to classify trees, bushes, and other types of

vegetation, whereas the NDWI (SD_{NDWI}) detected snow (rough snow; Fig. 4.4). We stretched computed NDVI and NDWI data into an interval of [0, 255].

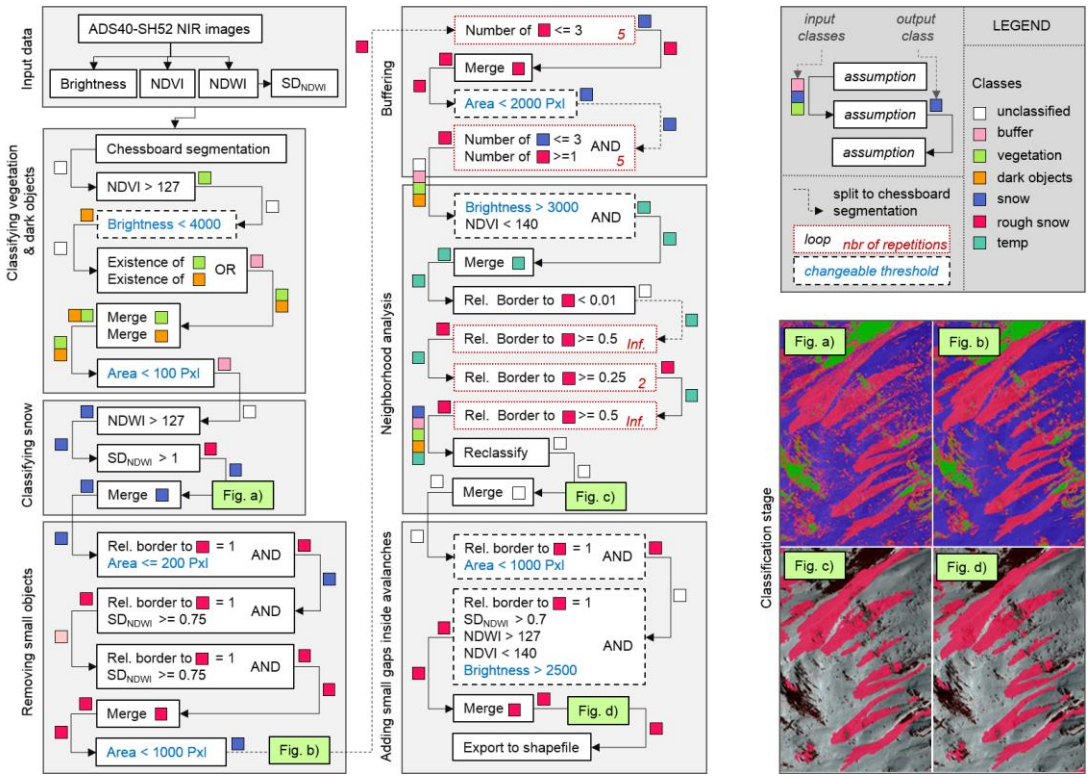

Figure 4.4 | Workflow for classifying snow avalanches with object-based image analysis (OBIA). The white boxes indicate the classification; dashed outlines feature the number of reiterations (red), and the local decision boundaries show change (blue). The colours of squares are coded to the input and output class in each step. Figs. a), b), c), and d) represent visual results of the sub-step classification.

4.4.1.1. Classifying vegetation, dark objects, and snow

In our first step, we segmented the data using a chessboard segmentation algorithm in eCognition 9.1.1 software, assigning a standalone segment to each single pixel (Fig. 4.4). We used the pixel values of snow-free areas obtained from NDVI and brightness to classify 'vegetation' and 'dark objects'. We classified vegetation as having positive NDVI values (corresponding to >127 in the stretched range), and dark objects as those with a brightness of <4,000 (Fig. 4.4). Because pixels on the border of vegetation and dark objects have mixed values, we assigned them to a separate 'buffer' class by reclassifying every pixel that shared a border with either 'vegetation' or 'dark objects' (existence of 'vegetation' or existence of 'dark objects'; Fig. 4.4), and then excluded this 'buffer' class from further analysis. We merged all segments classified as 'vegetation' and 'dark objects' and assigned all segment areas <6.25 m² (<100 pixels; Fig. 4.4) as being too small to buffer or divert an avalanche, and included these segments as potential areas where a snow avalanche could occur. All the size thresholds used in our OBIA workflow were set to the resolution of the data that were used and the size of the analysed avalanches. Similarly, we

classified pixels with a positive NDWI (>127 for stretched data) as snow and pixels with an additional roughness contrast (SD_{NDWI} >1) as 'rough snow', representing avalanches.

4.4.1.2. Removing small objects that do not represent avalanches

We then merged all snow pixels and reclassified 'rough snow' segments <12.5 m² (<200 pixels, Fig. 4.4). We thus included many pixels as parts of avalanche deposits that had escaped being classified as 'rough snow' in the previous step because of SD_{NDWI} values that were too low. We applied an assumption concerning the maximum area of segment that can be reclassified into the 'rough snow' class to avoid the inclusion of large, but smooth, areas inside avalanches. After comparing the segment values with their visual representation in an image, we observed that larger smooth areas that are inside the avalanche represent small ascents that were omitted by the avalanche, and should therefore not be assigned as a part of an avalanche. We similarly assumed that the boundary of 'rough snow' should be equal to 1 for both 'snow' and 'buffer' classes, which means that the segment lies completely within these two classes; however, this time we combined it with a SD_{NDWI} of ≥0.75 to include the segment as 'rough snow'. The thresholding value of the SD_{NDWI} was taken from the data histogram by analysing the rapid change in the counts of values on the histogram. We then merged the segments into the 'rough snow' class, with the exception of areas <62.5 m² (area <1,000 pixels; Fig. 4.4), assuming that they were too small to represent an avalanche.

4.4.1.3. Buffering

In further steps, we split all segments from the 'rough snow' class into smaller pieces, to reduce their artificially-complex shapes with bigger and more compact parts connected to neighbours by only a few pixels. In most cases, only some of these complex shapes represented an avalanche, whereas the remainder was 'rougher snow' due to vegetation effects. To simplify these shapes into separate parts, we used buffering to reclassify pixels from the 'rough snow' class as snow that had less than four neighbours classified as 'rough snow' (Fig. 4.4), repeating this step for both the 'snow' and 'rough snow' classes. To avoid undue growth of spurious pixels, we narrowed down the process to only pixels adjacent to at least one pixel classified as 'rough snow' (Fig. 4.4).

4.4.1.4. Neighbourhood analysis

At this stage, our classification still contained many misclassified parts of avalanches containing effects of vegetation, soil, or rocks. To assign these parts to the 'rough snow' class, we first reclassified all pixels from 'unclassified', 'buffer', 'vegetation', and 'dark objects' with brightness >3,000 and NDVI <140 into a new 'temp' class (Fig. 4.4). After merging the segments into the 'temp' class, we reclassified all segments bordering 'rough snow' <0.01 into

'unclassified' and discarded these from the analysis. For the remaining segments, after returning to chessboard segmentation to allow us to once again operate on single pixels, we reclassified all pixels from the 'temp' class sharing a border with 'rough snow' with at least two pixels (Fig. 4.4) iteratively. Because every pixel had only four neighbours, the assumption concerning two pixel neighbours stopped the infinite loop after only a few repetitions. To allow the inclusion of additional pixels, we therefore decreased the threshold on the relative border to ≥0.25 and performed the process twice more to allow more segments that were sharing the boundary with at least one 'rough snow' segment to be included in the 'rough snow' class. We did not run this process iteratively, because it would have reclassified all pixels assigned as 'temp', and our aim was to increase only compact 'rough snow' areas. Next, we once more applied an infinite loop regarding the relative border to 'rough snow'of ≥0.5, to increase previously-detected snow avalanches. These steps were crucial in closing areas inside the snow avalanches that due to the values of brightness and NDVI, were not assigned in the previous steps to the 'rough snow' class.

4.4.1.5. Adding small gaps inside avalanches

Finally, we focused on filling gaps inside the detected snow avalanches. We reclassified and merged gaps into avalanches by verifying their geometrical relation to 'rough snow'. After checking the layer statistics for every segment, we built an assumption that if a segment was completely within the 'rough snow' and its area was <1,000 pixels (62.5 m²), it was to be automatically reclassified into 'rough snow' (relative border to 'rough snow' = 1 and area <1,000 pixels; Fig. 4.4). Segments with >1,000 pixels reclassified into 'rough snow' were expected to fulfil additional rules concerning their roughness, brightness, occurrence of snow, and vegetation, because they may have represented a convex-upward form that could stay intact during the avalanche occurrence. Only segments with a high snow roughness that did not represented vegetation and were not too dark were added to the 'rough snow' class (relative border to 'rough snow' = 1, SD_{NDWI} >0.7, NDWI >127, NDVI <140, and brightness >2,500; Fig. 4.4). We exported all extracted snow avalanches into polygon shapefiles and compared these visually and quantitatively with manually-mapped reference data. The visual interpretation was important for verifying the distribution of errors and the completeness of classified avalanches.

4.4.2. Generating reference data

We created reference data by manually digitising avalanches from the images in ArcMap 10.3 software at scales between 1:800 and 1:1,500, depending on the complexity of the mapped avalanche. Manually digitising each area affected by the avalanche was necessary because avalanches occur only during the winter season when snow cover occurs, making them temporal events; the marks of their existence disappear when the snow cover melts, and therefore no complete reference data are available. Avalanches that were overlapping or bordering others were

counted as one. This means that polygons representing an avalanche in fact covered several smaller avalanches that had occurred in succession; in most cases, it was impossible to assess their relative sequence (Fig. 4.3). We mapped a total of 2,200 avalanche polygons for the data acquired in the winter of 2012/13, obtaining 13.6 km² of avalanche terrain or 6% of the study area. The reference data, as well as automatically-extracted avalanche polygons, are available online (https://uni-potsdam.maps.arcgis.com/apps/Cascade/index.html?appid=3b5ac4491b59480c8c6016139f285e88). We used the reference data to estimate several classification accuracy metrics, including Type I, Type II, and total errors (Sithole and Vosselman, 2004), overall, user's, and producer's accuracies (Congalton, 1991), Cohen's kappa (Cohen, 1960), and F-Score. Finally, we arbitrarily selected three 4-km² training sites (Fig. 4.3) for our OBIA algorithm, and reported these eight performance metrics for a larger 226.3 km² test area.

4.5. Results

4.5.1. Estimated accuracy

Our algorithm classified 10.7 km² as avalanche debris, which is 78.7% of the total area of the reference data mapped for the winter of 2012/13. Overall, 1,648 out of 2,200 avalanches were correctly identified; 1,126 were detected in terms of more than half their area, and for 615 avalanches this detection rate was >80%. These classified avalanches were spread out evenly throughout the study area (Fig. 4.5). Visual checks of the classification indicated that the runout zones were detected most reliably, whereas the release zones were the most problematic. Tracks

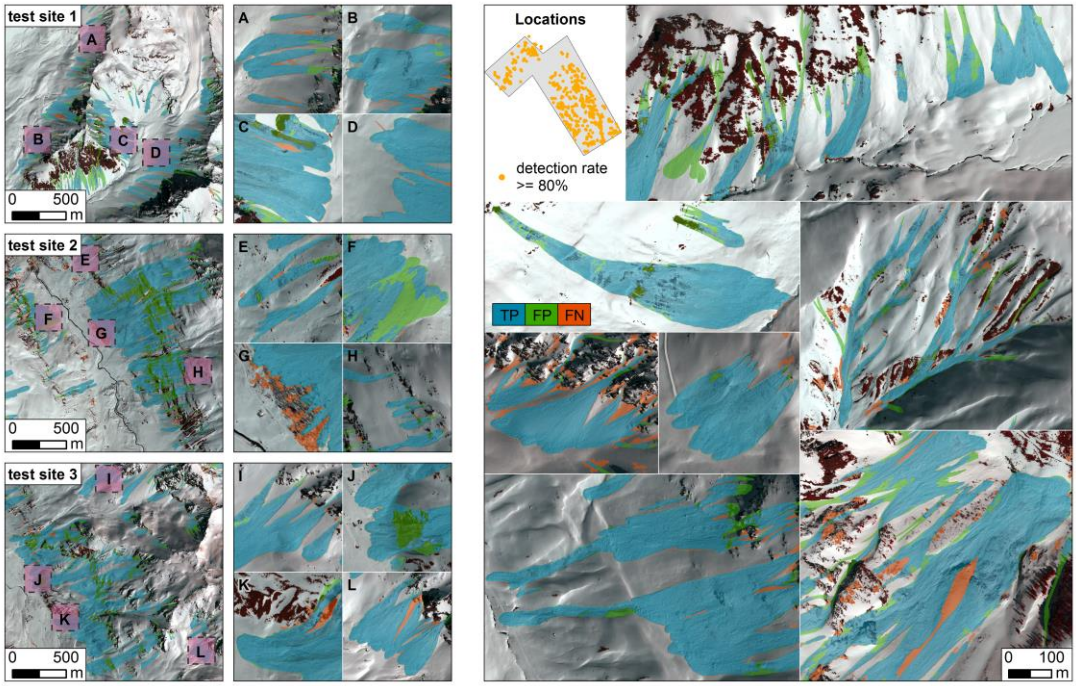

Figure 4.5 | Accuracy assessment of OBIA classification for training (test sites 1 – 3) and testing data together; avalanche debris are shaded with orange colour, where they were detected with an accuracy ≥80%. TP = true positive; FP = false positive; FN = false negative.

were detected mostly correctly where small patches of vegetation or soil were near or in the avalanche tracks. The highest estimated precision in detecting avalanche boundaries was in runout zones adjacent to smooth snow or unvegetated slopes. In some locations, a clear distinction between avalanche debris and smooth snow was not possible, especially for older deposits or snow drifts. Fresh avalanches were also detected with higher accuracy than were older and blurred ones.

The performance metrics estimated for our training sites were overall and user's accuracies of >0.9, and a Cohen's kappa of >0.8 (Table 4.1). The accuracy for the testing area yielded lower performance metrics, with a user's accuracy of 0.78. The producer's accuracy showed that 61% of the total avalanche area in the tested data was correctly identified. The overall Type II error was very low, indicating that few objects were falsely classified as avalanches, whereas the high Type I error showed that many, mostly old, snow avalanches remained undetected.

Table 4.1 | Performance metrics estimated for 4-km² training sites 1 – 3 (see Figures 4.3 and 4.5) and for the entire study area covering 226.3 km².

	Type I error	Type II error	Total error	Overall accuracy	Producer's accuracy	User's accuracy	Cohen's kappa	F-score
Site 1	0.23	0.01	0.05	0.95	0.77	0.91	0.81	0.83
Site 2	0.23	0.02	0.08	0.92	0.77	0.92	0.79	0.84
Site 3	0.16	0.02	0.05	0.95	0.84	0.93	0.85	0.88
Total	0.39	0.01	0.03	0.97	0.61	**0.78**	**0.67**	0.69

4.5.2. Influence of variables used for classification accuracy

We checked how brightness, NDVI, NDWI, and SD_{NDWI} derivatives evaluated for each classified avalanche affected the producer's accuracy. For each avalanche, we computed the mean for each derivative map using the values of all the pixels inside the avalanche. We found that avalanches that were extracted with the highest accuracy were generally also brighter (Fig. 4.6); an increase in producer's accuracy occurred with an increase in the mean brightness of avalanche. A similar, but, weaker correlation held for SD_{NDWI}. Neither NDVI nor NDWI had much of an influence on the classification accuracy. In addition, we verified if an avalanche's shape (roundness) and size (area) affected the detection rate. Similarly to NDVI and NDWI, however, we did not find any dependence (Fig. 4.6).

4.5.3. Topographic factors favourable for snow avalanches

We further analysed the topographic settings of the mapped avalanches. Most avalanches (1,422 out of 2,200) occurred between 1,900 and 2,600 m a.s.l., with a mode of approximately 2,400 m a.s.l., on slopes that were 20 – 40° (Fig. 4.7). One hundred thirty nine out of 193 of the highest-lying avalanches (>2,800 m a.s.l.) were small or very small events, according to the nomenclature of Bühler et al. (2009) and occurred in the southern part of our research area. Although the largest

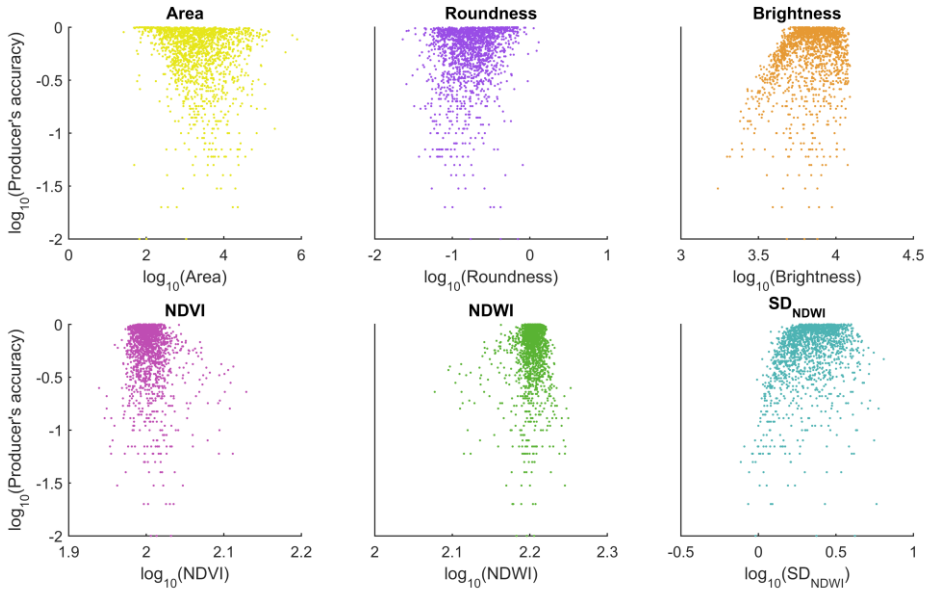

Figure 4.6 | The role of avalanche area, roundness, brightness, normalised difference vegetation index (NDVI), normalised difference water index (NDWI), and standard deviation of normalised difference water index (SD_{NDWI}) in the estimated accuracy, when detecting snow avalanches with our OBIA approach.

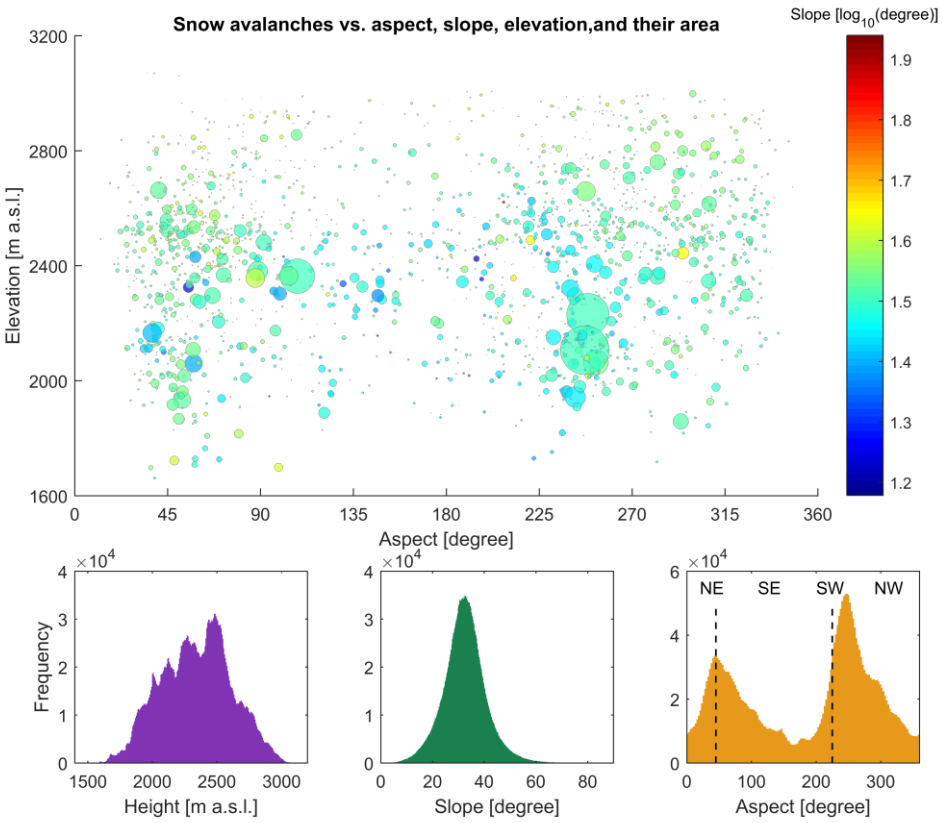

Figure 4.7 | Elevation, slope, and aspect of mapped reference avalanches with marked northeast and southwest directions in the winter of 2012/13. The values presented for every single avalanche represent the mean value of each pixel contained inside the reference avalanche polygon. Bubble size on the scatter plot is scaled to avalanche area.

avalanches occurred below 2,400 m a.s.l., most affected northeastern and the southwestern slopes, thus mimicking the major aspects of the mountain ranges (Fig. 4.3).

4.5.4. Density of avalanches

Using the reference data for the winter of 2012/13, we further analysed where most of the avalanches occurred. We computed centroid locations for each avalanche polygon, and estimated their spatial density using the *Kernel density* function in ArcGIS 10.3, with both point- and area-weighted inputs in a 2-km radius. We produced two maps because, due to the occurrence of multiple avalanches, our input centroids did not represent the total number of events. Consequently, a point-weighted map could have underestimated the real avalanche density, whereas an area-weighted map avoids this issue. The selected 2-km size of the bandwidth was large enough to avoid reproducing the pattern of input avalanche centroids, and small enough to reduce the smoothing of the point information. We found that avalanches clustered largely in the south-eastern part of the study area (125 smaller avalanches in inset 1, Fig. 4.8, of which 104 were <2,000 m²). The area-weighted spatial density of avalanches was highest on the slopes of Fluela Schwarzhorn, Sentischhorn, and Wuosthorn. The biggest avalanche in inset 2 on Figure 4.8 had an area of ~390,000 m².

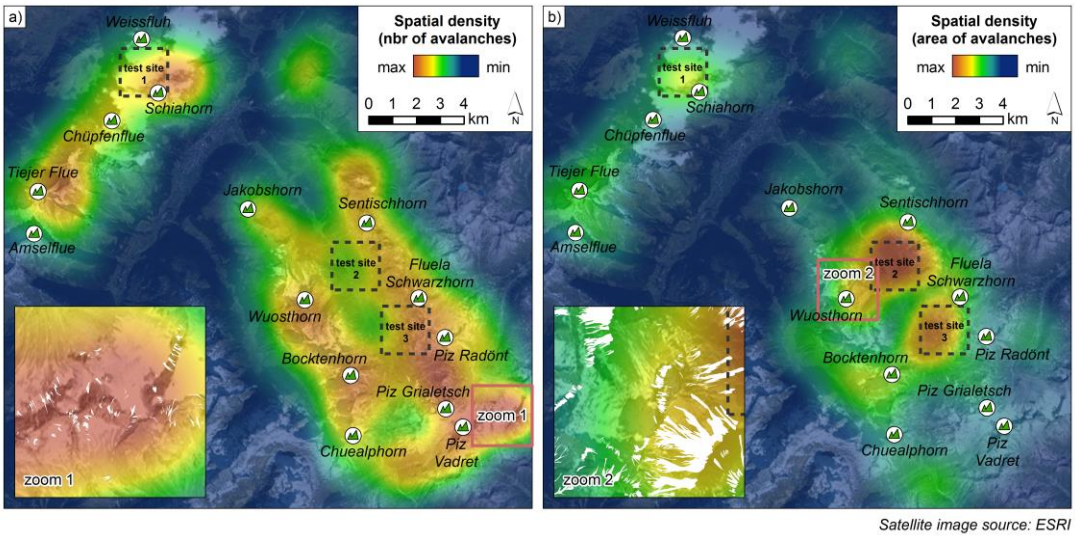

Figure 4.8 | Density maps showing the clustering of avalanches in the winter of 2012/13, with respect to their a) quantity, and b) size. The insets (zoom 1 and zoom 2) show the density maps with respect to manually-classified reference snow avalanche polygons shown in white. Outlined test sites 1 – 3 are the test sites that were used for developing our OBIA algorithm.

4.5.5. Automatic classification of snow-avalanche zones

Automatic delineation of release and runout zones from remote sensing data can be conducted by verifying the elevation values in each polygon that represents an avalanche. The simplest approach uses a flow length, which represents the distance along the flow path inside the avalanche, as an indicator in evaluating the probability of the release and the runout zones.

Herein, we suggest using the elevation values in an approach that allows exposure of local terrain height differences in the probability map. For example, applying the elevation for a release zone that occurs on very steep slopes determines that the highest probability will be represented only for a very small area, whereas on gentle slopes, the same probability will occur over a larger area, because the elevation differences are smaller than those of steep slopes.

We used a 2-m resolution digital surface model (DSM) derived from stereomatching of aerial ADS images to automatically detect release zones, tracks, and runout zones. Because we generated our reference data in the same resolution as the aerial images, we first resampled the DSM to 0.25-m resolution (Fig. 4.9). We then used the reference data to clip the DSM to each

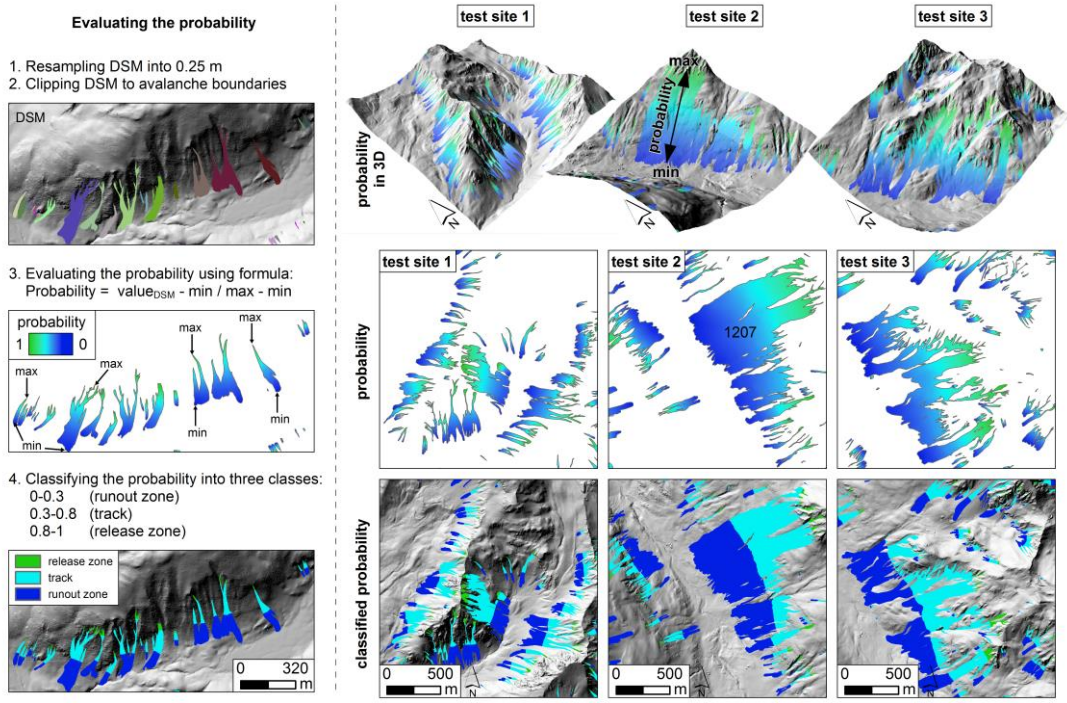

Figure 4.9 | Estimating the probability of an avalanche release area. A probability close to one indicates a pixel representing a release zone, whereas a probability close to zero indicates a runout zone in automatically classified data.

avalanche polygon using a key ID. DSMs acquired in this way were used to compute the probability of representing individual parts of an avalanche. We assumed that the maximum (minimum) elevation on which the snow avalanche occurs has the highest probability of being a release (runout) zone. We estimated the probability by normalising elevation data (Fig. 4.9) by subtracting the minimum value of DSM inside this avalanche from DSM pixel value, and dividing by the difference between the maximum and the minimum values inside each avalanche. Such stretching returns a 0 – 1 probability map for release areas. The thresholds in classifying the track are relative; we applied 0.3 – 0.8 as the thresholds, because most of our 2,200 manually-digitised polygons represented loose snow avalanches where the release zone constituted a small part, and the runout zone compared to the track constituted an even smaller part. When dealing

only with loose avalanches, the upper threshold for release areas may be set to a probability equal to 0.9. The selected thresholds worked well for single avalanches, where both the release zone and the runout zone were assigned correctly (Fig. 4.9). For avalanches with more complex shape and multiple avalanche arms (e.g. avalanche 1,207 on test site 2; Fig. 4.9), however, the release zones remain undetected, with the exception of only the highest-lying release areas.

4.6. Discussion

Automatic mapping of avalanches is crucial in mountainous regions to delineate susceptible areas and to produce cadastres for validating avalanche forecasting and hazard maps. Previous studies have demonstrated that a combination of aerial images and digital elevation models (Bühler et al., 2009), or aerial (Lato et al., 2012) and satellite (Larsen et al., 2013), or SAR images (Vickers et al., 2016) allow the detection of snow avalanche deposits; however, identifying release zones and tracks remains challenging. We have proposed an OBIA algorithm that tracks release zones, tracks, and runout zones in NIR images. We recommend using normalised derivatives NDWI and NDVI, instead of brightness, for classifying water (snow) and vegetation, respectively, because the thresholds allowing for classification of water and vegetation in these indices are stable (around zero) and widely applicable. Our approach upon expands previous work, as we have considered potential snow avalanches in snow-covered areas only (NDWI >127), whereas others have used brightness thresholds (Lato et al., 2012), with the danger of including other objects with similar values to those of snow. Rivers and lakes have similar values of NDWI, but are less bright than snow, we therefore combined NDWI and brightness in our model. We suggest using SD_{NDWI} to trace rough snow or avalanche debris. Estimated accuracy was high for detecting avalanches using the test data, and the random spread of avalanches detected with high accuracy through the whole research area suggests that the assumptions in our approach are broad enough to be applied for a large area.

To increase the accuracy of true positives in detecting release zones in our classification, a customised threshold for every data tile can be applied. In any case, we focused on developing a method that is transferable and works well for a greater area. We also wanted to test the usability of the image derivatives and verify how much information we could obtain from them when detecting snow avalanches. We therefore did not change any parameter or its threshold when applying the algorithm for other data tiles (Lato et al., 2012). We implemented several steps that allowed the classification of different avalanche scenarios that occur in diverse topographic conditions, such as single vs. multiple avalanche; small vs. large avalanche; avalanche revealing the ground or vegetation vs. avalanche that does not reveal the ground or vegetation; avalanche that is blocked by vegetation or other objects having high roughness vs. avalanche that is not adjacent to any rough object. These topographic conditions influence the appearance of

avalanches on images; therefore, the number of steps in our OBIA workflow is large. We found that OBIA is useful for complex shapes, because it allows the implementation of assumptions regarding each different situation. Additionally, this OBIA algorithm may be used and modified according to the need of the user and the data. For example, some steps in our OBIA workflow may be omitted, such as those used for filling the gaps inside the avalanche. If the data do not contain avalanches that reveal bare ground or vegetation, these steps may not improve the classification, because there will not be any gaps to reclassify. Additionally the number of loops in the shrinkage and growth steps depend on pixel size. With our 0.25-m resolution NIR images, we shrank and increased the segments of 1.25-m, which was sufficient to split segments into small parts; with higher (lower) resolution, the number of loops should be increased (decreased) accordingly. Previous studies have reported very high accuracy in separating vegetation and water using vegetation and water indices (Townshend and Justice, 1986; Ji et al., 2009); therefore, we assume that the NDVI, and NDWI thresholds are stable and may be easily transferable to other areas and data. Despite this, the thresholds for SD_{NDWI} should always be verified by analysing the mode of data distribution on a histogram of the SD_{NDWI}, testing the thresholding of data samples, and checking the thresholding results visually. We are aware that such visual checking may introduce some bias, although so far it is the most common way in OBIA to find the most suitable threshold.

The size and the shape of avalanches did not influence the classification accuracy if they were bigger than 2,000 pixels, which is what we regard as the minimum detectable size in our OBIA algorithm. We selected the minimum number of pixels necessary by analysing the reference data, where avalanches smaller than 2,000 pixels constituted only 7.5% of the total number of avalanches, and by taking into account the classification of avalanches with respect to their size. According to Bühler et al. (2009), very small avalanches are <100 m², which coincides with 2,000 pixels (125 m²). The parameters playing the biggest roles were brightness and the SD_{NDWI} (Fig. 4.6). Visual inspection showed that the easiest avalanche part to detect was the runout zone and the most difficult was the release zone, because release zones were not usually rough enough or did contain outcrops of the vegetation or bare ground. The correct detection of the track depended mostly on snow roughness and depth. In a case of low roughness values or a very thin snow cover revealing the ground and the vegetation, the track was not detected correctly or not detected at all.

The most difficult to classify were old avalanches where the bare ground cropped out or where vegetation occurred in the path of the avalanche. These avalanches did not meet the assumptions in our OBIA protocol and could not be classified correctly because they were not rough enough, or were too vegetated or dark due to thin snow cover. We tested different thresholds for the input layers and different neighbourhood assumptions in order to include these avalanches; however,

this resulted in more false positives, so the cost of correct classification of these avalanches was higher than the benefit. We therefore decided to stay with the same workflow and thresholding shown in Figure 4.4 for the whole study area.

Errors in automatic classification also occurred due to data tiling. Using an Intel Xeon E5-2667U processor with 256GB RAM memory, we were able to run our OBIA algorithm only for tiles of 6.25 km² (10,000 columns × 10,000 rows), requiring a computing time of ~30 minutes for each tile; our test in executing bigger tiles ended in crashing the computation in the eCognition software. In many cases the avalanches were therefore split into two or more neighbouring tiles, which influenced the correct detection of avalanche parts, especially those where the avalanches were spread across tiles or had small gaps.

Avalanches often have a tongue shape that may also be used as a property for classifying. In our test area, however, using such information may be insufficient, because we are dealing with avalanches repeated in the same location and merged avalanches, which have more complex shapes. In such cases, a new avalanche may partly cover previous avalanche, making it difficult to distinguish them. In addition, a few avalanches may simply have a more complex and difficult-to-interpret shape.

Our estimated avalanche density map and information concerning the most common prevalence of avalanches may be used to help generate a hazard map in mountainous areas. The most crucial issue, however, is whether the size or the number of avalanches is more important in such mapping. As mentioned by Eckerstorfer et al. (2016), only very small avalanches cause less damage; therefore, we suggest weighting the density map according to avalanche size to give more information regarding the degree of danger in a specific area.

Continuation of our research should contain verification of the transferability of our OBIA algorithm to data from different winter years for the area of Davos, Switzerland, which we have in our repository. In addition, future tests involving diverse areas across the World and different types of data (e.g. UAV) are desirable. An approach for distinguishing single and repeat avalanches at the same area should be developed, because it would give more detail about the quantity and the frequency of avalanches in a given area.

4.7. Conclusions

We have presented an automatic object-based image analysis (OBIA) approach to detecting snow avalanches and their release, track, and deposition zones for a large region from ADS80 NIR aerial images. We used image-derived parameters, including the normalised difference vegetation index (NDVI), and the normalised difference water index (NDWI) and its standard deviation (SD_{NDWI}), to separate vegetation, snow, and rough snow representing avalanche debris,

respectively. We applied buffering assumptions relying on the local neighbourhood of segments to remove salt-and-pepper noise and objects that were falsely assigned as avalanches, using the thresholding of derivatives obtained from NIR images. For an area of 226.3 km², our algorithm achieved producer's and user's accuracies of 0.61 and 0.78, respectively, and a Cohen's kappa of 0.67. Our algorithm uses only information taken from these images, from which the evaluated NDVI and NDWI indices are normalised, helping to transfer their thresholds to other areas. Our approach contains only three fixed parameters (NDVI, NDWI, and SD_{NDWI}) and two changeable parameters (brightness and segment area). The first depend on the spectral characteristics of images and the latter one depend on the resolution of images. Our OBIA workflow is not sequential when compared to that of Lato et al. (2012); the segments that do not fulfil assumptions in one step can still be considered as potential snow avalanches in the next steps. To assign potential snow avalanches, our method takes into account only the rough snow, which allows more reliable detection of avalanches. Our probability approach determines, in an automatic way, the highest and the lowest parts of the avalanche, and thus its release zone, track, and runout zone, which allows easy analysis of the topographic condition of areas where the avalanche starts and where the snow is deposited. For multiple avalanches with a complex shape, our probability map may not be sufficient to correctly identify all release and runout zones, but for single avalanches, it gives valuable results. For some avalanches, we were not able to judge visually if they were single or multiple; a discussion of this topic should therefore be undertaken. The probability approach may be used for any other mass movement landforms, such as landslides, to delineate their release and deposition zones. In the future, we plan to validate our snow avalanche algorithm for ADS data, which we have for other winters, and to verify its transferability to other NIR images, because successful results in this matter may offer a chance to improve hazard maps and avalanche forecasting in Switzerland.

Acknowledgments

This research was funded by the European Union under the Marie Curie Initial Training Network ALErT (Creation of an interactive CAP natural-hazard database), project-number: FP7-PEOPLE-2013-ITN-607996. The ADS80-SH92 airborne images used in the study were provided by the WSL- Institut für Schnee- und Lawinenforschung SLF, Davos, and Leica Geosystems AG (R. Wagner, N. Lämmer, F. Schapira). The authors would like to thank J. Wessels and B. Zweifel for providing historical snow avalanche data for Switzerland.

Supplementary material

The code for delineating snow avalanche boundaries is in the Appendix C.

Chapter 5

Conclusions

Automatic mapping of landforms diagnostic of natural hazards from remote sensing data is a challenging task, because each individual landform has its own properties that make it unique. It is therefore unlikely that the same workflow can be applied to track all these landforms together with the same level of the accuracy. Nonetheless, morphometric variables such as roughness contain information that characterises and distinguishes certain landforms from others. Previous studies have suggested many methods by which to derive topographic roughness (Smith, 2014). The curvature-based μ algorithm proposed in Chapter 2 allows the acquisition of terrain heterogeneity without any data detrending, and hence offers a novel advantage over previous DEM-derived methods (Haneberg et al., 2005; Cavalli et al., 2008). In this context, I will now revisit one central research question:

> ***RQ1.*** *Does curvature-derived surface roughness appropriately extract the properties of landforms diagnostic of natural hazards? How do the kernel and pixel sizes set for evaluated roughness affect the accuracy in detecting the analysed landforms diagnostic of natural hazards?*

The results of Chapter 2 demonstrate that the μ metric is insensitive to the slope of the terrain, and produces comparable or higher accuracy in detecting landforms, such as gullies, dunes, lava fields and landslides, than previously-proposed methods. This is demonstrated in Figure 2.13, where I compared our μ with several other algorithms for the same area and using the same reference data. Furthermore, the algorithm's simplicity, intuitive meaning and comprehensive documentation allow for its reproducibility by other users. The μ algorithm allows the delineation of the boundaries of landforms with high accuracy when selecting a proper kernel size, which, based on the results acquired herein, should be small. In our tested areas, a 5 × 5 kernel performed best for nearly all analysed landforms, because it was large enough to minimise the noise in the input data while being small enough to capture detailed local diversity of the terrain on our ALS data. This coincides with the results of Berti et al. (2013), who compared different surface roughness algorithms in detecting landslides. A bigger kernel gave higher accuracy only for large objects, such as lava fields (Table 2.2); however, it was at the cost of landform extent precision. I therefore recommend a 5 × 5 kernel as the default for tracking landforms with similar size and

similar data resolution to those I used in this study. Chapter 2 furthermore indicates that kernel size has a lower influence on the probability of detecting landforms than does data resolution, as correct detection can be disabled when the pixel size exceeds the size of the landform. Therefore, the resolution of the data in each case should be selected carefully by considering the size of the objects to be detected. This contradicts with the results of Grohmann et al. (2011), who stated that the kernel size and data resolution plays similarly important role. The limitation of my μ algorithm is that it is not capable of recognising the type of detected landforms, and is scale-dependent, and the user must manually select the kernel size and the resolution of data. An improvement of my method may focus on developing a method for automatic selection of the best kernel size and DTM resolution with respect to the analysed landform.

I argue that a simple assumption concerning roughness thresholding may be sufficient when dealing with easily-detectable landforms in a small area with a homogenous, in terms of roughness, environment. It may not be enough to detect landforms that are more complex, such as the landslides analysed herein, as the main scarp and the zone of material accumulation have different roughness's, with age influencing their roughness. LaHusen et al. (2016) stated that the roughness of landslides is influenced by the time when these objects were formed, and by the amount and strength of the exogenous processes that affected them. The authors found that in general, older landslides have lower roughness; therefore, even an application of several thresholds would not allow straightforward generalisations. This applies similarly to other indices, such as the water index, that might be derived from remote sensing data and are the subject of my next research question:

> ***RQ2.*** *What are the advantages and disadvantages of detecting landforms diagnostic of natural hazards from remote sensing data with their derived indices vs. visual information?*

Applying data-derived maps, such as water or vegetation indices, is also an advantage with respect to visual information read from the images. An example of a case when this is especially useful is when dealing with lakes that have different physical states of water, salinity, wave direction, and optical depth, because for such lakes, the brightness values will differ significantly (see Figure 3.2), making it difficult to classify them together as a single object. In addition, I demonstrated that a water (snow) index can be successfully used to delineate areas prone to avalanche occurrence. Compared to another study that considered avalanches as only pixels with high brightness (Lato et al., 2012), the approach presented herein offers a more convenient solution, because it considers only the areas covered by snow detected by the water index. Using only brightness encourages the misclassification of areas with high reflectance that have no snow cover. My algorithm excludes such areas and considers these as irrelevant for snow avalanches.

In addition, using a roughness metric (SD_{NDWI}) evaluated from water index allows distinguishing smooth and rough snow what helps to track avalanches.

Segmentation is the first step in the OBIA approach (Cheng and Han, 2016), so the chosen method controls the subsequent classification process. As presented in Figure 1.3, there are several segmentation methods available in the eCognition software. The most common algorithm used in OBIA is multiresolution segmentation (Baatz and Schäpe, 2000), which requires specification of the scale, shape and compactness of the segments. In this thesis, I used chessboard segmentation to classify snow avalanches and multiresolution segmentation to classify lakes with a set of their parameters, revisiting the third research question:

RQ3. *Are the segmentation method and its parameters the most significant when using OBIA? How the selected segmentation method controls the subsequent stages of classification?*

Previous studies (Drăguţ et al., 2010; Martha et al., 2011) have reported a requirement to use an automatic optimisation tool to minimise under- and over-segmentation when using multiresolution segmentation algorithm, yet the results of Chapter 3 indicate that to segment lakes from a standalone water index, such a tool might be redundant. Furthermore, it does not solve the issue of classifying objects that have a broad size range, such as lakes on the Tibetan Plateau, which range in area from <1 km² to 2,403 km². The lake detection algorithm proposed herein is designed for lakes with an area >10 km², but also allows the tracking of smaller lakes. Due to the selected scale in the segmentation process, however, the shape of these lakes is not as accurate as for larger lakes. The multiresolution segmentation algorithm additionally tends to simplify very complex lake shorelines (see Figure 3.9). Future solutions may thus desire to investigate, if not implement, chessboard segmentation instead. I surmise that applying additional steps that split these segments into smaller parts, where each segment represents an individual pixel, might decrease the number of misclassified areas, especially around the lake shorelines. This outcome I draw from my algorithm for detecting snow avalanches, where I used chessboard segmentation with an object size equal to unity as a primary scope for further OBIA workflow. Applying this algorithm allowed me to work on the pixel level, and was beneficial in developing neighbourhood assumptions. This is because it is easier to control how the classification is made for squared segments due to the known number of neighbours, their size and shape. For non-squared segments, these parameters for each segment may be different. I conclude that wrongly selected segmentation method and its parameters may significantly decrease the level of detecting objects, and further assumptions on segment size, geometry, and spatial relation will not be able to classify the segments with high accuracy.

One water index that I used in my study concerning delineating the boundaries of lakes in Section 3 was highly accurate in grouping frozen and non-frozen water altogether; nonetheless, it was not capable of automatically separating frozen lakes from glaciers over large areas. At this point, an OBIA approach is advantageous, as the method allows the combination of the spectral properties of data, different data types (i.e., images and elevation data) and their derivatives, analyses of the segment shape, size, and texture, and a spatial distribution of segments with respect to classification and other neighbouring segments. This revisits research question 4 of my thesis:

RQ4. *What are the advantages and disadvantages of OBIA in detecting lakes prone to seasonal ice cover in an area with glaciers?*

I found the OBIA approach suitable for classifying lakes, because it uses a straightforward manner to separate lakes from rivers. The Asymmetry parameter, as a leading assumption in this matter, is the measure that helped to separate rivers from lakes on the Tibetan Plateau. The examination of local relationships between the segments allows identification of the parts of lakes where the values of the water index do not exceed a predefined assumption of the thresholding value. Additionally, data concerning the local slope, derived from elevation data, assist to distinguish between lakes and glaciers. An advantage of my OBIA method, comparing to previous lakes extraction algorithms (Yamazaki et al., 2015; Sheng et al., 2016), is that it offers delineating lakes boundaries irrespectively of physical state of water what fills a gap in classifying lakes prone to seasonal ice cover like those on the Tibetan Plateau. My OBIA algorithm achieved an accuracy similar to those of Verpoorter et al. (2012), Jiang et al., (2014), and Jawak and Luis (2014). All these methods were tested on different areas of research and reference data, however. It is therefore necessary to point out that a fair comparison with other algorithms would be possible only if a reference benchmarks for lake areas existed in different environments. With the lack of such data, it is difficult to judge which method is or could be the best one, because every method is designed to solve different problem in different environments. For some instances, SRTM data may be used alone to detect water areas by applying the slope thresholding and verifying the roughness, which for water should be close to zero. These data were unable to be a main source in delineating the lake boundaries in 1995 and 2015 that I analysed in this thesis, because they represented the extent of the lakes for the time slice when the SRTM data were gathered. This also limits the use of SRTM data as a standalone data input in verifying the changes of lakes. Only the availability of elevation models with comparable resolution and accuracy for more time slices would allow such analysis.

Despite its numerous advantages, the OBIA approach also has its disadvantages, particularly in relation to the size and shape of the segments what was stressed by Cheng and Han (2016). The

selected segmentation algorithm will significantly influence subsequent steps. For example selecting chessboard segmentation with an object size equal to unity allows to work on pixel level with known number of neighbouring segments (four neighbouring segments), but limits gathering the statistics of every segment. Whereas multiresolution segmentation allows gathering the statistics, nonetheless the number of neighbouring segments varies for each segment. An incorrect parameter set in segmentation could decrease the possibility of correctly detecting objects because the segments may be too big/small, compact/loose, or homogeneous/heterogeneous – what is presented in Figure 3.5. Another point is operator bias in selecting the thresholds, algorithms and assumptions used in the OBIA approach. This can be an advantage, because the user can control the whole classification process; conversely, it can be a disadvantage, because such classification is always subjective. Further research should therefore focus on automation in selecting the thresholds, to reduce the bias produced by the operator. One way to reduce the subjectivity of the thresholding is to use normalised indices, which revisits the fifth research question of my thesis:

RQ5. *Which variables are the most significant in detecting snow avalanches from NIR images with OBIA?*

For detecting snow avalanches, the multiresolution segmentation algorithm did not distinguish object edges particularly well; therefore, similarly to Lato et al. (2012) I used the chessboard segmentation as a basis for further OBIA steps. The most useful indices for detecting avalanches were the water index and roughness, which allowed automatic mapping of areas covered by snow and areas with rough texture, respectively. The roughness metric (SD_{NDWI}) introduced herein is a new concept comparing to Bühler et al. (2009) and Lato et al. (2012) who as a measure of roughness used normalised difference angle index (NDAI), and dissimilarity evaluated from grey-level co-occurrence matrix (GLSM), respectively. Analysing the spectral values and classification of neighbouring segments was another important subject in assigning pixels that did represent snow avalanches but may not have been classified correctly due to their values of roughness, brightness, NDWI, or NDVI indices. Splitting an image into individual pixels limited the investigation of the mean, median, and standard deviation of each segment, which was possible with multiresolution segmentation, as it reduced the salt-and-pepper noise of the classification. Nevertheless, the neighbourhood analyses assisted in solving the issue of single pixels that have values that are too low or high to be sufficiently accepted into a given class. I found, however, that when phenomena were difficult to distinguish from other objects on remote sensing data, their detection rate might be low. Overall, my OBIA algorithm detected the avalanches with user's accuracy of 0.78 (Table 4.1.) for an area of 226.3 km², what is similar to the results of Bühler et al. (2009), yet lower than the algorithm of Lato et al. (2012). His method was applied over a smaller research area, however; and with changes in the classification

parameters in each test site. In addition, Larsen et al. (2013) pointed out that generation of snow avalanche outlines, which are used as reference data, is challenging. It is therefore difficult to compare these algorithms directly. Nevertheless, in my estimation, the accuracy achieved by my algorithm is sufficient for hazard mapping. A sufficient detection rate also depends on the purpose of the study, because detecting 0.78 of the total area of an avalanche that will be used to produce a hazard map may be sufficient, whereas detecting lakes with the same level of the accuracy (0.78), when the purpose is to verify their change in time, will not be sufficient because it will influence the change analysis, and correcting such data will take more time than digitising the lakes manually. The classification of objects that occurred at different times is a great challenge. Older landforms, such as snow avalanche debris lobes, may have a different texture than fresh ones. Thus, using the same threshold for old objects as for fresh objects will not allow them to be classified together with the same accuracy. One solution in this matter may be to run separate classifications, although that would require some detailed time-stamp information about each landform.

Cheng and Han (2016) stressed that the principal strength of an OBIA approach is the use of objects' shape, texture, and geometry, and the possibility of combining this information with GIS functionality and expert knowledge. They pointed out, however, that the biggest limitations are the full automation and the subjectivity of the rule sets. This is the main reason why, in my algorithms, I focused on normalised parameters, which reduce the level of subjectivity and allow for easy transferring of the approach to other areas with the same data. Normalised data are scaled the same, and thus a threshold selected for one data sample should be transferable to other samples of this data. In addition, if the selected threshold is not applicable to different data, it is easy to measure the range difference and find an explanation for it. This is the greatest strength of the OBIA algorithm presented herein. None of the previous methods designed for detecting snow avalanches from images suggest using a water (snow) index, even though it prevents erroneous classification of areas that are not covered by snow. In contrast, the greatest weakness of the OBIA algorithms presented herein is their dependency on pixel resolution. To use the workflows, one must bear in mind the data resolution that is used and how the data are stretched, because it will influence the results of the classification. Different stretching of data can result in incorrect thresholds (if one wants to use our algorithm with no changes), which will decrease the classification accuracy, whereas different data resolutions will affect the thresholds regarding size and the size of segments evaluated with multiresolution segmentation in my OBIA algorithm for detecting snow avalanches. For example, when using my lake boundary OBIA algorithm, the parameters in the multiresolution segmentation are keyed to LANDSAT images; therefore, when using them for other data types, such as those from the SENTINEL platform, they must be adapted accordingly. Similarly, the assumptions regarding object size in the OBIA algorithm for

snow avalanches are set to 0.25-cm ADS images, and will require adjustment when dealing with a different data resolution.

The performance metrics computed in this thesis measure the accuracy of classification, with each designed to verify a particular issue of the classification, and therefore they should be used in accordance with the purpose of the study. The overall accuracy (Congalton, 1991) is the simplest metric, which demonstrates the total number of correctly-classified pixels with respect to the total number of pixels in the matrix. This measure should be applied only when the number of pixels in each class has a comparable percentage of the total area of the analysis. When verifying only one class in the confusion matrix, this measure may not indicate that this class is accurately extracted. This is especially true if this class constitutes a small percentage of data with respect to other objects, such as the lakes in Chapter 3, because the percentage of another class in the matrix will be high; thus, in the case of a poor extraction of the first class, the total accuracy of the classification will be overestimated. In this matter, producer's and user's accuracies (Congalton, 1991) are more informative, because they capture how many pixels of the total number of pixels within the class have been correctly classified, and how many pixels from another class have been assigned to this class. This is relevant information, because my algorithm is capable of correctly detecting 69% of the total area of dunes (as in Chapter 2), but only 22% of all automatically-classified pixels were in fact dunes. Similar findings can be drawn from the type I and type II errors (Sithole and Vosselman, 2004; Table 2.4), which represent the number of pixels that were falsely rejected from or accepted to a class, respectively. Whereas the total error gives an overall view of the classification accuracy, the Cohen's kappa (Cohen, 1960) offers a superior overview of accuracy in relation to the abovementioned metrics, because it takes into consideration not only the agreement of the classification, but also the chance that the automatic algorithm can outperform a random classifier. The F-score measure is useful in verifying only one landform class in the classification accuracy without considering the landform background class. This measure should particularly be used for objects that make up a small percentage of the complete dataset, such as lakes in Section 3, because the measure requires only information about the pixels that belong to the class of interest, and whether these were correctly or falsely assigned to this class. The ROC (Swets, 1988) shown in Figures 2.6–2.9 and Figure 3.8 expresses the performance in separating the analysed object from the background of the data, and the AUC gives information about the probability of ranking randomly-chosen pixels that represent the analysed objects more highly than those representing the background. In a binary classification, the most significant metrics are the ROC, which verifies the performance of distinguishing the object from the background; the user's accuracy, which gives information about the number of classified objects that are in fact the objects of interest; and Cohen's kappa, which verifies whether the algorithm outperforms a random selection.

The main findings of this thesis demonstrate a high potential for detecting landforms diagnostic of natural hazards with OBIA, and the capabilities of the proposed algorithms should be further investigated. After the experience with this classification approach, I assume that more potential could be tied to a combination of segmentation methods. For example, the initial stage could perhaps use a pixel-level chessboard segmentation, whereas a second step might use multiresolution segmentation to produce homogenous and compact objects. In further exploration of OBIA capabilities, I would focus on analysing the relation of segments that do not share boundaries, but may represent the same object. An example of this is snow avalanches, which are numerous and with my algorithm are split into several parts where steep and bare slopes in the runout tracks escaped correct classification (Chapter 4).

A striking point that should be mentioned is the accuracy level with which the analysed phenomena were detected. A nearly flawless classification of lakes compared to flawed snow avalanche detection, with several undetected objects, raises the question of why one landforms can be tracked nearly perfectly and the other cannot. The level of accuracy depends on the information, which can be read from data by the algorithm, and on the similarity of objects. Deriving lakes from the water index evaluated from LANDSAT satellite images is easier than deriving avalanches based on roughness evaluated from NIR aerial images, because lakes usually have positive values on the water index, which allow for their successful detection, whereas the roughness of avalanches may differ from object to object, because it depends on the time slice between its occurrence and data collection, and on the environmental conditions of its occurrence. For example, an avalanche that reveals the ground or vegetation, or has partially melted due to the weather conditions, will have different roughness than another avalanche. In addition, reference data that are generated by manual digitisation are significant. The existence of a lake in the data is relatively easy to detect, whereas detection of a snow avalanche is not as trivial, because release zones may not be as clearly visible and distinguishable as runout zones. Similarly, avalanches that are old and blurred by the wind may be problematic, and could be classified as objects with uncertain membership in the avalanche class. In my estimation, achieving a similar level of accuracy for all phenomena analysed herein is therefore not feasible, at least not with the currently-available data and methods.

This thesis emphasised the methodological aspects involved in detecting natural hazard-related landforms. In addition, it investigated changes in lake size on the Tibetan Plateau and addressed part of the environmental context of these changes. The results demonstrate dynamic changes in water resources on the Tibetan Plateau, which are spread heterogeneously; this is consistent with the results of other studies (Ma et al., 2010; Lei et al., 2013; Fang et al., 2016). I observed the largest increase in the northeastern part of the Plateau, and the largest decrease in size in the southwestern part. The lakes did not change uniformly, so more detailed analysis of individual

changes, like this done for Nam Co by Liu et al. (2010), should be performed to find a direct cause and associate this change with other more regional and global changes. The same applies for snow avalanches, and the automatic detection of their deposits is a step forward in improving avalanche hazard maps. As I had only one time slice for the whole winter season my results may not show the complete distribution of avalanches during the whole winter. In addition, testing of my method using data acquired for different winter seasons by the WSL Institute for Snow and Avalanche Research SLF is desirable. Thus, acquiring data more frequently and combining the results achieved by automatic detection with hazard mapping are desirable to obtain a wider knowledge of the extent and frequency of avalanche occurrences.

I assume that the methods presented in this thesis may be portable in other areas dealing with the same landforms. The roughness algorithm may be used with any other digital elevation data, although the achieved results will depend on data resolution, as I tested my μ on SRTM data with 90 × 90 m resolution and found that the method works for detecting boundaries between larger landforms only. I demonstrated in Table 3.5 that the proposed algorithm for lake detection is transferable to areas with different environmental conditions with LANDSAT images, without changing any parameters in the OBIA workflow and yielded user's accuracy of >0.95 for five from six tested areas. I did not test if it is applicable for other released data, such as those from the SENTINEL platform, and therefore more testing is required. In addition, I have suggested a probability-based approach for delineating parts of avalanches (Fig. 4.9) and this may be used for other landforms, such as landslides and gullies.

Future research should place greater focus on testing the applicability of data derivatives, such as roughness, water and vegetation indices, in detecting landforms diagnostic of natural hazards from remote sensing technologies. In particular, verification of the portability of SD_{NDWI} as a measure of snow roughness is needed. As presented in this thesis, the attributes derived from digital elevation data and the land cover indices derived from images assist significantly in improving classification, especially in cases where simple analysis of the elevation and image pixel values within automatic classification methods is not sufficient to extract the objects with high accuracy. Future research should also test the applicability of μ for other data, such as those from terrestrial laser scanning, which have greater spatial resolution and therefore may be used to verify the roughness of the surface as the point cloud density if higher than those for ALS data. Similarly, I would recommend that the applicability of μ should be tested for elevation models generated using different data and techniques, such as stereomatching of aerial and UAV images, because the texture representing the surface on such data is different than that of LiDAR data. This may have an influence on different representations of roughness, which I did not analyse here.

In summary, the overall contribution of this thesis is that of providing methods that are sufficiently general so as to be transferable to other areas. All the proposed algorithms have been released as codes for ArcGIS and eCognition software tools, and their detailed documentation allows for further use and adaptation according to the requirements of the user. I hope that this work contributes to a greater focus on tracking natural hazards to maintain human lives and safety, and to improve hazard maps.

Appendix A

Code for evaluating curvature based terrain surface roughness

Copy the code and save as *.py file to use it in ArcMap 10.3. Input data to use the code should represent elevation raster data.

```
"""-------------------------------------------------------------------------------
 Script Name: Estimate surface roughness
 Description: Script generates a Roughness Index based on input digital terrain model (DTM).
                                    The approach for roughness estimation works on standard deviation differences
                                    in local terrain curvature derived from DTM. The values of the output roughness
                                    index raster layer means: low values > the lowest roughness,
                                    and high values > the highest roughness.
 Created By:  Karolina Korzeniowska.
 Date:       August 2015.
 -------------------------------------------------------------------------------"""
# -*- coding: utf-8 -*-
#
# Import arcpy module
import os
import arcpy
from arcpy import env
from arcpy.sa import *
#
# Check out the ArcGIS Spatial Analyst extension license
arcpy.CheckOutExtension("Spatial")
# Enable overwriting files
arcpy.env.overwriteOutput=True
#
# Set the input data
inRaster = arcpy.GetParameterAsText(0)
# Set the output data
outRaster = arcpy.GetParameterAsText(1)

# Set local variables
zFactor = 1.000
# Execute Curvature
outCurve = Curvature(inRaster, 1.000)

# Set local variables
neighborhood = NbrRectangle(5, 5, "CELL")
# Execute FocalStatistics (StDev)
outFocalStatistics2 = FocalStatistics(outCurve, neighborhood, "STD","")

# Execute Log10
outLog10 = Log10(outFocalStatistics2)
# Save the output Surface Roughness file
outLog10.save(outRaster)
```

Appendix B

Code for delineating lake boundaries

Copy the code and save as *.dcp file to use it in eCognition Developer 9.1. Input data to use the code are: Layer 1 – water index, Layer 2 – DEM derived slope map.

```
<?xml version="1.0" encoding="UTF-8"?>
<eCog.Proc UserName="Karolina" Company="" Copyright="" version="20140418" use-reproducable-poly="1" project-unit="5" engine-version="9.1.1" engine-build="2799" update-topology="0" distance_calculation="CG" resampling_compatibility="0">
<ruleset-info>
<name></name>
<author>Karolina</author>
<tags></tags>
<version></version>
<description></description>
<input></input>
<output></output>
</ruleset-info>
<ParamValueSetCntnr></ParamValueSetCntnr>
<ObjectDependencies>
<ImgLayers>
<ChnlProxyCntnr>
<Layers>
<ChnlProxy strName="Layer 1" flags="4">
<Assignment Chnl="0" MapName="main"></Assignment>
<LastAssignment Chnl="0" MapName="main"></LastAssignment>
<Scope GUID="00000000-0000-0000-0000-000000000000"></Scope>
</ChnlProxy>
<ChnlProxy strName="Layer 2" flags="4">
<Assignment Chnl="1" MapName="main"></Assignment>
<LastAssignment Chnl="1" MapName="main"></LastAssignment>
<Scope GUID="00000000-0000-0000-0000-000000000000"></Scope>
</ChnlProxy>
</Layers>
<Variables></Variables>
</ChnlProxyCntnr>
</ImgLayers>
<ThmLayers>
<ChnlProxyCntnr>
<Layers></Layers>
<Variables></Variables>
</ChnlProxyCntnr>
</ThmLayers>
<MapLvlProxyCntnr>
<MapLvlProxies>
<MapLvlProxy strName="New Level" bVrbl="0">
<Scope GUID="00000000-0000-0000-0000-000000000000"></Scope>
</MapLvlProxy>
</MapLvlProxies>
<MapLvlVrblValues></MapLvlVrblValues>
</MapLvlProxyCntnr>
<ProcVrblCntnr></ProcVrblCntnr>
<ClssHrchy EvalInvalid="1" MinProb="0.10000000000000001" NNSlope="0.20000000000000001" RdiResamplOptns="3">
<MapUnit>
<Map MapName="main" Unit="5"></Map>
</MapUnit>
<AllClss>
<Clss id="1" name="water" flag="0" iMaskID="-1" bUsePrntClr="0" dPrntClssBrghtns="0." termType="0" strUserName="Karolina" tChngTime="1457512452" bShow="0" Trans="0." sComment="">
<LcnsInfo sLcnsId="" sPwd=""></LcnsInfo>
<Scope GUID="00000000-0000-0000-0000-000000000000"></Scope>
<Color R="0" G="0" B="255"></Color>
<SharedInfo bShared="0" strInstGUID=""></SharedInfo>
</Clss>
<Clss id="2" name="rivers" flag="0" iMaskID="-1" bUsePrntClr="0" dPrntClssBrghtns="0." termType="0" strUserName="Karolina" tChngTime="1457512957" bShow="0" Trans="0." sComment="">
<LcnsInfo sLcnsId="" sPwd=""></LcnsInfo>
<Scope GUID="00000000-0000-0000-0000-000000000000"></Scope>
<Color R="0" G="255" B="0"></Color>
<SharedInfo bShared="0" strInstGUID=""></SharedInfo>
</Clss>
<Clss id="3" name="glaciers" flag="0" iMaskID="-1" bUsePrntClr="0" dPrntClssBrghtns="0." termType="0" strUserName="Karolina" tChngTime="1457513758" bShow="0" Trans="0." sComment="">
<LcnsInfo sLcnsId="" sPwd=""></LcnsInfo>
<Scope GUID="00000000-0000-0000-0000-000000000000"></Scope>
<Color R="255" G="128" B="0"></Color>
<SharedInfo bShared="0" strInstGUID=""></SharedInfo>
</Clss>
</AllClss>
<PropTree version="20100426">
<AllProps>
<PropDscr Flag="0" strUserName="Karolina" tChngTime="1457511670" group_id="shape.geom.object.prop">
<PropDscrId GUID="D9CC01FF-7C3D-4861-9608-38D8EB2D3CCC" InstID="Asymmetry"></PropDscrId>
<LcnsInfo sLcnsId="" sPwd=""></LcnsInfo>
<Scope GUID="00000000-0000-0000-0000-000000000000"></Scope>
<Params></Params>
</PropDscr>
<PropDscr Flag="65538" strUserName="Karolina" tChngTime="1457511670" group_id="ext.geom.object.prop">
```

<PropDscrId GUID="AF0D7167-ADE8-4240-AAA4-AC2C188E9AF5" InstID="Number of pixels"></PropDscrId>
<LcnsInfo sLcnsId="" sPwd=""></LcnsInfo>
<Scope GUID="00000000-0000-0000-0000-000000000000"></Scope>
<Params></Params>
</PropDscr>
<PropDscr Flag="2" strUserName="Karolina" tChngTime="1457518552" group_id="relbrdr.nghb.class.prop">
<PropDscrId GUID="AA7CAC99-696D-4983-8F48-D07C4F816F2C" InstID="Rel. border to glaciers"></PropDscrId>
<LcnsInfo sLcnsId="" sPwd=""></LcnsInfo>
<Scope GUID="00000000-0000-0000-0000-000000000000"></Scope>
<Params>
<DValue value="3" type="clssId" name="valClss"></DValue>
</Params>
</PropDscr>
<PropDscr Flag="2" strUserName="Karolina" tChngTime="1457512742" group_id="relbrdr.nghb.class.prop">
<PropDscrId GUID="AA7CAC99-696D-4983-8F48-D07C4F816F2C" InstID="Rel. border to water"></PropDscrId>
<LcnsInfo sLcnsId="" sPwd=""></LcnsInfo>
<Scope GUID="00000000-0000-0000-0000-000000000000"></Scope>
<Params>
<DValue value="1" type="clssId" name="valClss"></DValue>
</Params>
</PropDscr>
<PropDscr Flag="2" strUserName="Karolina" tChngTime="1458209191" group_id="num.nghb.class.prop">
<PropDscrId GUID="7D1F1A4B-9BFD-4b29-BA08-AA370D63669B" InstID="Number of water (0)"></PropDscrId>
<LcnsInfo sLcnsId="" sPwd=""></LcnsInfo>
<Scope GUID="00000000-0000-0000-0000-000000000000"></Scope>
<Params>
<DValue value="1" type="clssId" name="valClss"></DValue>
<DValue value="0" type="int" name="iDist"></DValue>
</Params>
</PropDscr>
<PropDscr Flag="2" strUserName="Karolina" tChngTime="1457511772" group_id="mean.chnl.object.prop">
<PropDscrId GUID="44411C83-609B-4758-93D3-FF62DF246855" InstID="Mean Layer 1"></PropDscrId>
<LcnsInfo sLcnsId="" sPwd=""></LcnsInfo>
<Scope GUID="00000000-0000-0000-0000-000000000000"></Scope>
<Params>
<DValue type="img_chnl" value="Layer 1" scope="" name="valChnl"></DValue>
</Params>
</PropDscr>
<PropDscr Flag="2" strUserName="Karolina" tChngTime="1457511772" group_id="mean.chnl.object.prop">
<PropDscrId GUID="44411C83-609B-4758-93D3-FF62DF246855" InstID="Mean Layer 2"></PropDscrId>
<LcnsInfo sLcnsId="" sPwd=""></LcnsInfo>
<Scope GUID="00000000-0000-0000-0000-000000000000"></Scope>
<Params>
<DValue type="img_chnl" value="Layer 2" scope="" name="valChnl"></DValue>
</Params>
</PropDscr>
</AllProps>
<UserGroups></UserGroups>
</PropTree>
<Brightness>
<Map MapName="main">
<ChnlWghtBrght>
<BrghtWght val="1." chnl="0"></BrghtWght>
<BrghtWght val="1." chnl="1"></BrghtWght>
</ChnlWghtBrght>
</Map>
</Brightness>
<AllVrblClss></AllVrblClss>
<AllSubClss>
<Clss Id="1" PrfdGrp="1">
<SubClss></SubClss>
<SubGrp></SubGrp>
</Clss>
<Clss Id="2" PrfdGrp="2">
<SubClss></SubClss>
<SubGrp></SubGrp>
</Clss>
<Clss Id="3" PrfdGrp="3">
<SubClss></SubClss>
<SubGrp></SubGrp>
</Clss>
</AllSubClss>
<AllTerm>
<Term TermEvalType="0">
<TermBase ClssId="1" flags="0" sComment="">
<Weight>
<DValue value="1" type="int"></DValue>
</Weight>
</TermBase>
</Term>
<Term TermEvalType="0">
<TermBase ClssId="2" flags="0" sComment="">
<Weight>
<DValue value="1" type="int"></DValue>
</Weight>
</TermBase>
</Term>
<Term TermEvalType="0">
<TermBase ClssId="3" flags="0" sComment="">
<Weight>
<DValue value="1" type="int"></DValue>
</Weight>
</TermBase>
</Term>
</AllTerm>
</ClssHrchy>
<MapVrblCntnr></MapVrblCntnr>
<FtrListVrblCntnr></FtrListVrblCntnr>
<CoordVrblCntnr></CoordVrblCntnr>
<ROIVrblCntnr></ROIVrblCntnr>
<ImgObjListVrblCntnr></ImgObjListVrblCntnr>
<ArrayCntnr>
<Arrays></Arrays>
<ArrayVrbls></ArrayVrbls>
</ArrayCntnr>
<Smpls>
<AllClss>
<SmplList ClssId="1"></SmplList>
<SmplList ClssId="2"></SmplList>
<SmplList ClssId="3"></SmplList>
</AllClss>
<AllProp></AllProp>
</Smpls>
<plugin-list>
<plugin name="eCognition Internal Process Algorithms" version="0.1"></plugin>
<plugin name="eCognition Internal Export Process Algorithms" version="0.1"></plugin>
<plugin name="eCognition Basic Process Algorithms" version="0.1"></plugin>
</plugin-list>
</ObjectDependencies>
<CustProcAlgrList></CustProcAlgrList>
<ProcessList>

<ProcBase Name="multiresolution segmentation" bLoopChg="0" bExpand="1" bActive="1" bAutoName="0" bSubrtn="0" sComment="">
<LcnsInfo sLcnsId="" sPwd=""></LcnsInfo>
<vrblValMaxCycle>
<DValue value="1." type="double"></DValue>
</vrblValMaxCycle>
<Algorithm guid="A8BA5775-CC39-4194-9A6A-A64872EE1F81">
<Params></Params>
</Algorithm>
<Domain guid="CC9F2C30-4DB0-4ef2-B864-63560D1D6BF3">
<Params>
<DValue type="threshold" name="valThrsh"></DValue>
<DValue type="threshold" name="valThrsh2"></DValue>
<DValue value="From Parent" type="string" name="valMap"></DValue>
</Params>
</Domain>
<SubProc>
<ProcBase Name="100 [shape:0.1 compct.:0.7] creating 'New Level'" bLoopChg="0" bExpand="1" bActive="1" bAutoName="1" bSubrtn="0" sComment="">
<LcnsInfo sLcnsId="" sPwd=""></LcnsInfo>
<vrblValMaxCycle>
<DValue value="1." type="double"></DValue>
</vrblValMaxCycle>
<Algorithm guid="6534F2E1-485B-406f-B990-350824399FA8">
<Params>
<DValue value="1" type="bool" name="bDoOverwrite"></DValue>
<DValue type="lvlName" name="valMapLvl">
<MapLvlProxy strName="New Level" bVrbl="0">
<Scope GUID="00000000-0000-0000-0000-000000000000"></Scope>
</MapLvlProxy>
</DValue>
<DValue value="4" type="int" name="eLvlUsage"></DValue>
<DValue value="5" type="int" name="iCompMode"></DValue>
<DValue type="vector" name="vImgLayerWghtVarOrValue">
<Values>
<DValue type="vector" indx="0">
<Values>
<DValue type="img_chnl" value="Layer 1" scope="" indx="0"></DValue>
<DValue value="1." type="double" indx="1"></DValue>
</Values>
</DValue>
</Values>
</DValue>
<DValue type="vector" name="vImgLayerWght">
<Values>
<DValue type="vector" indx="0">
<Values>
<DValue type="img_chnl" value="Layer 1" scope="" indx="0"></DValue>
<DValue value="1." type="double" indx="1"></DValue>
</Values>
</DValue>
</Values>
</DValue>
<DValue type="vector" name="vThmLayerFlags">
<Values></Values>
</DValue>
<DValue value="100." type="double" name="vrblValScale"></DValue>
<DValue value="0.10000000000000001" type="double" name="vrblHCShape"></DValue>
<DValue value="0.69999999999999996" type="double" name="vrblHCArea"></DValue>
</Params>
</Algorithm>
<Domain guid="682A3AA1-9F4F-4dae-9E44-5015DF867712">
<Params>
<DValue type="threshold" name="valThrsh"></DValue>
<DValue type="threshold" name="valThrsh2"></DValue>
<DValue value="From Parent" type="string" name="valMap"></DValue>
</Params>
</Domain>
<SubProc></SubProc>
</ProcBase>
<ProcBase Name="MNDWI" bLoopChg="0" bExpand="1" bActive="1" bAutoName="0" bSubrtn="0" sComment="">
<LcnsInfo sLcnsId="" sPwd=""></LcnsInfo>
<vrblValMaxCycle>
<DValue value="1." type="double"></DValue>
</vrblValMaxCycle>
<Algorithm guid="A8BA5775-CC39-4194-9A6A-A64872EE1F81">
<Params></Params>
</Algorithm>
<Domain guid="CC9F2C30-4DB0-4ef2-B864-63560D1D6BF3">
<Params>
<DValue type="threshold" name="valThrsh"></DValue>
<DValue type="threshold" name="valThrsh2"></DValue>
<DValue value="From Parent" type="string" name="valMap"></DValue>
</Params>
</Domain>
<SubProc>
<ProcBase Name="with Mean Layer 1 > 180 at New Level: water" bLoopChg="0" bExpand="1" bActive="1" bAutoName="1" bSubrtn="0" sComment="">
<LcnsInfo sLcnsId="" sPwd=""></LcnsInfo>
<vrblValMaxCycle>
<DValue value="1." type="double"></DValue>
</vrblValMaxCycle>
<Algorithm guid="3AC44F21-C6B2-4804-9929-BB18BE6F2051">
<Params>
<DValue value="1" type="clssId" name="valClass"></DValue>
</Params>
</Algorithm>
<Domain guid="CED621BD-F4D1-4ffa-A2F6-DB2BB1913E8C">
<Params>
<DValue type="lvlName" name="valMapLvl">
<MapLvlProxy strName="New Level" bVrbl="0">
<Scope GUID="00000000-0000-0000-0000-000000000000"></Scope>
</MapLvlProxy>
</DValue>
<DValue type="vector" name="mClssFltr">
<Values>
<DValue value="Disabled" type="string" indx="0"></DValue>
</Values>
</DValue>
<DValue type="threshold" name="valThrsh">
<TermThrsh>
<TermGroup eJoint="2">
<TermCondition eCmpr="3" eBaseUnit="0" eJoint="2">
<ProcVrblVal1>
<DValue type="propDscrId">
<PropDscrId GUID="44411C83-609B-4758-93D3-FF62DF246855" InstID="Mean Layer 1"></PropDscrId>
</DValue>
</ProcVrblVal1>
<ProcVrblVal2>
<DValue value="180." type="double"></DValue>
</ProcVrblVal2>
</TermCondition>
</TermGroup>
</TermThrsh>

```
</DValue>
<DValue type="threshold" name="valThrsh2"></DValue>
<DValue value="From Parent" type="string" name="valMap"></DValue>
<DValue value="From Parent" type="string" name="valROI"></DValue>
<DValue value="0" type="int" name="iNumMaxObj"></DValue>
<DValue value="4" type="int" name="iVersion"></DValue>
<DValue value="-1" type="int" name="iOldLvl"></DValue>
<DValue value="0" type="int" name="iOldDsplLvl"></DValue>
<DValue value="0" type="int" name="iOldDsplNumLvl"></DValue>
</Params>
</Domain>
<SubProc></SubProc>
</ProcBase>
<ProcBase Name="do" bLoopChg="0" bExpand="1" bActive="1" bAutoName="1" bSubrtn="0" sComment="">
<LcnsInfo sLcnsId="" sPwd=""></LcnsInfo>
<vrblValMaxCycle>
<DValue value="1." type="double"></DValue>
</vrblValMaxCycle>
<Algorithm guid="A8BA5775-CC39-4194-9A6A-A64872EE1F81">
<Params></Params>
</Algorithm>
<Domain guid="CC9F2C30-4DB0-4ef2-B864-63560D1D6BF3">
<Params>
<DValue type="threshold" name="valThrsh"></DValue>
<DValue type="threshold" name="valThrsh2"></DValue>
<DValue value="From Parent" type="string" name="valMap"></DValue>
</Params>
</Domain>
<SubProc>
<ProcBase Name="loop: unclassified with Mean Layer 1 > 160  and Rel. border to water > 0.25  and Mean Layer 2 &lt;= 0.5  at  New Level: water" bLoopChg="1" bExpand="1" bActive="1" bAutoName="1"
bSubrtn="0" sComment="">
<LcnsInfo sLcnsId="" sPwd=""></LcnsInfo>
<vrblValMaxCycle>
<DValue value="1" type="int"></DValue>
</vrblValMaxCycle>
<Algorithm guid="3AC44F21-C6B2-4804-9929-BB18BE6F2051">
<Params>
<DValue value="1" type="clssId" name="valClass"></DValue>
</Params>
</Algorithm>
<Domain guid="CED621BD-F4D1-4ffa-A2F6-DB2BB1913E8C">
<Params>
<DValue type="lvlName" name="valMapLvl">
<MapLvlProxy strName="New Level" bVrbl="0">
<Scope GUID="00000000-0000-0000-0000-000000000000"></Scope>
</MapLvlProxy>
</DValue>
<DValue type="vector" name="mClssFltr">
<Values>
<DValue value="Unclsfy" type="string" indx="0"></DValue>
<DValue value="User defined" type="string" indx="1"></DValue>
</Values>
</DValue>
<DValue type="threshold" name="valThrsh">
<TermThrsh>
<TermGroup eJoint="2">
<TermCondition eCmpr="3" eBaseUnit="0" eJoint="0">
<ProcVrblVal1>
<DValue type="propDscrId">
<PropDscrId GUID="44411C83-609B-4758-93D3-FF62DF246855" InstID="Mean Layer 1"></PropDscrId>
</DValue>
</ProcVrblVal1>
<ProcVrblVal2>
<DValue value="160." type="double"></DValue>
</ProcVrblVal2>
</TermCondition>
<TermCondition eCmpr="3" eBaseUnit="0" eJoint="0">
<ProcVrblVal1>
<DValue type="propDscrId">
<PropDscrId GUID="AA7CAC99-696D-4983-8F48-D07C4F816F2C" InstID="Rel. border to water"></PropDscrId>
</DValue>
</ProcVrblVal1>
<ProcVrblVal2>
<DValue value="0.25" type="double"></DValue>
</ProcVrblVal2>
</TermCondition>
<TermCondition eCmpr="1" eBaseUnit="0" eJoint="2">
<ProcVrblVal1>
<DValue type="propDscrId">
<PropDscrId GUID="44411C83-609B-4758-93D3-FF62DF246855" InstID="Mean Layer 2"></PropDscrId>
</DValue>
</ProcVrblVal1>
<ProcVrblVal2>
<DValue value="0.5" type="double"></DValue>
</ProcVrblVal2>
</TermCondition>
</TermGroup>
</TermThrsh>
</DValue>
<DValue type="threshold" name="valThrsh2"></DValue>
<DValue value="From Parent" type="string" name="valMap"></DValue>
<DValue value="From Parent" type="string" name="valROI"></DValue>
<DValue value="0" type="int" name="iNumMaxObj"></DValue>
<DValue value="4" type="int" name="iVersion"></DValue>
<DValue value="-1" type="int" name="iOldLvl"></DValue>
<DValue value="0" type="int" name="iOldDsplLvl"></DValue>
<DValue value="0" type="int" name="iOldDsplNumLvl"></DValue>
</Params>
</Domain>
<SubProc></SubProc>
</ProcBase>
<ProcBase Name="do" bLoopChg="0" bExpand="1" bActive="1" bAutoName="1" bSubrtn="0" sComment="">
<LcnsInfo sLcnsId="" sPwd=""></LcnsInfo>
<vrblValMaxCycle>
<DValue value="1." type="double"></DValue>
</vrblValMaxCycle>
<Algorithm guid="A8BA5775-CC39-4194-9A6A-A64872EE1F81">
<Params></Params>
</Algorithm>
<Domain guid="CC9F2C30-4DB0-4ef2-B864-63560D1D6BF3">
<Params>
<DValue type="threshold" name="valThrsh"></DValue>
<DValue type="threshold" name="valThrsh2"></DValue>
<DValue value="From Parent" type="string" name="valMap"></DValue>
</Params>
</Domain>
<SubProc>
<ProcBase Name="loop: unclassified with Mean Layer 1 > 150  and Rel. border to water > 0.4  at  New Level: water" bLoopChg="1" bExpand="1" bActive="1" bAutoName="1" bSubrtn="0" sComment="">
<LcnsInfo sLcnsId="" sPwd=""></LcnsInfo>
<vrblValMaxCycle>
<DValue value="1." type="double"></DValue>
```

```
</vrblValMaxCycle>
<Algorithm guid="3AC44F21-C6B2-4804-9929-BB18BE6F2051">
<Params>
<DValue value="1" type="clssId" name="valClass"></DValue>
</Params>
</Algorithm>
<Domain guid="CED621BD-F4D1-4ffa-A2F6-DB2BB1913E8C">
<Params>
<DValue type="lvlName" name="valMapLvl">
<MapLvlProxy strName="New Level" bVrbl="0">
<Scope GUID="00000000-0000-0000-0000-000000000000"></Scope>
</MapLvlProxy>
</DValue>
<DValue type="vector" name="mClssFltr">
<Values>
<DValue value="Unclsfy" type="string" indx="0"></DValue>
<DValue value="User defined" type="string" indx="1"></DValue>
</Values>
</DValue>
<DValue type="threshold" name="valThrsh">
<TermThrsh>
<TermGroup eJoint="2">
<TermCondition eCmpr="3" eBaseUnit="0" eJoint="0">
<ProcVrblVal1>
<DValue type="propDscrId">
<PropDscrId GUID="44411C83-609B-4758-93D3-FF62DF246855" InstID="Mean Layer 1"></PropDscrId>
</DValue>
</ProcVrblVal1>
<ProcVrblVal2>
<DValue value="150." type="double"></DValue>
</ProcVrblVal2>
</TermCondition>
<TermCondition eCmpr="3" eBaseUnit="0" eJoint="2">
<ProcVrblVal1>
<DValue type="propDscrId">
<PropDscrId GUID="AA7CAC99-696D-4983-8F48-D07C4F816F2C" InstID="Rel. border to water"></PropDscrId>
</DValue>
</ProcVrblVal1>
<ProcVrblVal2>
<DValue value="0.40000000000000002" type="double"></DValue>
</ProcVrblVal2>
</TermCondition>
</TermGroup>
</TermThrsh>
</DValue>
<DValue type="threshold" name="valThrsh2"></DValue>
<DValue value="From Parent" type="string" name="valMap"></DValue>
<DValue value="From Parent" type="string" name="valROI"></DValue>
<DValue value="0" type="int" name="iNumMaxObj"></DValue>
<DValue value="4" type="int" name="iVersion"></DValue>
<DValue value="-1" type="int" name="iOldLvl"></DValue>
<DValue value="0" type="int" name="iOldDsplLvl"></DValue>
<DValue value="0" type="int" name="iOldDsplNumLvl"></DValue>
</Params>
</Domain>
<SubProc></SubProc>
</ProcBase>
<ProcBase Name="classify rivers" bLoopChg="0" bExpand="1" bActive="1" bAutoName="0" bSubrtn="0" sComment="">
<LcnsInfo sLcnsId="" sPwd=""></LcnsInfo>
<vrblValMaxCycle>
<DValue value="1." type="double"></DValue>
</vrblValMaxCycle>
<Algorithm guid="A8BA5775-CC39-4194-9A6A-A64872EE1F81">
<Params></Params>
</Algorithm>
<Domain guid="CC9F2C30-4DB0-4ef2-B864-63560D1D6BF3">
<Params>
<DValue type="threshold" name="valThrsh"></DValue>
<DValue type="threshold" name="valThrsh2"></DValue>
<DValue value="From Parent" type="string" name="valMap"></DValue>
</Params>
</Domain>
<SubProc>
<ProcBase Name="water with Asymmetry > 0.85 and Rel. border to water &lt; 0.15 and Number of water (0) &lt; 2 at New Level: rivers" bLoopChg="0" bExpand="1" bActive="1" bAutoName="1" bSubrtn="0"
sComment="">
<LcnsInfo sLcnsId="" sPwd=""></LcnsInfo>
<vrblValMaxCycle>
<DValue value="1." type="double"></DValue>
</vrblValMaxCycle>
<Algorithm guid="3AC44F21-C6B2-4804-9929-BB18BE6F2051">
<Params>
<DValue value="2" type="clssId" name="valClass"></DValue>
</Params>
</Algorithm>
<Domain guid="CED621BD-F4D1-4ffa-A2F6-DB2BB1913E8C">
<Params>
<DValue type="lvlName" name="valMapLvl">
<MapLvlProxy strName="New Level" bVrbl="0">
<Scope GUID="00000000-0000-0000-0000-000000000000"></Scope>
</MapLvlProxy>
</DValue>
<DValue type="vector" name="mClssFltr">
<Values>
<DValue value="1" type="clssId" indx="0"></DValue>
<DValue value="User defined" type="string" indx="1"></DValue>
</Values>
</DValue>
<DValue type="threshold" name="valThrsh">
<TermThrsh>
<TermGroup eJoint="2">
<TermCondition eCmpr="3" eBaseUnit="0" eJoint="0">
<ProcVrblVal1>
<DValue type="propDscrId">
<PropDscrId GUID="D9CC01FF-7C3D-4861-9608-38D8EB2D3CCC" InstID="Asymmetry"></PropDscrId>
</DValue>
</ProcVrblVal1>
<ProcVrblVal2>
<DValue value="0.84999999999999998" type="double"></DValue>
</ProcVrblVal2>
</TermCondition>
<TermCondition eCmpr="2" eBaseUnit="0" eJoint="0">
<ProcVrblVal1>
<DValue type="propDscrId">
<PropDscrId GUID="AA7CAC99-696D-4983-8F48-D07C4F816F2C" InstID="Rel. border to water"></PropDscrId>
</DValue>
</ProcVrblVal1>
<ProcVrblVal2>
<DValue value="0.14999999999999999" type="double"></DValue>
</ProcVrblVal2>
</TermCondition>
<TermCondition eCmpr="2" eBaseUnit="0" eJoint="2">
```

<ProcVrblVal1>
<DValue type="propDscrId">
<PropDscrId GUID="7D1F1A4B-9BFD-4b29-BA08-AA370D63669B" InstID="Number of water (0)"></PropDscrId>
</DValue>
</ProcVrblVal1>
<ProcVrblVal2>
<DValue value="2." type="double"></DValue>
</ProcVrblVal2>
</TermCondition>
</TermGroup>
</TermThrsh>
</DValue>
<DValue type="threshold" name="valThrsh2"></DValue>
<DValue value="From Parent" type="string" name="valMap"></DValue>
<DValue value="From Parent" type="string" name="valROI"></DValue>
<DValue value="0" type="int" name="iNumMaxObj"></DValue>
<DValue value="4" type="int" name="iVersion"></DValue>
<DValue value="-1" type="int" name="iOldLvl"></DValue>
<DValue value="0" type="int" name="iOldDsplLvl"></DValue>
<DValue value="0" type="int" name="iOldDsplNumLvl"></DValue>
</Params>
</Domain>
<SubProc></SubProc>
</ProcBase>
<ProcBase Name="classify glaciers" bLoopChg="0" bExpand="1" bActive="1" bAutoName="0" bSubrtn="0" sComment="">
<LcnsInfo sLcnsId="" sPwd=""></LcnsInfo>
<vrblValMaxCycle>
<DValue value="1." type="double"></DValue>
</vrblValMaxCycle>
<Algorithm guid="A8BA5775-CC39-4194-9A6A-A64872EE1F81">
<Params></Params>
</Algorithm>
<Domain guid="CC9F2C30-4DB0-4ef2-B864-63560D1D6BF3">
<Params>
<DValue type="threshold" name="valThrsh"></DValue>
<DValue type="threshold" name="valThrsh2"></DValue>
<DValue value="From Parent" type="string" name="valMap"></DValue>
</Params>
</Domain>
<SubProc>
<ProcBase Name="water with Mean Layer 2 > 2 at New Level: glaciers" bLoopChg="0" bExpand="1" bActive="1" bAutoName="1" bSubrtn="0" sComment="">
<LcnsInfo sLcnsId="" sPwd=""></LcnsInfo>
<vrblValMaxCycle>
<DValue value="1." type="double"></DValue>
</vrblValMaxCycle>
<Algorithm guid="3AC44F21-C6B2-4804-9929-BB18BE6F2051">
<Params>
<DValue value="3" type="clssId" name="valClass"></DValue>
</Params>
</Algorithm>
<Domain guid="CED621BD-F4D1-4ffa-A2F6-DB2BB1913E8C">
<Params>
<DValue type="lvlName" name="valMapLvl">
<MapLvlProxy strName="New Level" bVrbl="0">
<Scope GUID="00000000-0000-0000-0000-000000000000"></Scope>
</MapLvlProxy>
</DValue>
<DValue type="vector" name="mClssFltr">
<Values>
<DValue value="1" type="clssId" indx="0"></DValue>
<DValue value="User defined" type="string" indx="1"></DValue>
</Values>
</DValue>
<DValue type="threshold" name="valThrsh">
<TermThrsh>
<TermGroup eJoint="2">
<TermCondition eCmpr="3" eBaseUnit="0" eJoint="2">
<ProcVrblVal1>
<DValue type="propDscrId">
<PropDscrId GUID="44411C83-609B-4758-93D3-FF62DF246855" InstID="Mean Layer 2"></PropDscrId>
</DValue>
</ProcVrblVal1>
<ProcVrblVal2>
<DValue value="2." type="double"></DValue>
</ProcVrblVal2>
</TermCondition>
</TermGroup>
</TermThrsh>
</DValue>
<DValue type="threshold" name="valThrsh2"></DValue>
<DValue value="From Parent" type="string" name="valMap"></DValue>
<DValue value="From Parent" type="string" name="valROI"></DValue>
<DValue value="0" type="int" name="iNumMaxObj"></DValue>
<DValue value="4" type="int" name="iVersion"></DValue>
<DValue value="-1" type="int" name="iOldLvl"></DValue>
<DValue value="0" type="int" name="iOldDsplLvl"></DValue>
<DValue value="0" type="int" name="iOldDsplNumLvl"></DValue>
</Params>
</Domain>
<SubProc></SubProc>
</ProcBase>
<ProcBase Name="classify water" bLoopChg="0" bExpand="1" bActive="1" bAutoName="0" bSubrtn="0" sComment="">
<LcnsInfo sLcnsId="" sPwd=""></LcnsInfo>
<vrblValMaxCycle>
<DValue value="1." type="double"></DValue>
</vrblValMaxCycle>
<Algorithm guid="A8BA5775-CC39-4194-9A6A-A64872EE1F81">
<Params></Params>
</Algorithm>
<Domain guid="CC9F2C30-4DB0-4ef2-B864-63560D1D6BF3">
<Params>
<DValue type="threshold" name="valThrsh"></DValue>
<DValue type="threshold" name="valThrsh2"></DValue>
<DValue value="From Parent" type="string" name="valMap"></DValue>
</Params>
</Domain>
<SubProc>
<ProcBase Name="glaciers with Rel. border to water > 0.4 and Rel. border to glaciers <= 0.1 at New Level: water" bLoopChg="0" bExpand="1" bActive="1" bAutoName="1" bSubrtn="0" sComment="">
<LcnsInfo sLcnsId="" sPwd=""></LcnsInfo>
<vrblValMaxCycle>
<DValue value="1." type="double"></DValue>
</vrblValMaxCycle>
<Algorithm guid="3AC44F21-C6B2-4804-9929-BB18BE6F2051">
<Params>
<DValue value="1" type="clssId" name="valClass"></DValue>
</Params>
</Algorithm>
<Domain guid="CED621BD-F4D1-4ffa-A2F6-DB2BB1913E8C">
<Params>
<DValue type="lvlName" name="valMapLvl">
<MapLvlProxy strName="New Level" bVrbl="0">

<Scope GUID="00000000-0000-0000-0000-000000000000"></Scope>
</MapLvlProxy>
</DValue>
<DValue type="vector" name="mClssFltr">
<Values>
<DValue value="3" type="clssId" indx="0"></DValue>
<DValue value="User defined" type="string" indx="1"></DValue>
</Values>
</DValue>
<DValue type="threshold" name="valThrsh">
<TermThrsh>
<TermGroup eJoint="2">
<TermCondition eCmpr="3" eBaseUnit="0" eJoint="0">
<ProcVrblVal1>
<DValue type="propDscrId">
<PropDscrId GUID="AA7CAC99-696D-4983-8F48-D07C4F816F2C" InstID="Rel. border to water"></PropDscrId>
</DValue>
</ProcVrblVal1>
<ProcVrblVal2>
<DValue value="0.40000000000000002" type="double"></DValue>
</ProcVrblVal2>
</TermCondition>
<TermCondition eCmpr="1" eBaseUnit="0" eJoint="2">
<ProcVrblVal1>
<DValue type="propDscrId">
<PropDscrId GUID="AA7CAC99-696D-4983-8F48-D07C4F816F2C" InstID="Rel. border to glaciers"></PropDscrId>
</DValue>
</ProcVrblVal1>
<ProcVrblVal2>
<DValue value="0.10000000000000001" type="double"></DValue>
</ProcVrblVal2>
</TermCondition>
</TermGroup>
</TermThrsh>
</DValue>
<DValue type="threshold" name="valThrsh2"></DValue>
<DValue value="From Parent" type="string" name="valMap"></DValue>
<DValue value="From Parent" type="string" name="valROI"></DValue>
<DValue value="0" type="int" name="iNumMaxObj"></DValue>
<DValue value="4" type="int" name="iVersion"></DValue>
<DValue value="-1" type="int" name="iOldLvl"></DValue>
<DValue value="0" type="int" name="iOldDsplLvl"></DValue>
<DValue value="0" type="int" name="iOldDsplNumLvl"></DValue>
</Params>
</Domain>
<SubProc></SubProc>
</ProcBase>
<ProcBase Name="classify glaciers" bLoopChg="0" bExpand="1" bActive="1" bAutoName="0" bSubrtn="0" sComment="">
<LcnsInfo sLcnsId="" sPwd=""></LcnsInfo>
<vrblValMaxCycle>
<DValue value="1." type="double"></DValue>
</vrblValMaxCycle>
<Algorithm guid="A8BA5775-CC39-4194-9A6A-A64872EE1F81">
<Params></Params>
</Algorithm>
<Domain guid="CC9F2C30-4DB0-4ef2-B864-63560D1D6BF3">
<Params>
<DValue type="threshold" name="valThrsh"></DValue>
<DValue type="threshold" name="valThrsh2"></DValue>
<DValue value="From Parent" type="string" name="valMap"></DValue>
</Params>
</Domain>
<SubProc>
<ProcBase Name="water with Rel. border to glaciers >= 0.4 and Rel. border to water < 0.1 and Mean Layer 2 > 0.5 at New Level: glaciers" bLoopChg="0" bExpand="1" bActive="1" bAutoName="1" bSubrtn="0" sComment="">
<LcnsInfo sLcnsId="" sPwd=""></LcnsInfo>
<vrblValMaxCycle>
<DValue value="1." type="double"></DValue>
</vrblValMaxCycle>
<Algorithm guid="3AC44F21-C6B2-4804-9929-BB18BE6F2051">
<Params>
<DValue value="3" type="clssId" name="valClass"></DValue>
</Params>
</Algorithm>
<Domain guid="CED621BD-F4D1-4ffa-A2F6-DB2BB1913E8C">
<Params>
<DValue type="lvlName" name="valMapLvl">
<MapLvlProxy strName="New Level" bVrbl="0">
<Scope GUID="00000000-0000-0000-0000-000000000000"></Scope>
</MapLvlProxy>
</DValue>
<DValue type="vector" name="mClssFltr">
<Values>
<DValue value="1" type="clssId" indx="0"></DValue>
<DValue value="User defined" type="string" indx="1"></DValue>
</Values>
</DValue>
<DValue type="threshold" name="valThrsh">
<TermThrsh>
<TermGroup eJoint="2">
<TermCondition eCmpr="4" eBaseUnit="0" eJoint="0">
<ProcVrblVal1>
<DValue type="propDscrId">
<PropDscrId GUID="AA7CAC99-696D-4983-8F48-D07C4F816F2C" InstID="Rel. border to glaciers"></PropDscrId>
</DValue>
</ProcVrblVal1>
<ProcVrblVal2>
<DValue value="0.40000000000000002" type="double"></DValue>
</ProcVrblVal2>
</TermCondition>
<TermCondition eCmpr="2" eBaseUnit="0" eJoint="0">
<ProcVrblVal1>
<DValue type="propDscrId">
<PropDscrId GUID="AA7CAC99-696D-4983-8F48-D07C4F816F2C" InstID="Rel. border to water"></PropDscrId>
</DValue>
</ProcVrblVal1>
<ProcVrblVal2>
<DValue value="0.10000000000000001" type="double"></DValue>
</ProcVrblVal2>
</TermCondition>
<TermCondition eCmpr="3" eBaseUnit="0" eJoint="2">
<ProcVrblVal1>
<DValue type="propDscrId">
<PropDscrId GUID="44411C83-609B-4758-93D3-FF62DF246855" InstID="Mean Layer 2"></PropDscrId>
</DValue>
</ProcVrblVal1>
<ProcVrblVal2>
<DValue value="0.5" type="double"></DValue>
</ProcVrblVal2>
</TermCondition>
</TermGroup>

```
</TermThrsh>
</DValue>
<DValue type="threshold" name="valThrsh2"></DValue>
<DValue value="From Parent" type="string" name="valMap"></DValue>
<DValue value="From Parent" type="string" name="valROI"></DValue>
<DValue value="0" type="int" name="iNumMaxObj"></DValue>
<DValue value="4" type="int" name="iVersion"></DValue>
<DValue value="-1" type="int" name="iOldLvl"></DValue>
<DValue value="0" type="int" name="iOldDsplLvl"></DValue>
<DValue value="0" type="int" name="iOldDsplNumLvl"></DValue>
</Params>
</Domain>
<SubProc></SubProc>
</ProcBase>
<ProcBase Name="do" bLoopChg="0" bExpand="1" bActive="1" bAutoName="1" bSubrtn="0" sComment="">
<LcnsInfo sLcnsId="" sPwd=""></LcnsInfo>
<vrblValMaxCycle>
<DValue value="1." type="double"></DValue>
</vrblValMaxCycle>
<Algorithm guid="A8BA5775-CC39-4194-9A6A-A64872EE1F81">
<Params></Params>
</Algorithm>
<Domain guid="CC9F2C30-4DB0-4ef2-B864-63560D1D6BF3">
<Params>
<DValue type="threshold" name="valThrsh"></DValue>
<DValue type="threshold" name="valThrsh2"></DValue>
<DValue value="From Parent" type="string" name="valMap"></DValue>
</Params>
</Domain>
<SubProc>
<ProcBase Name="rivers with Mean Layer 2 > 1  at  New Level: glaciers" bLoopChg="0" bExpand="1" bActive="1" bAutoName="1" bSubrtn="0" sComment="">
<LcnsInfo sLcnsId="" sPwd=""></LcnsInfo>
<vrblValMaxCycle>
<DValue value="1." type="double"></DValue>
</vrblValMaxCycle>
<Algorithm guid="3AC44F21-C6B2-4804-9929-BB18BE6F2051">
<Params>
<DValue value="3" type="clssId" name="valClass"></DValue>
</Params>
</Algorithm>
<Domain guid="CED621BD-F4D1-4ffa-A2F6-DB2BB1913E8C">
<Params>
<DValue type="lvlName" name="valMapLvl">
<MapLvlProxy strName="New Level" bVrbl="0">
<Scope GUID="00000000-0000-0000-0000-000000000000"></Scope>
</MapLvlProxy>
</DValue>
<DValue type="vector" name="mClssFltr">
<Values>
<DValue value="2" type="clssId" indx="0"></DValue>
<DValue value="User defined" type="string" indx="1"></DValue>
</Values>
</DValue>
<DValue type="threshold" name="valThrsh">
<TermThrsh>
<TermGroup eJoint="2">
<TermCondition eCmpr="3" eBaseUnit="0" eJoint="2">
<ProcVrblVal1>
<DValue type="propDscrId">
<PropDscrId GUID="44411C83-609B-4758-93D3-FF62DF246855" InstID="Mean Layer 2"></PropDscrId>
</DValue>
</ProcVrblVal1>
<ProcVrblVal2>
<DValue value="1." type="double"></DValue>
</ProcVrblVal2>
</TermCondition>
</TermGroup>
</TermThrsh>
</DValue>
<DValue type="threshold" name="valThrsh2"></DValue>
<DValue value="From Parent" type="string" name="valMap"></DValue>
<DValue value="From Parent" type="string" name="valROI"></DValue>
<DValue value="0" type="int" name="iNumMaxObj"></DValue>
<DValue value="4" type="int" name="iVersion"></DValue>
<DValue value="-1" type="int" name="iOldLvl"></DValue>
<DValue value="0" type="int" name="iOldDsplLvl"></DValue>
<DValue value="0" type="int" name="iOldDsplNumLvl"></DValue>
</Params>
</Domain>
<SubProc></SubProc>
</ProcBase>
<ProcBase Name="merge" bLoopChg="0" bExpand="1" bActive="1" bAutoName="0" bSubrtn="0" sComment="">
<LcnsInfo sLcnsId="" sPwd=""></LcnsInfo>
<vrblValMaxCycle>
<DValue value="1." type="double"></DValue>
</vrblValMaxCycle>
<Algorithm guid="A8BA5775-CC39-4194-9A6A-A64872EE1F81">
<Params></Params>
</Algorithm>
<Domain guid="CC9F2C30-4DB0-4ef2-B864-63560D1D6BF3">
<Params>
<DValue type="threshold" name="valThrsh"></DValue>
<DValue type="threshold" name="valThrsh2"></DValue>
<DValue value="From Parent" type="string" name="valMap"></DValue>
</Params>
</Domain>
<SubProc>
<ProcBase Name="water at  New Level: merge region" bLoopChg="0" bExpand="1" bActive="1" bAutoName="1" bSubrtn="0" sComment="">
<LcnsInfo sLcnsId="" sPwd=""></LcnsInfo>
<vrblValMaxCycle>
<DValue value="1." type="double"></DValue>
</vrblValMaxCycle>
<Algorithm guid="2328636B-BAD3-4f5d-B5AA-FC209A0BFB65">
<Params>
<DValue value="0" type="bool" name="bFsnUp"></DValue>
<DValue type="vector" name="vThmLayerFlags">
<Values></Values>
</DValue>
</Params>
</Algorithm>
<Domain guid="CED621BD-F4D1-4ffa-A2F6-DB2BB1913E8C">
<Params>
<DValue type="lvlName" name="valMapLvl">
<MapLvlProxy strName="New Level" bVrbl="0">
<Scope GUID="00000000-0000-0000-0000-000000000000"></Scope>
</MapLvlProxy>
</DValue>
<DValue type="vector" name="mClssFltr">
<Values>
<DValue value="1" type="clssId" indx="0"></DValue>
<DValue value="User defined" type="string" indx="1"></DValue>
```

```
</Values>
</DValue>
<DValue type="threshold" name="valThrsh"></DValue>
<DValue type="threshold" name="valThrsh2"></DValue>
<DValue value="From Parent" type="string" name="valMap"></DValue>
<DValue value="From Parent" type="string" name="valROI"></DValue>
<DValue value="0" type="int" name="iNumMaxObj"></DValue>
<DValue value="4" type="int" name="iVersion"></DValue>
<DValue value="-1" type="int" name="iOldLvl"></DValue>
<DValue value="0" type="int" name="iOldDsplLvl"></DValue>
<DValue value="0" type="int" name="iOldDsplNumLvl"></DValue>
</Params>
</Domain>
<SubProc></SubProc>
</ProcBase>
<ProcBase Name="do" bLoopChg="0" bExpand="1" bActive="1" bAutoName="1" bSubrtn="0" sComment="">
<LcnsInfo sLcnsId="" sPwd=""></LcnsInfo>
<vrblValMaxCycle>
<DValue value="1." type="double"></DValue>
</vrblValMaxCycle>
<Algorithm guid="A8BA5775-CC39-4194-9A6A-A64872EE1F81">
<Params></Params>
</Algorithm>
<Domain guid="CC9F2C30-4DB0-4ef2-B864-63560D1D6BF3">
<Params>
<DValue type="threshold" name="valThrsh"></DValue>
<DValue type="threshold" name="valThrsh2"></DValue>
<DValue value="From Parent" type="string" name="valMap"></DValue>
</Params>
</Domain>
<SubProc>
<ProcBase Name="water at  New Level: export object shapes to ObjectShapes" bLoopChg="0" bExpand="1" bActive="1" bAutoName="1" bSubrtn="0" sComment="">
<LcnsInfo sLcnsId="" sPwd=""></LcnsInfo>
<vrblValMaxCycle>
<DValue value="1." type="double"></DValue>
</vrblValMaxCycle>
<Algorithm guid="E8AAA2C4-4DCA-4684-A918-87E7C53CDC8D">
<Params>
<DValue value="0" type="int" name="eExportMode"></DValue>
<DValue value="ObjectShapes" type="string" name="strExportItem"></DValue>
<DValue value="-1" type="procVarId" name="vrblExportItem"></DValue>
<DValue value="E:\Landsat\2005\lakes\water_x.shp" type="string" name="strExportPath"></DValue>
<DValue value="0" type="bool" name="bExportSeries"></DValue>
<DValue value="&lt;?xml version=&quot;1.0&quot; encoding=&quot;UTF-8&quot;?>&#xA;&lt;ExportInfo SingleFilePerWksp=&quot;0&quot; SingleFilePerItem=&quot;1&quot; ExportItem=&quot;ObjectShapes&quot; ExportType=&quot;Vector&quot; DriverID=&quot;SHP&quot; ExportPath=&quot;E:\Landsat\2005\lakes\water_x.shp&quot;>&lt;/ExportInfo>" type="string" name="strExportItemInfo"></DValue>
<DValue value="temporary" type="string" name="valExportTempLayer"></DValue>
<DValue type="vector" name="vColInfo">
<Values></Values>
</DValue>
<DValue value="0" type="bool" name="bUseFtrList"></DValue>
<DValue value="Click to edit attribute table" type="string" name="EditAttrTbl"></DValue>
<DValue value="-1" type="procVarId" name="FeatureListAttrTbl"></DValue>
<DValue value="3" type="int" name="eGeomType"></DValue>
<DValue value="5" type="int" name="eExprtType"></DValue>
<DValue value="0" type="bool" name="bUse3DCoords"></DValue>
<DValue value="1" type="bool" name="bShpUseGeocoding"></DValue>
<DValue value="0" type="int" name="eCoordOrient"></DValue>
<DValue value="SHP" type="string" name="eExprtFormat"></DValue>
<DValue value="" type="string" name="featClassName"></DValue>
<DValue type="img_chnl" value="" name="pRefChnl"></DValue>
<DValue value="{:ArcSDE.Connect.Dir}\default.das" type="string" name="exprtStorageLocFile"></DValue>
<DValue value="0,2000000" type="string" name="spatDomainOffset"></DValue>
<DValue value="1000" type="string" name="spatDomainPrec"></DValue>
</Params>
</Algorithm>
<Domain guid="CED621BD-F4D1-4ffa-A2F6-DB2BB1913E8C">
<Params>
<DValue type="lvlName" name="valMapLvl">
<MapLvlProxy strName="New Level" bVrbl="0">
<Scope GUID="00000000-0000-0000-0000-000000000000"></Scope>
</MapLvlProxy>
</DValue>
<DValue type="vector" name="mClssFltr">
<Values>
<DValue value="1" type="clssId" indx="0"></DValue>
<DValue value="User defined" type="string" indx="1"></DValue>
</Values>
</DValue>
<DValue type="threshold" name="valThrsh"></DValue>
<DValue type="threshold" name="valThrsh2"></DValue>
<DValue value="From Parent" type="string" name="valMap"></DValue>
<DValue value="From Parent" type="string" name="valROI"></DValue>
<DValue value="0" type="int" name="iNumMaxObj"></DValue>
<DValue value="4" type="int" name="iVersion"></DValue>
<DValue value="-1" type="int" name="iOldLvl"></DValue>
<DValue value="0" type="int" name="iOldDsplLvl"></DValue>
<DValue value="0" type="int" name="iOldDsplNumLvl"></DValue>
</Params>
</Domain>
<SubProc></SubProc>
</ProcBase>
</SubProc>
</ProcBase>
</SubProc>
</ProcBase>
</SubProc>
</ProcBase>
</SubProc>
</ProcBase>
</SubProc>
</ProcBase>
</SubProc>
</ProcBase>
</SubProc>
</ProcBase>
</SubProc>
</ProcBase>
</SubProc>
</ProcBase>
</SubProc>
</ProcBase>
</SubProc>
</ProcBase>
</ProcessList>
<ExportedItems>
<item name="ObjectShapes" type="Vector" driver="SHP" ext="shp" path="E:\Landsat\2005\lakes\water_x.shp"></item>
</ExportedItems>
<LcnsIds></LcnsIds>
</eCog.Proc>
```

Appendix C

Code for delineating snow avalanche boundaries

Copy the code and save as *.dcp file to use it in eCognition Developer 9.1. Input data to use the code are: Layers 1, 2, and 3 – NIR image bands, Layer 4 – water index, Layer 5 – SD of water index, Layer 6 – vegetation index.


```
<?xml version="1.0" encoding="UTF-8"?>
<eCog.Proc UserName="korzeniowska" Company="" Copyright="" version="20140418" use-reproducable-poly="1" project-unit="5" engine-version="9.1.1" engine-build="2799" update-topology="0"
distance_calculation="CG" resampling_compatibility="0" ver="1">
<ruleset-info>
<name></name>
<author>Karolina</author>
<tags></tags>
<version></version>
<description></description>
<input></input>
<output></output>
</ruleset-info>
<ParamValueSetCntnr></ParamValueSetCntnr>
<ObjectDependencies>
<ImgLayers>
<ChnlProxyCntnr>
<Layers>
<ChnlProxy strName="Layer 1" flags="4">
<Assignment Chnl="0" MapName="main"></Assignment>
<LastAssignment Chnl="0" MapName="main"></LastAssignment>
<Scope GUID="00000000-0000-0000-0000-000000000000"></Scope>
</ChnlProxy>
<ChnlProxy strName="Layer 4" flags="4">
<Assignment Chnl="3" MapName="main"></Assignment>
<LastAssignment Chnl="3" MapName="main"></LastAssignment>
<Scope GUID="00000000-0000-0000-0000-000000000000"></Scope>
</ChnlProxy>
<ChnlProxy strName="Layer 5" flags="4">
<Assignment Chnl="4" MapName="main"></Assignment>
<LastAssignment Chnl="4" MapName="main"></LastAssignment>
<Scope GUID="00000000-0000-0000-0000-000000000000"></Scope>
</ChnlProxy>
<ChnlProxy strName="Layer 6" flags="4">
<Assignment Chnl="5" MapName="main"></Assignment>
<LastAssignment Chnl="5" MapName="main"></LastAssignment>
<Scope GUID="00000000-0000-0000-0000-000000000000"></Scope>
</ChnlProxy>
</Layers>
<Variables></Variables>
</ChnlProxyCntnr>
</ImgLayers>
<ThmLayers>
<ChnlProxyCntnr>
<Layers></Layers>
<Variables></Variables>
</ChnlProxyCntnr>
</ThmLayers>
<MapLvlProxyCntnr>
<MapLvlProxies>
<MapLvlProxy strName="New Level" bVrbl="0">
<Assignment MapLvl="2" MapName="main"></Assignment>
<Scope GUID="00000000-0000-0000-0000-000000000000"></Scope>
</MapLvlProxy>
<MapLvlProxy strName="Segmentation 1" bVrbl="0">
<Assignment MapLvl="1" MapName="main"></Assignment>
<Scope GUID="00000000-0000-0000-0000-000000000000"></Scope>
</MapLvlProxy>
</MapLvlProxies>
<MapLvlVrblValues></MapLvlVrblValues>
</MapLvlProxyCntnr>
<ProcVrblCntnr></ProcVrblCntnr>
<ClssHrchy EvalInvalid="1" MinProb="0.10000000000000001" NNSlope="0.20000000000000001" RdiResamplOptns="3">
<MapUnit>
<Map MapName="main" Unit="5"></Map>
</MapUnit>
<AllClss>
<Clss id="1" name="rough_snow" flag="0" iMaskID="-1" bUsePrntClr="0" dPrntClssBrghtns="0." termType="0" strUserName="Karolina" tChngTime="1476970041" bShow="0" Trans="0." sComment="">
<LcnsInfo sLcnsId="" sPwd=""></LcnsInfo>
<Scope GUID="00000000-0000-0000-0000-000000000000"></Scope>
<Color R="0" G="255" B="255"></Color>
<SharedInfo bShared="0" strInstGUID=""></SharedInfo>
</Clss>
<Clss id="2" name="vegetation" flag="0" iMaskID="-1" bUsePrntClr="0" dPrntClssBrghtns="0." termType="0" strUserName="Karolina" tChngTime="1476943566" bShow="0" Trans="0." sComment="">
<LcnsInfo sLcnsId="" sPwd=""></LcnsInfo>
<Scope GUID="00000000-0000-0000-0000-000000000000"></Scope>
<Color R="0" G="128" B="0"></Color>
```

<SharedInfo bShared="0" strInstGUID=""></SharedInfo>
</Clss>
<Clss id="3" name="veg_buffor" flag="0" iMaskID="-1" bUsePrntClr="0" dPrntClssBrghtns="0." termType="0" strUserName="Karolina" tChngTime="1476882917" bShow="0" Trans="0." sComment="">
<LcnsInfo sLcnsId="" sPwd=""></LcnsInfo>
<Scope GUID="00000000-0000-0000-0000-000000000000"></Scope>
<Color R="255" G="0" B="255"></Color>
<SharedInfo bShared="0" strInstGUID=""></SharedInfo>
</Clss>
<Clss id="4" name="dark_objects" flag="0" iMaskID="-1" bUsePrntClr="0" dPrntClssBrghtns="0." termType="0" strUserName="Karolina" tChngTime="1476968918" bShow="0" Trans="0." sComment="">
<LcnsInfo sLcnsId="" sPwd=""></LcnsInfo>
<Scope GUID="00000000-0000-0000-0000-000000000000"></Scope>
<Color R="0" G="0" B="128"></Color>
<SharedInfo bShared="0" strInstGUID=""></SharedInfo>
</Clss>
<Clss id="5" name="snow" flag="0" iMaskID="-1" bUsePrntClr="0" dPrntClssBrghtns="0." termType="0" strUserName="Karolina" tChngTime="1477290012" bShow="0" Trans="0." sComment="">
<LcnsInfo sLcnsId="" sPwd=""></LcnsInfo>
<Scope GUID="00000000-0000-0000-0000-000000000000"></Scope>
<Color R="255" G="192" B="87"></Color>
<SharedInfo bShared="0" strInstGUID=""></SharedInfo>
</Clss>
<Clss id="6" name="test" flag="0" iMaskID="-1" bUsePrntClr="0" dPrntClssBrghtns="0." termType="0" strUserName="Karolina" tChngTime="1477580709" bShow="0" Trans="0." sComment="">
<LcnsInfo sLcnsId="" sPwd=""></LcnsInfo>
<Scope GUID="00000000-0000-0000-0000-000000000000"></Scope>
<Color R="255" G="0" B="0"></Color>
<SharedInfo bShared="0" strInstGUID=""></SharedInfo>
</Clss>
</AllClss>
<PropTree version="20100426">
<AllProps>
<PropDscr Flag="2" strUserName="Karolina" tChngTime="1476866023" group_id="cntrnghb.pixel.chnl.object.prop">
<PropDscrId GUID="F166AA8A-C445-4c0d-8598-84720BE03D97" InstID="Contrast to neighbor pixels Layer 4 (0)"></PropDscrId>
<LcnsInfo sLcnsId="" sPwd=""></LcnsInfo>
<Scope GUID="00000000-0000-0000-0000-000000000000"></Scope>
<Params>
<DValue type="img_chnl" value="Layer 4" scope="" name="valChnl"></DValue>
<DValue value="0" type="int" name="iDist"></DValue>
</Params>
</PropDscr>
<PropDscr Flag="2" strUserName="Karolina" tChngTime="1476866042" group_id="cntrnghb.pixel.chnl.object.prop">
<PropDscrId GUID="F166AA8A-C445-4c0d-8598-84720BE03D97" InstID="Contrast to neighbor pixels Layer 4 (1)"></PropDscrId>
<LcnsInfo sLcnsId="" sPwd=""></LcnsInfo>
<Scope GUID="00000000-0000-0000-0000-000000000000"></Scope>
<Params>
<DValue type="img_chnl" value="Layer 4" scope="" name="valChnl"></DValue>
<DValue value="1" type="int" name="iDist"></DValue>
</Params>
</PropDscr>
<PropDscr Flag="2" strUserName="Karolina" tChngTime="1476865937" group_id="brdrcntrst.pixel.chnl.object.prop">
<PropDscrId GUID="EA1C8F1D-A983-4860-A019-04927B30BFFF" InstID="Border Contrast Layer 4"></PropDscrId>
<LcnsInfo sLcnsId="" sPwd=""></LcnsInfo>
<Scope GUID="00000000-0000-0000-0000-000000000000"></Scope>
<Params>
<DValue type="img_chnl" value="Layer 4" scope="" name="valChnl"></DValue>
</Params>
</PropDscr>
<PropDscr Flag="2" strUserName="Karolina" tChngTime="1476873693" group_id="dirmean.shape.texture.object.prop">
<PropDscrId GUID="E2921CE0-1920-4cde-8A23-E00C3C4FBCB9" InstID="Direction of sub-objects: mean (1)"></PropDscrId>
<LcnsInfo sLcnsId="" sPwd=""></LcnsInfo>
<Scope GUID="00000000-0000-0000-0000-000000000000"></Scope>
<Params>
<DValue value="1" type="int" name="iDist"></DValue>
</Params>
</PropDscr>
<PropDscr Flag="2" strUserName="Karolina" tChngTime="1476866129" group_id="edge.pixel.chnl.object.prop">
<PropDscrId GUID="BDA5AE6B-A63C-467d-A1AA-2B9D8347286C" InstID="Edge Contrast of neighbor pixels (Prototype) Layer 4 (3)"></PropDscrId>
<LcnsInfo sLcnsId="" sPwd=""></LcnsInfo>
<Scope GUID="00000000-0000-0000-0000-000000000000"></Scope>
<Params>
<DValue type="img_chnl" value="Layer 4" scope="" name="valChnl"></DValue>
<DValue value="3" type="int" name="iDist"></DValue>
</Params>
</PropDscr>
<PropDscr Flag="65538" strUserName="Karolina" tChngTime="1476426603" group_id="ext.geom.object.prop">
<PropDscrId GUID="AF0D7167-ADE8-4240-AAA4-AC2C188E9AF5" InstID="Number of pixels"></PropDscrId>
<LcnsInfo sLcnsId="" sPwd=""></LcnsInfo>
<Scope GUID="00000000-0000-0000-0000-000000000000"></Scope>
<Params></Params>
</PropDscr>
<PropDscr Flag="2" strUserName="Karolina" tChngTime="1477028025" group_id="relbrdr.nghb.class.prop">
<PropDscrId GUID="AA7CAC99-696D-4983-8F48-D07C4F816F2C" InstID="Rel. border to rough_snow"></PropDscrId>
<LcnsInfo sLcnsId="" sPwd=""></LcnsInfo>
<Scope GUID="00000000-0000-0000-0000-000000000000"></Scope>
<Params>
<DValue value="1" type="clssId" name="valClss"></DValue>
</Params>
</PropDscr>
<PropDscr Flag="2" strUserName="Karolina" tChngTime="1477384127" group_id="relbrdr.nghb.class.prop">
<PropDscrId GUID="AA7CAC99-696D-4983-8F48-D07C4F816F2C" InstID="Rel. border to test"></PropDscrId>
<LcnsInfo sLcnsId="" sPwd=""></LcnsInfo>
<Scope GUID="00000000-0000-0000-0000-000000000000"></Scope>
<Params>
<DValue value="6" type="clssId" name="valClss"></DValue>
</Params>
</PropDscr>
<PropDscr Flag="2" strUserName="Karolina" tChngTime="1477384783" group_id="relbrdr.nghb.class.prop">
<PropDscrId GUID="AA7CAC99-696D-4983-8F48-D07C4F816F2C" InstID="Rel. border to snow"></PropDscrId>
<LcnsInfo sLcnsId="" sPwd=""></LcnsInfo>
<Scope GUID="00000000-0000-0000-0000-000000000000"></Scope>
<Params>
<DValue value="5" type="clssId" name="valClss"></DValue>
</Params>
</PropDscr>
<PropDscr Flag="2" strUserName="korzeniowska" tChngTime="1480338375" group_id="num.nghb.class.prop">
<PropDscrId GUID="7D1F1A4B-9BFD-4b29-BA08-AA370D63669B" InstID="Number of snow (0)"></PropDscrId>
<LcnsInfo sLcnsId="" sPwd=""></LcnsInfo>
<Scope GUID="00000000-0000-0000-0000-000000000000"></Scope>
<Params>
<DValue value="5" type="clssId" name="valClss"></DValue>
<DValue value="0" type="int" name="iDist"></DValue>
</Params>
</PropDscr>
<PropDscr Flag="2" strUserName="Karolina" tChngTime="1476867099" group_id="num.nghb.class.prop">
<PropDscrId GUID="7D1F1A4B-9BFD-4b29-BA08-AA370D63669B" InstID="Number of water (0)"></PropDscrId>
<LcnsInfo sLcnsId="" sPwd=""></LcnsInfo>
<Scope GUID="00000000-0000-0000-0000-000000000000"></Scope>
<Params>
<DValue value="1" type="clssId" name="valClss"></DValue>
<DValue value="0" type="int" name="iDist"></DValue>
</Params>
</PropDscr>
<PropDscr Flag="2" strUserName="Karolina" tChngTime="1476884311" group_id="num.nghb.class.prop">

<PropDscrId GUID="7D1F1A4B-9BFD-4b29-BA08-AA370D63669B" InstID="Number of veg_buffor (0)"></PropDscrId>
<LcnsInfo sLcnsId="" sPwd=""></LcnsInfo>
<Scope GUID="00000000-0000-0000-0000-000000000000"></Scope>
<Params>
<DValue value="3" type="clssId" name="valClss"></DValue>
<DValue value="0" type="int" name="iDist"></DValue>
</Params>
</PropDscr>
<PropDscr Flag="2" strUserName="Karolina" tChngTime="1476867490" group_id="mean.chnl.object.prop">
<PropDscrId GUID="44411C83-609B-4758-93D3-FF62DF246855" InstID="Mean Layer 6"></PropDscrId>
<LcnsInfo sLcnsId="" sPwd=""></LcnsInfo>
<Scope GUID="00000000-0000-0000-0000-000000000000"></Scope>
<Params>
<DValue type="img_chnl" value="Layer 6" scope="" name="valChnl"></DValue>
</Params>
</PropDscr>
<PropDscr Flag="2" strUserName="Karolina" tChngTime="1476867271" group_id="mean.chnl.object.prop">
<PropDscrId GUID="44411C83-609B-4758-93D3-FF62DF246855" InstID="Mean Layer 5"></PropDscrId>
<LcnsInfo sLcnsId="" sPwd=""></LcnsInfo>
<Scope GUID="00000000-0000-0000-0000-000000000000"></Scope>
<Params>
<DValue type="img_chnl" value="Layer 5" scope="" name="valChnl"></DValue>
</Params>
</PropDscr>
<PropDscr Flag="2" strUserName="Karolina" tChngTime="1476426936" group_id="mean.chnl.object.prop">
<PropDscrId GUID="44411C83-609B-4758-93D3-FF62DF246855" InstID="Mean Layer 4"></PropDscrId>
<LcnsInfo sLcnsId="" sPwd=""></LcnsInfo>
<Scope GUID="00000000-0000-0000-0000-000000000000"></Scope>
<Params>
<DValue type="img_chnl" value="Layer 4" scope="" name="valChnl"></DValue>
</Params>
</PropDscr>
<PropDscr Flag="2" strUserName="Karolina" tChngTime="1476964170" group_id="mean.chnl.object.prop">
<PropDscrId GUID="44411C83-609B-4758-93D3-FF62DF246855" InstID="Mean Layer 1"></PropDscrId>
<LcnsInfo sLcnsId="" sPwd=""></LcnsInfo>
<Scope GUID="00000000-0000-0000-0000-000000000000"></Scope>
<Params>
<DValue type="img_chnl" value="Layer 1" scope="" name="valChnl"></DValue>
</Params>
</PropDscr>
<PropDscr Flag="2" strUserName="korzeniowska" tChngTime="1480401313" group_id="exist.nghb.class.prop">
<PropDscrId GUID="3A00174B-817F-4dc5-9E59-0A32562CBDDA" InstID="Existence of rough_snow (0)"></PropDscrId>
<LcnsInfo sLcnsId="" sPwd=""></LcnsInfo>
<Scope GUID="00000000-0000-0000-0000-000000000000"></Scope>
<Params>
<DValue value="1" type="clssId" name="valClss"></DValue>
<DValue value="0" type="int" name="iDist"></DValue>
</Params>
</PropDscr>
<PropDscr Flag="2" strUserName="Karolina" tChngTime="1476944091" group_id="exist.nghb.class.prop">
<PropDscrId GUID="3A00174B-817F-4dc5-9E59-0A32562CBDDA" InstID="Existence of dark_objects (0)"></PropDscrId>
<LcnsInfo sLcnsId="" sPwd=""></LcnsInfo>
<Scope GUID="00000000-0000-0000-0000-000000000000"></Scope>
<Params>
<DValue value="4" type="clssId" name="valClss"></DValue>
<DValue value="0" type="int" name="iDist"></DValue>
</Params>
</PropDscr>
<PropDscr Flag="2" strUserName="Karolina" tChngTime="1476875391" group_id="exist.nghb.class.prop">
<PropDscrId GUID="3A00174B-817F-4dc5-9E59-0A32562CBDDA" InstID="Existence of water (2)"></PropDscrId>
<LcnsInfo sLcnsId="" sPwd=""></LcnsInfo>
<Scope GUID="00000000-0000-0000-0000-000000000000"></Scope>
<Params>
<DValue value="1" type="clssId" name="valClss"></DValue>
<DValue value="2" type="int" name="iDist"></DValue>
</Params>
</PropDscr>
<PropDscr Flag="2" strUserName="Karolina" tChngTime="1476879031" group_id="exist.nghb.class.prop">
<PropDscrId GUID="3A00174B-817F-4dc5-9E59-0A32562CBDDA" InstID="Existence of vegetation (0)"></PropDscrId>
<LcnsInfo sLcnsId="" sPwd=""></LcnsInfo>
<Scope GUID="00000000-0000-0000-0000-000000000000"></Scope>
<Params>
<DValue value="2" type="clssId" name="valClss"></DValue>
<DValue value="0" type="int" name="iDist"></DValue>
</Params>
</PropDscr>
<PropDscr Flag="2" strUserName="Karolina" tChngTime="1476969143" group_id="exist.nghb.class.prop">
<PropDscrId GUID="3A00174B-817F-4dc5-9E59-0A32562CBDDA" InstID="Existence of veg_buffor (0)"></PropDscrId>
<LcnsInfo sLcnsId="" sPwd=""></LcnsInfo>
<Scope GUID="00000000-0000-0000-0000-000000000000"></Scope>
<Params>
<DValue value="3" type="clssId" name="valClss"></DValue>
<DValue value="0" type="int" name="iDist"></DValue>
</Params>
</PropDscr>
<PropDscr Flag="2" strUserName="Karolina" tChngTime="1476426603" group_id="mean.chnl.object.prop">
<PropDscrId GUID="16B7A5B4-D807-4ab1-B769-D536B3C26B20" InstID="Brightness"></PropDscrId>
<LcnsInfo sLcnsId="" sPwd=""></LcnsInfo>
<Scope GUID="00000000-0000-0000-0000-000000000000"></Scope>
<Params></Params>
</PropDscr>
<PropDscr Flag="65536" strUserName="Karolina" tChngTime="1476426603" group_id="ext.geom.object.prop">
<PropDscrId GUID="03E04ED0-94DD-45ee-801E-14D70E6E2417" InstID="Area"></PropDscrId>
<LcnsInfo sLcnsId="" sPwd=""></LcnsInfo>
<Scope GUID="00000000-0000-0000-0000-000000000000"></Scope>
<DUnitInfo Conversion="0" UnitType="1" Dim="2"></DUnitInfo>
<Params></Params>
</PropDscr>
</AllProps>
<UserGroups></UserGroups>
</PropTree>
<Brightness>
<Map MapName="main">
<ChnlWghtBrght>
<BrghtWght val="1." chnl="0"></BrghtWght>
<BrghtWght val="1." chnl="1"></BrghtWght>
<BrghtWght val="1." chnl="2"></BrghtWght>
<BrghtWght val="0." chnl="3"></BrghtWght>
<BrghtWght val="0." chnl="4"></BrghtWght>
<BrghtWght val="0." chnl="5"></BrghtWght>
</ChnlWghtBrght>
</Map>
</Brightness>
<AllVrblClss></AllVrblClss>
<AllSubClss>
<Clss Id="1" PrfdGrp="1">
<SubClss></SubClss>
<SubGrp></SubGrp>
</Clss>
<Clss Id="2" PrfdGrp="2">
<SubClss></SubClss>

<SubGrp></SubGrp>
</Clss>
<Clss Id="3" PrfdGrp="3">
<SubClss></SubClss>
<SubGrp></SubGrp>
</Clss>
<Clss Id="4" PrfdGrp="4">
<SubClss></SubClss>
<SubGrp></SubGrp>
</Clss>
<Clss Id="5" PrfdGrp="5">
<SubClss></SubClss>
<SubGrp></SubGrp>
</Clss>
<Clss Id="6" PrfdGrp="6">
<SubClss></SubClss>
<SubGrp></SubGrp>
</Clss>
</AllSubClss>
<AllTerm>
<Term TermEvalType="0">
<TermBase ClssId="1" flags="0" sComment="">
<Weight>
<DValue value="1" type="int"></DValue>
</Weight>
</TermBase>
</Term>
<Term TermEvalType="0">
<TermBase ClssId="2" flags="0" sComment="">
<Weight>
<DValue value="1" type="int"></DValue>
</Weight>
</TermBase>
</Term>
<Term TermEvalType="0">
<TermBase ClssId="3" flags="0" sComment="">
<Weight>
<DValue value="1" type="int"></DValue>
</Weight>
</TermBase>
</Term>
<Term TermEvalType="0">
<TermBase ClssId="4" flags="0" sComment="">
<Weight>
<DValue value="1" type="int"></DValue>
</Weight>
</TermBase>
</Term>
<Term TermEvalType="0">
<TermBase ClssId="5" flags="0" sComment="">
<Weight>
<DValue value="1" type="int"></DValue>
</Weight>
</TermBase>
</Term>
<Term TermEvalType="0">
<TermBase ClssId="6" flags="0" sComment="">
<Weight>
<DValue value="1" type="int"></DValue>
</Weight>
</TermBase>
</Term>
</AllTerm>
</ClssHrchy>
<MapVrblCntnr></MapVrblCntnr>
<FtrListVrblCntnr></FtrListVrblCntnr>
<CoordVrblCntnr></CoordVrblCntnr>
<ROIVrblCntnr></ROIVrblCntnr>
<ImgObjListVrblCntnr></ImgObjListVrblCntnr>
<ArrayCntnr>
<Arrays></Arrays>
<ArrayVrbls></ArrayVrbls>
</ArrayCntnr>
<Smpls>
<AllClss>
<SmplList ClssId="1"></SmplList>
<SmplList ClssId="2"></SmplList>
<SmplList ClssId="3"></SmplList>
<SmplList ClssId="4"></SmplList>
<SmplList ClssId="5"></SmplList>
<SmplList ClssId="6"></SmplList>
</AllClss>
<AllProp></AllProp>
</Smpls>
<plugin-list>
<plugin name="eCognition Internal Process Algorithms" version="0.1"></plugin>
<plugin name="eCognition Internal Export Process Algorithms" version="0.1"></plugin>
<plugin name="eCognition Basic Process Algorithms" version="0.1"></plugin>
</plugin-list>
</ObjectDependencies>
<CustProcAlgrList></CustProcAlgrList>
<ProcessList>
<ProcBase Name="Chessboard segmentation" bLoopChg="0" bExpand="1" bActive="1" bAutoName="0" bSubrtn="0" sComment="">
<LcnsInfo sLcnsId="" sPwd=""></LcnsInfo>
<vrblValMaxCycle>
<DValue value="1." type="double"></DValue>
</vrblValMaxCycle>
<Algorithm guid="A8BA5775-CC39-4194-9A6A-A64872EE1F81">
<Params></Params>
</Algorithm>
<Domain guid="CC9F2C30-4DB0-4ef2-B864-63560D1D6BF3">
<Params>
<DValue type="threshold" name="valThrsh"></DValue>
<DValue type="threshold" name="valThrsh2"></DValue>
<DValue value="From Parent" type="string" name="valMap"></DValue>
</Params>
</Domain>
<SubProc>
<ProcBase Name="chess board: 1 creating 'New Level'" bLoopChg="0" bExpand="1" bActive="1" bAutoName="1" bSubrtn="0" sComment="">
<LcnsInfo sLcnsId="" sPwd=""></LcnsInfo>
<vrblValMaxCycle>
<DValue value="1." type="double"></DValue>
</vrblValMaxCycle>
<Algorithm guid="0F96C846-956C-405f-AC42-81EBA4D1A755">
<Params>
<DValue value="1" type="int" name="vrblObjSize"></DValue>
<DValue type="lvlName" name="valMapLvl">
<MapLvlProxy strName="New Level" bVrbl="0">
<Assignment MapLvl="2" MapName="main"></Assignment>
<Scope GUID="00000000-0000-0000-0000-000000000000"></Scope>
</MapLvlProxy>

```
</DValue>
<DValue value="1" type="bool" name="bDoOverwrite"></DValue>
<DValue type="vector" name="vGisChnlProxy">
<Values></Values>
</DValue>
</Params>
</Algorithm>
<Domain guid="682A3AA1-9F4F-4dae-9E44-5015DF867712">
<Params>
<DValue type="threshold" name="valThrsh"></DValue>
<DValue type="threshold" name="valThrsh2"></DValue>
<DValue value="From Parent" type="string" name="valMap"></DValue>
</Params>
</Domain>
<SubProc></SubProc>
</ProcBase>
<ProcBase Name="at  New Level: copy creating 'Segmentation 1' above" bLoopChg="0" bExpand="1" bActive="1" bAutoName="1" bSubrtn="0" sComment="">
<LcnsInfo sLcnsId="" sPwd=""></LcnsInfo>
<vrblValMaxCycle>
<DValue value="1." type="double"></DValue>
</vrblValMaxCycle>
<Algorithm guid="422F931B-FB82-4853-A773-2A821FE23893">
<Params>
<DValue type="lvlName" name="valMapLvl">
<MapLvlProxy strName="Segmentation 1" bVrbl="0">
<Assignment MapLvl="1" MapName="main"></Assignment>
<Scope GUID="00000000-0000-0000-0000-000000000000"></Scope>
</MapLvlProxy>
</DValue>
<DValue value="1" type="bool" name="bUp"></DValue>
</Params>
</Algorithm>
<Domain guid="CED621BD-F4D1-4ffa-A2F6-DB2BB1913E8C">
<Params>
<DValue type="lvlName" name="valMapLvl">
<MapLvlProxy strName="New Level" bVrbl="0">
<Assignment MapLvl="2" MapName="main"></Assignment>
<Scope GUID="00000000-0000-0000-0000-000000000000"></Scope>
</MapLvlProxy>
</DValue>
<DValue type="vector" name="mClssFltr">
<Values>
<DValue value="Disabled" type="string" indx="0"></DValue>
</Values>
</DValue>
<DValue type="threshold" name="valThrsh"></DValue>
<DValue type="threshold" name="valThrsh2"></DValue>
<DValue value="From Parent" type="string" name="valMap"></DValue>
<DValue value="From Parent" type="string" name="valROI"></DValue>
<DValue value="0" type="int" name="iNumMaxObj"></DValue>
<DValue value="4" type="int" name="iVersion"></DValue>
<DValue value="-1" type="int" name="iOldLvl"></DValue>
<DValue value="0" type="int" name="iOldDsplLvl"></DValue>
<DValue value="0" type="int" name="iOldDsplNumLvl"></DValue>
</Params>
</Domain>
<SubProc></SubProc>
</ProcBase>
<ProcBase Name="find dark objects and vegetation" bLoopChg="0" bExpand="1" bActive="1" bAutoName="0" bSubrtn="0" sComment="">
<LcnsInfo sLcnsId="" sPwd=""></LcnsInfo>
<vrblValMaxCycle>
<DValue value="1." type="double"></DValue>
</vrblValMaxCycle>
<Algorithm guid="A8BA5775-CC39-4194-9A6A-A64872EE1F81">
<Params></Params>
</Algorithm>
<Domain guid="CC9F2C30-4DB0-4ef2-B864-63560D1D6BF3">
<Params>
<DValue type="threshold" name="valThrsh"></DValue>
<DValue type="threshold" name="valThrsh2"></DValue>
<DValue value="From Parent" type="string" name="valMap"></DValue>
</Params>
</Domain>
<SubProc>
<ProcBase Name="unclassified with Mean Layer 6 > 127  at  Segmentation 1: vegetation" bLoopChg="0" bExpand="1" bActive="1" bAutoName="1" bSubrtn="0" sComment="">
<LcnsInfo sLcnsId="" sPwd=""></LcnsInfo>
<vrblValMaxCycle>
<DValue value="1." type="double"></DValue>
</vrblValMaxCycle>
<Algorithm guid="3AC44F21-C6B2-4804-9929-BB18BE6F2051">
<Params>
<DValue value="2" type="clssId" name="valClass"></DValue>
</Params>
</Algorithm>
<Domain guid="CED621BD-F4D1-4ffa-A2F6-DB2BB1913E8C">
<Params>
<DValue type="lvlName" name="valMapLvl">
<MapLvlProxy strName="Segmentation 1" bVrbl="0">
<Assignment MapLvl="1" MapName="main"></Assignment>
<Scope GUID="00000000-0000-0000-0000-000000000000"></Scope>
</MapLvlProxy>
</DValue>
<DValue type="vector" name="mClssFltr">
<Values>
<DValue value="Unclsfy" type="string" indx="0"></DValue>
<DValue value="User defined" type="string" indx="1"></DValue>
</Values>
</DValue>
<DValue type="threshold" name="valThrsh">
<TermThrsh>
<TermGroup eJoint="2">
<TermCondition eCmpr="3" eBaseUnit="0" eJoint="2">
<ProcVrblVal1>
<DValue type="propDscrId">
<PropDscrId GUID="44411C83-609B-4758-93D3-FF62DF246855" InstID="Mean Layer 6"></PropDscrId>
</DValue>
</ProcVrblVal1>
<ProcVrblVal2>
<DValue value="127." type="double"></DValue>
</ProcVrblVal2>
</TermCondition>
</TermGroup>
</TermThrsh>
</DValue>
<DValue type="threshold" name="valThrsh2"></DValue>
<DValue value="From Parent" type="string" name="valMap"></DValue>
<DValue value="From Parent" type="string" name="valROI"></DValue>
<DValue value="0" type="int" name="iNumMaxObj"></DValue>
<DValue value="4" type="int" name="iVersion"></DValue>
<DValue value="-1" type="int" name="iOldLvl"></DValue>
<DValue value="0" type="int" name="iOldDsplLvl"></DValue>
```

```
<DValue value="0" type="int" name="iOldDsplNumLvl"></DValue>
</Params>
</Domain>
<SubProc></SubProc>
</ProcBase>
<ProcBase Name="unclassified with Brightness &lt; 4000  at  Segmentation 1: dark_objects" bLoopChg="0" bExpand="1" bActive="1" bAutoName="1" bSubrtn="0" sComment="">
<LcnsInfo sLcnsId="" sPwd=""></LcnsInfo>
<vrblValMaxCycle>
<DValue value="1." type="double"></DValue>
</vrblValMaxCycle>
<Algorithm guid="3AC44F21-C6B2-4804-9929-BB18BE6F2051">
<Params>
<DValue value="4" type="clssId" name="valClass"></DValue>
</Params>
</Algorithm>
<Domain guid="CED621BD-F4D1-4ffa-A2F6-DB2BB1913E8C">
<Params>
<DValue type="lvlName" name="valMapLvl">
<MapLvlProxy strName="Segmentation 1" bVrbl="0">
<Assignment MapLvl="1" MapName="main"></Assignment>
<Scope GUID="00000000-0000-0000-0000-000000000000"></Scope>
</MapLvlProxy>
</DValue>
<DValue type="vector" name="mClssFltr">
<Values>
<DValue value="Unclsfy" type="string" indx="0"></DValue>
<DValue value="User defined" type="string" indx="1"></DValue>
</Values>
</DValue>
<DValue type="threshold" name="valThrsh">
<TermThrsh>
<TermGroup eJoint="2">
<TermCondition eCmpr="2" eBaseUnit="0" eJoint="2">
<ProcVrblVal1>
<DValue type="propDscrId">
<PropDscrId GUID="16B7A5B4-D807-4ab1-B769-D536B3C26B20" InstID="Brightness"></PropDscrId>
</DValue>
</ProcVrblVal1>
<ProcVrblVal2>
<DValue value="4000." type="double"></DValue>
</ProcVrblVal2>
</TermCondition>
</TermGroup>
</TermThrsh>
</DValue>
<DValue type="threshold" name="valThrsh2"></DValue>
<DValue value="From Parent" type="string" name="valMap"></DValue>
<DValue value="From Parent" type="string" name="valROI"></DValue>
<DValue value="0" type="int" name="iNumMaxObj"></DValue>
<DValue value="4" type="int" name="iVersion"></DValue>
<DValue value="-1" type="int" name="iOldLvl"></DValue>
<DValue value="0" type="int" name="iOldDsplLvl"></DValue>
<DValue value="0" type="int" name="iOldDsplNumLvl"></DValue>
</Params>
</Domain>
<SubProc></SubProc>
</ProcBase>
<ProcBase Name="create a buffor around dark objects and vegetation" bLoopChg="0" bExpand="1" bActive="1" bAutoName="0" bSubrtn="0" sComment="">
<LcnsInfo sLcnsId="" sPwd=""></LcnsInfo>
<vrblValMaxCycle>
<DValue value="1." type="double"></DValue>
</vrblValMaxCycle>
<Algorithm guid="A8BA5775-CC39-4194-9A6A-A64872EE1F81">
<Params></Params>
</Algorithm>
<Domain guid="CC9F2C30-4DB0-4ef2-B864-63560D1D6BF3">
<Params>
<DValue type="threshold" name="valThrsh"></DValue>
<DValue type="threshold" name="valThrsh2"></DValue>
<DValue value="From Parent" type="string" name="valMap"></DValue>
</Params>
</Domain>
<SubProc>
<ProcBase Name="unclassified with Existence of vegetation (0) > 0  or Existence of dark_objects (0) > 0  at  Segmentation 1: veg_buffor" bLoopChg="0" bExpand="1" bActive="1" bAutoName="1" bSubrtn="0"
sComment="">
<LcnsInfo sLcnsId="" sPwd=""></LcnsInfo>
<vrblValMaxCycle>
<DValue value="1." type="double"></DValue>
</vrblValMaxCycle>
<Algorithm guid="3AC44F21-C6B2-4804-9929-BB18BE6F2051">
<Params>
<DValue value="3" type="clssId" name="valClass"></DValue>
</Params>
</Algorithm>
<Domain guid="CED621BD-F4D1-4ffa-A2F6-DB2BB1913E8C">
<Params>
<DValue type="lvlName" name="valMapLvl">
<MapLvlProxy strName="Segmentation 1" bVrbl="0">
<Assignment MapLvl="1" MapName="main"></Assignment>
<Scope GUID="00000000-0000-0000-0000-000000000000"></Scope>
</MapLvlProxy>
</DValue>
<DValue type="vector" name="mClssFltr">
<Values>
<DValue value="Unclsfy" type="string" indx="0"></DValue>
<DValue value="User defined" type="string" indx="1"></DValue>
</Values>
</DValue>
<DValue type="threshold" name="valThrsh">
<TermThrsh>
<TermGroup eJoint="2">
<TermCondition eCmpr="3" eBaseUnit="0" eJoint="1">
<ProcVrblVal1>
<DValue type="propDscrId">
<PropDscrId GUID="3A00174B-817F-4dc5-9E59-0A32562CBDDA" InstID="Existence of vegetation (0)"></PropDscrId>
</DValue>
</ProcVrblVal1>
<ProcVrblVal2>
<DValue value="0." type="double"></DValue>
</ProcVrblVal2>
</TermCondition>
<TermCondition eCmpr="3" eBaseUnit="0" eJoint="2">
<ProcVrblVal1>
<DValue type="propDscrId">
<PropDscrId GUID="3A00174B-817F-4dc5-9E59-0A32562CBDDA" InstID="Existence of dark_objects (0)"></PropDscrId>
</DValue>
</ProcVrblVal1>
<ProcVrblVal2>
<DValue value="0." type="double"></DValue>
</ProcVrblVal2>
</TermCondition>
```

```
</TermGroup>
</TermThrsh>
</DValue>
<DValue type="threshold" name="valThrsh2"></DValue>
<DValue value="From Parent" type="string" name="valMap"></DValue>
<DValue value="From Parent" type="string" name="valROI"></DValue>
<DValue value="0" type="int" name="iNumMaxObj"></DValue>
<DValue value="4" type="int" name="iVersion"></DValue>
<DValue value="-1" type="int" name="iOldLvl"></DValue>
<DValue value="0" type="int" name="iOldDsplLvl"></DValue>
<DValue value="0" type="int" name="iOldDsplNumLvl"></DValue>
</Params>
</Domain>
<SubProc></SubProc>
</ProcBase>
<ProcBase Name="dark_objects at  Segmentation 1: merge region" bLoopChg="0" bExpand="1" bActive="1" bAutoName="1" bSubrtn="0" sComment="">
<LcnsInfo sLcnsId="" sPwd=""></LcnsInfo>
<vrblValMaxCycle>
<DValue value="1." type="double"></DValue>
</vrblValMaxCycle>
<Algorithm guid="2328636B-BAD3-4f5d-B5AA-FC209A0BFB65">
<Params>
<DValue value="0" type="bool" name="bFsnUp"></DValue>
<DValue type="vector" name="vThmLayerFlags">
<Values></Values>
</DValue>
</Params>
</Algorithm>
<Domain guid="CED621BD-F4D1-4ffa-A2F6-DB2BB1913E8C">
<Params>
<DValue type="lvlName" name="valMapLvl">
<MapLvlProxy strName="Segmentation 1" bVrbl="0">
<Assignment MapLvl="1" MapName="main"></Assignment>
<Scope GUID="00000000-0000-0000-0000-000000000000"></Scope>
</MapLvlProxy>
</DValue>
<DValue type="vector" name="mClssFltr">
<Values>
<DValue value="4" type="clssId" indx="0"></DValue>
<DValue value="User defined" type="string" indx="1"></DValue>
</Values>
</DValue>
<DValue type="threshold" name="valThrsh"></DValue>
<DValue type="threshold" name="valThrsh2"></DValue>
<DValue value="From Parent" type="string" name="valMap"></DValue>
<DValue value="From Parent" type="string" name="valROI"></DValue>
<DValue value="0" type="int" name="iNumMaxObj"></DValue>
<DValue value="4" type="int" name="iVersion"></DValue>
<DValue value="-1" type="int" name="iOldLvl"></DValue>
<DValue value="0" type="int" name="iOldDsplLvl"></DValue>
<DValue value="0" type="int" name="iOldDsplNumLvl"></DValue>
</Params>
</Domain>
<SubProc></SubProc>
</ProcBase>
<ProcBase Name="vegetation at  Segmentation 1: merge region" bLoopChg="0" bExpand="1" bActive="1" bAutoName="1" bSubrtn="0" sComment="">
<LcnsInfo sLcnsId="" sPwd=""></LcnsInfo>
<vrblValMaxCycle>
<DValue value="1." type="double"></DValue>
</vrblValMaxCycle>
<Algorithm guid="2328636B-BAD3-4f5d-B5AA-FC209A0BFB65">
<Params>
<DValue value="0" type="bool" name="bFsnUp"></DValue>
<DValue type="vector" name="vThmLayerFlags">
<Values></Values>
</DValue>
</Params>
</Algorithm>
<Domain guid="CED621BD-F4D1-4ffa-A2F6-DB2BB1913E8C">
<Params>
<DValue type="lvlName" name="valMapLvl">
<MapLvlProxy strName="Segmentation 1" bVrbl="0">
<Assignment MapLvl="1" MapName="main"></Assignment>
<Scope GUID="00000000-0000-0000-0000-000000000000"></Scope>
</MapLvlProxy>
</DValue>
<DValue type="vector" name="mClssFltr">
<Values>
<DValue value="2" type="clssId" indx="0"></DValue>
<DValue value="User defined" type="string" indx="1"></DValue>
</Values>
</DValue>
<DValue type="threshold" name="valThrsh"></DValue>
<DValue type="threshold" name="valThrsh2"></DValue>
<DValue value="From Parent" type="string" name="valMap"></DValue>
<DValue value="From Parent" type="string" name="valROI"></DValue>
<DValue value="0" type="int" name="iNumMaxObj"></DValue>
<DValue value="4" type="int" name="iVersion"></DValue>
<DValue value="-1" type="int" name="iOldLvl"></DValue>
<DValue value="0" type="int" name="iOldDsplLvl"></DValue>
<DValue value="0" type="int" name="iOldDsplNumLvl"></DValue>
</Params>
</Domain>
<SubProc></SubProc>
</ProcBase>
<ProcBase Name="dark_objects, vegetation with Area &amp;lt; 100 Pxl at  Segmentation 1: veg_buffor" bLoopChg="0" bExpand="1" bActive="1" bAutoName="1" bSubrtn="0" sComment="">
<LcnsInfo sLcnsId="" sPwd=""></LcnsInfo>
<vrblValMaxCycle>
<DValue value="1." type="double"></DValue>
</vrblValMaxCycle>
<Algorithm guid="3AC44F21-C6B2-4804-9929-BB18BE6F2051">
<Params>
<DValue value="3" type="clssId" name="valClass"></DValue>
</Params>
</Algorithm>
<Domain guid="CED621BD-F4D1-4ffa-A2F6-DB2BB1913E8C">
<Params>
<DValue type="lvlName" name="valMapLvl">
<MapLvlProxy strName="Segmentation 1" bVrbl="0">
<Assignment MapLvl="1" MapName="main"></Assignment>
<Scope GUID="00000000-0000-0000-0000-000000000000"></Scope>
</MapLvlProxy>
</DValue>
<DValue type="vector" name="mClssFltr">
<Values>
<DValue value="4" type="clssId" indx="0"></DValue>
<DValue value="2" type="clssId" indx="1"></DValue>
<DValue value="User defined" type="string" indx="2"></DValue>
</Values>
</DValue>
<DValue type="threshold" name="valThrsh">
```

```
<TermThrsh>
<TermGroup eJoint="2">
<TermCondition eCmpr="2" eBaseUnit="1" eJoint="2">
<ProcVrblVal1>
<DValue type="propDscrId">
<PropDscrId GUID="03E04ED0-94DD-45ee-801E-14D70E6E2417" InstID="Area"></PropDscrId>
</DValue>
</ProcVrblVal1>
<ProcVrblVal2>
<DValue value="100." type="double"></DValue>
</ProcVrblVal2>
</TermCondition>
</TermGroup>
</TermThrsh>
</DValue>
<DValue type="threshold" name="valThrsh2"></DValue>
<DValue value="From Parent" type="string" name="valMap"></DValue>
<DValue value="From Parent" type="string" name="valROI"></DValue>
<DValue value="0" type="int" name="iNumMaxObj"></DValue>
<DValue value="4" type="int" name="iVersion"></DValue>
<DValue value="-1" type="int" name="iOldLvl"></DValue>
<DValue value="0" type="int" name="iOldDsplLvl"></DValue>
<DValue value="0" type="int" name="iOldDsplNumLvl"></DValue>
</Params>
</Domain>
<SubProc></SubProc>
</ProcBase>
<ProcBase Name="veg_buffor at  Segmentation 1: merge region" bLoopChg="0" bExpand="1" bActive="1" bAutoName="1" bSubrtn="0" sComment="">
<LcnsInfo sLcnsId="" sPwd=""></LcnsInfo>
<vrblValMaxCycle>
<DValue value="1." type="double"></DValue>
</vrblValMaxCycle>
<Algorithm guid="2328636B-BAD3-4f5d-B5AA-FC209A0BFB65">
<Params>
<DValue value="0" type="bool" name="bFsnUp"></DValue>
<DValue type="vector" name="vThmLayerFlags">
<Values></Values>
</DValue>
</Params>
</Algorithm>
<Domain guid="CED621BD-F4D1-4ffa-A2F6-DB2BB1913E8C">
<Params>
<DValue type="lvlName" name="valMapLvl">
<MapLvlProxy strName="Segmentation 1" bVrbl="0">
<Assignment MapLvl="1" MapName="main"></Assignment>
<Scope GUID="00000000-0000-0000-0000-000000000000"></Scope>
</MapLvlProxy>
</DValue>
<DValue type="vector" name="mClssFltr">
<Values>
<DValue value="3" type="clssId" indx="0"></DValue>
<DValue value="User defined" type="string" indx="1"></DValue>
</Values>
</DValue>
<DValue type="threshold" name="valThrsh"></DValue>
<DValue type="threshold" name="valThrsh2"></DValue>
<DValue value="From Parent" type="string" name="valMap"></DValue>
<DValue value="From Parent" type="string" name="valROI"></DValue>
<DValue value="0" type="int" name="iNumMaxObj"></DValue>
<DValue value="4" type="int" name="iVersion"></DValue>
<DValue value="-1" type="int" name="iOldLvl"></DValue>
<DValue value="0" type="int" name="iOldDsplLvl"></DValue>
<DValue value="0" type="int" name="iOldDsplNumLvl"></DValue>
</Params>
</Domain>
<SubProc></SubProc>
</ProcBase>
<ProcBase Name="classify snow" bLoopChg="0" bExpand="1" bActive="1" bAutoName="0" bSubrtn="0" sComment="">
<LcnsInfo sLcnsId="" sPwd=""></LcnsInfo>
<vrblValMaxCycle>
<DValue value="1." type="double"></DValue>
</vrblValMaxCycle>
<Algorithm guid="A8BA5775-CC39-4194-9A6A-A64872EE1F81">
<Params></Params>
</Algorithm>
<Domain guid="CC9F2C30-4DB0-4ef2-B864-63560D1D6BF3">
<Params>
<DValue type="threshold" name="valThrsh"></DValue>
<DValue type="threshold" name="valThrsh2"></DValue>
<DValue value="From Parent" type="string" name="valMap"></DValue>
</Params>
</Domain>
<SubProc>
<ProcBase Name="unclassified with Mean Layer 4 > 127  at  Segmentation 1: snow" bLoopChg="0" bExpand="1" bActive="1" bAutoName="1" bSubrtn="0" sComment="">
<LcnsInfo sLcnsId="" sPwd=""></LcnsInfo>
<vrblValMaxCycle>
<DValue value="1." type="double"></DValue>
</vrblValMaxCycle>
<Algorithm guid="3AC44F21-C6B2-4804-9929-BB18BE6F2051">
<Params>
<DValue value="5" type="clssId" name="valClass"></DValue>
</Params>
</Algorithm>
<Domain guid="CED621BD-F4D1-4ffa-A2F6-DB2BB1913E8C">
<Params>
<DValue type="lvlName" name="valMapLvl">
<MapLvlProxy strName="Segmentation 1" bVrbl="0">
<Assignment MapLvl="1" MapName="main"></Assignment>
<Scope GUID="00000000-0000-0000-0000-000000000000"></Scope>
</MapLvlProxy>
</DValue>
<DValue type="vector" name="mClssFltr">
<Values>
<DValue value="Unclsfy" type="string" indx="0"></DValue>
<DValue value="User defined" type="string" indx="1"></DValue>
</Values>
</DValue>
<DValue type="threshold" name="valThrsh">
<TermThrsh>
<TermGroup eJoint="2">
<TermCondition eCmpr="3" eBaseUnit="0" eJoint="2">
<ProcVrblVal1>
<DValue type="propDscrId">
<PropDscrId GUID="44411C83-609B-4758-93D3-FF62DF246855" InstID="Mean Layer 4"></PropDscrId>
</DValue>
</ProcVrblVal1>
<ProcVrblVal2>
<DValue value="127." type="double"></DValue>
</ProcVrblVal2>
</TermCondition>
</TermGroup>
```

```
</TermThrsh>
</DValue>
<DValue type="threshold" name="valThrsh2"></DValue>
<DValue value="From Parent" type="string" name="valMap"></DValue>
<DValue value="From Parent" type="string" name="valROI"></DValue>
<DValue value="0" type="int" name="iNumMaxObj"></DValue>
<DValue value="4" type="int" name="iVersion"></DValue>
<DValue value="-1" type="int" name="iOldLvl"></DValue>
<DValue value="0" type="int" name="iOldDsplLvl"></DValue>
<DValue value="0" type="int" name="iOldDsplNumLvl"></DValue>
</Params>
</Domain>
<SubProc></SubProc>
</ProcBase>
<ProcBase Name="classify rough snow using contrast on NDWI" bLoopChg="0" bExpand="1" bActive="1" bAutoName="0" bSubrtn="0" sComment="">
<LcnsInfo sLcnsId="" sPwd=""></LcnsInfo>
<vrblValMaxCycle>
<DValue value="1." type="double"></DValue>
</vrblValMaxCycle>
<Algorithm guid="A8BA5775-CC39-4194-9A6A-A64872EE1F81">
<Params></Params>
</Algorithm>
<Domain guid="CC9F2C30-4DB0-4ef2-B864-63560D1D6BF3">
<Params>
<DValue type="threshold" name="valThrsh"></DValue>
<DValue type="threshold" name="valThrsh2"></DValue>
<DValue value="From Parent" type="string" name="valMap"></DValue>
</Params>
</Domain>
<SubProc>
<ProcBase Name="snow with Mean Layer 5 > 1  at  Segmentation 1: rough_snow" bLoopChg="0" bExpand="1" bActive="1" bAutoName="1" bSubrtn="0" sComment="">
<LcnsInfo sLcnsId="" sPwd=""></LcnsInfo>
<vrblValMaxCycle>
<DValue value="1." type="double"></DValue>
</vrblValMaxCycle>
<Algorithm guid="3AC44F21-C6B2-4804-9929-BB18BE6F2051">
<Params>
<DValue value="1" type="clssId" name="valClass"></DValue>
</Params>
</Algorithm>
<Domain guid="CED621BD-F4D1-4ffa-A2F6-DB2BB1913E8C">
<Params>
<DValue type="lvlName" name="valMapLvl">
<MapLvlProxy strName="Segmentation 1" bVrbl="0">
<Assignment MapLvl="1" MapName="main"></Assignment>
<Scope GUID="00000000-0000-0000-0000-000000000000"></Scope>
</MapLvlProxy>
</DValue>
<DValue type="vector" name="mClssFltr">
<Values>
<DValue value="5" type="clssId" indx="0"></DValue>
<DValue value="User defined" type="string" indx="1"></DValue>
</Values>
</DValue>
<DValue type="threshold" name="valThrsh">
<TermThrsh>
<TermGroup eJoint="2">
<TermCondition eCmpr="3" eBaseUnit="0" eJoint="2">
<ProcVrblVal1>
<DValue type="propDscrId">
<PropDscrId GUID="44411C83-609B-4758-93D3-FF62DF246855" InstID="Mean Layer 5"></PropDscrId>
</DValue>
</ProcVrblVal1>
<ProcVrblVal2>
<DValue value="1." type="double"></DValue>
</ProcVrblVal2>
</TermCondition>
</TermGroup>
</TermThrsh>
</DValue>
<DValue type="threshold" name="valThrsh2"></DValue>
<DValue value="From Parent" type="string" name="valMap"></DValue>
<DValue value="From Parent" type="string" name="valROI"></DValue>
<DValue value="0" type="int" name="iNumMaxObj"></DValue>
<DValue value="4" type="int" name="iVersion"></DValue>
<DValue value="-1" type="int" name="iOldLvl"></DValue>
<DValue value="0" type="int" name="iOldDsplLvl"></DValue>
<DValue value="0" type="int" name="iOldDsplNumLvl"></DValue>
</Params>
</Domain>
<SubProc></SubProc>
</ProcBase>
<ProcBase Name="reclassify small objects" bLoopChg="0" bExpand="1" bActive="1" bAutoName="0" bSubrtn="0" sComment="">
<LcnsInfo sLcnsId="" sPwd=""></LcnsInfo>
<vrblValMaxCycle>
<DValue value="1." type="double"></DValue>
</vrblValMaxCycle>
<Algorithm guid="A8BA5775-CC39-4194-9A6A-A64872EE1F81">
<Params></Params>
</Algorithm>
<Domain guid="CC9F2C30-4DB0-4ef2-B864-63560D1D6BF3">
<Params>
<DValue type="threshold" name="valThrsh"></DValue>
<DValue type="threshold" name="valThrsh2"></DValue>
<DValue value="From Parent" type="string" name="valMap"></DValue>
</Params>
</Domain>
<SubProc>
<ProcBase Name="snow at  Segmentation 1: merge region" bLoopChg="0" bExpand="1" bActive="1" bAutoName="1" bSubrtn="0" sComment="">
<LcnsInfo sLcnsId="" sPwd=""></LcnsInfo>
<vrblValMaxCycle>
<DValue value="1." type="double"></DValue>
</vrblValMaxCycle>
<Algorithm guid="2328636B-BAD3-4f5d-B5AA-FC209A0BFB65">
<Params>
<DValue value="0" type="bool" name="bFsnUp"></DValue>
<DValue type="vector" name="vThmLayerFlags">
<Values></Values>
</DValue>
</Params>
</Algorithm>
<Domain guid="CED621BD-F4D1-4ffa-A2F6-DB2BB1913E8C">
<Params>
<DValue type="lvlName" name="valMapLvl">
<MapLvlProxy strName="Segmentation 1" bVrbl="0">
<Assignment MapLvl="1" MapName="main"></Assignment>
<Scope GUID="00000000-0000-0000-0000-000000000000"></Scope>
</MapLvlProxy>
</DValue>
<DValue type="vector" name="mClssFltr">
<Values>
```

```
<DValue value="5" type="clssId" indx="0"></DValue>
<DValue value="User defined" type="string" indx="1"></DValue>
</Values>
</DValue>
<DValue type="threshold" name="valThrsh"></DValue>
<DValue type="threshold" name="valThrsh2"></DValue>
<DValue value="From Parent" type="string" name="valMap"></DValue>
<DValue value="From Parent" type="string" name="valROI"></DValue>
<DValue value="0" type="int" name="iNumMaxObj"></DValue>
<DValue value="4" type="int" name="iVersion"></DValue>
<DValue value="-1" type="int" name="iOldLvl"></DValue>
<DValue value="0" type="int" name="iOldDsplLvl"></DValue>
<DValue value="0" type="int" name="iOldDsplNumLvl"></DValue>
</Params>
</Domain>
<SubProc></SubProc>
</ProcBase>
<ProcBase Name="snow with Rel. border to rough_snow = 1  and Area &lt;= 200 Pxl at  Segmentation 1: rough_snow" bLoopChg="0" bExpand="1" bActive="1" bAutoName="1" bSubrtn="0" sComment="">
<LcnsInfo sLcnsId="" sPwd=""></LcnsInfo>
<vrblValMaxCycle>
<DValue value="1." type="double"></DValue>
</vrblValMaxCycle>
<Algorithm guid="3AC44F21-C6B2-4804-9929-BB18BE6F2051">
<Params>
<DValue value="1" type="clssId" name="valClass"></DValue>
</Params>
</Algorithm>
<Domain guid="CED621BD-F4D1-4ffa-A2F6-DB2BB1913E8C">
<Params>
<DValue type="lvlName" name="valMapLvl">
<MapLvlProxy strName="Segmentation 1" bVrbl="0">
<Assignment MapLvl="1" MapName="main"></Assignment>
<Scope GUID="00000000-0000-0000-0000-000000000000"></Scope>
</MapLvlProxy>
</DValue>
<DValue type="vector" name="mClssFltr">
<Values>
<DValue value="5" type="clssId" indx="0"></DValue>
<DValue value="User defined" type="string" indx="1"></DValue>
</Values>
</DValue>
<DValue type="threshold" name="valThrsh">
<TermThrsh>
<TermGroup eJoint="2">
<TermCondition eCmpr="5" eBaseUnit="0" eJoint="0">
<ProcVrblVal1>
<DValue type="propDscrId">
<PropDscrId GUID="AA7CAC99-696D-4983-8F48-D07C4F816F2C" InstID="Rel. border to rough_snow"></PropDscrId>
</DValue>
</ProcVrblVal1>
<ProcVrblVal2>
<DValue value="1." type="double"></DValue>
</ProcVrblVal2>
</TermCondition>
<TermCondition eCmpr="1" eBaseUnit="1" eJoint="2">
<ProcVrblVal1>
<DValue type="propDscrId">
<PropDscrId GUID="03E04ED0-94DD-45ee-801E-14D70E6E2417" InstID="Area"></PropDscrId>
</DValue>
</ProcVrblVal1>
<ProcVrblVal2>
<DValue value="200." type="double"></DValue>
</ProcVrblVal2>
</TermCondition>
</TermGroup>
</TermThrsh>
</DValue>
<DValue type="threshold" name="valThrsh2"></DValue>
<DValue value="From Parent" type="string" name="valMap"></DValue>
<DValue value="From Parent" type="string" name="valROI"></DValue>
<DValue value="0" type="int" name="iNumMaxObj"></DValue>
<DValue value="4" type="int" name="iVersion"></DValue>
<DValue value="-1" type="int" name="iOldLvl"></DValue>
<DValue value="0" type="int" name="iOldDsplLvl"></DValue>
<DValue value="0" type="int" name="iOldDsplNumLvl"></DValue>
</Params>
</Domain>
<SubProc></SubProc>
</ProcBase>
<ProcBase Name="snow with Rel. border to rough_snow = 1 and Mean Layer 5 >= 0.75  at  Segmentation 1: rough_snow" bLoopChg="0" bExpand="1" bActive="1" bAutoName="1" bSubrtn="0" sComment="">
<LcnsInfo sLcnsId="" sPwd=""></LcnsInfo>
<vrblValMaxCycle>
<DValue value="1." type="double"></DValue>
</vrblValMaxCycle>
<Algorithm guid="3AC44F21-C6B2-4804-9929-BB18BE6F2051">
<Params>
<DValue value="1" type="clssId" name="valClass"></DValue>
</Params>
</Algorithm>
<Domain guid="CED621BD-F4D1-4ffa-A2F6-DB2BB1913E8C">
<Params>
<DValue type="lvlName" name="valMapLvl">
<MapLvlProxy strName="Segmentation 1" bVrbl="0">
<Assignment MapLvl="1" MapName="main"></Assignment>
<Scope GUID="00000000-0000-0000-0000-000000000000"></Scope>
</MapLvlProxy>
</DValue>
<DValue type="vector" name="mClssFltr">
<Values>
<DValue value="5" type="clssId" indx="0"></DValue>
<DValue value="User defined" type="string" indx="1"></DValue>
</Values>
</DValue>
<DValue type="threshold" name="valThrsh">
<TermThrsh>
<TermGroup eJoint="2">
<TermCondition eCmpr="5" eBaseUnit="0" eJoint="0">
<ProcVrblVal1>
<DValue type="propDscrId">
<PropDscrId GUID="AA7CAC99-696D-4983-8F48-D07C4F816F2C" InstID="Rel. border to rough_snow"></PropDscrId>
</DValue>
</ProcVrblVal1>
<ProcVrblVal2>
<DValue value="1." type="double"></DValue>
</ProcVrblVal2>
</TermCondition>
<TermCondition eCmpr="4" eBaseUnit="0" eJoint="2">
<ProcVrblVal1>
<DValue type="propDscrId">
<PropDscrId GUID="44411C83-609B-4758-93D3-FF62DF246855" InstID="Mean Layer 5"></PropDscrId>
</DValue>
```

```
</ProcVrblVal1>
<ProcVrblVal2>
<DValue value="0.75" type="double"></DValue>
</ProcVrblVal2>
</TermCondition>
</TermGroup>
</TermThrsh>
</DValue>
<DValue type="threshold" name="valThrsh2"></DValue>
<DValue value="From Parent" type="string" name="valMap"></DValue>
<DValue value="From Parent" type="string" name="valROI"></DValue>
<DValue value="0" type="int" name="iNumMaxObj"></DValue>
<DValue value="4" type="int" name="iVersion"></DValue>
<DValue value="-1" type="int" name="iOldLvl"></DValue>
<DValue value="0" type="int" name="iOldDsplLvl"></DValue>
<DValue value="0" type="int" name="iOldDsplNumLvl"></DValue>
</Params>
</Domain>
<SubProc></SubProc>
</ProcBase>
<ProcBase Name="veg_buffor with Rel. border to rough_snow = 1  and Mean Layer 5 >= 0.75  at  Segmentation 1: rough_snow" bLoopChg="0" bExpand="1" bActive="1" bAutoName="1" bSubrtn="0"
sComment="">
<LcnsInfo sLcnsId="" sPwd=""></LcnsInfo>
<vrblValMaxCycle>
<DValue value="1." type="double"></DValue>
</vrblValMaxCycle>
<Algorithm guid="3AC44F21-C6B2-4804-9929-BB18BE6F2051">
<Params>
<DValue value="1" type="clssId" name="valClass"></DValue>
</Params>
</Algorithm>
<Domain guid="CED621BD-F4D1-4ffa-A2F6-DB2BB1913E8C">
<Params>
<DValue type="lvlName" name="valMapLvl">
<MapLvlProxy strName="Segmentation 1" bVrbl="0">
<Assignment MapLvl="1" MapName="main"></Assignment>
<Scope GUID="00000000-0000-0000-0000-000000000000"></Scope>
</MapLvlProxy>
</DValue>
<DValue type="vector" name="mClssFltr">
<Values>
<DValue value="3" type="clssId" indx="0"></DValue>
<DValue value="User defined" type="string" indx="1"></DValue>
</Values>
</DValue>
<DValue type="threshold" name="valThrsh">
<TermThrsh>
<TermGroup eJoint="2">
<TermCondition eCmpr="5" eBaseUnit="0" eJoint="0">
<ProcVrblVal1>
<DValue type="propDscrId">
<PropDscrId GUID="AA7CAC99-696D-4983-8F48-D07C4F816F2C" InstID="Rel. border to rough_snow"></PropDscrId>
</DValue>
</ProcVrblVal1>
<ProcVrblVal2>
<DValue value="1." type="double"></DValue>
</ProcVrblVal2>
</TermCondition>
<TermCondition eCmpr="4" eBaseUnit="0" eJoint="2">
<ProcVrblVal1>
<DValue type="propDscrId">
<PropDscrId GUID="44411C83-609B-4758-93D3-FF62DF246855" InstID="Mean Layer 5"></PropDscrId>
</DValue>
</ProcVrblVal1>
<ProcVrblVal2>
<DValue value="0.75" type="double"></DValue>
</ProcVrblVal2>
</TermCondition>
</TermGroup>
</TermThrsh>
</DValue>
<DValue type="threshold" name="valThrsh2"></DValue>
<DValue value="From Parent" type="string" name="valMap"></DValue>
<DValue value="From Parent" type="string" name="valROI"></DValue>
<DValue value="0" type="int" name="iNumMaxObj"></DValue>
<DValue value="4" type="int" name="iVersion"></DValue>
<DValue value="-1" type="int" name="iOldLvl"></DValue>
<DValue value="0" type="int" name="iOldDsplLvl"></DValue>
<DValue value="0" type="int" name="iOldDsplNumLvl"></DValue>
</Params>
</Domain>
<SubProc></SubProc>
</ProcBase>
<ProcBase Name="rough_snow at  Segmentation 1: merge region" bLoopChg="0" bExpand="1" bActive="1" bAutoName="1" bSubrtn="0" sComment="">
<LcnsInfo sLcnsId="" sPwd=""></LcnsInfo>
<vrblValMaxCycle>
<DValue value="1." type="double"></DValue>
</vrblValMaxCycle>
<Algorithm guid="2328636B-BAD3-4f5d-B5AA-FC209A0BFB65">
<Params>
<DValue value="0" type="bool" name="bFsnUp"></DValue>
<DValue type="vector" name="vThmLayerFlags">
<Values></Values>
</DValue>
</Params>
</Algorithm>
<Domain guid="CED621BD-F4D1-4ffa-A2F6-DB2BB1913E8C">
<Params>
<DValue type="lvlName" name="valMapLvl">
<MapLvlProxy strName="Segmentation 1" bVrbl="0">
<Assignment MapLvl="1" MapName="main"></Assignment>
<Scope GUID="00000000-0000-0000-0000-000000000000"></Scope>
</MapLvlProxy>
</DValue>
<DValue type="vector" name="mClssFltr">
<Values>
<DValue value="1" type="clssId" indx="0"></DValue>
<DValue value="User defined" type="string" indx="1"></DValue>
</Values>
</DValue>
<DValue type="threshold" name="valThrsh"></DValue>
<DValue type="threshold" name="valThrsh2"></DValue>
<DValue value="From Parent" type="string" name="valMap"></DValue>
<DValue value="From Parent" type="string" name="valROI"></DValue>
<DValue value="0" type="int" name="iNumMaxObj"></DValue>
<DValue value="4" type="int" name="iVersion"></DValue>
<DValue value="-1" type="int" name="iOldLvl"></DValue>
<DValue value="0" type="int" name="iOldDsplLvl"></DValue>
<DValue value="0" type="int" name="iOldDsplNumLvl"></DValue>
</Params>
</Domain>
```

```
<SubProc></SubProc>
</ProcBase>
<ProcBase Name="rough_snow with Area &lt; 1000 Pxl at  Segmentation 1: snow" bLoopChg="0" bExpand="1" bActive="1" bAutoName="1" bSubrtn="0" sComment="">
<LcnsInfo sLcnsId="" sPwd=""></LcnsInfo>
<vrblValMaxCycle>
<DValue value="1." type="double"></DValue>
</vrblValMaxCycle>
<Algorithm guid="3AC44F21-C6B2-4804-9929-BB18BE6F2051">
<Params>
<DValue value="5" type="clssId" name="valClass"></DValue>
</Params>
</Algorithm>
<Domain guid="CED621BD-F4D1-4ffa-A2F6-DB2BB1913E8C">
<Params>
<DValue type="lvlName" name="valMapLvl">
<MapLvlProxy strName="Segmentation 1" bVrbl="0">
<Assignment MapLvl="1" MapName="main"></Assignment>
<Scope GUID="00000000-0000-0000-0000-000000000000"></Scope>
</MapLvlProxy>
</DValue>
<DValue type="vector" name="mClssFltr">
<Values>
<DValue value="1" type="clssId" indx="0"></DValue>
<DValue value="User defined" type="string" indx="1"></DValue>
</Values>
</DValue>
<DValue type="threshold" name="valThrsh">
<TermThrsh>
<TermGroup eJoint="2">
<TermCondition eCmpr="2" eBaseUnit="1" eJoint="2">
<ProcVrblVal1>
<DValue type="propDscrId">
<PropDscrId GUID="03E04ED0-94DD-45ee-801E-14D70E6E2417" InstID="Area"></PropDscrId>
</DValue>
</ProcVrblVal1>
<ProcVrblVal2>
<DValue value="1000." type="double"></DValue>
</ProcVrblVal2>
</TermCondition>
</TermGroup>
</TermThrsh>
</DValue>
<DValue type="threshold" name="valThrsh2"></DValue>
<DValue value="From Parent" type="string" name="valMap"></DValue>
<DValue value="From Parent" type="string" name="valROI"></DValue>
<DValue value="0" type="int" name="iNumMaxObj"></DValue>
<DValue value="4" type="int" name="iVersion"></DValue>
<DValue value="-1" type="int" name="iOldLvl"></DValue>
<DValue value="0" type="int" name="iOldDsplLvl"></DValue>
<DValue value="0" type="int" name="iOldDsplNumLvl"></DValue>
</Params>
</Domain>
<SubProc></SubProc>
</ProcBase>
<ProcBase Name="at  Segmentation 1: convert to sub-objects" bLoopChg="0" bExpand="1" bActive="1" bAutoName="1" bSubrtn="0" sComment="">
<LcnsInfo sLcnsId="" sPwd=""></LcnsInfo>
<vrblValMaxCycle>
<DValue value="1." type="double"></DValue>
</vrblValMaxCycle>
<Algorithm guid="51AF1228-39D3-4ffc-8530-71FACCA812B7">
<Params></Params>
</Algorithm>
<Domain guid="CED621BD-F4D1-4ffa-A2F6-DB2BB1913E8C">
<Params>
<DValue type="lvlName" name="valMapLvl">
<MapLvlProxy strName="Segmentation 1" bVrbl="0">
<Assignment MapLvl="1" MapName="main"></Assignment>
<Scope GUID="00000000-0000-0000-0000-000000000000"></Scope>
</MapLvlProxy>
</DValue>
<DValue type="vector" name="mClssFltr">
<Values>
<DValue value="Disabled" type="string" indx="0"></DValue>
</Values>
</DValue>
<DValue type="threshold" name="valThrsh"></DValue>
<DValue type="threshold" name="valThrsh2"></DValue>
<DValue value="From Parent" type="string" name="valMap"></DValue>
<DValue value="From Parent" type="string" name="valROI"></DValue>
<DValue value="0" type="int" name="iNumMaxObj"></DValue>
<DValue value="4" type="int" name="iVersion"></DValue>
<DValue value="-1" type="int" name="iOldLvl"></DValue>
<DValue value="0" type="int" name="iOldDsplLvl"></DValue>
<DValue value="0" type="int" name="iOldDsplNumLvl"></DValue>
</Params>
</Domain>
<SubProc></SubProc>
</ProcBase>
<ProcBase Name="remove salt pepper noise" bLoopChg="0" bExpand="1" bActive="1" bAutoName="0" bSubrtn="0" sComment="">
<LcnsInfo sLcnsId="" sPwd=""></LcnsInfo>
<vrblValMaxCycle>
<DValue value="1." type="double"></DValue>
</vrblValMaxCycle>
<Algorithm guid="A8BA5775-CC39-4194-9A6A-A64872EE1F81">
<Params></Params>
</Algorithm>
<Domain guid="CC9F2C30-4DB0-4ef2-B864-63560D1D6BF3">
<Params>
<DValue type="threshold" name="valThrsh"></DValue>
<DValue type="threshold" name="valThrsh2"></DValue>
<DValue value="From Parent" type="string" name="valMap"></DValue>
</Params>
</Domain>
<SubProc>
<ProcBase Name="5x: rough_snow with Number of rough_snow (0) &lt;= 3  at  Segmentation 1: snow" bLoopChg="0" bExpand="1" bActive="1" bAutoName="1" bSubrtn="0" sComment="">
<LcnsInfo sLcnsId="" sPwd=""></LcnsInfo>
<vrblValMaxCycle>
<DValue value="5." type="double"></DValue>
</vrblValMaxCycle>
<Algorithm guid="3AC44F21-C6B2-4804-9929-BB18BE6F2051">
<Params>
<DValue value="5" type="clssId" name="valClass"></DValue>
</Params>
</Algorithm>
<Domain guid="CED621BD-F4D1-4ffa-A2F6-DB2BB1913E8C">
<Params>
<DValue type="lvlName" name="valMapLvl">
<MapLvlProxy strName="Segmentation 1" bVrbl="0">
<Assignment MapLvl="1" MapName="main"></Assignment>
<Scope GUID="00000000-0000-0000-0000-000000000000"></Scope>
</MapLvlProxy>
```

```
</DValue>
<DValue type="vector" name="mClssFltr">
<Values>
<DValue value="1" type="clssId" indx="0"></DValue>
<DValue value="User defined" type="string" indx="1"></DValue>
</Values>
</DValue>
<DValue type="threshold" name="valThrsh">
<TermThrsh>
<TermGroup eJoint="2">
<TermCondition eCmpr="1" eBaseUnit="0" eJoint="2">
<ProcVrblVal1>
<DValue type="propDscrId">
<PropDscrId GUID="7D1F1A4B-9BFD-4b29-BA08-AA370D63669B" InstID="Number of water (0)"></PropDscrId>
</DValue>
</ProcVrblVal1>
<ProcVrblVal2>
<DValue value="3." type="double"></DValue>
</ProcVrblVal2>
</TermCondition>
</TermGroup>
</TermThrsh>
</DValue>
<DValue type="threshold" name="valThrsh2"></DValue>
<DValue value="From Parent" type="string" name="valMap"></DValue>
<DValue value="From Parent" type="string" name="valROI"></DValue>
<DValue value="0" type="int" name="iNumMaxObj"></DValue>
<DValue value="4" type="int" name="iVersion"></DValue>
<DValue value="-1" type="int" name="iOldLvl"></DValue>
<DValue value="0" type="int" name="iOldDsplLvl"></DValue>
<DValue value="0" type="int" name="iOldDsplNumLvl"></DValue>
</Params>
</Domain>
<SubProc></SubProc>
</ProcBase>
<ProcBase Name="rough_snow at  Segmentation 1: merge region" bLoopChg="0" bExpand="1" bActive="1" bAutoName="1" bSubrtn="0" sComment="">
<LcnsInfo sLcnsId="" sPwd=""></LcnsInfo>
<vrblValMaxCycle>
<DValue value="1." type="double"></DValue>
</vrblValMaxCycle>
<Algorithm guid="2328636B-BAD3-4f5d-B5AA-FC209A0BFB65">
<Params>
<DValue value="0" type="bool" name="bFsnUp"></DValue>
<DValue type="vector" name="vThmLayerFlags">
<Values></Values>
</DValue>
</Params>
</Algorithm>
<Domain guid="CED621BD-F4D1-4ffa-A2F6-DB2BB1913E8C">
<Params>
<DValue type="lvlName" name="valMapLvl">
<MapLvlProxy strName="Segmentation 1" bVrbl="0">
<Assignment MapLvl="1" MapName="main"></Assignment>
<Scope GUID="00000000-0000-0000-0000-000000000000"></Scope>
</MapLvlProxy>
</DValue>
<DValue type="vector" name="mClssFltr">
<Values>
<DValue value="1" type="clssId" indx="0"></DValue>
<DValue value="User defined" type="string" indx="1"></DValue>
</Values>
</DValue>
<DValue type="threshold" name="valThrsh"></DValue>
<DValue type="threshold" name="valThrsh2"></DValue>
<DValue value="From Parent" type="string" name="valMap"></DValue>
<DValue value="From Parent" type="string" name="valROI"></DValue>
<DValue value="0" type="int" name="iNumMaxObj"></DValue>
<DValue value="4" type="int" name="iVersion"></DValue>
<DValue value="-1" type="int" name="iOldLvl"></DValue>
<DValue value="0" type="int" name="iOldDsplLvl"></DValue>
<DValue value="0" type="int" name="iOldDsplNumLvl"></DValue>
</Params>
</Domain>
<SubProc></SubProc>
</ProcBase>
<ProcBase Name="rough_snow with Area &amp;lt; 2000 Pxl at  Segmentation 1: snow" bLoopChg="0" bExpand="1" bActive="1" bAutoName="1" bSubrtn="0" sComment="">
<LcnsInfo sLcnsId="" sPwd=""></LcnsInfo>
<vrblValMaxCycle>
<DValue value="1." type="double"></DValue>
</vrblValMaxCycle>
<Algorithm guid="3AC44F21-C6B2-4804-9929-BB18BE6F2051">
<Params>
<DValue value="5" type="clssId" name="valClass"></DValue>
</Params>
</Algorithm>
<Domain guid="CED621BD-F4D1-4ffa-A2F6-DB2BB1913E8C">
<Params>
<DValue type="lvlName" name="valMapLvl">
<MapLvlProxy strName="Segmentation 1" bVrbl="0">
<Assignment MapLvl="1" MapName="main"></Assignment>
<Scope GUID="00000000-0000-0000-0000-000000000000"></Scope>
</MapLvlProxy>
</DValue>
<DValue type="vector" name="mClssFltr">
<Values>
<DValue value="1" type="clssId" indx="0"></DValue>
<DValue value="User defined" type="string" indx="1"></DValue>
</Values>
</DValue>
<DValue type="threshold" name="valThrsh">
<TermThrsh>
<TermGroup eJoint="2">
<TermCondition eCmpr="2" eBaseUnit="1" eJoint="2">
<ProcVrblVal1>
<DValue type="propDscrId">
<PropDscrId GUID="03E04ED0-94DD-45ee-801E-14D70E6E2417" InstID="Area"></PropDscrId>
</DValue>
</ProcVrblVal1>
<ProcVrblVal2>
<DValue value="2000." type="double"></DValue>
</ProcVrblVal2>
</TermCondition>
</TermGroup>
</TermThrsh>
</DValue>
<DValue type="threshold" name="valThrsh2"></DValue>
<DValue value="From Parent" type="string" name="valMap"></DValue>
<DValue value="From Parent" type="string" name="valROI"></DValue>
<DValue value="0" type="int" name="iNumMaxObj"></DValue>
<DValue value="4" type="int" name="iVersion"></DValue>
<DValue value="-1" type="int" name="iOldLvl"></DValue>
```

<DValue value="0" type="int" name="iOldDsplLvl"></DValue>
<DValue value="0" type="int" name="iOldDsplNumLvl"></DValue>
</Params>
</Domain>
<SubProc></SubProc>
</ProcBase>
<ProcBase Name="at Segmentation 1: convert to sub-objects" bLoopChg="0" bExpand="1" bActive="1" bAutoName="1" bSubrtn="0" sComment="">
<LcnsInfo sLcnsId="" sPwd=""></LcnsInfo>
<vrblValMaxCycle>
<DValue value="1." type="double"></DValue>
</vrblValMaxCycle>
<Algorithm guid="51AF1228-39D3-4ffc-8530-71FACCA812B7">
<Params></Params>
</Algorithm>
<Domain guid="CED621BD-F4D1-4ffa-A2F6-DB2BB1913E8C">
<Params>
<DValue type="lvlName" name="valMapLvl">
<MapLvlProxy strName="Segmentation 1" bVrbl="0">
<Assignment MapLvl="1" MapName="main"></Assignment>
<Scope GUID="00000000-0000-0000-0000-000000000000"></Scope>
</MapLvlProxy>
</DValue>
<DValue type="vector" name="mClssFltr">
<Values>
<DValue value="Disabled" type="string" indx="0"></DValue>
</Values>
</DValue>
<DValue type="threshold" name="valThrsh"></DValue>
<DValue type="threshold" name="valThrsh2"></DValue>
<DValue value="From Parent" type="string" name="valMap"></DValue>
<DValue value="From Parent" type="string" name="valROI"></DValue>
<DValue value="0" type="int" name="iNumMaxObj"></DValue>
<DValue value="4" type="int" name="iVersion"></DValue>
<DValue value="-1" type="int" name="iOldLvl"></DValue>
<DValue value="0" type="int" name="iOldDsplLvl"></DValue>
<DValue value="0" type="int" name="iOldDsplNumLvl"></DValue>
</Params>
</Domain>
<SubProc></SubProc>
</ProcBase>
<ProcBase Name="5x: snow with Number of snow (0) <= 3 and Number of rough_snow (0) >= 1 at Segmentation 1: rough_snow" bLoopChg="0" bExpand="1" bActive="1" bAutoName="1" bSubrtn="0" sComment="">
<LcnsInfo sLcnsId="" sPwd=""></LcnsInfo>
<vrblValMaxCycle>
<DValue value="5." type="double"></DValue>
</vrblValMaxCycle>
<Algorithm guid="3AC44F21-C6B2-4804-9929-BB18BE6F2051">
<Params>
<DValue value="1" type="clssId" name="valClass"></DValue>
</Params>
</Algorithm>
<Domain guid="CED621BD-F4D1-4ffa-A2F6-DB2BB1913E8C">
<Params>
<DValue type="lvlName" name="valMapLvl">
<MapLvlProxy strName="Segmentation 1" bVrbl="0">
<Assignment MapLvl="1" MapName="main"></Assignment>
<Scope GUID="00000000-0000-0000-0000-000000000000"></Scope>
</MapLvlProxy>
</DValue>
<DValue type="vector" name="mClssFltr">
<Values>
<DValue value="5" type="clssId" indx="0"></DValue>
<DValue value="User defined" type="string" indx="1"></DValue>
</Values>
</DValue>
<DValue type="threshold" name="valThrsh">
<TermThrsh>
<TermGroup eJoint="2">
<TermCondition eCmpr="1" eBaseUnit="0" eJoint="0">
<ProcVrblVal1>
<DValue type="propDscrId">
<PropDscrId GUID="7D1F1A4B-9BFD-4b29-BA08-AA370D63669B" InstID="Number of snow (0)"></PropDscrId>
</DValue>
</ProcVrblVal1>
<ProcVrblVal2>
<DValue value="3." type="double"></DValue>
</ProcVrblVal2>
</TermCondition>
<TermCondition eCmpr="4" eBaseUnit="0" eJoint="2">
<ProcVrblVal1>
<DValue type="propDscrId">
<PropDscrId GUID="7D1F1A4B-9BFD-4b29-BA08-AA370D63669B" InstID="Number of water (0)"></PropDscrId>
</DValue>
</ProcVrblVal1>
<ProcVrblVal2>
<DValue value="1." type="double"></DValue>
</ProcVrblVal2>
</TermCondition>
</TermGroup>
</TermThrsh>
</DValue>
<DValue type="threshold" name="valThrsh2"></DValue>
<DValue value="From Parent" type="string" name="valMap"></DValue>
<DValue value="From Parent" type="string" name="valROI"></DValue>
<DValue value="0" type="int" name="iNumMaxObj"></DValue>
<DValue value="4" type="int" name="iVersion"></DValue>
<DValue value="-1" type="int" name="iOldLvl"></DValue>
<DValue value="0" type="int" name="iOldDsplLvl"></DValue>
<DValue value="0" type="int" name="iOldDsplNumLvl"></DValue>
</Params>
</Domain>
<SubProc></SubProc>
</ProcBase>
<ProcBase Name="reclassify vegetation, dark objects, and buffer" bLoopChg="0" bExpand="1" bActive="1" bAutoName="0" bSubrtn="0" sComment="">
<LcnsInfo sLcnsId="" sPwd=""></LcnsInfo>
<vrblValMaxCycle>
<DValue value="1." type="double"></DValue>
</vrblValMaxCycle>
<Algorithm guid="A8BA5775-CC39-4194-9A6A-A64872EE1F81">
<Params></Params>
</Algorithm>
<Domain guid="CC9F2C30-4DB0-4ef2-B864-63560D1D6BF3">
<Params>
<DValue type="threshold" name="valThrsh"></DValue>
<DValue type="threshold" name="valThrsh2"></DValue>
<DValue value="From Parent" type="string" name="valMap"></DValue>
</Params>
</Domain>
<SubProc>
<ProcBase Name="dark_objects, veg_buffor, vegetation, unclassified with Brightness > 3000 and Mean Layer 6 < 140 at Segmentation 1: test" bLoopChg="0" bExpand="1" bActive="1" bAutoName="1" bSubrtn="0" sComment="">

<LcnsInfo sLcnsId="" sPwd=""></LcnsInfo>
<vrblValMaxCycle>
<DValue value="1." type="double"></DValue>
</vrblValMaxCycle>
<Algorithm guid="3AC44F21-C6B2-4804-9929-BB18BE6F2051">
<Params>
<DValue value="6" type="clssId" name="valClass"></DValue>
</Params>
</Algorithm>
<Domain guid="CED621BD-F4D1-4ffa-A2F6-DB2BB1913E8C">
<Params>
<DValue type="lvlName" name="valMapLvl">
<MapLvlProxy strName="Segmentation 1" bVrbl="0">
<Assignment MapLvl="1" MapName="main"></Assignment>
<Scope GUID="00000000-0000-0000-0000-000000000000"></Scope>
</MapLvlProxy>
</DValue>
<DValue type="vector" name="mClssFltr">
<Values>
<DValue value="4" type="clssId" indx="0"></DValue>
<DValue value="3" type="clssId" indx="1"></DValue>
<DValue value="2" type="clssId" indx="2"></DValue>
<DValue value="Unclsfy" type="string" indx="3"></DValue>
<DValue value="User defined" type="string" indx="4"></DValue>
</Values>
</DValue>
<DValue type="threshold" name="valThrsh">
<TermThrsh>
<TermGroup eJoint="2">
<TermCondition eCmpr="3" eBaseUnit="0" eJoint="0">
<ProcVrblVal1>
<DValue type="propDscrId">
<PropDscrId GUID="16B7A5B4-D807-4ab1-B769-D536B3C26B20" InstID="Brightness"></PropDscrId>
</DValue>
</ProcVrblVal1>
<ProcVrblVal2>
<DValue value="3000." type="double"></DValue>
</ProcVrblVal2>
</TermCondition>
<TermCondition eCmpr="2" eBaseUnit="0" eJoint="2">
<ProcVrblVal1>
<DValue type="propDscrId">
<PropDscrId GUID="44411C83-609B-4758-93D3-FF62DF246855" InstID="Mean Layer 6"></PropDscrId>
</DValue>
</ProcVrblVal1>
<ProcVrblVal2>
<DValue value="140." type="double"></DValue>
</ProcVrblVal2>
</TermCondition>
</TermGroup>
</TermThrsh>
</DValue>
<DValue type="threshold" name="valThrsh2"></DValue>
<DValue value="From Parent" type="string" name="valMap"></DValue>
<DValue value="From Parent" type="string" name="valROI"></DValue>
<DValue value="0" type="int" name="iNumMaxObj"></DValue>
<DValue value="4" type="int" name="iVersion"></DValue>
<DValue value="-1" type="int" name="iOldLvl"></DValue>
<DValue value="0" type="int" name="iOldDsplLvl"></DValue>
<DValue value="0" type="int" name="iOldDsplNumLvl"></DValue>
</Params>
</Domain>
<SubProc></SubProc>
</ProcBase>
<ProcBase Name="test at Segmentation 1: merge region" bLoopChg="0" bExpand="1" bActive="1" bAutoName="1" bSubrtn="0" sComment="">
<LcnsInfo sLcnsId="" sPwd=""></LcnsInfo>
<vrblValMaxCycle>
<DValue value="1." type="double"></DValue>
</vrblValMaxCycle>
<Algorithm guid="2328636B-BAD3-4f5d-B5AA-FC209A0BFB65">
<Params>
<DValue value="0" type="bool" name="bFsnUp"></DValue>
<DValue type="vector" name="vThmLayerFlags">
<Values></Values>
</DValue>
</Params>
</Algorithm>
<Domain guid="CED621BD-F4D1-4ffa-A2F6-DB2BB1913E8C">
<Params>
<DValue type="lvlName" name="valMapLvl">
<MapLvlProxy strName="Segmentation 1" bVrbl="0">
<Assignment MapLvl="1" MapName="main"></Assignment>
<Scope GUID="00000000-0000-0000-0000-000000000000"></Scope>
</MapLvlProxy>
</DValue>
<DValue type="vector" name="mClssFltr">
<Values>
<DValue value="6" type="clssId" indx="0"></DValue>
<DValue value="User defined" type="string" indx="1"></DValue>
</Values>
</DValue>
<DValue type="threshold" name="valThrsh"></DValue>
<DValue type="threshold" name="valThrsh2"></DValue>
<DValue value="From Parent" type="string" name="valMap"></DValue>
<DValue value="From Parent" type="string" name="valROI"></DValue>
<DValue value="0" type="int" name="iNumMaxObj"></DValue>
<DValue value="4" type="int" name="iVersion"></DValue>
<DValue value="-1" type="int" name="iOldLvl"></DValue>
<DValue value="0" type="int" name="iOldDsplLvl"></DValue>
<DValue value="0" type="int" name="iOldDsplNumLvl"></DValue>
</Params>
</Domain>
<SubProc></SubProc>
</ProcBase>
<ProcBase Name="test with Rel. border to rough_snow < 0.01 at Segmentation 1: unclassified" bLoopChg="0" bExpand="1" bActive="1" bAutoName="1" bSubrtn="0" sComment="">
<LcnsInfo sLcnsId="" sPwd=""></LcnsInfo>
<vrblValMaxCycle>
<DValue value="1." type="double"></DValue>
</vrblValMaxCycle>
<Algorithm guid="3AC44F21-C6B2-4804-9929-BB18BE6F2051">
<Params>
<DValue value="-1" type="clssId" name="valClass"></DValue>
</Params>
</Algorithm>
<Domain guid="CED621BD-F4D1-4ffa-A2F6-DB2BB1913E8C">
<Params>
<DValue type="lvlName" name="valMapLvl">
<MapLvlProxy strName="Segmentation 1" bVrbl="0">
<Assignment MapLvl="1" MapName="main"></Assignment>
<Scope GUID="00000000-0000-0000-0000-000000000000"></Scope>
</MapLvlProxy>

```
</DValue>
<DValue type="vector" name="mClssFltr">
<Values>
<DValue value="6" type="clssId" indx="0"></DValue>
<DValue value="User defined" type="string" indx="1"></DValue>
</Values>
</DValue>
<DValue type="threshold" name="valThrsh">
<TermThrsh>
<TermGroup eJoint="2">
<TermCondition eCmpr="2" eBaseUnit="0" eJoint="2">
<ProcVrblVal1>
<DValue type="propDscrId">
<PropDscrId GUID="AA7CAC99-696D-4983-8F48-D07C4F816F2C" InstID="Rel. border to rough_snow"></PropDscrId>
</DValue>
</ProcVrblVal1>
<ProcVrblVal2>
<DValue value="1.e-002" type="double"></DValue>
</ProcVrblVal2>
</TermCondition>
</TermGroup>
</TermThrsh>
</DValue>
<DValue type="threshold" name="valThrsh2"></DValue>
<DValue value="From Parent" type="string" name="valMap"></DValue>
<DValue value="From Parent" type="string" name="valROI"></DValue>
<DValue value="0" type="int" name="iNumMaxObj"></DValue>
<DValue value="4" type="int" name="iVersion"></DValue>
<DValue value="-1" type="int" name="iOldLvl"></DValue>
<DValue value="0" type="int" name="iOldDsplLvl"></DValue>
<DValue value="0" type="int" name="iOldDsplNumLvl"></DValue>
</Params>
</Domain>
<SubProc></SubProc>
</ProcBase>
<ProcBase Name="at  Segmentation 1: convert to sub-objects" bLoopChg="0" bExpand="1" bActive="1" bAutoName="1" bSubrtn="0" sComment="">
<LcnsInfo sLcnsId="" sPwd=""></LcnsInfo>
<vrblValMaxCycle>
<DValue value="1." type="double"></DValue>
</vrblValMaxCycle>
<Algorithm guid="51AF1228-39D3-4ffc-8530-71FACCA812B7">
<Params></Params>
</Algorithm>
<Domain guid="CED621BD-F4D1-4ffa-A2F6-DB2BB1913E8C">
<Params>
<DValue type="lvlName" name="valMapLvl">
<MapLvlProxy strName="Segmentation 1" bVrbl="0">
<Assignment MapLvl="1" MapName="main"></Assignment>
<Scope GUID="00000000-0000-0000-0000-000000000000"></Scope>
</MapLvlProxy>
</DValue>
<DValue type="vector" name="mClssFltr">
<Values>
<DValue value="Disabled" type="string" indx="0"></DValue>
</Values>
</DValue>
<DValue type="threshold" name="valThrsh"></DValue>
<DValue type="threshold" name="valThrsh2"></DValue>
<DValue value="From Parent" type="string" name="valMap"></DValue>
<DValue value="From Parent" type="string" name="valROI"></DValue>
<DValue value="0" type="int" name="iNumMaxObj"></DValue>
<DValue value="4" type="int" name="iVersion"></DValue>
<DValue value="-1" type="int" name="iOldLvl"></DValue>
<DValue value="0" type="int" name="iOldDsplLvl"></DValue>
<DValue value="0" type="int" name="iOldDsplNumLvl"></DValue>
</Params>
</Domain>
<SubProc></SubProc>
</ProcBase>
<ProcBase Name="loop: test with Rel. border to rough_snow >= 0.5  at  Segmentation 1: rough_snow" bLoopChg="1" bExpand="1" bActive="1" bAutoName="1" bSubrtn="0" sComment="">
<LcnsInfo sLcnsId="" sPwd=""></LcnsInfo>
<vrblValMaxCycle>
<DValue value="5." type="double"></DValue>
</vrblValMaxCycle>
<Algorithm guid="3AC44F21-C6B2-4804-9929-BB18BE6F2051">
<Params>
<DValue value="1" type="clssId" name="valClass"></DValue>
</Params>
</Algorithm>
<Domain guid="CED621BD-F4D1-4ffa-A2F6-DB2BB1913E8C">
<Params>
<DValue type="lvlName" name="valMapLvl">
<MapLvlProxy strName="Segmentation 1" bVrbl="0">
<Assignment MapLvl="1" MapName="main"></Assignment>
<Scope GUID="00000000-0000-0000-0000-000000000000"></Scope>
</MapLvlProxy>
</DValue>
<DValue type="vector" name="mClssFltr">
<Values>
<DValue value="6" type="clssId" indx="0"></DValue>
<DValue value="User defined" type="string" indx="1"></DValue>
</Values>
</DValue>
<DValue type="threshold" name="valThrsh">
<TermThrsh>
<TermGroup eJoint="2">
<TermCondition eCmpr="4" eBaseUnit="0" eJoint="2">
<ProcVrblVal1>
<DValue type="propDscrId">
<PropDscrId GUID="AA7CAC99-696D-4983-8F48-D07C4F816F2C" InstID="Rel. border to rough_snow"></PropDscrId>
</DValue>
</ProcVrblVal1>
<ProcVrblVal2>
<DValue value="0.5" type="double"></DValue>
</ProcVrblVal2>
</TermCondition>
</TermGroup>
</TermThrsh>
</DValue>
<DValue type="threshold" name="valThrsh2"></DValue>
<DValue value="From Parent" type="string" name="valMap"></DValue>
<DValue value="From Parent" type="string" name="valROI"></DValue>
<DValue value="0" type="int" name="iNumMaxObj"></DValue>
<DValue value="4" type="int" name="iVersion"></DValue>
<DValue value="-1" type="int" name="iOldLvl"></DValue>
<DValue value="0" type="int" name="iOldDsplLvl"></DValue>
<DValue value="0" type="int" name="iOldDsplNumLvl"></DValue>
</Params>
</Domain>
<SubProc></SubProc>
</ProcBase>
```

<ProcBase Name="2x: test with Rel. border to rough_snow >= 0.25 at Segmentation 1: rough_snow" bLoopChg="0" bExpand="1" bActive="1" bAutoName="1" bSubrtn="0" sComment="">
<LcnsInfo sLcnsId="" sPwd=""></LcnsInfo>
<vrblValMaxCycle>
<DValue value="2." type="double"></DValue>
</vrblValMaxCycle>
<Algorithm guid="3AC44F21-C6B2-4804-9929-BB18BE6F2051">
<Params>
<DValue value="1" type="clssId" name="valClass"></DValue>
</Params>
</Algorithm>
<Domain guid="CED621BD-F4D1-4ffa-A2F6-DB2BB1913E8C">
<Params>
<DValue type="lvlName" name="valMapLvl">
<MapLvlProxy strName="Segmentation 1" bVrbl="0">
<Assignment MapLvl="1" MapName="main"></Assignment>
<Scope GUID="00000000-0000-0000-0000-000000000000"></Scope>
</MapLvlProxy>
</DValue>
<DValue type="vector" name="mClssFltr">
<Values>
<DValue value="6" type="clssId" indx="0"></DValue>
<DValue value="User defined" type="string" indx="1"></DValue>
</Values>
</DValue>
<DValue type="threshold" name="valThrsh">
<TermThrsh>
<TermGroup eJoint="2">
<TermCondition eCmpr="4" eBaseUnit="0" eJoint="2">
<ProcVrblVal1>
<DValue type="propDscrId">
<PropDscrId GUID="AA7CAC99-696D-4983-8F48-D07C4F816F2C" InstID="Rel. border to rough_snow"></PropDscrId>
</DValue>
</ProcVrblVal1>
<ProcVrblVal2>
<DValue value="0.25" type="double"></DValue>
</ProcVrblVal2>
</TermCondition>
</TermGroup>
</TermThrsh>
</DValue>
<DValue type="threshold" name="valThrsh2"></DValue>
<DValue value="From Parent" type="string" name="valMap"></DValue>
<DValue value="From Parent" type="string" name="valROI"></DValue>
<DValue value="0" type="int" name="iNumMaxObj"></DValue>
<DValue value="4" type="int" name="iVersion"></DValue>
<DValue value="-1" type="int" name="iOldLvl"></DValue>
<DValue value="0" type="int" name="iOldDsplLvl"></DValue>
<DValue value="0" type="int" name="iOldDsplNumLvl"></DValue>
</Params>
</Domain>
<SubProc></SubProc>
</ProcBase>
<ProcBase Name="loop: test with Rel. border to rough_snow >= 0.5 at Segmentation 1: rough_snow" bLoopChg="1" bExpand="1" bActive="1" bAutoName="1" bSubrtn="0" sComment="">
<LcnsInfo sLcnsId="" sPwd=""></LcnsInfo>
<vrblValMaxCycle>
<DValue value="5." type="double"></DValue>
</vrblValMaxCycle>
<Algorithm guid="3AC44F21-C6B2-4804-9929-BB18BE6F2051">
<Params>
<DValue value="1" type="clssId" name="valClass"></DValue>
</Params>
</Algorithm>
<Domain guid="CED621BD-F4D1-4ffa-A2F6-DB2BB1913E8C">
<Params>
<DValue type="lvlName" name="valMapLvl">
<MapLvlProxy strName="Segmentation 1" bVrbl="0">
<Assignment MapLvl="1" MapName="main"></Assignment>
<Scope GUID="00000000-0000-0000-0000-000000000000"></Scope>
</MapLvlProxy>
</DValue>
<DValue type="vector" name="mClssFltr">
<Values>
<DValue value="6" type="clssId" indx="0"></DValue>
<DValue value="User defined" type="string" indx="1"></DValue>
</Values>
</DValue>
<DValue type="threshold" name="valThrsh">
<TermThrsh>
<TermGroup eJoint="2">
<TermCondition eCmpr="4" eBaseUnit="0" eJoint="2">
<ProcVrblVal1>
<DValue type="propDscrId">
<PropDscrId GUID="AA7CAC99-696D-4983-8F48-D07C4F816F2C" InstID="Rel. border to rough_snow"></PropDscrId>
</DValue>
</ProcVrblVal1>
<ProcVrblVal2>
<DValue value="0.5" type="double"></DValue>
</ProcVrblVal2>
</TermCondition>
</TermGroup>
</TermThrsh>
</DValue>
<DValue type="threshold" name="valThrsh2"></DValue>
<DValue value="From Parent" type="string" name="valMap"></DValue>
<DValue value="From Parent" type="string" name="valROI"></DValue>
<DValue value="0" type="int" name="iNumMaxObj"></DValue>
<DValue value="4" type="int" name="iVersion"></DValue>
<DValue value="-1" type="int" name="iOldLvl"></DValue>
<DValue value="0" type="int" name="iOldDsplLvl"></DValue>
<DValue value="0" type="int" name="iOldDsplNumLvl"></DValue>
</Params>
</Domain>
<SubProc></SubProc>
</ProcBase>
<ProcBase Name="dark_objects, snow, test, veg_buffor, vegetation at Segmentation 1: unclassified" bLoopChg="0" bExpand="1" bActive="1" bAutoName="1" bSubrtn="0" sComment="">
<LcnsInfo sLcnsId="" sPwd=""></LcnsInfo>
<vrblValMaxCycle>
<DValue value="1." type="double"></DValue>
</vrblValMaxCycle>
<Algorithm guid="3AC44F21-C6B2-4804-9929-BB18BE6F2051">
<Params>
<DValue value="-1" type="clssId" name="valClass"></DValue>
</Params>
</Algorithm>
<Domain guid="CED621BD-F4D1-4ffa-A2F6-DB2BB1913E8C">
<Params>
<DValue type="lvlName" name="valMapLvl">
<MapLvlProxy strName="Segmentation 1" bVrbl="0">
<Assignment MapLvl="1" MapName="main"></Assignment>
<Scope GUID="00000000-0000-0000-0000-000000000000"></Scope>
</MapLvlProxy>

```
</DValue>
<DValue type="vector" name="mClssFltr">
<Values>
<DValue value="4" type="clssId" indx="0"></DValue>
<DValue value="5" type="clssId" indx="1"></DValue>
<DValue value="6" type="clssId" indx="2"></DValue>
<DValue value="3" type="clssId" indx="3"></DValue>
<DValue value="2" type="clssId" indx="4"></DValue>
<DValue value="User defined" type="string" indx="5"></DValue>
</Values>
</DValue>
<DValue type="threshold" name="valThrsh"></DValue>
<DValue type="threshold" name="valThrsh2"></DValue>
<DValue value="From Parent" type="string" name="valMap"></DValue>
<DValue value="From Parent" type="string" name="valROI"></DValue>
<DValue value="0" type="int" name="iNumMaxObj"></DValue>
<DValue value="4" type="int" name="iVersion"></DValue>
<DValue value="-1" type="int" name="iOldLvl"></DValue>
<DValue value="0" type="int" name="iOldDsplLvl"></DValue>
<DValue value="0" type="int" name="iOldDsplNumLvl"></DValue>
</Params>
</Domain>
<SubProc></SubProc>
</ProcBase>
<ProcBase Name="unclassified at  Segmentation 1: merge region" bLoopChg="0" bExpand="1" bActive="1" bAutoName="1" bSubrtn="0" sComment="">
<LcnsInfo sLcnsId="" sPwd=""></LcnsInfo>
<vrblValMaxCycle>
<DValue value="1." type="double"></DValue>
</vrblValMaxCycle>
<Algorithm guid="2328636B-BAD3-4f5d-B5AA-FC209A0BFB65">
<Params>
<DValue value="0" type="bool" name="bFsnUp"></DValue>
<DValue type="vector" name="vThmLayerFlags">
<Values></Values>
</DValue>
</Params>
</Algorithm>
<Domain guid="CED621BD-F4D1-4ffa-A2F6-DB2BB1913E8C">
<Params>
<DValue type="lvlName" name="valMapLvl">
<MapLvlProxy strName="Segmentation 1" bVrbl="0">
<Assignment MapLvl="1" MapName="main"></Assignment>
<Scope GUID="00000000-0000-0000-0000-000000000000"></Scope>
</MapLvlProxy>
</DValue>
<DValue type="vector" name="mClssFltr">
<Values>
<DValue value="Unclsfy" type="string" indx="0"></DValue>
<DValue value="User defined" type="string" indx="1"></DValue>
</Values>
</DValue>
<DValue type="threshold" name="valThrsh"></DValue>
<DValue type="threshold" name="valThrsh2"></DValue>
<DValue value="From Parent" type="string" name="valMap"></DValue>
<DValue value="From Parent" type="string" name="valROI"></DValue>
<DValue value="0" type="int" name="iNumMaxObj"></DValue>
<DValue value="4" type="int" name="iVersion"></DValue>
<DValue value="-1" type="int" name="iOldLvl"></DValue>
<DValue value="0" type="int" name="iOldDsplLvl"></DValue>
<DValue value="0" type="int" name="iOldDsplNumLvl"></DValue>
</Params>
</Domain>
<SubProc></SubProc>
</ProcBase>
<ProcBase Name="unclassified with Rel. border to rough_snow = 1  and Area &amp;lt; 1000 Pxl at  Segmentation 1: rough_snow" bLoopChg="0" bExpand="1" bActive="1" bAutoName="1" bSubrtn="0"
sComment="">
<LcnsInfo sLcnsId="" sPwd=""></LcnsInfo>
<vrblValMaxCycle>
<DValue value="1." type="double"></DValue>
</vrblValMaxCycle>
<Algorithm guid="3AC44F21-C6B2-4804-9929-BB18BE6F2051">
<Params>
<DValue value="1" type="clssId" name="valClass"></DValue>
</Params>
</Algorithm>
<Domain guid="CED621BD-F4D1-4ffa-A2F6-DB2BB1913E8C">
<Params>
<DValue type="lvlName" name="valMapLvl">
<MapLvlProxy strName="Segmentation 1" bVrbl="0">
<Assignment MapLvl="1" MapName="main"></Assignment>
<Scope GUID="00000000-0000-0000-0000-000000000000"></Scope>
</MapLvlProxy>
</DValue>
<DValue type="vector" name="mClssFltr">
<Values>
<DValue value="Unclsfy" type="string" indx="0"></DValue>
<DValue value="User defined" type="string" indx="1"></DValue>
</Values>
</DValue>
<DValue type="threshold" name="valThrsh">
<TermThrsh>
<TermGroup eJoint="2">
<TermCondition eCmpr="5" eBaseUnit="0" eJoint="0">
<ProcVrblVal1>
<DValue type="propDscrId">
<PropDscrId GUID="AA7CAC99-696D-4983-8F48-D07C4F816F2C" InstID="Rel. border to rough_snow"></PropDscrId>
</DValue>
</ProcVrblVal1>
<ProcVrblVal2>
<DValue value="1." type="double"></DValue>
</ProcVrblVal2>
</TermCondition>
<TermCondition eCmpr="2" eBaseUnit="1" eJoint="2">
<ProcVrblVal1>
<DValue type="propDscrId">
<PropDscrId GUID="03E04ED0-94DD-45ee-801E-14D70E6E2417" InstID="Area"></PropDscrId>
</DValue>
</ProcVrblVal1>
<ProcVrblVal2>
<DValue value="1000." type="double"></DValue>
</ProcVrblVal2>
</TermCondition>
</TermGroup>
</TermThrsh>
</DValue>
<DValue type="threshold" name="valThrsh2"></DValue>
<DValue value="From Parent" type="string" name="valMap"></DValue>
<DValue value="From Parent" type="string" name="valROI"></DValue>
<DValue value="0" type="int" name="iNumMaxObj"></DValue>
<DValue value="4" type="int" name="iVersion"></DValue>
<DValue value="-1" type="int" name="iOldLvl"></DValue>
```

<DValue value="0" type="int" name="iOldDsplLvl"></DValue>
<DValue value="0" type="int" name="iOldDsplNumLvl"></DValue>
</Params>
</Domain>
<SubProc></SubProc>
</ProcBase>
<ProcBase Name="unclassified with Brightness > 2500 and Mean Layer 4 > 120 and Mean Layer 5 > 0.7 and Mean Layer 6 < 140 and Rel. border to rough_snow = 1 at Segmentation 1: rough_snow" bLoopChg="0" bExpand="1" bActive="1" bAutoName="1" bSubrtn="0" sComment="">
<LcnsInfo sLcnsId="" sPwd=""></LcnsInfo>
<vrblValMaxCycle>
<DValue value="1." type="double"></DValue>
</vrblValMaxCycle>
<Algorithm guid="3AC44F21-C6B2-4804-9929-BB18BE6F2051">
<Params>
<DValue value="1" type="clssId" name="valClass"></DValue>
</Params>
</Algorithm>
<Domain guid="CED621BD-F4D1-4ffa-A2F6-DB2BB1913E8C">
<Params>
<DValue type="lvlName" name="valMapLvl">
<MapLvlProxy strName="Segmentation 1" bVrbl="0">
<Assignment MapLvl="1" MapName="main"></Assignment>
<Scope GUID="00000000-0000-0000-0000-000000000000"></Scope>
</MapLvlProxy>
</DValue>
<DValue type="vector" name="mClssFltr">
<Values>
<DValue value="Unclsfy" type="string" indx="0"></DValue>
<DValue value="User defined" type="string" indx="1"></DValue>
</Values>
</DValue>
<DValue type="threshold" name="valThrsh">
<TermThrsh>
<TermGroup eJoint="2">
<TermCondition eCmpr="3" eBaseUnit="0" eJoint="0">
<ProcVrblVal1>
<DValue type="propDscrId">
<PropDscrId GUID="16B7A5B4-D807-4ab1-B769-D536B3C26B20" InstID="Brightness"></PropDscrId>
</DValue>
</ProcVrblVal1>
<ProcVrblVal2>
<DValue value="2500." type="double"></DValue>
</ProcVrblVal2>
</TermCondition>
<TermCondition eCmpr="3" eBaseUnit="0" eJoint="0">
<ProcVrblVal1>
<DValue type="propDscrId">
<PropDscrId GUID="44411C83-609B-4758-93D3-FF62DF246855" InstID="Mean Layer 4"></PropDscrId>
</DValue>
</ProcVrblVal1>
<ProcVrblVal2>
<DValue value="120." type="double"></DValue>
</ProcVrblVal2>
</TermCondition>
<TermCondition eCmpr="3" eBaseUnit="0" eJoint="0">
<ProcVrblVal1>
<DValue type="propDscrId">
<PropDscrId GUID="44411C83-609B-4758-93D3-FF62DF246855" InstID="Mean Layer 5"></PropDscrId>
</DValue>
</ProcVrblVal1>
<ProcVrblVal2>
<DValue value="0.6999999999999996" type="double"></DValue>
</ProcVrblVal2>
</TermCondition>
<TermCondition eCmpr="2" eBaseUnit="0" eJoint="0">
<ProcVrblVal1>
<DValue type="propDscrId">
<PropDscrId GUID="44411C83-609B-4758-93D3-FF62DF246855" InstID="Mean Layer 6"></PropDscrId>
</DValue>
</ProcVrblVal1>
<ProcVrblVal2>
<DValue value="140." type="double"></DValue>
</ProcVrblVal2>
</TermCondition>
<TermCondition eCmpr="5" eBaseUnit="0" eJoint="2">
<ProcVrblVal1>
<DValue type="propDscrId">
<PropDscrId GUID="AA7CAC99-696D-4983-8F48-D07C4F816F2C" InstID="Rel. border to rough_snow"></PropDscrId>
</DValue>
</ProcVrblVal1>
<ProcVrblVal2>
<DValue value="1." type="double"></DValue>
</ProcVrblVal2>
</TermCondition>
</TermGroup>
</TermThrsh>
</DValue>
<DValue type="threshold" name="valThrsh2"></DValue>
<DValue value="From Parent" type="string" name="valMap"></DValue>
<DValue value="From Parent" type="string" name="valROI"></DValue>
<DValue value="0" type="int" name="iNumMaxObj"></DValue>
<DValue value="4" type="int" name="iVersion"></DValue>
<DValue value="-1" type="int" name="iOldLvl"></DValue>
<DValue value="0" type="int" name="iOldDsplLvl"></DValue>
<DValue value="0" type="int" name="iOldDsplNumLvl"></DValue>
</Params>
</Domain>
<SubProc></SubProc>
</ProcBase>
<ProcBase Name="rough_snow at Segmentation 1: merge region" bLoopChg="0" bExpand="1" bActive="1" bAutoName="1" bSubrtn="0" sComment="">
<LcnsInfo sLcnsId="" sPwd=""></LcnsInfo>
<vrblValMaxCycle>
<DValue value="1." type="double"></DValue>
</vrblValMaxCycle>
<Algorithm guid="2328636B-BAD3-4f5d-B5AA-FC209A0BFB65">
<Params>
<DValue value="0" type="bool" name="bFsnUp"></DValue>
<DValue type="vector" name="vThmLayerFlags">
<Values></Values>
</DValue>
</Params>
</Algorithm>
<Domain guid="CED621BD-F4D1-4ffa-A2F6-DB2BB1913E8C">
<Params>
<DValue type="lvlName" name="valMapLvl">
<MapLvlProxy strName="Segmentation 1" bVrbl="0">
<Assignment MapLvl="1" MapName="main"></Assignment>
<Scope GUID="00000000-0000-0000-0000-000000000000"></Scope>
</MapLvlProxy>
</DValue>
<DValue type="vector" name="mClssFltr">

```
<Values>
<DValue value="1" type="clssId" indx="0"></DValue>
<DValue value="User defined" type="string" indx="1"></DValue>
</Values>
</DValue>
<DValue type="threshold" name="valThrsh"></DValue>
<DValue type="threshold" name="valThrsh2"></DValue>
<DValue value="From Parent" type="string" name="valMap"></DValue>
<DValue value="From Parent" type="string" name="valROI"></DValue>
<DValue value="0" type="int" name="iNumMaxObj"></DValue>
<DValue value="4" type="int" name="iVersion"></DValue>
<DValue value="-1" type="int" name="iOldLvl"></DValue>
<DValue value="0" type="int" name="iOldDsplLvl"></DValue>
<DValue value="0" type="int" name="iOldDsplNumLvl"></DValue>
</Params>
</Domain>
<SubProc></SubProc>
</ProcBase>
<ProcBase Name="rough_snow at  Segmentation 1: export object shapes to ObjectShapes" bLoopChg="0" bExpand="1" bActive="1" bAutoName="1" bSubrtn="0" sComment="">
<LcnsInfo sLcnsId="" sPwd=""></LcnsInfo>
<vrblValMaxCycle>
<DValue value="1." type="double"></DValue>
</vrblValMaxCycle>
<Algorithm guid="E8AAA2C4-4DCA-4684-A918-87E7C53CDC8D">
<Params>
<DValue value="0" type="int" name="eExportMode"></DValue>
<DValue value="ObjectShapes" type="string" name="strExportItem"></DValue>
<DValue value="-1" type="procVarId" name="vrblExportItem"></DValue>
<DValue value="D:\Korzeniowska\2013\automatic\snow_avalanches_automatic_X.shp" type="string" name="strExportPath"></DValue>
<DValue value="0" type="bool" name="bExportSeries"></DValue>
<DValue value="&lt;?xml version=&quot;1.0&quot; encoding=&quot;UTF-8&quot;?>&#xA;&lt;ExportInfo SingleFilePerWksp=&quot;0&quot; SingleFilePerItem=&quot;1&quot;
ExportItem=&quot;ObjectShapes&quot; ExportType=&quot;Vector&quot; DriverID=&quot;SHP&quot;
ExportPath=&quot;D:\Korzeniowska\2013\automatic\snow_avalanches_automatic_X.shp&quot;>&lt;/ExportInfo>" type="string" name="strExportItemInfo"></DValue>
<DValue value="temporary" type="string" name="valExportTempLayer"></DValue>
<DValue type="vector" name="vColInfo">
<Values></Values>
</DValue>
<DValue value="0" type="bool" name="bUseFtrList"></DValue>
<DValue value="Click to edit attribute table" type="string" name="EditAttrTbl"></DValue>
<DValue value="-1" type="procVarId" name="FeatureListAttrTbl"></DValue>
<DValue value="3" type="int" name="eGeomType"></DValue>
<DValue value="5" type="int" name="eExprtType"></DValue>
<DValue value="0" type="bool" name="bUse3DCoords"></DValue>
<DValue value="1" type="bool" name="bShpUseGeocoding"></DValue>
<DValue value="0" type="int" name="eCoordOrient"></DValue>
<DValue value="SHP" type="string" name="eExprtFormat"></DValue>
<DValue value="" type="string" name="featClassName"></DValue>
<DValue type="img_chnl" value="" name="pRefChnl"></DValue>
<DValue value="{:ArcSDE.Connect.Dir}\default.das" type="string" name="exprtStorageLocFile"></DValue>
<DValue value="700000,100000" type="string" name="spatDomainOffset"></DValue>
<DValue value="1000" type="string" name="spatDomainPrec"></DValue>
</Params>
</Algorithm>
<Domain guid="CED621BD-F4D1-4ffa-A2F6-DB2BB1913E8C">
<Params>
<DValue type="lvlName" name="valMapLvl">
<MapLvlProxy strName="Segmentation 1" bVrbl="0">
<Assignment MapLvl="1" MapName="main"></Assignment>
<Scope GUID="00000000-0000-0000-0000-000000000000"></Scope>
</MapLvlProxy>
</DValue>
<DValue type="vector" name="mClssFltr">
<Values>
<DValue value="1" type="clssId" indx="0"></DValue>
<DValue value="User defined" type="string" indx="1"></DValue>
</Values>
</DValue>
<DValue type="threshold" name="valThrsh"></DValue>
<DValue type="threshold" name="valThrsh2"></DValue>
<DValue value="From Parent" type="string" name="valMap"></DValue>
<DValue value="From Parent" type="string" name="valROI"></DValue>
<DValue value="0" type="int" name="iNumMaxObj"></DValue>
<DValue value="4" type="int" name="iVersion"></DValue>
<DValue value="-1" type="int" name="iOldLvl"></DValue>
<DValue value="0" type="int" name="iOldDsplLvl"></DValue>
<DValue value="0" type="int" name="iOldDsplNumLvl"></DValue>
</Params>
</Domain>
<SubProc></SubProc>
</ProcBase>
</SubProc>
</ProcBase>
</SubProc>
</ProcBase>
</SubProc>
</ProcBase>
</SubProc>
</ProcBase>
</SubProc>
</ProcBase>
</SubProc>
</ProcBase>
</SubProc>
</ProcBase>
</SubProc>
</ProcBase>
<ProcBase Name="delete 'New Level'" bLoopChg="0" bExpand="1" bActive="1" bAutoName="1" bSubrtn="0" sComment="">
<LcnsInfo sLcnsId="" sPwd=""></LcnsInfo>
<vrblValMaxCycle>
<DValue value="1." type="double"></DValue>
</vrblValMaxCycle>
<Algorithm guid="4D72CCF3-EB44-4dcb-B5E1-70CA007D50CE">
<Params>
<DValue type="lvlName" name="valMapLvl">
<MapLvlProxy strName="New Level" bVrbl="0">
<Assignment MapLvl="2" MapName="main"></Assignment>
<Scope GUID="00000000-0000-0000-0000-000000000000"></Scope>
</MapLvlProxy>
</DValue>
</Params>
</Algorithm>
<Domain guid="CC9F2C30-4DB0-4ef2-B864-63560D1D6BF3">
<Params>
<DValue type="threshold" name="valThrsh"></DValue>
<DValue type="threshold" name="valThrsh2"></DValue>
<DValue value="From Parent" type="string" name="valMap"></DValue>
</Params>
</Domain>
<SubProc></SubProc>
</ProcBase>
<ProcBase Name="delete 'Segmentation 1'" bLoopChg="0" bExpand="1" bActive="1" bAutoName="1" bSubrtn="0" sComment="">
```

<LcnsInfo sLcnsId="" sPwd=""></LcnsInfo>
<vrblValMaxCycle>
<DValue value="1." type="double"></DValue>
</vrblValMaxCycle>
<Algorithm guid="4D72CCF3-EB44-4dcb-B5E1-70CA007D50CE">
<Params>
<DValue type="lvlName" name="valMapLvl">
<MapLvlProxy strName="Segmentation 1" bVrbl="0">
<Assignment MapLvl="1" MapName="main"></Assignment>
<Scope GUID="00000000-0000-0000-0000-000000000000"></Scope>
</MapLvlProxy>
</DValue>
</Params>
</Algorithm>
<Domain guid="CC9F2C30-4DB0-4ef2-B864-63560D1D6BF3">
<Params>
<DValue type="threshold" name="valThrsh"></DValue>
<DValue type="threshold" name="valThrsh2"></DValue>
<DValue value="From Parent" type="string" name="valMap"></DValue>
</Params>
</Domain>
<SubProc></SubProc>
</ProcBase>
</ProcessList>
<ExportedItems>
<item name="ObjectShapes" type="Vector" driver="SHP" ext="shp" path="D:\Korzeniowska\2013\automatic\snow_avalanches_automatic_X.shp"></item>
</ExportedItems>
<LcnsIds></LcnsIds>
</eCog.Proc>

Bibliography

ADGGS: Alaska Division of Geological & Geophysical Surveys, Elevation Datasets in Alaska. (2015) [Online]. Available at: http://maps.dggs.alaska.gov/elevationdata/, Accessed on: June 2015.

Arp, C.D., Jones, B.M., Lu, Z., Whitman, M.S., 2012. Shifting balance of thermokarst lake ice regimes across the Arctic Coastal Plain of northern Alaska. Geophysical Research Letters 39, 1-5.

Aubrey, B., Nuth, C., Olaf, S., Hölbling, D., Strozzi, T., Ringkjøb, P., 2015. Remote sensing of environment automated classification of debris-covered glaciers combining optical, SAR and topographic data in an object-based environment. Remote Sensing of Environment 170, 372-387.

Avni, Y., 2005. Gully incision as a key factor in desertification in an arid environment, the Negev highlands, Israel. Catena 63, 185-220.

Baatz, M., Schäpe, A., 2000. Multiresolution Segmentation: an optimization approach for high quality multi-scale image segmentation. In: Strobl, J.; Blaschke, T.; Griesebner, G. (Eds.), Angewandte Geographische Informationsverarbeitung XII. Beiträge Zum AGIT-Symposium Salzburg 2000, Karlsruhe, Herbert Wichmann Verlag, 12-23.

Badoux, A., Andres, A., Techel, F., Hegg, C., 2016. Natural hazard fatalities in Switzerland from 1946 to 2015. Natural Hazards and Earth System Science 16, 2747-2768.

Bagli, S., Schweizer, J., 2009. Characteristics of wet-snow avalanche activity: 20 years of observations from a high alpine valley (Dischma, Switzerland). Natural Hazards 50, 97-108.

Bai, J., Chen, X., Li, J., Yang, L., Fang, H., 2011, Changes in the area of inland lakes in arid regions of central Asia during the past 30 years. Environmental Monitoring and Assessment 178, 247-256.

Baruch, A., Filin, S., 2011. Detection of gullies in roughly textured terrain using airborne laser scanning data. ISPRS Journal of Photogrammetry and Remote Sensing 665, 564-578.

Berti, M., Corsini, A., Daehne, A., 2013. Comparative analysis of surface roughness algorithms for the identification of active landslides. Geomorphology 182, 1-18.

Bishop, M.P., James, L.A., Shroder Jr, J.F., Walsh, S.J., 2012. Geospatial technologies and digital geomorphological mapping: Concepts, issues and research. Geomorphology 137, 5-26.

Blaschke, T., 2010. Object based image analysis for remote sensing. ISPRS Journal of Photogrammetry and Remote Sensing 65, 2-16.

Blaschke, T., Hay, G.J., Kelly, M., Lang, S., Hofmann, P., Addink, E., Feitosa, R.Q., van der Meer, F., van der Werff, H., van Coillie, F., Tiede, D., 2014. Geographic object-based image analysis - towards a new paradigm. ISPRS Journal of Photogrammetry and Remote Sensing 87, 180-191.

Booth, A.M., Roering, J.J., Perron, J.T., 2009. Automated landslide mapping using spectral analysis and high-resolution topographic data: Puget Sound lowlands, Washington, and Portland Hills, Oregon. Geomorphology 109, 132-147.

Brasington, J., Vericat, D., Rychkov, I., 2012. Modelling river bed morphology, roughness and surface sedimentology using high resolution terrestrial laser scanning. Water Resources Research 48, W11519.

Bründl, M., Etter, H.J., Steiniger, M., Klingler, C., Rhyner, J., Ammann, W.J., 2004. System Sciences IFKIS – A basis for managing avalanche risk in settlements and on roads in Switzerland. Natural Hazards and Earth System Science 4, 257-262.

Bühler, Y., Adams, M.S., Bösch, R., Stoffel, A., 2016. Mapping snow depth in alpine terrain with unmanned aerial systems (UASs): Potential and limitations. The Cryosphere 10, 1075-1088.

Bühler, Y., Adams, M.S., Stoffel, A., Boesch, R., 2017. Photogrammetric reconstruction of homogenous snow surfaces in alpine terrain applying near-infrared UAS imagery surfaces in alpine terrain applying near-infrared UAS imagery. International Journal of Remote Sensing 0, 1-24.

Bühler, Y., Hüni, A., Christen, M., Meister, R., Kellerberger, T., 2009. Automated detection and mapping of avalanche deposits using airborne optical remote sensing data. Cold Regions Science and Technology 57, 99-106.

Bühler, Y., Meier, L., Ginzler, C., 2015. Potential of operational high spatial resolution near-infrared remote sensing instruments for snow surface type mapping. IEEE Geoscience and Remote Sensing Letters 12, 821-825.

Byrne, G.F., Crapper, P.F., Mayo, K.K., 1980. Monitoring land-cover change by principal component analysis of multitemporal Landsat data. Remote Sensing of Environment 10, 175-184.

Carn, S.A., Clarisse, L., Prata, A.J., 2016. Multi-decadal satellite measurements of global volcanic degassing. Journal of Volcanology and Geothermal Research 311, 99-134.

Castebrunet, H., Eckert, N., Giraud, G., 2012. Snow and weather climatic control on snow avalanche occurrence fluctuations over 50 yr in the French Alps. Climate of the Past 8, 855-875.

Cavalli, M., Marchi, L., 2008. Characterisation of the surface morphology of an alpine alluvial fan using airborne LiDAR. Natural Hazards and Earth System Sciences 8, 323-333.

Cavalli, M., Tarolli, P., Marchi, L., Fontana, G.D., 2008. The effectiveness of airborne LiDAR data in the recognition of channel-bed morphology. Catena 73, 249-260.

Chand, P., Sharma, M.C., 2015. Glacier changes in the Ravi basin, north-western Himalaya (India) during the last four. Global and Planetary Change 135, 133-147.

Chander, G., Markham, B.L., Helder, D.L., 2009. Summary of current radiometric calibration coefficients for Landsat MSS, TM, ETM+, and EO-1 ALI sensors. Remote Sensing of Environment 113, 893-903.

Chen, W., Li, X., Wang, Y., Chen, G., Liu, S., 2014. Forested landslide detection using LiDAR data and the random forest algorithm: A case study of the Three Gorges, China. Remote Sensing of Environment 152, 291-301.

Chen, Y., Shi, P., Fung, T., Wang, J., Li, X., 2007. Object-oriented classification for urban land cover mapping with ASTER imagery. International Journal of Remote Sensing 28, 4645-4651.

Cheng, G., Han, J., 2016. A survey on object detection in optical remote sensing images. ISPRS Journal of Photogrammetry and Remote Sensing 117, 11-28.

Christen, M., Kowalski, J., Bartelt, P., 2010. RAMMS: Numerical simulation of dense snow avalanches in three-dimensional terrain. Cold Regions Science and Technology 63, 1-14.

Collins, J.B., Woodcock, C.E., 1996. An assessment of several linear change detection techniques for mapping forest mortality using multitemporal Landsat TM data. Remote Sensing of Environment 56, 66-77.

Cohen, J., 1960. A coefficient of agreement for nominal scales. Educational and Psychological Measurement 20, 37-46.

Congalton, R.G., 1991. A review of assessing the accuracy of classification of remotely sensed data. Remote Sensing of Environment 37, 35-46.

Conoscenti, C., Angileri, S., Cappadonia, C., Rotigliano, E., Agnesi, V., Märker, M., 2014. Gully erosion susceptibility assessment by means of GIS-based logistic regression: A case of Sicily (Italy). Geomorphology 204, 399-411.

Deardorff, N.D., Cashman, K.V., 2012. Emplacement conditions of the c. 1,600-year BP Collier Cone lava flow, Oregon: A LiDAR investigation. Bulletin of Volcanology 74, 2051-2066.

Deus, D., Gloaguen, R., 2013. Remote sensing analysis of lake dynamics in semi-arid regions: Implication for water resource management. Lake Manyara, East African Rift, Northern Tanzania. Water 5, 698-727.

Dey, V., Zhang, Y., Zhong, M., Engineering, G., 2010. A review on image segmentation techniques with remote sensing perspective, In: Wagner, W., Székely, B. (Eds.): ISPRS TC VII Symposium – 100 Years ISPRS, Vienna, Austria, July 5–7, 2010, IAPRS, Vol. XXXVIII, Part 7A, 31-42.

Drăguţ, L., Eisank, C., 2012. Automated object-based classification of topography from SRTM data. Geomorphology 141-142, 21-33.

Drăguţ, L., Tiede, D., Levick, S.R., 2010. ESP: a tool to estimate scale parameter for multiresolution image segmentation of remotely sensed data. International Journal of Geographical Information Science 24, 859-871.

d'Oleire-Oltmanns, S., Eisank, C., Drăgut, L., Blaschke, T., 2013. An object-based workflow to extract landforms at multiple scales from two distinct data types. IEEE Geoscience and Remote Sensing Letters 10, 947-951.

d'Oleire-Oltmanns, S., Marzolff, I., Tiede, D., Blaschke, T., 2014. Detection of gully-affected areas by applying Object-Based Image Analysis (OBIA) in the region of Taroudannt, Morocco. Remote Sensing 6, 8287-8309.

Dunne, T., Whipple, K.X., Aubry, B.F., 1995. Microtopography of hillslopes and initiation of channels by Horton overland flow. In: Natural and Anthropogenic Influences in Fluvial Geomorphology: The Wolman Volume, Geophysical Monograph, Costa EJ, Miller AJ, Potter KW, Wilcock PR (eds). 89 American Geophysical Union: Ashington, DC, 27-44.

Eckerstorfer, M. Bühler, Y., Frauenfelder, R., Malnes, E., 2016. Remote sensing of snow avalanches: Recent advances, potential, and limitations. Cold Regions Science and Technology 121, 126-140.

Eckerstorfer, M., Malnes, E., 2015. Manual detection of snow avalanche debris using high-resolution Radarsat-2 SAR images Radarsat-2 SAR images. Cold Regions Science and Technology 120, 205-218.

Eisank, C., Smith, M., Hillier, J., 2014. Assessment of multiresolution segmentation for delimiting drumlins in digital elevation models. Geomorphology 214, 452-464.

ESRI LiDAR Processing Toolbox. (2016) [Online]. Available at: https://www.arcgis.com/home/item.html?id=73bf90dc110f46d6ac4c10400cdc7c1d, Accessed on: June 2016.

Evans, I.S., 1972. General geomorphometry, derivations of altitude and descriptive statistics. In: Spatial Analysis in Geomorphology. London: Mathuen & Co., Ltd., 17-90.

Evans, M., Lindsay, J., 2010. High resolution quantification of gully erosion in upland peatlands at the landscape scale. Earth Surface Processes and Landforms 35, 876-886.

Fang, Y., Cheng, W., Zhang, Y., Wang, N., Zhao, S., Zhou, C., Chen, X., Bao, A., 2016. Changes in inland lakes on the Tibetan Plateau over the past 40 years. Journal of Geographical Science 26, 415-438.

Feyisa, G.L., Meilby, H., Fensholt, R., Proud, S.R., 2014. Automated water extraction index: A new technique for surface water mapping using Landsat imagery. Remote Sensing of Environment 140, 23-35.

Fisher, A., Flood, N., Danaher, T., 2016. Comparing Landsat water index methods for automated water classification in eastern Australia. Remote Sensing of Environment 175, 167-182.

Fitzpatrick, A.A.W., Hubbard, A.L., Box, J.E, Quincey, D.J., Van As, D., Mikkelsen, A.P.B., Doyle, S.H., Dow, C.F., Hasholt, B., Jones, G.A., 2014. A decade (2002-2012) of supraglacial lake volume estimates across Russell Glacier, West Greenland. Cryosphere 8, 107-121.

Frankel, K.L., Dolan, J.F., 2007. Characterizing arid region alluvial fan surface roughness with airborne laser swath mapping digital topographic data. Journal of Geophysical Research 112, 1-14.

Frazier, P.S., Page, K.J., 2000. Water body detection and delineation with Landsat TM data. Photogrammetric Engineering & Remote Sensing 66, 1461-1467.

Friedl, M.A., Sulla-Menashe, D., Tan, B., Schneider, A., Ramankutty, N., Sibley, A., Huang, X., 2010. MODIS Collection 5 global land cover: Algorithm refinements and characterization of new datasets. Remote Sensing of Environment 114, 168-182.

Gao, H., Birkett, C., Lettenmaier, D.P., 2012. Global monitoring of large reservoir storage from satellite remote sensing. Water Resources Research 48, 1-12.

Gill, J.C., Malamud, B.D., 2017. Earth-Science reviews anthropogenic processes, natural hazards, and interactions in a multi-hazard framework. Earth-Science Reviews 166, 246-269.

Glenn, N.F., Streutker, D.R., Chadwick, D.J., Thackray, G.D., 2006. Analysis of LiDAR-derived topographic information for characterizing and differentiating landslide morphology and activity. Geomorphology 73, 131-148.

Grohmann, C.H., Riccomini, C., 2009. Comparison of roving-window and search-window techniques for characterising landscape morphometry. Computers & Geosciences 35, 2164-2169.

Grohmann, C.H., Smith, M.J., Riccomini, C., 2011. Multiscale analysis of topographic surface roughness in the Midland Valley, Scotland. IEEE Transactions on Geoscience and Remote Sensing: 49(4), 1200- 1213.

Grohmann, C.H., 2015. Effects of spatial resolution on slope and aspect derivation for regional-scale analysis. Computers & Geosciences 77, 111-117.

Habib, T., Gay, M., Chanussot, J., Bertolino, P., 2006. Segmentation of high resolution satellite images SPOT applied to lake detection. International Geoscience and Remote Sensing Symposium, Denver, CO, USA, 31 July-4August 2006, 3680-3683.

Hansen, M.C., Loveland, T.R., 2012. A review of large area monitoring of land cover change using Landsat data. Remote Sensing of Environment 122, 66-74.

Haneberg, W.C., Creighton, A.L., Medley, E.W., Jonas, D.A., 2005. Use of LiDAR to assess slope hazards at the Lihir gold mine, Papua New Guinea. In: Proceeding, International Conference on Landslide Risk Management. Vancouver, British Columbia, May-June, Supplementary CD.

Hani, A.F., Sathyamoorthy, D., Asirvadam, V.S., 2011. A method for computation of surface roughness of digital elevation model terrain via multiscale analysis. Computers & Geosciences 37, 177-192.

Haralick, R.M., Sternberg, S.R., Zhuang, X., 1987. Image analysis using mathematical Morphology. IEEE Transactions on Pattern Analysis and Machine Intelligence 9, 532-550.

Helming, K., Roth, C.H., Wolf, R., Diestel, H., 1993. Characterization of rainfall-microrelief interactions with runoff using parameters derived from Digital Elevation Models (DEMs). Soil Technology 6, 273-286.

Hodgson, M.E., 1995. What cell size does the computed slope/aspect angle represent? Photogrammetric Engineering & Remote Sensing 61, 513-517.

Hoffman, R., Krotkov, E., 1989. Terrain roughness measurement from elevation maps. In: Proceedings of the SPIE, Mobile Robots IV, Chun WH, Wolfe WJ (eds). 1195, 104-114.

Höfle, B., Griesbaum, L., Forbriger, M., 2013. GIS-based detection of gullies in terrestrial LiDAR data of the Cerro Llamoca Peatland (Peru). Remote Sensing 5, 5851-5870.

Hölbling, D., Friedl, B., Eisank, C., 2015. An object-based approach for semi-automated landslide change detection and attribution of changes to landslide classes in northern Taiwan. Earth Science Informatics 8, 327-335.

Immerzeel, W.W., van Beek, L.P.H., Bierkens, M.F.P., 2010. Climate change will affect the Asian Water Towers. Science 328, 1382-1385.

Immerzeel, W.W., Kraaijenbrink, P.D.A., Shea, J.M., Shrestha, A.B., Pellicciotti, F., Bierkens, M.F.P., De Jong, S.M., 2014. High-resolution monitoring of Himalayan glacier dynamics using unmanned aerial vehicles. Remote Sensing of Environment 150, 93-103.

Ionita, I., Fullen, M.A., Zgłobicki, W., 2015. Gully erosion as a natural and human-induced hazard. Natural Hazards 79, S1-S5.

Jaboyedoff, M., Oppikofer, T., Abellán, A., Derron, M.-H., Loye, A., Metzger, R., Pedrazzini, A., 2012. Use of LIDAR in landslide investigations: A review. Natural Hazards 65, 5-28.

James, L.A., Watson, D.G., Hansen, W.F., 2007. Using LiDAR data to map gullies and headwater streams under forest canopy: South Carolina, USA. Catena 71, 132-144.

Jawak, S.D., Luis, A.J., 2014. A semiautomatic extraction of Antarctic lake features using Worldview-2 imagery. Photogrammetric Engineering & Remote Sensing 80, 33-46.

Jawak, S.D., Kulkarni, K., Luis, A.J., 2015. A review on extraction of lakes from remotely sensed optical satellite data with a special focus on cryospheric lakes. Advances in Remote Sensing 4, 196-213.

Ji, L., Zhang, L., Wylie, B., 2009. Analysis of dynamic thresholds for the normalized difference water index. Photogrammetric Engineering & Remote Sensing 75, 1307-1317.

Jiang, H., Feng, M., Zhu, Y., Lu, N., Huang, J., Xiao, T., 2014. An automated method for extracting rivers and lakes from Landsat imagery. Remote Sensing 6, 5067-5089.

Kimerling, A.J., Buckley, A.R., Muehrcke, P.C., Muehrcke, J.O. (eds), 2011. Map Use: Reading Analysis Interpretation, Seventh Edition, ESRI Press, Redlands, California: 610.

Korzeniowska, K., Pfeifer, N., Mandlburger, G., Lugmayr, A., 2014. Experimental evaluation of ALS point cloud ground extraction tools over different terrain slope and land-cover types. International Journal of Remote Sensing 13, 4673-4697.

Kraaijenbrink, P.D.A., Shea, J.M., Pellicciotti, F., de Jong, S.M., Immerzeel, W.W., 2016. Remote sensing of environment object-based analysis of unmanned aerial vehicle imagery to map and characterise surface features on a debris-covered glacier. Remote Sensing of Environment 186, 581-595.

Kreslavsky, M.A., Head, III J.W., 1999. Kilometer-scale slopes on Mars and their correlation with geologic units: Initial results from Mars Orbiter Laser Altimeter (MOLA) data. Journal of Geophysical Research 104, 911-924.

LaHusen, S.R., Duvell, A.R., Booth, A.M., Montgomery, D.R., 2016. Surface roughness dating of long-runout landslide near Oso, Washington (USA), reveals persistent postglacial hillslope instability. Geology 44, 111-114.

Lam, D.K., Remmel, T.K., Drezner, T.D., 2011. Tracking desertification in California using remote sensing: A sand dune encroachment approach. Remote Sensing 3, 1-13.

Larsen, S.Ø., Salberg, A., Solberg, R., 2013. Automatic avalanche mapping using texture classification of optical satellite imagery. In: Lasaponara, R., Masini, N., Biscione, M. (Eds.), EARSeL, 2013. Towards Horizon 2020, pp. 399-410.

Lato, M.J., Frauenfelder, R., Bühler, Y., 2012. Automated detection of snow avalanche deposits: Segmentation and classification of optical remote sensing imagery. Natural Hazards and Earth System Science 12, 2893-2906.

Li, J., Sheng, Y., Luo, J., 2011. Automatic extraction of Himalayan glacial lakes with remote sensing. Journal of Remote Sensing 15, 29-43.

Li, S., MacMillan, R.A., Loob, D.A., McConkey, B.G., Moulin, A., Fraser, W.R., 2011. Lidar DEM error analyses and topographic depression identification in a hummocky landscape in the prairie region of Canada. Geomorphology 129, 263-275.

Liu, J., Kang, S., Gong, T., Lu, A., 2010. Growth of a high-elevation large inland lake, associated with climate change and permafrost degradation in Tibet. Hydrology and Earth System Science 14, 481-489.

Liu, S., Hodgson, M.E., 2016. Satellite image collection modeling for large area hazard emergency response. ISPRS Journal of Photogrammetry and Remote Sensing 118, 13-21.

Liu, X., Chen, B., 2000. Climatic warming in the Tibetan Plateau during recent decades. International Journal of Climatology 20, 1729-1742.

Lei, Y., Yao, T., Bird, B.W., Yang, K., Zhai, J., Sheng, Y., 2013. Coherent lake growth on the central Tibetan Plateau since the 1970s : Characterization and attribution. Journal of Hydrology 483, 61-67.

Lu, P., Stumpf, A., Kerle, N., Casagli, N., 2011. Object-oriented change detection for landslide rapid mapping. IEEE Geoscience and Remote Sensing Letters 8, 701-705.

Lunetta, R.S., Knight, J.F., Ediriwickrema, J., Lyon, J.G., Worthy, L.D., 2006. Land-cover change detection using multi-temporal MODIS NDVI data. Remote Sensing of Environment 105, 142-154.

Ma, R., Duan, H., Hu, C., Feng, X., Li, A., Ju, W., Jiang, J., Yang, G., 2010. A half - century of changes in China's lakes : Global warming or human influence? Geophysical Research Letters 37, 2-7.

Martha, T.R., Kerle, N., Van Westen, C.J., Jetten, V., Kumar, K.V., 2011. Segment optimization and data-driven thresholding for knowledge-based landslide detection by object-based image analysis. IEEE Transactions on Geoscience and Remote Sensing 49, 4928-4943.

Martha, T.R., Kerle, N., van Westen, C.J., Jetten, V., Vinod Kumar, K., 2012. Object-oriented analysis of multi-temporal panchromatic images for creation of historical landslide inventories. ISPRS Journal of Photogrammetry and Remote Sensing 67, 105-119.

Martinez-Casasnovas, J.A., 2003. A spatial information technology approach for the mapping and quantification of gully erosion. Catena 50, 293-308.

Marzolff, I., Poesen, J., 2009. The potential of 3D gully monitoring with GIS using high-resolution aerial photography and digital photogrammetry system. Geomorphology 111, 48-60.

Mason, D.C., Trigg, M., Garcia-Pintado, J., Cloke, H.L., Neal, J.C., Bates, P.D., 2016. Remote sensing of environment improving the TanDEM-X digital elevation model for flood modelling using flood extents from synthetic aperture radar images. Remote Sensing of Environment 173, 15-28.

MATLAB and Statistics Toolbox Release 2014b, The MathWorks, Inc., Natick, Massachusetts, United States.

McClung, D., Schaerer, P., 2006. The Avalanche Handbook. The Mountaineers Book, Seattle.

McClung, D.M., 2016. Avalanche character and fatalities in the high mountains of Asia. Annals of Glaciology 57, 114-118.

McFeeters, S.K., 1996. The use of the normalized difference water index (NDWI) in the delineation of open water features. International Journal of Remote Sensing 17, 1425-1432.

McFeeters, S.K., 2013. Using the normalized difference water index (NDWI) within a geographic information system to detect swimming pools for mosquito abatement: A practical approach. Remote Sensing 5, 3544-3561.

McKean, J., Roering, J., 2004. Objective landslide detection and surface morphology mapping using high-resolution airborne laser altimetry. Geomorphology 57, 331-351.

Melesse, A.M., Weng, Q., Thenkabail, P.S., Seney, G.B., 2007. Remote sensing sensors and applications in environmental resources mapping and modelling. Sensors 7, 3209-3241.

Milenković, M., Pfeifer, N., Glira, P., 2015. Applying terrestrial laser scanning for soil surface roughness assessment. Remote Sensing 7, 2007-2045.

Mueller, N., Lewis, A., Roberts, D., Ring, S., Melrose, R., Sixsmith, J., Lymburner, L., McIntyre, A., Tan, P., Curnow, S., Ip, A., 2016. Water observations from space: Mapping surface water from 25 years of Landsat imagery across Australia. Remote Sensing of Environment 174, 341–352.

Murray, N.J., Phinn, S.R., Clemens, R.S., Roelfsema, C.M., Fuller, R.A., 2012. Continental scale mapping of tidal flats across east Asia using the Landsat archive. Remote Sensing 4, 3417-3426.

Myint, S.W., Yuan, M., Cerveny, R.S., Giri, C.P., 2008. Comparison of remote sensing image processing techniques to identify tornado damage areas from Landsat TM data. Sensors 8, 1128-1156.

Nath, R.K., Deb, S.K., 2010. Water-body area extraction from high resolution satellite images-An introduction, review, and comparison. International Journal of Image Processing 3, 353-372.

Open Topography. (2015) [Online]. Available at: http://opentopo.sdsc.edu/, Accessed on: June 2015.

Otsu, N., 1979. A threshold selection method from Gray-level histograms. IEEE Transactions on Systems, Man, and Cybernetics SMC-9(1), 62-66.

Ouma, Y.O., Tateishi, R., 2006. A water index for rapid mapping of shoreline changes of five East African Rift Valley lakes: An empirical analysis using Landsat TM and ETM+ data. International Journal of Remote Sensing 27, 3153-3181.

Passalacqua, P., Trung, T.D., Foufoula-Georgiou, E., Sapiro, G., Dietrich, W.E., 2010. A geometric framework for channel network extraction from LiDAR: Nonlinear diffusion and geodetic paths. Journal of Geophysical Research 115, 1-18.

Pedersen, G.B.M., 2016. Semi-automatic classification of glaciovolcanic landforms : An object-based mapping approach based on geomorphometry. Journal of Volcanology and Geothermal Research 311, 29-40.

Perroy, R.L., 2009. Quantifying land degradation and vegetation recovery on southwestern Santa Cruz Island, California. Ph.D. Thesis, UCSB, Santa Barbara, California.

Perroy, R.L., Bookhagen, B., Asner, G.P., Chadwick, O.A., 2010. Comparison of gully erosion estimates using airborne and ground-based LiDAR on Santa Cruz Island, California. Geomorphology 118, 288-300.

Peter, K.D., d'Oleire-Oltmanns, S., Ries, J.B., Marzolff, I., Hssaine, A.A., 2014. Soil erosion in gully catchments affected by land-levelling measures in the Souss basin, Morocco, analysed by rainfall simulation and UAV remote sensing data. Catena 113, 24-40.

Phan, V. H., Lindenbergh, R., Menenti, M., 2012. ICESat derived elevation changes of Tibetan lakes between 2003 and 2009. International Journal of Applied Earth Observation and Geoinformation 17, 12-22.

Pike, R.J., 1988. The geometric signature: Quantifying landslide-terrain types from digital elevation models. Mathematical Geology 20, 491-511.

Pike, R.J., 2000. Geomorphometry – diversity in quantitative surface analysis. Progress in Physical Geography 24, 1-20.

Poesen, J., 2011. Challenges in gully erosion research. Landform Analysis 17, 5-9.

Poesen, J., Nachtergaele, J., Verstraeten, G., Velentin, C., 2003. Gully erosion and environmental change: Importance and research needs. Catena 50, 91-133.

Pollyea, R.M., Fairley, J.P., 2011. Estimating surface roughness of terrestrial laser scan data using orthogonal distance regression. Geology 39, 623-626.

Pope, A., Rees, W.G., 2014. Impact of spatial, spectral, and radiometric properties of multispectral imagers on glacier surface classification. Remote Sensing of Environment 141, 1-13.

Potter, K.N., Zobeck, T.M., Hagen, L.J., 1990. A microrelief index to estimate soil erodibility by wind. Transactions of ASAE 33, 151-155.

Price, J.C., 1994. How unique are spectral signatures? Remote Sensing of Environment 49, 181-186.

Qiu, J., 2008. The Third Pole. Nature 454, 393-396.

Reuter, H. I., Nelson, A., Jarvis, A., 2007. An evaluation of void-filling interpolation methods for SRTM data. International Journal of Geographical Information Science 21, 983-1008.

Riley, S.J., De Gloria, S.D., Elliot, R., 1999. A terrain ruggedness index that quantifies topographic heterogeneity. Intermountain Journal of Sciences 5, 23-27.

Roering, J.J., Marshall, J., Booth, A.M., Mort, M., Jin, Q., 2010. Evidence for biotic controls on topography and soil production. Earth and Planetary Science Letters 298, 183-190.

Rogers, A.S., Kearney, M. S., 2004. Reducing signature variability in unmixing coastal marsh Thematic Mapper scenes using spectral indices. International Journal of Remote Sensing 25, 2317-2335.

Rokni, K., Ahmad, A., Selamat, A., Hazini, S., 2014. Water feature extraction and change detection using multitemporal Landsat imagery. Remote Sensing 6, 4173-4189.

Ryu, J.H., Won, J.S., Min, K.D., 2002. Waterline extraction from Landsat TM data in a tidal flat a case study in Gomso Bay, Korea. Remote Sensing of Environment 83, 442-456.

Sagy, A., Axen, G.J., 2007. Evolution of fault-surface roughness with slip. Geology 35, 283-286.

Saho, P.K., Soltani, S., Wong, A.K.C., Chen, Y.C., 1988. A survey of thresholding techniques. Computer Vision, Graphics, and Image Processing 41, 233-260.

Schmidt, J., Evans, I.S., Brinkmann, J., 2003. Comparison of polynomial models for land surface calculation. International Journal of Geographical Information Science 17, 797-814.

Sezgin, M., Sankur, B., 2004. Survey over image thresholding techniques and quantitative performance evaluation. Journal of Electronic Imaging 13, 146-165.

Schneider, A., 2012. Monitoring land cover change in urban and peri-urban areas using dense time stacks of Landsat satellite data and a data mining approach. Remote Sensing of Environment 124, 689-704.

Schweizer, J., Jamieson, J.B., 2001. Snow cover properties for skier triggering of avalanches. Cold Regions Science and Technology 33, 207-221.

Schweizer, J., Jamieson, J.B., Schneebeli, M., 2003. Snow avalanche formation. Reviews of Geophysics 41, 1-25.

Sekhon, N.S., Hassan, Q.K., Sleep, R.W., 2010. Evaluating potential of MODIS-based indices in determining “snow gone” stage over forest-dominant regions. Remote Sensing 2, 1348-1363.

Shao, Z.G., Zhu, D.G., Meng, X.G., Zheng, D.X., Qiao, Z.J., Bin Yang, C., Han, J.E., Yu, J., Meng, Q.W., Lü, R.P., 2007. Characteristics of the change of major lakes on the Qinghai-Tibet Plateau in the last 25 years. Geological Bulletin of China 26, 1633-1645.

Shary, P.A., 1995. Land surface gravity points classification by a complete system of curvatures. Mathematical Geology 27, 373-390.

Sheng, Y., Song, C., Wang, J., Lyons, E.A., Knox, B.R., Cox, J.S., Gao, F., 2016. Representative lake water extent mapping at continental scales using multi-temporal Landsat-8 imagery. Remote Sensing of Environment 185, 129-141.

Shepard, M.K., Campbell, B.A., Bulmer, M.H., Farr, T.G., Gaddis, L.R., Plaut, J.J., 2001. The roughness of natural terrain: A planetary and remote sensing perspective. Journal of Geophysical Research 106, 777-795.

Shruthi, R.B.V., Kerle, N., Jetten, V., 2011. Object-based gully feature extraction using high spatial resolution imagery. Geomorphology 134, 260-268.

Shruthi, R.B.V, Kerle, N., Jetten, V., Abdellah, L., Machmach, I., 2015. Quantifying temporal changes in gully erosion areas with object oriented analysis. Catena 128, 262-277.

Singh, A., 1989. Review article digital change detection techniques using remotely-sensed data. International Journal of Remote Sensing 10, 989-1003.

Sithole, G., Vosselman, G., 2004. Experimental comparison of filter algorithms for bare-Earth extraction from airborne laser scanning point clouds. ISPRS Journal of Photogrammetry and Remote Sensing 59, 85-101.

SLIDO: Statewide Landslide Information Layer for Oregon. (2015) [Online]. Available at: http://www.oregongeology.org/slido/, Accessed on: June 2015.

Smith, M.W., 2014. Roughness in the Earth Sciences. Earth-Science Reviews 136, 202-225.

Song, C., Huang, B., Ke, L., 2013. Modeling and analysis of lake water storage changes on the Tibetan Plateau using multi-mission satellite data. Remote Sensing of Environment 135, 25-35.

Song, C., Huang, B., Ke, L., Richards, K.S., 2014a. Remote sensing of alpine lake water environment changes on the Tibetan Plateau and surroundings: A review. ISPRS Journal of Photogrammetry and Remote Sensing 92, 26-37.

Song, C., Huang, B., Ke, L., Richards, K.S., 2014b. Seasonal and abrupt changes in the water level of closed lakes on the Tibetan Plateau and implications for climate impacts. Journal of Hydrology 514, 131-144.

Stehman, S.V., 1997. Selecting and interpreting measures of thematic classification accuracy. Remote Sensing of Environment 62, 77-89.

Stöcker, C., Eltner, A., Karrasch, P., 2015. Measuring gullies by synergetic application of UAV and close range photogrammetry – A case study from Andalusia, Spain. Catena 132, 1-11.

Strumpf, A., Kerle, N., 2011. Object-oriented mapping of landslides using Random Forests. Remote Sensing of Environment 115, 2564-2577.

Swets, J.A., 1988. Measuring the accuracy of diagnostic systems. Science 240, 1285-1293.

Techel, F., Jarry, F., Kronthaler, G., Mitterer, S., Nairz, P., Pavsek, M., Valt, M., Darms, G., 2016. Avalanche fatalities in the European Alps: Long-term trends and statistics. Geographica Helvetica 71, 147-159.

Techel, F., Zweifel, B., Winkler, K., 2015. Analysis of avalanche risk factors in backcountry terrain based on usage frequency and accident data in Switzerland. Natural Hazards and Earth System Science 15, 1985-1997.

Thouret, J., Kassouk, Z., Gupta, A., Chin, S., Solikhin, A., 2015. Remote Sensing of Environment Tracing the evolution of 2010 Merapi volcanic deposits (Indonesia) based on object-oriented classification and analysis of multi-temporal, very high resolution images. Remote Sensing of Environment 170, 350-371.

Torri, D., Poesen, J., 2014. A review of topographic threshold conditions for gully head development in different environments. Earth-Science Reviews 130, 73-85.

Townshend, J.R.G., Justice, C.O., 1986. Analysis of the dynamics of African vegetation using the normalized difference vegetation index. International Journal of Remote Sensing 7, 1435-1445.

Trevisani, S., Cavalli, M., Marchi, L., 2012. Surface texture analysis of a high-resolution DTM: Interpreting an alpine basin. Geomorphology 161-162, 26-39.

Trevisani, S., Rocca, M., 2015. MAD: Robust image texture analysis for application in high resolution geomorphometry. Computers & Geosciences 81, 78-92.

Trimble, 2015. eCognition Developer Reference Book. Westminster, USA, 1-512.

Turker, M., Sumer, E., 2008. Building-based damage detection due to earthquake using the watershed segmentation of the post-event aerial images. International Journal of Remote Sensing 29, 3073-3089.

Van Den Eeckhaut, M., Kerle, N., Poesen, J., Hervas, J., 2012. Object-oriented identification of forested landslides with derivatives of single pulse LiDAR data. Geomorphology 173-174, 30-42.

Van der Sande, C.J., de Jong, S.M., de Roo, A.P.J., 2003. A segmentation and classification approach of IKONOS-2 imagery for land cover mapping to assist flood risk and flood damage assessment. International Journal of Applied Earth Observation 4, 217-229.

Vanmaercke, M., Poesen, J., Van Mele, B., Demuzere, M., Bruynseels, A., Golosov, V., Bezerra, J.F.R., Boylsov, S., Dvinskih, A., Frankl, A., Fuseina, Y., Guerra, A.J.T., Haregeweyn, N., Ionita, I., Imwangana, F.M., Moeyersons, J., Moshe, I., Samani, A.N., Niacsu, L., Nyssen, J., Otsuki, Y., Radoane, M., Rysin, I., Ryzhov, Y.V., Yermolaev, O., 2016. How fast do gully headcuts retreat. Earth-Science Reviews 154, 336-355.

Varma, M., Zisserman, A., 2004. A statistical approach to texture classification from single images. International Journal of Computer Vision 62, 61-81.

Verpoorter, C., Kutser, T., Tranvik, L.J., 2012. Automated mapping of water bodies using Landsat multispectral data. Limnology and Oceanography: Methods 10, 1037-1050.

Vickers, H., Eckerstorfer, M., Malnes, E., Larsen, Y., Hindberg, H., 2016. A method for automated snow avalanche debris detection through use of Synthetic Aperture Radar (SAR) imaging. Earth and Space Science 3, 446-462.

Wang, C., 2016. A remote sensing perspective of alpine grasslands on the Tibetan Plateau: Better or worse under 'Tibet Warming'? Remote Sensing Applications: Society and Environment 3, 36-44.

Wang, X., Gong, P., Zhao, Y., Xu, Y., Cheng, X., Niu, Z., Luo, Z., Huang, H., Sun, F., Li, X., 2013. Water-level changes in China's large lakes determined from ICESat/GLAS data. Remote Sensing of Environment 132, 131-144.

Wilhelm, C., Wiesinger, T., Bründl, M., Ammann, W., 1999. The avalanche winter 1999 in Switzerland - An overview. Proc. of the 2000 International Snow Science Workshop. Montana, USA, pp. 487-494.

Xu, H., 2006. Modification of normalised difference water index (NDWI) to enhance open water features in remotely sensed imagery. International Journal of Remote Sensing 27, 3025-3033.

Yamazaki, D., Trigg, M.A., Ikeshima, D., 2015. Development of a global ~90m water body map using multi-temporal Landsat images. Remote Sensing of Environment 171, 337-351.

Yang, K., Smith, L.C., 2013. Supraglacial streams on the Greenland ice sheet delineated from combined spectral-shape information in high-resolution satellite imagery. IEEE Geoscience and Remote Sensing Letters 10, 801-805.Valentin, C., Poesen, J., Li, Y., 2005. Gully erosion: Impacts, factors and control. Catena 63, 132-153.

Yang, M., Nelson, F.E., Shiklomanov, N.I., Guo, D., Wan, G., 2010. Permafrost degradation and its environmental effects on the Tibetan Plateau: A review of recent research. Earth-Science Reviews 103, 31-44.

Yang, W., Yao, T., Xu, B., Wu, G., Ma, L., Xin, X., 2008. Quick ice mass loss and abrupt retreat of the maritime glaciers in the Kangri Karpo Mountains, southeast Tibetan Plateau. Chinese Science Bulletin 53, 2547-2551.

Yang, X., Lu, X., 2014. Drastic change in China's lakes and reservoirs over the past decades. Scientific Reports 4, 1-10.

Yao, T., Thompson, L.G., Mosbrugger, V., Zhang, F., Ma, Y., Luo, T., Xu, B., Yang, X., Tayal, S., Jilani, R., Fayziev, R., 2012. Third Pole Environment (TPE). Environmental Development 3, 52-64.

Yao, T., Thompson, L., Yang, W., Yu, W., Gao, Y., Guo, X., Yang, X., Duan, K., Zhao, H., Xu, B., Pu, J., Lu, A., Xiang, Y., Kattel, D.B., Joswiak, D., 2012. Different glacier status with atmospheric circulations in Tibetan Plateau and surroundings. Nature Climate Change 2, 663-667.

Zevenbergen, L.W., Thorne, C.R., 1987. Quantitative analysis of land surface topography. Earth Surface Processes and Landforms 12, 47-56.

Zhang, G., Xie, H., Kang, S., Yi, D., Ackley, S.F., 2011. Monitoring lake level changes on the Tibetan Plateau using ICESat altimetry data (2003-2009). Remote Sensing of Environment 115, 1733-1742.

Zhang, Y., Yao, T., Ma, Y., 2011. Climatic changes have led to significant expansion of endorheic lakes in Xizang (Tibet) since 1995. Sciences in Cold and Arid Regions 3, 463-467.

Zhu, L.P., Xie, M.P., Wu, Y.H., 2010. Quantitative analysis of lake area variations and the influence factors from 1971 to 2004 in the Nam Co basin of the Tibetan Plateau. Chinese Science Bulletin 55, 1294-1303.

Zhu, W., Jia, S., Lv, A., 2014. Monitoring the fluctuation of Lake Qinghai using multi-source remote sensing data. Remote Sensing 6, 10457-10482.